TECHNICAL UNIVERSITY OF MOLDOVA

JOURNAL OF ENGINEERING SCIENCE

Technical and applied scientific publication founded on 9 February 1995
Alternative title: Meridian ingineresc

2024
Vol. XXXI (4)

ISSN 2587-3474
eISSN 2587-3482

TECHNICAL UNIVERSITY OF MOLDOVA (PUBLISHING HOUSE)
„TEHNICA UTM" (PRINTING HOUSE)

According to the Decision of the NAQAER No. 12 from 23.02.2024, JES is classified as B+ journal

Main subjects areas of the Journal of Engineering Science:

A. Industrial Engineering

- Mechanical Engineering and Technologies
- Applied Engineering Sciences and Management
- Materials Science and New Technologies
- Electrical Engineering and Power Electronics
- Energy systems
- Light Industry, New Technologies and Design
- Industrial and Applied Mathematics
- Vehicle and Transport Engineering

B. Electronics and Computer Science

- Electronics and Communication
- Microelectronics and Nanotechnologies
- Biomedical Engineering
- Computers and Information Technology
- Automation

C. Architecture, Civil and Environmental Engineering

- Architecture, Urbanism and Cadaster
- Civil Engineering and Management
- Energy Efficiency and New Building Materials
- Environmental Engineering

D. Food Engineering

- Food Technologies and Food Processes
- Food Industry and Management
- Biotechnologies, Food Chemistry and Food Safety
- Equipment for Food Industries

The structure of the journal corresponds to the classification of scientific publications: ***Engineering, Multidisciplinary.***

How to publish a paper:

1. Send the manuscript and information about the author to the **Editorial Board address:** jes@meridian.utm.md
2. Manuscripts are accepted only in English, by e-mail, in template file (www.jes.utm.md)
3. After a review, you will be notified of the editorial board's decision.
4. After the Journal has been published, we will send it to you immediately by mail.

Editor-in-Chief
Dr. hab. prof. univ. Viorel BOSTAN
Technical University of Moldova
viorel.bostan@adm.utm.md

Editorial Board

Responsible Editor
Dr. hab. Rodica STURZA
Editorial Board address: jes@meridian.utm.md

Editorial Production:
Dr. hab. Aliona Ghendov-Moșanu
Dr. Nicolae Trifan
Dr. Svetlana Caterinciuc
Dr. Rodica Cujba

CONTENT

CUPRINS

C. Architecture, Civil and Environmental Engineering

D. Food Engineering

Journal of Engineering Science *Vol. XXXI, no. 4 (2024), pp. 8 - 21*
Fascicle *Industrial Engineering* *ISSN 2587-3474*
Topic *Mechanical Engineering and Technologies* *eISSN 2587-3482*

https://doi.org/10.52326/jes.utm.2024.31(4).01
UDC 629.78:534.1(478)

STRUCTURAL ANALYSIS AND VIBRATION TESTING OF THE TUMnanoSAT MICROSATELLITE

Viorel Bostan, ORCID: 0000-0002-2422-3538,
Marin Guțu *, ORCID: 0000-0002-3745-0289,
Vladimir Melnic, ORCID: 0000-0003-4180-3654,
Alexei Martîniuc, ORCID: 0000-0003-3407-3016

Technical University of Moldova, 168 Stefan cel Mare Blvd., Chisinau, Republic of Moldova
* Corresponding author: Marin Guțu, *marin.gutu@pmai.utm.md*

Received: 10. 30. 2024
Accepted: 12. 14. 2024

Abstract. One of the important verification steps before the launch of the nanosatellite developed at Technical University of Moldova (TUMnanoSAT) was vibration testing of the real model. These tests were carried out according to the requirements submitted by the Japan Aerospace Exploration Agency (JAXA) in collaboration with which the launch of our nanosatellite was possible. Thus, in order to validate the structural integrity of CubeSat nanosatellites under launch loads, a 1U TestPod was designed and manufactured. This work presents hands-on experience of the vibration testing of the TUMnanoSAT microsatellite and simulation of static and dynamic loads. The dynamic behavior was analyzed by checking the harmonic oscillations (modal analysis and random vibrations) in order to avoid critical frequency (140 Hz). The testing facilities were provided by the Space Science Institute from Bucharest. The microsatellite was vibration tested in X, Y and Z axis directions according to special requirements. The numerical calculation model was developed in ANSYS Workbench. Comparison of the experimental results and numerical modal tests showed a good correlation within 10%.

Keywords: *CubeSat, modal survey, random vibration, static loads, simulation.*

Rezumat. Una dintre etapele importante de verificare înainte de lansarea nanosatelitului dezvoltat la Universitatea Tehnică a Moldovei (UTM) (TUMnanoSAT) a fost testarea la vibrații a modelului real. Aceste teste au fost efectuate în conformitate cu cerințele prezentate de Agenția Japoneză de Explorare Aerospațială (JAXA) în colaborare cu care a fost posibilă lansarea nanosatelitului nostru. Astfel, pentru a valida integritatea structurală a nanosatelitului de tip CubeSat sub sarcini de lansare, a fost proiectat și fabricat un TestPod 1U. Această lucrare prezintă experiența practică a testelor de vibrații a microsatelitului TUMnanoSAT și simularea sarcinilor statice și dinamice. Comportamentul dinamic a fost analizat prin verificarea oscilațiilor armonice (analiză modală și vibrații aleatorii) pentru a evita frecvența critică (140 Hz). Instalațiile de testare au fost puse la dispoziție de Institutul de Științe Spațiale din București. Microsatelitul a fost testat la vibrații în direcțiile axelor X, Y și Z în conformitate cu cerințele speciale. Modelul de calcul numeric a fost dezvoltat în

ANSYS Workbench. Comparația dintre rezultatele experimentale și testele modale numerice a arătat o bună corelație în limita a 10%.

Cuvinte cheie: *CubeSat, studiu modal, vibrații aleatorii, sarcini statice, simulare.*

1. Introduction

The CubeSat concept was first introduced in 1999 at Stanford University's Space Systems Development Laboratory and since then has gained widespread adoption across the globe. It was originally intended as an educational tool to allow students and researchers to design, build, and deploy small satellites at a fraction of the cost of traditional missions. Over time, CubeSats have become an important tool for commercial, governmental, and academic space missions. The current microsatellite launch project was achieved within the Cooperation Program for CubeSat Implementation of the International Space Station (ISS) from Japan, using the "KiboCUBE" experiment module. Such project is intended to provide the PhD and master students from Technical University of Moldova (TUM) the capacity to join the research for space technology and engages engineering students in a multi-disciplinary design process that will leverage their academic expertise across all backgrounds [1-3].

The standard CubeSat design is the 1-Unit (1U) CubeSat, which is a cube-shaped satellite measuring 100x100x113.3 mm and weighing up to 1.33 kg. CubeSats are typically launched as secondary payloads aboard larger rockets, often using deployers like the Small Satellites Orbital Deployer (SSOD), allowing reducing launch costs significantly.

Strict standards have been established for the structural integrity of CubeSats to withstand high static and dynamic loads during launch, while also ensuring the safety of nearby satellites. Like larger satellites, CubeSats must undergo rigorous testing to ensure they will function properly in the harsh space environment.

This includes thermal testing, vibration testing (to simulate launch conditions), and vacuum testing (to simulate the vacuum of space). The stiffness of structure must be designed so that its fundamental longitudinal and lateral frequencies meet the minimum values specified by the selected launcher. In addition to the necessary tests, thanks to the progress of computer technologies and numerical discretization methods, in the last decade various studies and simulations of the static and dynamic behavior of microsatellites have been carried out. Extensive recent research indicating methods for testing and analyzing the vibrations of satellites using ANSYS software are presented in the works [4–6]. Another interesting vibration analysis in COMSOL software and testing of a 6U CubeSat propulsion system is reported in the master thesis [7]. Aspects regarding the reduction of vibrations between the launcher and the satellite are presented in the master thesis [8] through the use of insulating materials.

A comprehensive approach to the design, analysis and optimization of a 2U Cubesat microsatellite using MSC Nastran software was performed by a team from University of Patras [9]. This work presents hands on experience of the vibration testing of the 1U TUMnanoSAT microsatellite, the simulation of the modal analysis and the correlation of the obtained results.

The testing facilities were provided by the Space Science Institute from Bucharest. The microsatellite was vibration-tested in the X, Y and Z axis directions. The numerical calculation model was elaborated in ANSYS Workbench 2021. Finally, the simulation results were validated with that of testing.

2. Numerical structural analysis of the microsatellite

2.1. Elaboration of the numerical calculation model

One of the stages of satellite design is the analysis of the behavior according to the operating conditions. This analysis consists of running virtual tests that may include the manufacturability test, an allowable stress analysis test, and the dynamic response analysis test. Carrying out such studies on the models leads to the optimization of the parts and increasing the ability to function in the desired environment. The virtual model of the satellite structure is tested several times, eliminating a good part of the real tests and achieving cost reduction. At the same time, the mass of the parts is also optimized, determining its minimum value to have an adequate structural strength.

Before conducting virtual satellite tests, it is necessary to prepare the appropriate geometry and establish the boundary conditions. For most spacecraft, including satellites, the greatest stresses occur during launch. These include g-acceleration (longitudinal and lateral) and random and harmonic vibration stress over different frequency ranges. The g-acceleration value is provided by the company that will provide the launch of the satellite. Once all the loads and launch characteristics are known, the structure can be modeled and tested using various modeling and simulation software (SolidWorks, Fusion 360, ANSYS, etc.). These applications provide various modules for manufacturability simulation and structural analysis of the created models. Manufacturability tests make it easy to determine the machining conditions of parts so that users can estimate the time, complexity and cost required to make them. Structural analysis tests facilitate the determination of the strength of the satellite assembly under specified launch and flight characteristics.

The geometry of the TUMnanoSAT satellite was developed in the SolidWorks 2020 software. The geometry was then imported into ANSYS Mechanical 2021 for finite element discretization and boundary condition imposition. All component elements were modeled with simplified geometries and equivalent masses were imposed to obtain the center of gravity approximately at the geometric center (Figure 1).

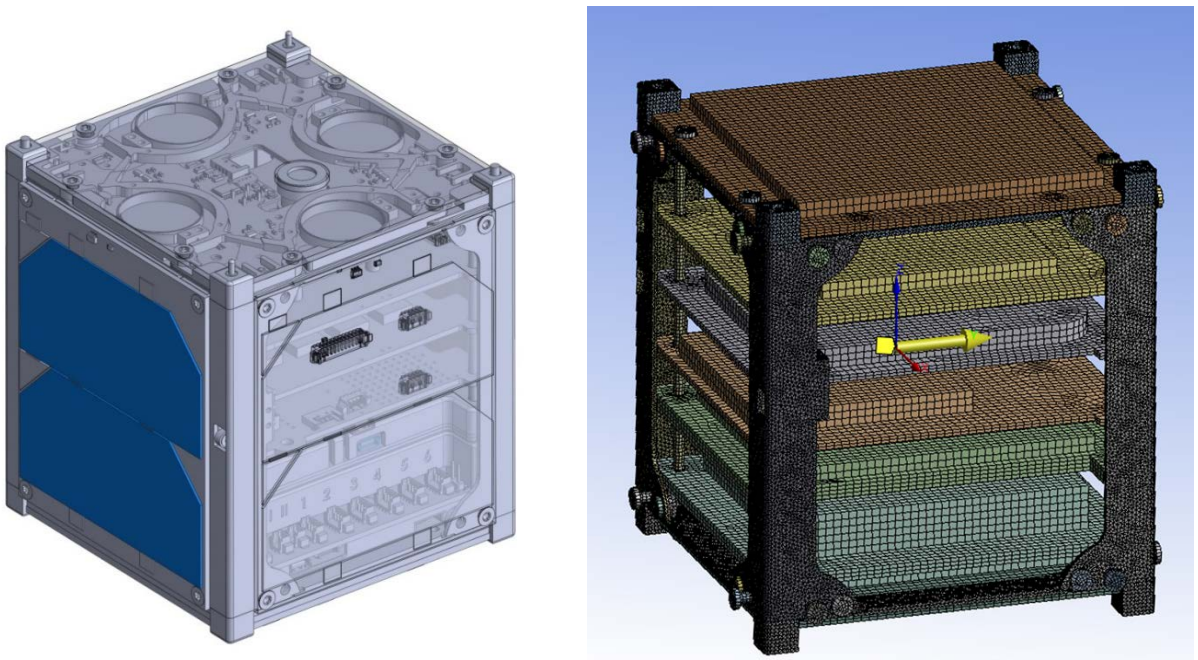

Figure 1. TUMnanoSAT 3D model and numerical calculation meshed model.

In order to perform the finite element analysis of the satellite in good conditions, the following simplifications were imposed:

- All internal components not on the main stress path have been replaced with a simulated point mass inside the structure. This mass is located at the center of the satellite or at the center of the simulated component and is connected to the main structure.

- The mass of external components outside the main structure, such as solar cells, has been included as a point mass fixed with the respective screws;

- Global bonded contact condition is used on fastener threads to eliminate errors created by bolts and complex geometry. The frictionless sliding contact condition is used at the component interface.

- Unnecessary threads and holes were suppressed from the structure parts;

- For the materials used, their real properties are applied;

- All fastening elements (screws) are pre-tensioned with axial forces equivalent to the admissible torque (Table 1).

In the result of the simulations, the following parameters of interest were analyzed: von Mises stresses, displacement, deformation and safety factor. After a series of simulations, the critical areas (where the safety factor is at the admissible limit) were detected and measures were taken to exclude them, such as changing the geometry or materials.

Table 1

Axial load of fastener

Type	Nominal diameter, m	Initial torque, Nm	Axial load, N
M3	0.003	0.63	1050

The imposed constraint conditions are presented in the Table 2 and the values of the static loads acting on the nanosatellite structure are presented in the Table 3."

Table 2

Constraint condition

Natural Frequency Analysis	-Z face of rails	Fixed Geometry (no translations)
	+Z face of rails	Fixed Geometry (no translations)
	Surface of rails contacted with J-SSOD	No constraint
	Thread face / contacted material	Global bonded contact
	Boundary condition between other materials	Frictionless sliding contact
Static Load Analysis / Bolt Analysis	-Z face of rails	Fixed Geometry (no translations)
	+Z face of rails	No constraint
	Surface of rails contacted with J-SSOD	No constraint
	Thread face / contacted material	Global bonded contact
	Bolt head / contacted material	Global bonded contact
	Boundary condition between other materials	Frictionless sliding contact

Table 3

Loading condition

	Loading condition	Applied location	Value
Natural Frequency Analysis	No load	-	-
Static Load Analysis / Bolt Analysis	Force	+Z face of rails	46.6N (each rail)
	Gravity / pretension	-	9 G (direction is changed in each analysis cases)

2.2. Static loads analysis

The model of the TUMnanoSAT satellite was tested (virtually) on the stress conditions for the three directions of the coordinate system (denoted by the letters A, B and C). The 3D mesh model of the satellite with the imposed loads for one case is presented in Figure 2.

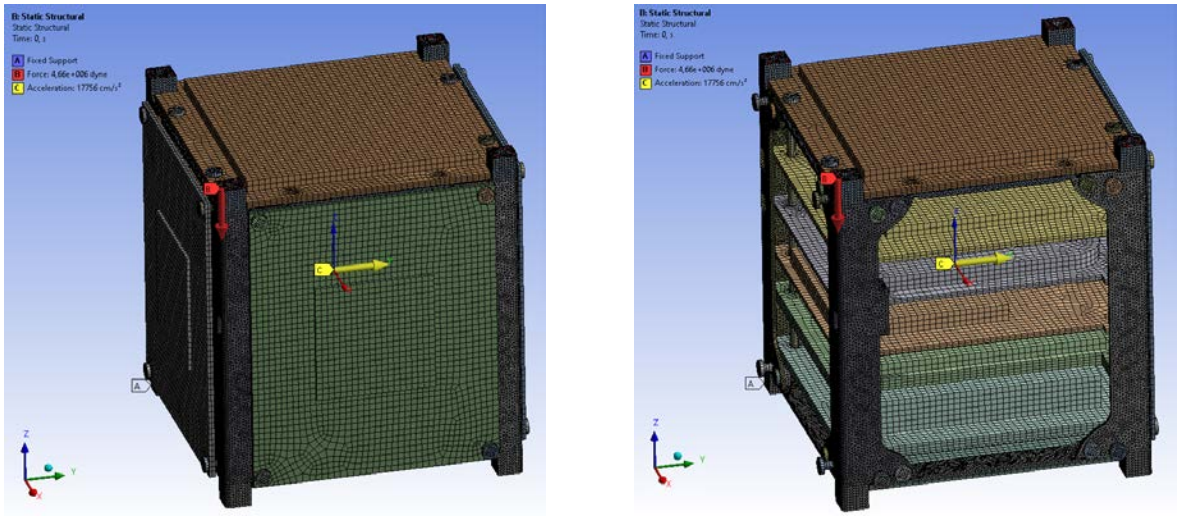

Figure 2. TUMnanoSAT 3D mesh model.

The analysis conditions are presented in Tables 4–6 and contain the following aspects:

a) Using the launcher's quasi-static acceleration levels, the model was subjected to a static load of 9G (88.3 $m \cdot s^{-2}$) in-plane with the launch axis (1G = 9.81 $m \cdot s^{-2}$);

b) An axial force of 46.6 N is applied to each rail;

c) Each rail is rigidly fixed at the base (-Z axis).

Table 4

Load applied on FEM (analysis A)

Load	X axis	Y axis	Z axis
Compressive Load	-	-	46.6 N
Static Load	9G	-	-

Table 5

Load applied on FEM (analysis B)

Load	X axis	Y axis	Z axis
Compressive Load	-	-	46.6 N
Static Load	-	9G	-

Table 6

Load applied on FEM (analysis C)

Load	X axis	Y axis	Z axis
Compressive Load	-	-	46.6 N
Static Load	-	-	9G

The results of the microsatellite model simulations are presented in Tables 7 – 9 for the three cases. After several trials and settings, the maximum von Mises stress values were obtained as 74 MPa, 67.6 MPa, and 10.3 MPa in analysis A, B, and C, respectively.

The margin of safety for the various frame components was calculated with the relationship below using a safety factor of 1.5 for the yield strength (F_{ty}) and 2.0 for the tensile strength (F_{tu}).

$$\mathrm{MS} = \frac{F_{tu}}{S_{max} \times FS} - 1 \geq 0. \quad (1)$$

The strength structure must also meet the following condition:

$$\frac{S_{max}}{F_{tu}} < 30\%, \quad (2)$$

where: S_{max} - maximum applied stress; F_{tu} - ultimate strength of the material.

Table 7

Satellite parts stresses and margin of safety (analysis A)

Part	Material	Max. Stress (S_{max}) (MPa)	Yield Strength Fty (MPa)	Ultimate Strength, Ftu(MPa)	MS*1 ⩾0 (yield) FS*2=1.5	MS*1 ⩾0 (Ultim.) FS*2=2	Smax/Ftu <30[%]
Main structure frame	Al 6061	74	275	310	1.48	1.09	23.9
Stacking rod	Al 6061	26.4	275	310	5.94	4.87	8.5

*1: Margin of safety, *2: Factor of safety

Table 8

Satellite parts stresses and margin of safety (analysis B)

Part	Material	Max. Stress (Smax) (MPa)	Yield Strength F_{ty} (MPa)	Ultimate Strength, F_{tu}(MPa)	MS*1 ⩾0 (yield) FS*2=1.5	MS*1 ⩾0 (Ultim.) FS*2=2	Smax/F_{tu} <30[%]
Main structure frame	Al 6061	67.6	275	310	1.71	1.29	21.8
Stacking rod	Al 6061	24.2	275	310	6.58	5.40	7.8

Table 9

Satellite parts stresses and margin of safety (analysis C)

Part	Material	Max. Stress (Smax) (MPa)	Yield Strength F_{ty} (MPa)	Ultimate Strength, F_{tu}(MPa)	MS*1 ⩾0 (yield) FS*2=1.5	MS*1 ⩾0 (Ultim.) FS*2=2	Smax/F_{tu} <30[%]
Main structure frame	Al 6061	10.3	275	310	16.80	14.05	3.3
Stacking rod	Al 6061	7.1	275	310	24.82	20.83	2.3

For example, in Figure 3, selective views of the constraint conditions and the distribution of equivalent stresses on the elements of the satellite structure for the Z direction load case are presented.

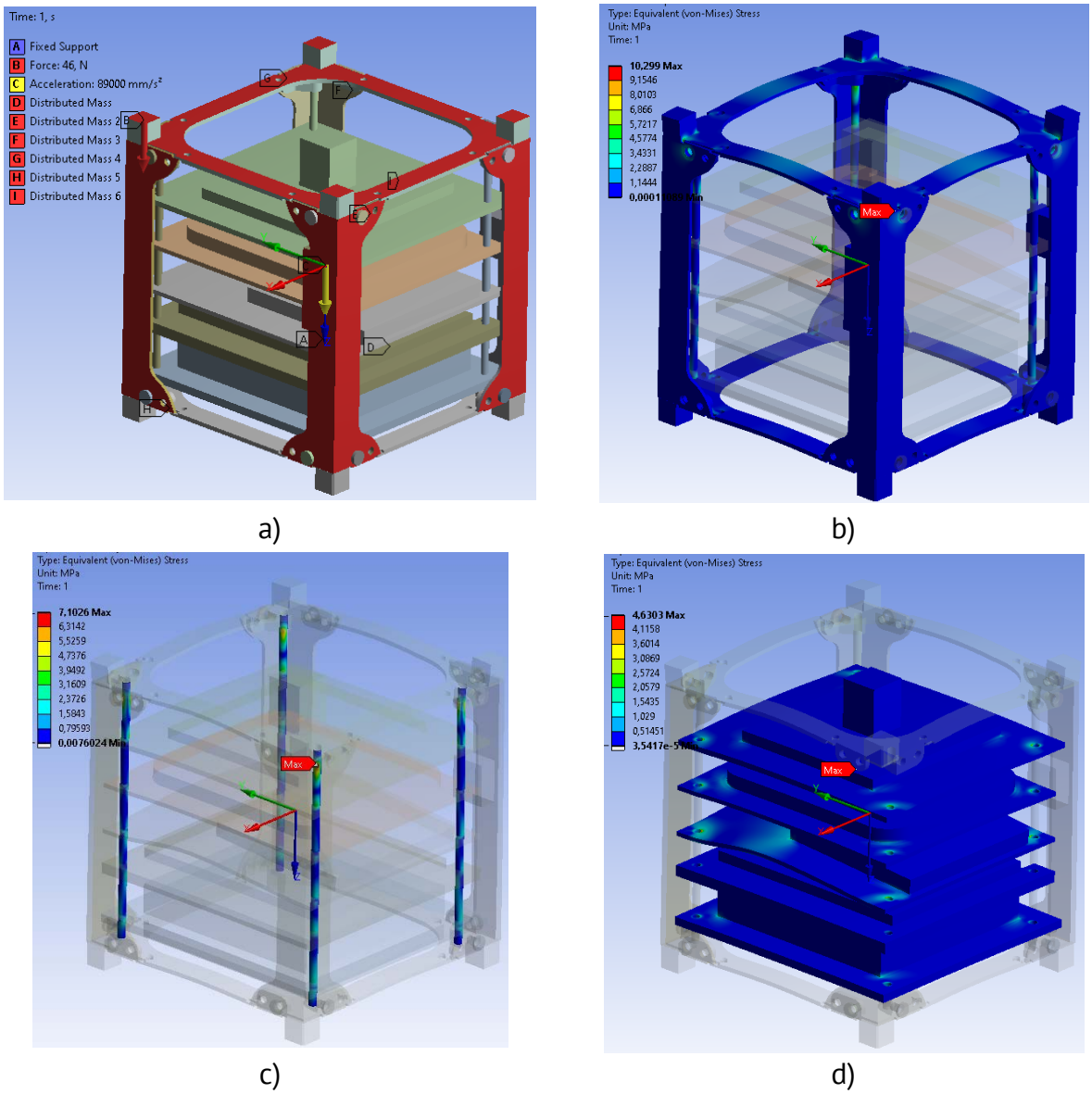

Figure 3. Result for analysis C (Z direction acceleration): a) load location; b) distribution of equivalent stress in main structure frame; c) – in stacking rod; d) – in internal components.

2.3. Dynamic loads analysis

The dynamic behavior of the satellite is analyzed by checking the harmonic oscillations (eigenfrequencies). These checks are necessary to detect the occurrence of the resonance phenomenon. The checking of the harmonic oscillation shapes and eigenfrequencies was performed using the ANSYS Modal Analysis application in the Workbench platform. The simulations were performed separately for TestPod and microsatellite. The 3D model of the TestPod was developed in the SolidWoks 2020 application, Figure 4a. The numerical calculation model was elaborated in ANSYS Workbench after the geometry was imported. The model was discretized into more than 122800 finite elements, Figure 4b.

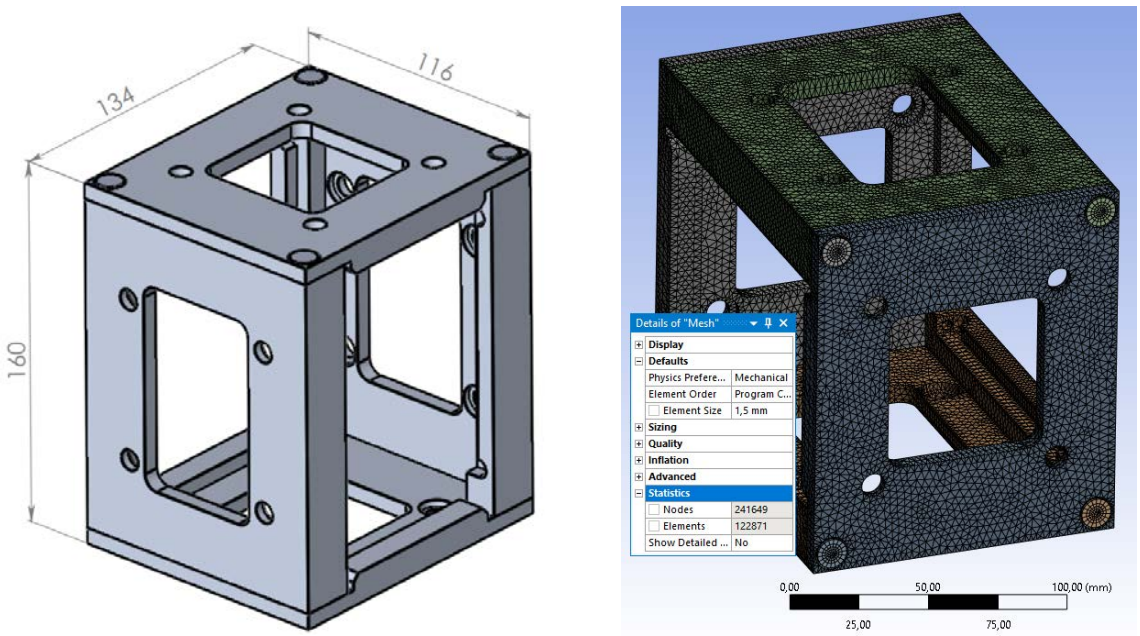

a) b)

Figure 4. TestPod modal analysis calculation model: a) geometry; b) discretized model.

In order to cover the frequency range 20-2000 Hz in which the vibration tests take place, it was sufficient to set six natural frequency modes. The first principal mode of the TestPod deformation for the axis Y and Z is presented in Figure 5.

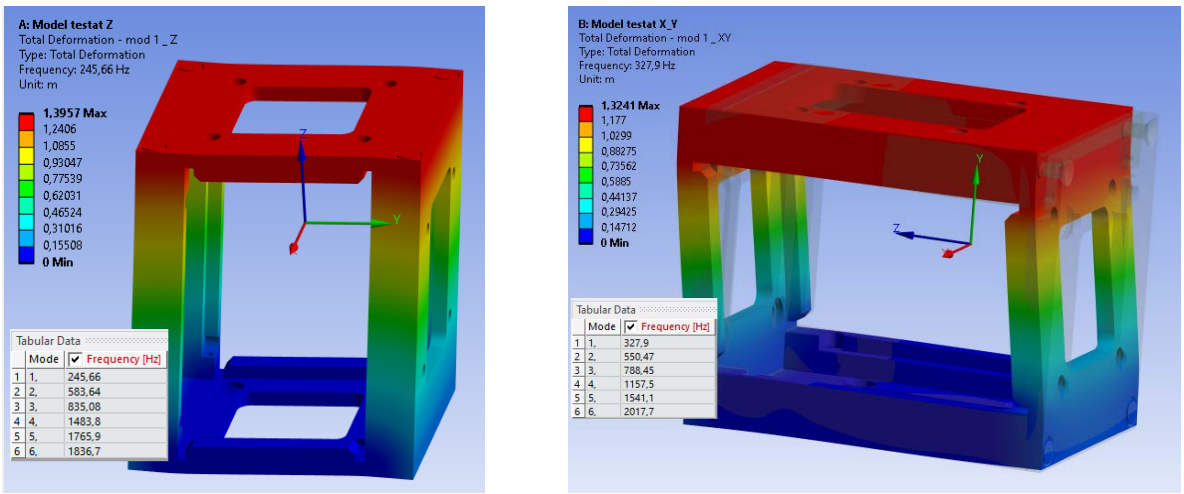

a) b)

Figure 5. TestPod first eigenform: a) Y axis; b) Z axis.

The microsatellite modal analysis simulation took place according to JAXA recommendations. Thus, to simplify the computational model of the microsatellite, the PV cells on the 6 faces were replaced by equivalent masses. In order to emulate the microsatellite mounting conditions in TestPod, the four rails of the satellite structure were fixed at both ends, similar to the boundary conditions presented in [10]. The numerical calculation model is the same as in the static analysis (Figure 1). The modal analysis is a general one and has not been done distinctly on the 3 axes due to software limitations. On the other hand, validating the results of the simulations is more difficult because during the vibration tests the measurements are made only on the TestPod body. The first eigenform of the microsatellite vibration and 6 natural frequency range are illustrated in Figure 6*a*. For comparison, a simulation was performed under the conditions of fixing only one end of the rails of the satellite structure. The results are presented in Figure 6b.

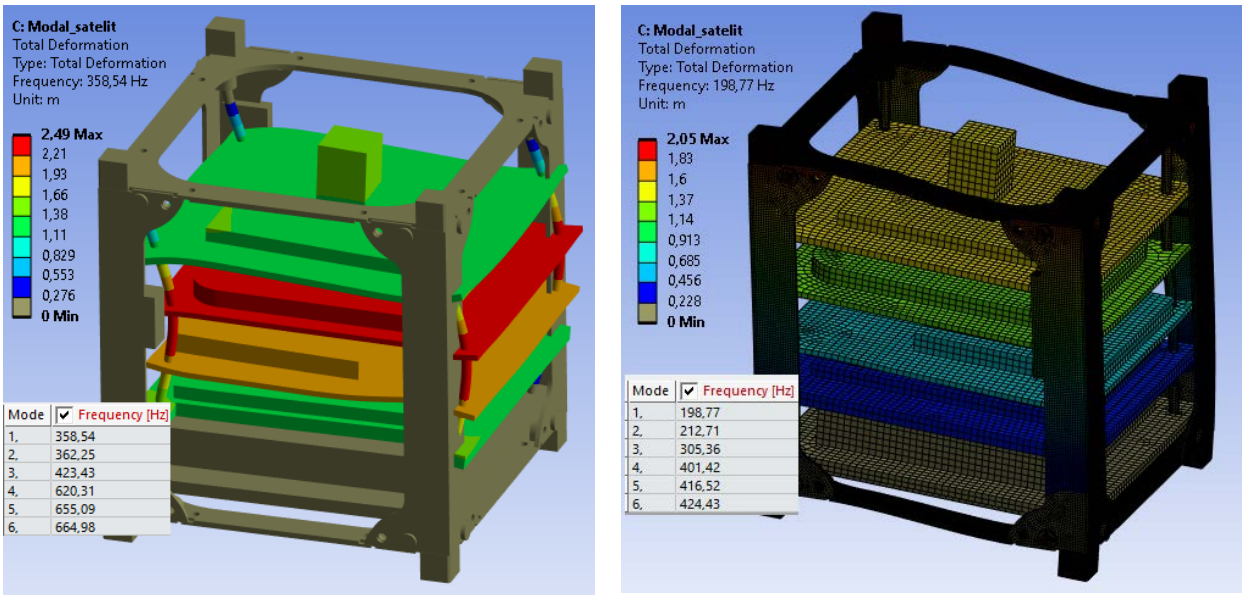

a) b)

Figure 6. Microsatellite first eigenform: a) 4 rails both fixed end; b) 4 rails one fixed end.

3. Experimental vibration testing

2.1. Equipment and work steps

The microsatellite vibration test methodology foresees the following verification: the presence of fractures in the main structure; the main structure must satisfy the specified natural frequency (>140 Hz); the natural frequency before and after testing must remain unchanged; fracture of glass elements such as photovoltaic cells; loosening of fasteners.

Vibration tests were performed along the X, Y and Z axes and according CubeSat general testing flow diagram [11]. These include low level sinusoidal scanning (modal survey) and random vibration [12]. Low-level sinusoidal scanning is suitable for model checking of simple structures with relatively rigid components whose flexibility is limited to mounting brackets or frequency isolation devices.

Before the nanosatellite test, according to the requirements, the empty TestPod was tested on the Y and Z axes (for the X axis the nanosatellite can be repositioned inside the Pod). The TestPod was designed and manufactured at TUM FabLab facilities according 1U CubeSat standard and available testing facilities requirements at Bucharest Space Science Institute.

According to JEM Small Satellites Orbital Deployer the following test sequences should be performed, Table 10.

Table 10

Test sequence

Sequence	Test Contents
Before vibration test	Visual inspection of satellite
X, Y, Z – axis test*	Random vibration test (without satellite) Satellite setup Modal survey Random vibration test Modal survey
After vibration test	Visual inspection of satellite Function test of satellite

The TestPod mounted on the test Jig is presented in Figure 7a and with nanosatellite inside - Figure 7b. The attached accelerometer generates a voltage signal that corresponds to the amount of vibration and the frequency of vibration the machine is producing.

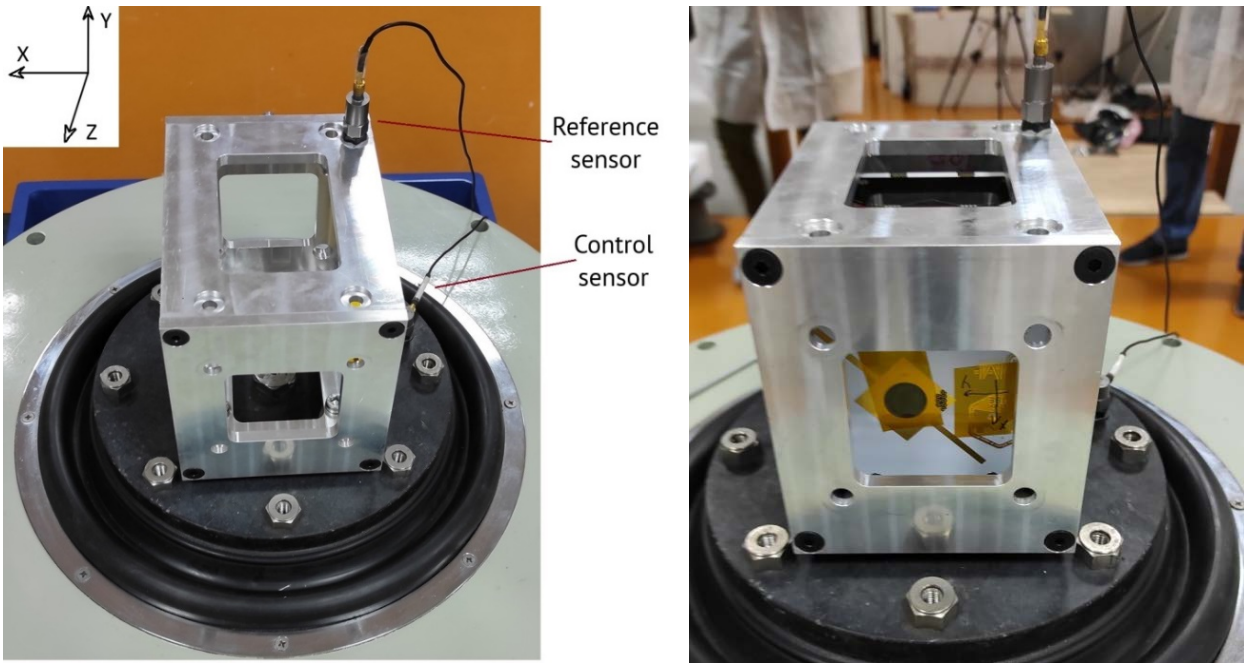

a) b)

Figure 7. CubeSat test configuration: a) empty TestPod; b) TestPod with satellite.

The characterization of random vibration typically results in a frequency spectrum of Power Spectral Density (PSD) or acceleration response over frequency domain (ASD) which designates the mean square value of some magnitude passed by a filter, divided by the bandwidth of the filter.

This parameter is measured in g^2/Hz. The random vibrations are generated by the operation of the space launcher propulsion system and by the vibro-acoustic response of the adjacent structure, [13]. Vibration test level is presented in the Table 11.

The random vibration test control sensor response for the axis X is presented in Figures 8a (empty TestPod) and 8b (with Satellite). For the other axes the diagrams do not show significant differences.

Table 11

Random vibration test level

Freq. [Hz]	PSD [G^2/Hz]
20	0.02
40	0.02
80	0.04
500	0.04
2000	0.01
Overall	6.79 Grms
Duration	1 min/axis
Direction	3 axes each

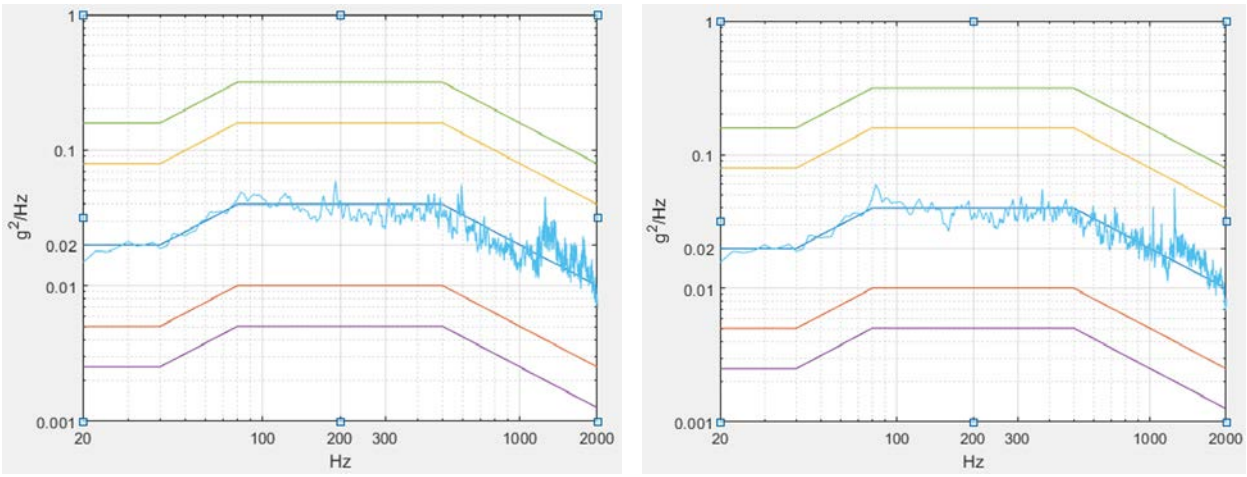

a) b)

Figure 8. Random vibration test control sensor response for the axis X; *a)* and *b)* random vibration test control sensor response.

As can be seen on the diagram, different colored profiles are drawn to indicate the limits of permissible and critical vibration level, Table 12.

Table 12

Admissible and critical limits of the vibration level

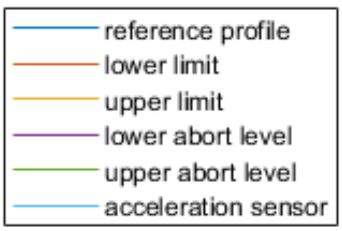

Reference profile: a baseline or target vibration level that the system is expected to achieve under normal operating conditions.
Lower limit: the minimum acceptable level of vibration. Any reading below this line may indicate a problem, such as insufficient excitation or sensor failure.
Upper limit: the maximum allowable level of vibration under normal operating conditions. Exceeding this limit may suggest potential component damage or wear.
Lower and Upper abort level: This is a critical threshold. If the measured vibration level exceeds this limit, the system should be shut down immediately to prevent further damage.
Acceleration sensor: This line represents the actual measured vibration levels obtained from the acceleration sensor (real-time data).

The test level in the modal study is shown in Table 13. Acceleration data measured by modal survey are illustrated in Figure 9. The blue line graph shows the response of the acceleration sensor.

Table 13

Modal survey vibration environment

Measurement axis	Frequency, Hz	Amplitude, G	Sweep Rate, Oct/min	Sweep Direction
Each axis	20~2000	0.5	1	Sweep up/Once

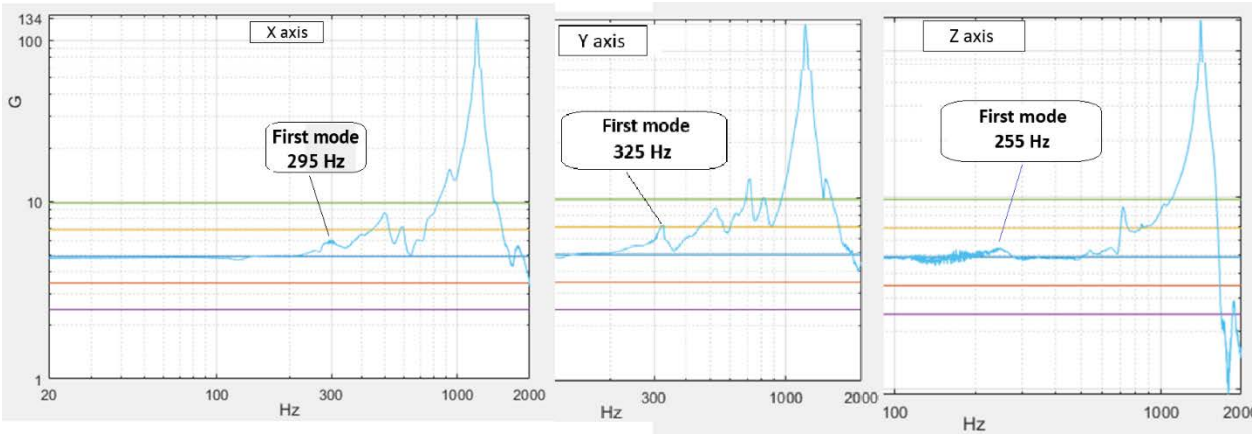

Figure 9. Modal testing results.

3. Results and discussions

No distortion or damage to the TUMnanoSAT microsatellite and solar battery was observed during and after vibration tests. Also, by visual inspection, no loosening of the main structure fasteners and no damage to the glass elements (camera lens and PV cells) were found. The natural frequency at the lowest order of TUMnanoSAT was above 140 Hz, which satisfies the stiffness requirements specified by JAXA.

Static load analysis shows the following results. The value of minimum margin of safety obtained for yield strength is 1.48 and for ultimate strength is 1.09 satisfying the condition (1). Another resistance condition (2) calculated with the ratio of maximum applied stress and ultimate strength of the material <30% is also satisfies (the maximum value obtained ≈24%). The maximum equivalent stress (74 MPa) occurred in main structure frame made from Al 6061. For the comparison, in the research carried on 3U CubeSat structure analysis [14] made from Aluminum alloy 6061 and 6082 with very close properties, the maximum stress was 76.2 MPa and occurred in the C-rib of the middle stack.

Vibration tests also validate the computational model and simulations of the dynamic stresses of the microsatellite within acceptable limits. The natural frequencies of the first modes obtained in the simulations and experiments are included in Table 14.

Table 14

Experimental and numerical modal test results comparison

Axis	1st mode test freq., Hz	1st mode simulation freq., Hz		Results sensitivity, %
		TestPod	Microsatelite	
X	295	328	359	0.9 – 9.5
Y	325			
Z	255	246		

The maximum difference in the results is less than 10%. For the comparison, the difference in frequency of simulation and test results presented in the paper [15] is less than 5%. Another research [16] demonstrates the first six natural frequencies of the test pod were generated with an average 7% error and an average 4% error for the first eight modes of the test pod with mass model assembly.

The main source of errors can be attributed to the geometrical complexity of the microsatellite assembly whose geometry was simplified in the numerical model in order to save time and computing resources. On the other hand, strict requirements on the accuracy of the simulations were not imposed. In further research we propose to develop a computational model, simulation and testing of a 2U CubeSat prototype.

5. Conclusions

The TUMnanoSAT design meets the structural requirements for space purposes. The static and dynamic analyzes show that the assembly is robust and will withstand high static and dynamic loads during the launch. The value of minimum margin of safety obtained for yield strength is 1.48 and for ultimate strength is 1.09 satisfying the condition (1). Another resistance condition (2) calculated with the ratio of maximum applied stress and ultimate strength of the material <30% is also satisfies (the maximum value obtained ≈24%).

Vibration tests also validate the computational model and simulations of the dynamic stresses of the microsatellite within acceptable limits. The maximum difference in frequency of simulation and test results is less than 10%.

The computational model is experimentally validated with good accuracy and can be applied for the analysis of microsatellites with different configuration.

Conflicts of interest: The authors declare no conflict of interest.

References

1. Bostan, V.; Secrieru, N.; Ilco, V.; Melnic, V.; Martîniuc, A.; Varzaru, V. TUMnanoSAT nanosatellite and Kibocube program. In: *13th International Conference on Communications (COMM),* 2020 Jun 18, pp. 503-508. https://doi.org/10.1109/COMM48946.2020.9142025
2. Bostan, V.; Bostan, I.; Ilco, V.; Melnic, V.; Martiniuc, A.; Vărzaru, V.; Secrieru, N.; Guțu, M.; Verjbițki, V.i; Magariu, N.; Lupan, O. *KIBOCUBE Program: Challenges and experience of the Technical University of Moldova in nanosatellite development*. Bons Office, Chisinau, Republic of Moldova, 2022, 259 p. [in Romanian].
3. Cappelletti, C.; Robson, D. *CubeSat missions and applications*, Cubesat Handbook. Academic Press, Nottingham, United Kingdom 2021, pp. 53-65, https://doi.org/10.1016/B978-0-12-817884-3.00002-3
4. George, I. B.; Hesham, H. I.; Mina, A. F. Static and random vibration analyses of a university CubeSat project. *Journal of Physics*: *Conf. Ser.* 2019, 1264, doi:10.1088/1742-6596/1264/1/012019.
5. Herrera-Arroyave, J. E.; Bermúdez-Reyes, B.; Ferrer-Pérez, J. A.; Colin, A. CubeSat system structural design. In: *67th International Astronautical Congress*, Guadalajara, Mexico, 2016, 67.
6. Warnakulasuriya, H. S. Vibration analysis and testing of a satellite structure during its launch and in-flight stages. Second cycle (master), Politecnico di Torino, Italy, 2021.
7. Girijadevi, L. T. Vibration analysis and testing of a 6U CubeSat propulsion system. Second cycle (master), KTH Royal Institute of Technology, Stockholm, Sweden, June 2023.
8. Furger, S. Analysis and mitigation of the Cubesat dynamic environment. Second cycle (master), California Polytechnic State University, USA, May 2013.
9. Ampatzoglou, A.; Kostopoulos, V. Design, analysis, optimization, manufacturing, and testing of a 2U Cubesat. *International Journal of Aerospace Engineering* 2018, 9724263, https://doi.org/10.1155/2018/9724263
10. Raviprasad, S.; Nayak, N. S. Dynamic analysis and verification of structurally optimized Nano-Satellite systems. *Journal of Aerospace Science and Technology* 2015, pp. 78-90. doi: 10.17265/2332-8258/2015.02.005

11. Morettini, G.; Zucca, G.; Braccesi, C.; Cianetti, F.; Dionigi, M. CubeSat spatial expedition: An overview from design to experimental verification. In: *IOP Conf. Ser.: Mater. Sci. Eng.* 2021, 1038, 012026. DOI: 10.1088/1757-899X/1038/1/012026
12. Sakamoto, H. *Introduction to Nano-Satellite Structures*. Tokyo Institute of Technology, Japan 2021 Available online: https://www.unoosa.org/documents/pdf/psa/access2space4all/KiboCUBE/AcademySeason2/On-demand_Pre-recorded_Lectures/KiboCUBE_Academy_2021_OPL11.pdf (accessed on 28.11.2024).
13. Romero-Alva, V.; Roman-Gonzalez, A. Nanosatellite Vibration Test Equipmentn. In: *68th International Astronautical Congress*, Sep 2017, Adelaide, Austria, 2017.
14. Eriksson, C. J. Finite element analysis of stresses in the MIST CubeSat due to dynamic loads during launch. Second cycle (master), KTH Royal Institute of Technology, Stockholm, Sweden, 2021.
15. Elshaal, A.; Okasha, M.; Sulaeman, E.; Halim Jallad, A.; Aizat, W. F.; Alzubaidi, A. B., Structural Analysis of AlAinSat-1 CubeSat. *The Egyptian Journal of Remote Sensing and Space Sciences* 2024, 27(3), pp. 532-546. https://doi.org/10.1016/j.ejrs.2024.06.006
16. Rivera, P.; Elghandour, E.; Wu, X. Numerical analysis study to validate experimental vibration results of CubeSats. *Inderscience Enterprises* 2021, 5(4), pp. 285-313.

Citation: Bostan, V.; Guțu, M.; Melnic, V.; Martîniuc, A. Structural analysis and vibration testing of the TUMnanoSAT microsatellite. *Journal of Engineering Science* 2024, XXXI (4), pp. 8-21. https://doi.org/10.52326/jes.utm.2024.31(3).01.

Submission of manuscripts: jes@meridian.utm.md

Journal of Engineering Science *Vol. XXXI, no. 4 (2024), pp. 22 - 32*
Fascicle *Industrial Engineering* *ISSN 2587-3474*
Topic *Applied Engineering Sciences and Management* *eISSN 2587-3482*

https://doi.org/10.52326/jes.utm.2024.31(4).02
UDC 616-089.226:681.586:004.8

ADVANCEMENTS IN SENSOR TECHNOLOGY FOR AUTONOMOUS WALKER

Isabel Seguí Verdú [1*], ORCID: 0009-0009-5976-3348,
Larisa Dunai [1], ORCID: 0000-0002-5076-0695,
Lilia Sava [2], ORCID: 0000-0002-4318-9486

[1] *Universitat Politècnica de València, C/Camino de Vera s/N. Valencia, 46022, Spain*
[2] *Technical University of Moldova, 168 Stefan cel Mare, Blvd., Chisinau, Republic of Moldova*
* Corresponding author: Isabel Seguí Verdú, *issever@doctor.upv.es*

Received: 11. 11. 2024
Accepted: 12. 18. 2024

Abstract. This study presents a detailed analysis of gait trajectory and orientation using Time of Flight sensors and Inertial Measurement Units during controlled movement tests in a robotic walker. The tests were performed on three distinct path configurations: straight-line, rectangular, and lemniscate paths. The Time-of-Flight sensors measured changes in distance, while the Inertial Measurement Units captured yaw and orientation data. Notably, during sharp turns, the Time-of-Flight sensors detected significant distance fluctuations corresponding to the directional changes captured by the Inertial Measurement Units yaw data. The results highlight the effectiveness of combining Time of Flight and Inertial Measurement Units data to track stable movement, detect sudden turns, and monitor orientation adjustments in complex trajectories. This combined approach can offer critical insights for gait analysis, rehabilitation, and robotics navigation.

Keywords: *walker, rollator, sensors, Inertial Measurement Units; Time-of-Flight sensors.*

Rezumat. Acest studiu prezintă o analiză detaliată a traiectoriei și orientării mersului, utilizând senzori Timpul de Zbor și Unități de Măsurare Inerțială, în timpul testelor de mișcare controlată efectuate cu un cadru robotic de mers. Testele au fost realizate pe trei configurații distincte de traseu: linie dreaptă, traseu dreptunghiular și traiectorie în formă de lemniscată. Senzorii Timpul de Zbor au măsurat modificările distanței, în timp ce Unități de Măsurare Inerțială a înregistrat datele privind yaw-ul și orientarea. În mod remarcabil, în timpul virajelor bruște, senzorii Timpul de Zbor au detectat fluctuații semnificative ale distanței, corespunzătoare schimbărilor de direcție înregistrate de datele yaw ale Unități de Măsurare Inerțială. Rezultatele evidențiază eficiența combinării datelor Timpul de Zbor și Unități de Măsurare Inerțială pentru a urmări mișcarea stabilă, a detecta virajele bruște și a monitoriza ajustările de orientare în traiectorii complexe. Această abordare combinată poate oferi perspective esențiale pentru analiza mersului, reabilitare și navigația robotică.

Cuvinte cheie: *cadru de mers, rollator, senzori, unități de măsurare* inerțială, *senzori, Timpul de Zbor.*

1. Introduction

By 2050, the world's populace will encounter a significant demographic transformation, characterized by a pronounced increment in the older demographic. The proportion of the demographic aged 65 years and above is projected to rise from 10% in the year 2022 to 16% by the year 2050 [1]. Even more remarkable is the anticipated triple of the cohort aged 80 and over during the same timeframe [2,3]. This swift proliferation of the senior population has generated increased interest in developing technologies designed to enhance senior citizens' quality of life, independence, and security.

Regions such as Japan, the United States, and Europe are among those exhibiting the highest percentages of elderly populations. In these areas, the global market for medical walking aids is forecasted to expand by 5% between 2022 and 2029 [4,5]

Furthermore, the World Health Organization (WHO) estimates that approximately 2.5 billion people worldwide [6] will require one or more assistive devices, underscoring the growing need for such technologies. Maintaining personal autonomy in old age is not only essential for physical health but also critical for psychological well-being. Walking aids, therefore, are increasingly used not just in therapeutic settings, but also in the day-to-day lives of senior citizens.

Among the essential technologies that support aging populations, walkers play a vital role. These devices have long been relied upon for providing mobility and independence to individuals with limited movement capabilities. Nonetheless, despite their prevalent application, conventional walkers frequently exhibit deficiencies concerning their functionality and flexibility in accommodating the evolving requirements of their users. As a result, there is a growing demand for innovations that enhance their functionality through intelligent monitoring systems and improved design. These improvements are not only crucial for facilitating movement but also for ensuring safety and monitoring the health of the elderly users who depend on them [7].

Considering these challenges, this paper presents the concept and evolution of a "smart walker," which is intended to support older adults in their everyday tasks. In contrast to conventional walkers, this innovative model integrates cutting-edge sensors capable of monitoring and evaluating the user's movements, thereby providing significant insights into their ambulation patterns. This information can subsequently be employed to identify potential problems such as balance issues or a heightened risk of falls. By incorporating user input throughout the design phase, the walker seeks to tackle real-life challenges while remaining cost-effective, ensuring that these cutting-edge technologies are available to a wider demographic of elderly individuals.

2. Materials and Methods

2.1. Surveys

The initial phase in the creation of this smart walker involves conducting thorough surveys with current walker users. In the survey 55 elderly people participated. The objective of these investigations was to collect data regarding the obstacles encountered by users and to ascertain prospective domains for enhancement in the design and operational efficacy of current walking aids. Among the most mentioned issues were challenges with maneuverability, insufficient feedback on walking performance, and safety concerns, especially regarding fall prevention. By administering these surveys, participants emphasized the need for a mobility aid that not only promotes walking but also provides real-time feedback on their gait dynamics and stability while moving.

The data gathered from the surveys, as shown in the Figure 1, provide valuable insights into the demographic distribution and the types of walkers currently used by individuals. It is imperative to acknowledge that a substantial proportion, exceeding fifty percent (51%), of the individuals surveyed were aged over 80 years, indicating that the necessity for advanced mobility assistance devices is particularly paramount for this age group. Furthermore, 27% of participants belong to the 71-80 age bracket, which further underscores the necessity of developing devices that specifically address the requirements of elderly individuals. Interestingly, only 11% of users were under the age of 60, underscoring that most walker users are from the senior population, where mobility challenges are more prevalent.

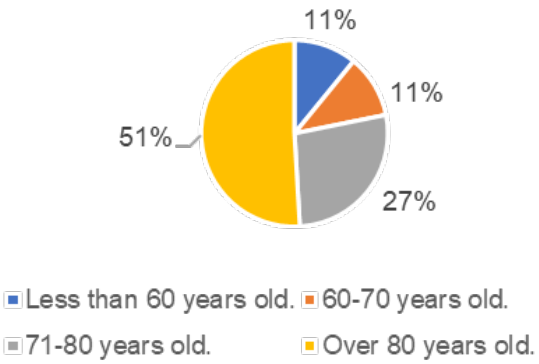

Figure 1. Age distribution of walkers users.

The Figure 2 reveals that a significant majority (73%) of users rely on walkers equipped with four wheels, suggesting that these devices are preferred for their stability and ease of use. However, 14% of users still utilize walkers without wheels, which may indicate a demand for greater support, but potentially at the expense of manoeuvrability. Utilization of walkers equipped with two wheels was reported by 9% of the participants, whereas a minor fraction (4%) of the respondents abstained from disclosing information pertaining to their specific type of walker. These results underscore the importance of incorporating real-time feedback mechanisms into walker designs, particularly for most users who are in the 80+ age bracket and primarily using four-wheeled walkers. For these users, safety and balance monitoring are critical due to the higher risk of falls. By focusing on these demographic and user preference insights, the development of the smart walker can address the most pressing concerns, ensuring that the device not only provides mobility support but also enhances safety and gait stability for older adults who are the primary users of such devices.

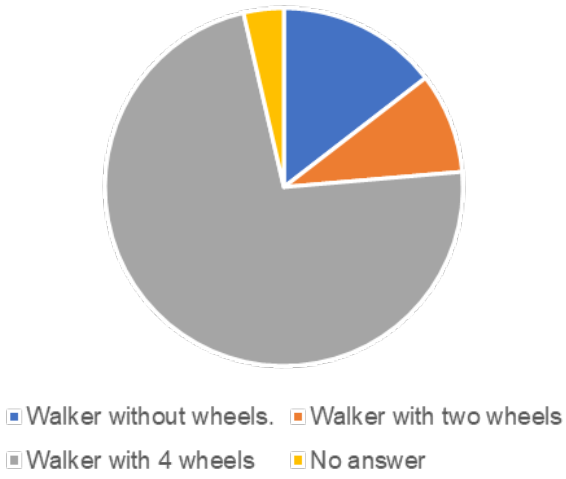

Figure 2. Types of walkers used by current users.

2.2. Prototype Design

The development of a smart walker began by sourcing cost-efficient components, including sensors and batteries, guided by user feedback to ensure practicality and affordability. The team modified a commercial walker by designing and installing prototypical supports for essential components such as batteries, screens, and regulators. These modifications allowed for the seamless integration of a custom-designed electronic board equipped with multiple sensors.

The constituent elements of the prototype were conceptualized employing Autodesk Inventor© and subsequently manufactured via additive manufacturing techniques, specifically utilizing polylactic acid (PLA) and resin materials, as illustrated in Figure 3. The selection of these materials was predicated on their robust durability and minimal weight characteristics, which are paramount for optimizing user comfort and facilitating ease of utilization.

As seen in Figure 3, the battery, controller, and other components were strategically placed to optimize the walker's functionality.

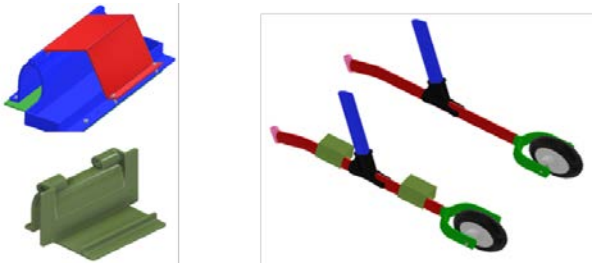

Figure 3. Age Distribution of Walkers Users.

Thanks to 3D printing, using materials such as polylactic acid (PLA) and resins, it is much easier and cheaper to create prototypes. In this way, it is possible to perfect at a lower cost the different prototypes of the parts that are necessary for our final prototype.

2.3. Design the electronic board

The inclusion of sensors in mobility aids such as walkers is crucial for monitoring and improving gait performance, especially for elderly users. These sensors assess gait in real time and provide precise data on speed, balance, and stability. This information helps detect gait issues that could indicate health problems or an increased risk of falls [8].

The electronic board, designed for scalability (Figure 4), uses a low-power ESP32 microcontroller with multiple communication interfaces and a 32-bit processor for real-time data processing. This setup allows for future updates and improvements.

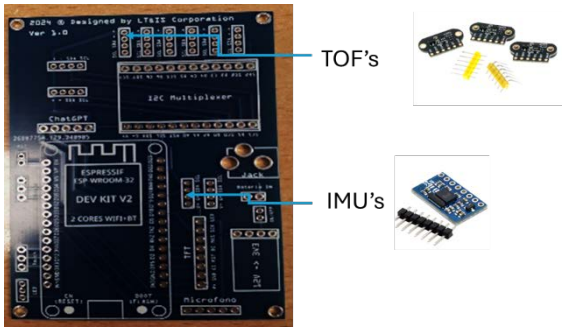

Figure 4. ESP32 Development Board with Integrated I2C Multiplexer, IMU BNO055 [9] and Sensor Connections VL53L1X [10].

The sensors integrated into the walker record speed, direction, and balance during use. The primary goal is for users to feel supported by technology, not overwhelmed by it. This data can be analyzed in real time to alert the user or caregiver of any unusual movement patterns that might suggest a higher risk of falling.

Various sensors have been incorporated on this board, including proximity sensors, heart rate sensors, and pressure modules. However, in this article we will focus specifically on the Time of Flight (ToF) and Inertial Measurement Unit (IMU) sensors [11,12]. These sensors are critical for motion analysis and accurate distance measurement, allowing for better stability assessment and early detection of imbalances during device use. When deciding where to locate the IMU, we analyzed which part of the walker would be best and decided to integrate everything within the board to protect the sensor [13].

2.4. Time of Flight sensors for user legs detection

Time-of-Flight (TOF) sensors are incorporated into robotic walker systems to provide precise, real-time distance measurements between the user's legs and the walker. These sensors operate by measuring the time it takes for emitted light to reflect off the user's legs, enabling accurate detection of leg position and movement, even during dynamic locomotion. The data collected by the TOF sensors is non-intrusive, high-resolution, and processed in real time, supporting critical functionalities such as gait cycle identification, continuous monitoring of leg motion and posture, and dynamic adjustment of the walker's speed to synchronize with the user's walking velocity.

The primary objective of integrating TOF sensors is to enhance gait analysis by offering detailed spatiotemporal metrics. These include measurements of step length and width, walking speed, and cadence, as well as postural assessments to evaluate alignment and stability.

$$Step\ Length = |x_{n+1} - x_n|, \tag{1}$$

where: x_n is the position of one foot and x_{n+1} is the position of the opposite foot in the forward direction.

$$Step\ Width = \left|d_{left} - d_{right}\right|, \tag{2}$$

where: $d_{left}\ and\ d_{right}$ are the distances from the sensor to the left and right legs respectively.

This information allows for the characterization of the user's walking patterns and facilitates improvements in mobility and ergonomics. By tracking these parameters, the sensors estimate walking speed and step frequency, enabling the robotic walker to adapt dynamically to the user's pace, ensuring synchronized operation.

TOF sensors also play a vital role in ensuring user safety and system adaptability. The system can autonomously halt or adjust its behaviour in response to irregularities in the user's gait, providing enhanced support and mobility. The integration of TOF sensors in robotic walkers creates a reliable platform for advanced gait analysis and real-time adaptability, significantly improving user mobility, stability, and rehabilitation outcomes.

2.5. Wrapping effect of the IMU correction

Due to the cyclical nature of angular measurements from Inertial Measurement Unit (IMU) sensors, particularly when orientation is represented using Euler angles or yaw-pitch-roll conventions, a phenomenon known as the wrapping effect can occur. Angular data is

typically constrained within a fixed range (e.g., -180° to 180° or 0° to 360°), and transitions across these boundaries may result in discontinuities in the data, manifesting as abrupt changes or "jumps" in the recorded values.

The wrapping effect interfere real-time navigation, gait analysis, and trajectory prediction in robotic walkers. Effectively managing this issue ensures seamless data interpretation, enabling reliable performance even in complex environments. To address this issue and prevent the wrapping effect, is necessary to correct the IMU values using the following equation.

$$\theta_{unwrap}(n) = \theta(n) + 2\pi \cdot k \tag{3}$$

where: $\theta(n)$ is the original angle at index n; k is an integer correction factor, adjusted based on whether the difference between consecutive angles $\theta(n) - \theta(n-1)$ exceeds a threshold, typically set to π radians.

3. Results and Discussion

Three road configurations were used to test performance and maneuverability as in [14].

The length of the routes in the case of the rectangle is 4 meters deep and 1.2 meters wide as can be seen in Figure 5.

- Straight Line Tests (Red): These tests focused on basic metrics like speed, acceleration, and stability on a straight path without turns.
- Rectangular Road Tests (Green): This phase introduced right-angle turns, simulating urban conditions and evaluating the ability to handle sharp directional changes.
- Lemniscate Curve Tests (Orange): The final tests involved a more complex path shaped like a lemniscate curve to assess agility and control through continuous directional changes and sharp turns.

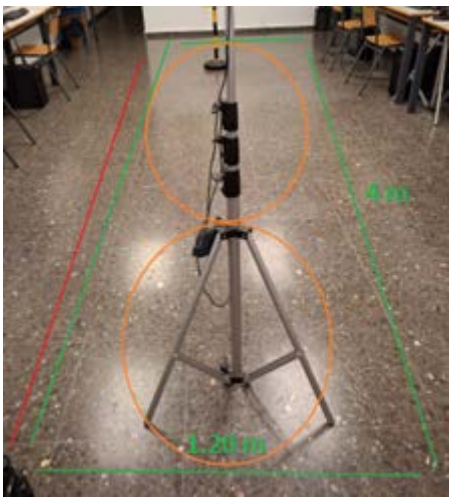

Figure 5. Paths configurations used in the laboratory test with the developed walker.
(It is originally developed by the authors).

In Figure 6, the TOF sensors are strategically positioned to detect the movement of the legs rather than focusing on the feet. This setup is designed to capture the dynamic range and motion of the legs, which provides more relevant data for gait analysis for our objective. Monitoring leg detection [15], rather than foot movement, is important because the legs provide a clearer picture of gait patterns, balance, and overall mobility in the walker.

Figure 6. Developed Walker with electronic board integrated in its structure.

The feet, on the other hand, are more influenced by minor changes in terrain or posture, which could distort the data related to the biomechanics of walking. Therefore, TOF sensors are better positioned to track the legs for a more accurate representation of the user's motion and gait characteristics.

In Figure 7, we can observe the representation of the trajectory and orientation analysis based on data obtained from 2 TOF's and 1 IMU sensors during a straight-line movement. The yaw angle in degrees indicates the orientation. TOF1 and TOF2 show the distance measurements captured by the TOF sensors during the movement. In the first samples (0-30), there is a significant increase in the measurements, indicating an initial movement but these movements were initial and stopped movements during the test, just movements of the legs. After those values, the fluctuations reflect adjustments in the measured distance as the person progresses, suggesting small movements or variations in the terrain.

The Yaw angle value, remains almost constant, indicating that the movement was mainly in a straight line without major turns. This is key for verifying directional stability during a straight path.

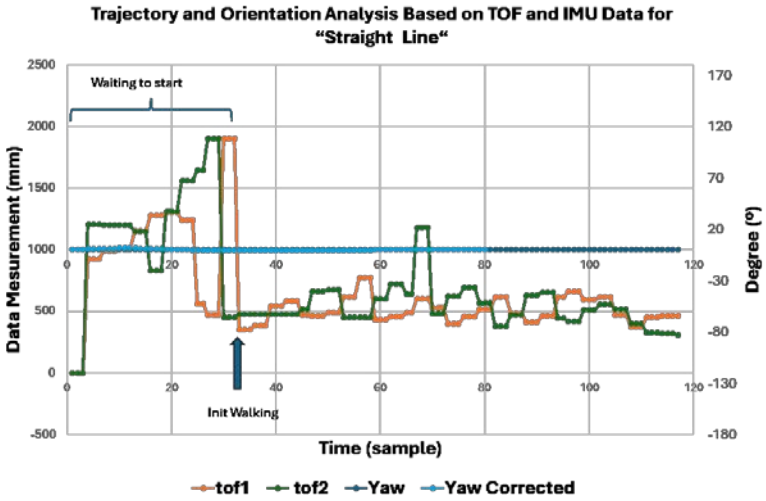

Figure 7. Visualization of a straight-line trajectory captured using Time of Flight (TOF) sensors combined with Inertial Measurement Units (IMUs).

In Figure 8, the analysis of trajectory and orientation during a rectangular-shaped movement is shown where TOF and IMU data were used to detect changes in distance and orientation. The horizontal sections of the trajectory are visible in the stable parts of the TOF1 and TOF2 lines. These parts represent when the subject is moving along the straight sections of the rectangle. The values for TOF1 and TOF2 remain relatively stable during these periods,

indicating that the distance to the environment does not change significantly, similar to what was observed in Figure 7 when analyzing the straight-line movement.

Figure 8 shows pronounced fluctuations and peaks in the TOF1 and TOF2 lines during the sharp turns of the rectangular trajectory. These are especially evident when the measurements increase or decrease rapidly, reflecting the abrupt directional changes, nearly 180º, as the subject turns the corners of the rectangle.

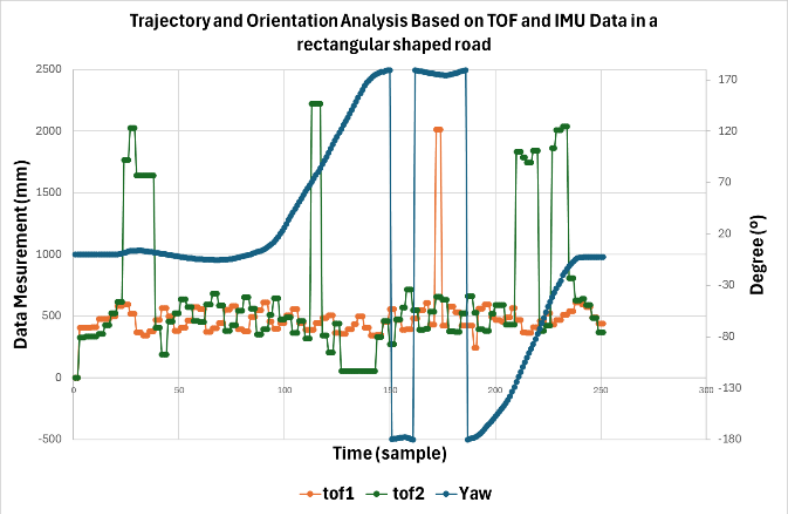

Figure 8. Visualization of a rectangular-shaped road trajectory captured using TOF/IMU sensors.

The rectangle is not wide, and there is little displacement needed to perform these turns, as can be seen in the following figure.

The yaw angle captures changes in orientation. As expected in the narrow rectangle, the yaw values show a rapid transition during the turns, where the orientation changes sharply. The IMU *wrapping effect* is also evident during these segments, as the yaw angle wraps around due to the IMU's limitations in representing continuous rotational data, leading to sudden changes in yaw values near ±180º.

This Figure 9 demonstrates how TOF and IMU sensors can detect both stable linear movements and sharp directional changes in a rectangular trajectory with a Yaw corrected from the unwrapping effect.

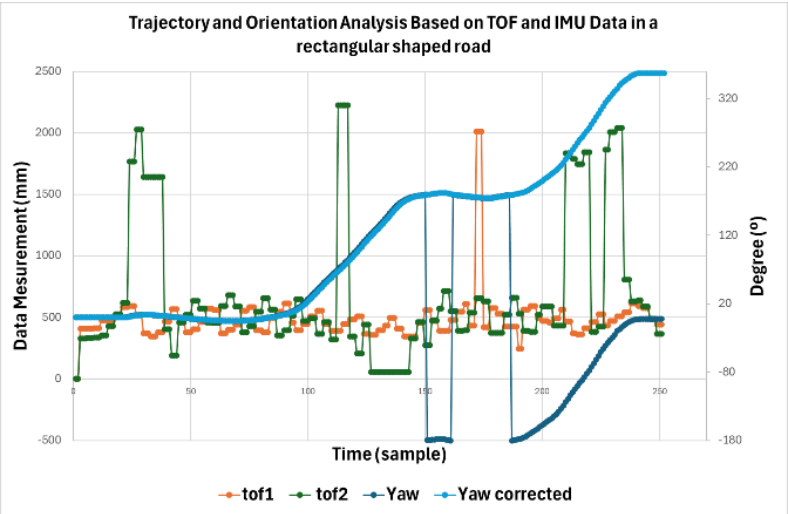

Figure 9. Visualization of a rectangular-shaped road trajectory captured using TOF/IMU sensors with corrected YAW of the wrapping effect.

In Figure 10, we observe how the TOF and IMU data together reflect the subject's movement through a lemniscate path. The TOF data show peaks that correspond to sharp turns in the trajectory. These peaks occur precisely at points where the subject is performing a directional change, aligning with the pronounced curves in the Yaw angle.

Yaw angle measures the orientation or rotation of the subject as they follow the lemniscate curve. The Yaw corrected line remains smooth, indicating how the IMU compensates for continuous directional changes and the wrapping effect during the Lemniscate Curve Tests. Around the middle of Figure 10, particularly after sample 150, there is a clear transition in Yaw, representing the subject making a significant turn along the curve. This transition highlights both large and small orientation adjustments, demonstrating the complexity of the lemniscate trajectory.

Overall, this Figure 10 illustrates how TOF data can detect sudden changes in direction, while the IMU provides detailed orientation information, compensating for the continuous directional shifts experienced in such complex paths. The combination of TOF and IMU allows for accurate tracking of both stable movements and abrupt turns throughout Lemniscate Curve Tests.

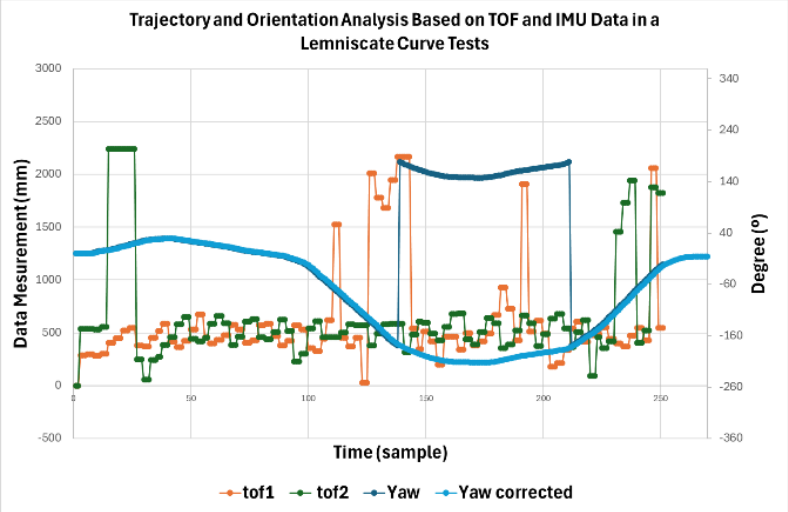

Figure 10. Visualization of the third test using a path shaped as a lemniscate curve.

According to the empirical data and analytical findings derived from the Time of Flight (TOF) and Inertial Measurement Unit (IMU) sensors depicted in the preceding figures. The combination of TOF and IMU sensors significantly increases the overall reliability and accuracy of the developed system. TOF sensors accurately detect variations in step distance, while the speed of these alterations indicates the individual's walking speed. This dual-sensor methodology provides comprehensive data on gait movement onset and gait speed.

TOF sensors exhibit marked efficacy in recognising abrupt directional deviations, as substantiated by pronounced spikes in the data. Concurrently, the IMU facilitates the smoothing of the yaw angle and mitigates challenges such as angle unwrapping. The TOF sensors specifically document alterations in foot movement, delivering real-time insights into the dynamics of walking.

Our inquiry reveals the capability to detect sudden gait modifications and abrupt directional shifts utilizing strategically positioned sensors and Inertial Measurement Units (IMUs). This proficiency is pivotal for comprehending and analysing distinctive locomotion patterns, particularly in individuals exhibiting atypical gait characteristics. By meticulously

capturing these swift transitions, our methodology provides profound biomechanical insights essential in contexts that necessitate stability and adaptive directional responses, such as rehabilitation or mobility assistance devices.

The lemniscate trajectory effectively encapsulates the curves users may encounter in urban environments. It serves as a valuable instrument for our testing, simulating authentic conditions. Our analysis indicates that the IMU data enables us to investigate the turning maneuvers along the lemniscate curve, while the TOF sensors yield detailed information regarding foot positioning and step count during locomotion.

The rationale underpinning our methodology resides in the high precision and immediate feedback our sensor system provides. By integrating IMUs with other sensors, we amass nuanced data that contributes to advancing sophisticated assistive technologies, including robotic walking aids or prosthetics. This data-centric strategy guarantees that forthcoming innovations can dynamically adapt to users' requirements, enhancing stability and safety across diverse environments.

Our testing identified areas for improvement in the performance of TOF sensors. For example, we observed that people with very thin legs or who walked with their legs too close together were sometimes not detected, which slightly affected the accuracy of the data. To improve our system, we propose integrating two TOF sensors per leg into future walker designs, providing greater redundancy and improving detection accuracy. Additionally, we noticed that low light conditions affected the performance of the TOF. To address this, we plan to add LED lights to the walker to improve visibility and ensure the sensors work optimally in both the front and rear sections.

These observations highlight opportunities for refinement and emphasise the importance of the proposed improvements, which will ensure more consistent and reliable data collection in various scenarios.

5. Conclusions

The combination of TOF and IMU sensors provides a robust system for analyzing movement trajectory and orientation changes, especially in complex paths like the lemniscate curve for robotic walkers.

TOF sensors are highly effective in detecting sharp directional changes, as evidenced by the pronounced peaks during turns, while the IMU's yaw data accurately reflects orientation shifts.

In narrow trajectories, such as the rectangular path, the system captures abrupt 180° turns, providing valuable insights into directional stability and control. The IMU wrapping effect, particularly in yaw measurements, requires consideration, as it can influence data interpretation when continuous rotations occur.

These findings demonstrate the potential application of this sensor fusion technique in fields like rehabilitation, robotics, and human motion tracking, where accurate trajectory and orientation analysis are essential.

Conflicts of Interest: The authors declare no conflict of interest.

References

1. Ageing and health (who.int). Available online: https://www.who.int/news-room/fact-sheets/detail/ageing-and-health#:~ (accessed on 05 November 2024).
2. Ageing, United Nations. Available online: https://www.un.org/en/global-issues/ageing (accessed on 05 November 2024).

3. World population projected to reach 9.8 billion in 2050, and 11.2 billion in 2100, United Nations. Available online: https://www.un.org/en/desa/world-population-projected-reach-98-billion-2050-and-112-billion-2100 (accessed on 05 November 2024).
4. Medical Mobility Aids Market Projected to Surge with 6-7% Growth over 2024-2029. Available online: https://meditechinsights.com/medical-mobility-aids-market/ (accessed on 05 November 2024).
5. Walking Aids Market Size & Share Report, 2022 - 2030. Available online: https://www.grandviewresearch.com/industry-analysis/walking-aids-market (accessed on 05 November 2024).
6. Assistive technology. Available online: https://www.who.int/news-room/fact-sheets/detail/assistive-technology (accessed on 05 November 2024).
7. Seguí-Verdú, I.; Dunai, L.; Antonio-Daviu, J. A. Exploring Ergonomic Advancements and Smart Technologies in Future Walkers. In: *IEEE 33rd International Symposium on Industrial Electronics* (ISIE), Ulsan, Korea, 2024, pp. 1-8, doi: 10.1109/ISIE54533.2024.10595750.
8. Ruiz-Ruiz, L.; Jimenez, A. R.; Garcia-Villamil, G.; Seco, F. Detecting Fall Risk and Frailty in Elders with Inertial Motion Sensors: A Survey of Significant Gait Parameters. *Sensors* 2021, 21(20), 6918.
9. Loureiro, M.; Machado, F.; Mello, R.; Frizera, A.Ensuring Proper Interaction: VR-Based Visual Feedback Interface for Smart Walker Training. In: *10th IEEE RAS/EMBS International Conference for Biomedical Robotics and Biomechatronics* (BioRob), Heidelberg, Germany, 2024, pp. 419-424, doi: https://doi.org/10.1109/BioRob60516.2024.10719706
10. Solikh, S.; Imammudin, A. M.; Rakhmania, A. E. Design and Development of Assistive Canes for the Blind Based on IoT-Integrated Fuzzy Logic Using LiDAR Sensor Time of Flight VL53L1X. *Journal of Telecommunication Network* (Jurnal Jaringan Telekomunikasi), 2024, 14(1), pp. 56-64.
11. Farhangian, F.; Sefidgar, M.; Landry, R.J. Applying a ToF/IMU-Based Multi-Sensor Fusion Architecture in Pedestrian Indoor Navigation Methods. Sensors 2021, 21, 3615. doi: https://doi.org/10.3390/s21113615
12. Valadão, C.; Bastos, T.; Frizera, A.; Carelli, R. Towards a Smart Walker controller for physiotherapy and rehabilitation purposes. In: *23rd International Symposium on Industrial Electronics* (ISIE), Istanbul, Turkey, 2014, pp. 1578-1583, doi: https://doi.org/10.1109/ISIE.2014.6864850
13. Jao, C. -S.; Wang, Y.; Shkel, A. M. A Zero Velocity Detector for Foot-mounted Inertial Navigation Systems Aided by Downward-facing Range Sensor. In: *IEEE Sensors*, Rotterdam, Netherlands, 2020, pp. 1-4, doi: https://doi.org/10.1109/SENSORS47125.2020.9278755
14. Valadão, C.; Caldeira, E.; Bastos-Filho, T.; Frizera-Neto, A.; Carelli, R. A New Controller for a Smart Walker Based on Human-Robot Formation. Sensors 2016, 16, 1116. https://doi.org/10.3390/s16071116
15. Scheidegger, W. M.; de Mello, R.C.; Sierra M, S.D.; Jimenez, M.F.; Múnera, M.C.; Cifuentes, C. A.; Frizera-Neto, A. A Novel Multimodal Cognitive Interaction for Walker-Assisted Rehabilitation Therapies. In: IEEE 16th International Conference on Rehabilitation Robotics (ICORR), Toronto, Canada, 2019, pp. 905-910, doi: https://doi.org/10.1109/ICORR.2019.8779469

Citation: Verdú, I.S.; Dunai, L.; Sava, L. Advancements in sensor technology for autonomous walker. *Journal of Engineering Science* 2024, XXXI (4), pp. 22-32. https://doi.org/10.52326/jes.utm.2024.31(3).03.

Submission of manuscripts: jes@meridian.utm.md

Journal of Engineering Science *Vol. XXXI, no. 4 (2024), pp. 33 - 54*
Fascicle *Industrial Engineering* *ISSN 2587-3474*
Topic *Applied Engineering Sciences and Management* *eISSN 2587-3482*

https://doi.org/10.52326/jes.utm.2024.31(4).03
UDC 656.121.072:303.72(478-25)

MEASURING PASSENGER SATISFACTION IN URBAN PUBLIC TRANSPORT IN CHISINAU

Igor Rotaru [1] *, ORCID: 0000-0003-3636-4896,
Andrei Rusu [2, 3], ORCID: 0000-0002-0259-3060

[1] *Technical University of Moldova, 168 Ștefan cel Mare Blvd., Chisinau, Republic of Moldova*
[2] *Moldova State University, VAIMCS, 5 Academiei str., Chisinau, Republic of Moldova*
[3] *Ovidius University of Constanta, 124 Mamaia Blvd., Constanta, Romania*
* Corresponding author: Igor Rotaru, *igor.rotaru@tran.utm.md* Andrei Rusu, *andrei.rusu@math.md*

Received: 10. 24. 2024
Accepted: 11. 22. 2024

Abstract. The quality of services provided by the urban public transport system plays an essential role in determining the level of satisfaction of a city's inhabitants and in improving their quality of life. The analysis of the methods used to assess the quality of urban transport services reveals the need to adopt new concepts that more realistically reflect the various aspects of their quality. A critical aspect identified is the fact that traditional methods for assessing the quality of urban passenger transport fail to fully integrate the subjective perceptions of users. They usually focus on technical, operational or economic parameters, neglecting the importance of the personal experience and satisfaction felt by passengers. The integration of subjective perceptions and the use of advanced evaluation methods contribute to the development of a public transport system that better meets passengers' expectations, stimulating the use of public transport and reducing the negative impact on the urban environment.This article represents an application of the principal component analysis (PCA) method to assess the quality of services provided by the urban public transport system using the data collected during the study.This approach will allow for a more balanced assessment focused on the real needs of passengers, thus providing more solid support for decision-making and the implementation of measures to improve urban public transport.

Keywords: *urban public transport system, quality indicators, Principal Component Analysis, case study.*

Rezumat. Calitatea serviciilor oferite de sistemul de transport public urban joacă un rol esențial în determinarea nivelului de satisfacție al locuitorilor unui oraș și în îmbunătățirea calității vieții acestora. Analiza metodelor utilizate pentru evaluarea calității serviciilor de transport urban relevă necesitatea adoptării unor concepte noi care să reflecte mai real diversele aspecte ale calității acestora. Un aspect critic identificat este faptul că metodele tradiționale de evaluare a calității transportului urban de pasageri nu reușesc să integreze complet percepțiile subiective ale utilizatorilor. Acestea se concentrează, de obicei, pe parametrii tehnici, exploataţionali sau economici, neglijând importanța experienței personale și a satisfacției resimțite de călători. Integrarea percepțiilor subiective și utilizarea unor

metode avansate de evaluare contribuie la dezvoltarea unui sistem de transport piblic care răspunde mai bine așteptărilor pasagerilor, stimulând utilizarea transportului public și reducând impactul negativ asupra mediului urban. Acet articol reprezintă o aplicare a metodei analizei componentelor principale (PCA), pentru aprecierea calitaţii serviciilor oferite de sistemul de transport public urban folosind datele colectate pe parcursul studiului. Această abordare va permite o evaluare mai echilibrată și orientată spre nevoile reale ale pasagerilor, oferind astfel un suport mai solid pentru luarea deciziilor și pentru implementarea măsurilor de îmbunătățire a transportului public urban.

Cuvinte cheie: *sistem de transport public urban, indicatori de calitate, Analiza Componentelor Principale , studiu de caz.*

1. Introduction

At the end of the 19th century and at the beginning of the 20th century, many scientists, sociologists, economists, and engineers focused on the laws governing population movement, which ultimately led to the organization and subsequent development of transportation of people, and particularly public transportation of people [1,2].

Simultaneously with the development of public transport, the emphasis has been placed on transport quality based on indicators that reflect efficiency, accessibility, sustainability and user satisfaction [3,4].

Often the assessment of public transport quality is carried out through direct indicators, either technical and operational indicators or economic indicators, such as those described in the normative acts of the Chisinau City Hall [5,6].

The goal of the paper is to determine the factors that influence the overall satisfaction of the users of the public urban transport in the municipality Chisinau by using the principle component analysis method. The tools used to conduct the analysis are based on programming language of Python and the appropriate specialized libraries.

The goal of the paper is to use the statistical method known as principal component analysis (PCA) that is a statistical technique which analyze data that contains observations described by some inter-correlated numerical variables. The method is usually used to extract the important information from the statistical data and then represent that data in a set of new orthogonal variables called principal components. From the mathematics perspective the PCA is determined by eigenvectors and eigenvalues. Eigenvectors and eigenvalues are numbers and vectors associated to square matrices. Together they provide the eigen-decomposition of a matrix, which analyzes the structure of this matrix such as correlation, covariance, or cross-product matrices. This method was first described by Pearson [7] in 1901 and Hotelling [8] in 1933. More modern explanations and applications of the PCA method in industry, research areas as chemistry, data analysis, physics, multifactor analysis, etc, can be found in [9-14].

2. Description of the data

We use in our paper the results of the survey conducted in November 2022 in the municipality of Chisinau regarding the satisfaction of the passengers of the urban public transport in Chisinau. The survey was conducted by a team of specialists from the Technical University of Moldova at the request of the Chisinau City Hall. The method used in survey was a face-to-face interview. More details about the the survey can be found in [6]. The analyzed data is presented in the excel file: DB_sondaj_pasageri_initial.xlsx [15]. The file

contains information regarding the gender of the respondent, age group of the responder, whether the respondent lives in Chisinau or in the suburbs, the type of public transport used, type of urban transport used, frequency of public transport use, availability of information on routes and there scheduling, the conditions in the stop stations, conditions in the vehicles, and various satisfaction metrics, such as availability, readability of schedules, and general satisfaction with public transport. Actually the data was collected on papers, and the xlsx file is the result of its digitalization. The total number of collected parameters is 47 (see the list of fitures F1, …, F47 below the Figure 5).

3. Description of the method used

In the paper we use the Principal Component Analysis method [7-14] to analyse the data. The basic reason to choose the method is that is allows to reduce the dimensionality of the problem (in our our case from 47 parameters to less ones – may be 2, 3, or 5). In the following we will briefly describe the method that involve next steps:

1. Standardization of data.
2. Covariance Matrix Computation.
3. Computation of Eigenvalues and Eigenvectors of the Covariance Matrix.
4. Selection of Principal Components.
5. Project Data onto New Feature Space.
6. Interpret results.

In the following we give brief explanations of the above steps.

3.1. Standardization of data

Since Principal Component Analysis method is sensitive to the scale of the data it is important to standardize the dataset. This ensures that all variables contribute equally to the analysis, regardless of their original scales. Thus for each feature subtract the mean and divide by the standard deviation so that each feature has a mean of 0 and a standard deviation of 1, so use the formula:

$$z = \frac{x - \mu}{\sigma}, \tag{1}$$

where: x is the original data, μ is the mean value, and σ is the standard deviation.

Observation. In order to apply the standardization all data must have numerical values (in order to be able to apply formula (1) above). If some data is not numerical, may be it can be assign numbers to non-numerical data. The method can not be applied if data can not be represented on a scale.

3.2. Covariance matrix computation

It is known that covariance matrix shows how much the variables vary with each other. It's essential for understanding the relationships between the variables in the dataset, so we have to calculate the covariance matrix of the standardized data. If there is a $n \times p$ dataset (with n samples and p variables) the covariance matrix is a $p \times p$ matrix, where each element $C(i, j)$ represents the covariance between variable i and variable j. The covariance between two variables X and Y is computed by the well-known formula:

$$Cov(X, Y) = \frac{1}{n-1} \sum_{i=1}^{n} (X_i - \mu_X)(Y_i - \mu_Y) \tag{2}$$

In (2) μ_X represents the mean value of the registered samples X_i for variable X, and μ_Y represents the mean value of the registered samples Y_i for variable Y.

3.3. Computation of eigenvalues and eigenvectors of the Covariance matrix

Eigenvalues and eigenvectors are useful in the process of identification of the principal components. More about eigenvectors and eigenvalues can be found in [16]. The eigenvectors determine the directions of the new feature space, and the eigenvalues show the amount of variance carried in each direction. The eigenvectors are the principal components, and the corresponding eigenvalues give the amount of variance each component explains. To calculate the eigenvalues and eigenvectors from the covariance matrix involve two steps: computation of the eigenvalues, then determine the corresponding eigenvalues λ are determined from the equation:

$$C \cdot v = \lambda \cdot v, \tag{3}$$

where: C is the covariance matrix, v is the eigenvector, and λ is the eigenvalue.

3.4. Selection of Principal Components

The eigenvalues tell us the amount of variance each principal component explains. We typically select the top k eigenvectors corresponding to the largest eigenvalues, which represent the principal components.

The goal is to keep components that explain most of the variance (usually the first few components).

3.5. Project Data onto New Feature Space

Finally, we project the original standardized data onto the new feature space using the selected principal components. The new dataset Z is computed as:

$$Z = X \cdot W, \tag{4}$$

where: W is the matrix of the selected eigenvectors.

3.6. Interpret the results

The transformed data will have fewer dimensions (principal components), and the variance explained by each principal component can help determine how much information is retained after the reduction. We can plot the explained variance or cumulative variance to assess how many principal components to keep.

4. Case study

In the following we apply the steps of PCA method described earlier in the article to the data.

4.1 Standartization of data

In order to apply the PCA method to the raw data we have to standardize it. According to observation in 3.1. “Standardization of Data” initially we have to get all data as numerical values.

Analizing the data we found out that it contains some columns that are not even numerical one. They are related to the gender of the respondent, to the age interval of the responder, whether the responder lives in Chisinau or lives in the surburbs, how often the responder uses the public transport, and the overall satisfaction of the responder with the

public transport. We apply next transformation to the data: for each such column with non-numerical data we change the value to an appropriate numerical one as it is noted below:

- Gender of the responder:
  - Female → 0,
  - Male → 1,
- Age of the respondent:
  - 12-18 → 1
  - 18-27 → 2
  - 28-37 → 3
  - 38-47 → 4
  - 48-57 → 5
  - 58-64 → 6
  - > 64 → 7
- Reponder lives in Chisinau or in the surburb:
  - Chisinau → 0
  - Surburb → 1
- How often the respondent uses the public transport:
  - Satisfied, but there are comments → 3,
  - Absolutely unsatisfied → 1,
  - Absolutely satisfied → 4.

In oder to do all these manipulations with the data in the initial excel file we use the following python code. The result is the excel file: DB_sondaj_pasageri_numeric.xlsx. The python code is presented bellow.

```
import pandas as pd

# Load the Excel file
file_path = "DB_sondaj_pasageri_initial.xlsx"
excel_data = pd.ExcelFile(file_path)

# Display sheet names to understand the structure of the file
excel_data.sheet_names

# Load the data from 'Sheet1'
data = pd.read_excel(file_path, sheet_name="Sheet1")

# Display the first few rows to understand the structure
data.head()

# Let's review non-numerical columns in the dataset
non_numerical_columns = data.select_dtypes(include=["object"]).columns

# List the unique values in non-numerical columns to determine how to encode
them
non_numerical_columns_unique_values = {
   col: data[col].unique() for col in non_numerical_columns
```

```
}

non_numerical_columns_unique_values

# Apply transformations to non-numerical columns

# 1. Encode 'Gender of the responder'
data["Gender of the responder "] = data["Gender of the responder "].replace(
   {"Female": 0, "Male": 1}
)

# 2. Encode 'Age of the respondent'
data["Age of the respondent "] = data["Age of the respondent "].replace(
   {
      "12-18": 1,
      "18-27": 2,
      "28-37": 3,
      "38-47": 4,
      "48-57": 5,
      "58-64": 6,
      "> 64": 7,
   }
)

# 3. Encode ' Do you live in Chisinau or in the suburbs '
data["Do you live in Chisinau or in the suburbs "] = data[
   " Do you live in Chisinau or in the suburbs "
].replace({"Chisinau": 0, "Suburb": 1})

# 4. Encode 'What mode of transport do you use most often to travel'
data["What mode of transport do you use most often to travel"] = data[
   "What mode of transport do you use most often to travel"
].replace(
   {
      "Trolleybus": 1,
      "City bus": 2,
      "Minibus": 3,
      "Suburban bus": 4,
   }
)

# 5. Encode 'How often do you use public transport'
data["How often do you use public transport"] = data[
   "How often do you use public transport"
].replace(
   {
```

```
            "6-7 days a week": 6,
            "5 days a week": 5,
            "3-4 days a week": 4,
            "1-2 days a week": 3,
            "About 1-3 times a month": 2,
            "Every 2-3 months": 1,
            "Every 4-6 months": 0.5,
            "Once a year": 0.25,
        }
    )

    # 6. Encode 'General satisfaction with public transport in Chisinau'
    data["General satisfaction with public transport in Chisinau"] = data[
        "General satisfaction with public transport in Chisinau"
    ].replace(
        {
            "Satisfied, but there are comments": 3,
            "Absolutely dissatisfied": 1,
            "Absolutely satisfied": 4,
        }
    )

    # Save the modified data into a new Excel file
    output_path = "DB_sondaj_pasageri_numeric.xlsx"
    data.to_excel(output_path, index=False)

    output_path
```

The code above actually documents by itself the transformation of non-numerical data into a numerical one.

Since all the data in the table already have a numeric value, we can apply the standardization procedure to it in order to get for every feature (column) in the table the mean value to be equal to 0, and the standard deviation to be equal to 1. To do this we use the following snippet of python program:

```
    # Standardize the data
    scaler = StandardScaler()
    standardized_data = scaler.fit_transform(data)

    # Convert the standardized data back to a DataFrame for easier manipulation and
export
    standardized_df = pd.DataFrame(standardized_data, columns=data.columns)

    # Save the standardized data to a new Excel file
```

```
standardized_output_path = 'DB_sondaj_pasageri_standardized_final.xlsx'
standardized_df.to_excel(standardized_output_path, index=False)

standardized_output_path
```

4.2 Covariance Matrix Computation

Next step on the road to the goal of finding out the principal components of the data is to calculate the covariance matrix. This is achieved by the help of the following program:

```
import pandas as pd

# Load the dataset
data = pd.read_excel('DB_sondaj_pasageri_standardized_final.xlsx')

# Calculate the covariance matrix
covariance_matrix = data.cov()

# Save the covariance matrix to a CSV file
covariance_matrix.to_csv('DB_sondaj-Covariance-matrix-of-standardized-data.csv')
```

4.3 Computation of Eigenvalues and Eigenvectors of the Covariance Matrix

Let us calculate now the eigenvalues and the corresponding eigenvectors of the covariance matrix obtained at the previous step. Again we use a specialized python library and the corresponding functions in order to get it.

```
# Importing necessary libraries for eigenvalue calculation
import numpy as np

# Calculate the eigenvalues and eigenvectors of the covariance matrix
eigenvalues, eigenvectors = np.linalg.eig(covariance_matrix)

# Creating a DataFrame to show both eigenvalues and their corresponding
eigenvectors
eigen_details = pd.DataFrame(eigenvectors, columns=[f'Eigenvector_{i+1}' for i in
range(eigenvectors.shape[1])])
eigen_details.insert(0, 'Eigenvalue', eigenvalues)

# Display the details of the calculation to the user
tools.display_dataframe_to_user(name="Eigenvalues and Eigenvectors",
dataframe=eigen_details)
```

According to the results the explained variance can be calculated by:

```
# Calculating the explained variance for each eigenvalue
total_variance = np.sum(eigenvalues)
explained_variance_ratio = [(i / total_variance) * 100 for i in eigenvalues]

# Creating a DataFrame to display the explained variance
explained_variance_df = pd.DataFrame({
    'Eigenvalue': eigenvalues,
    'Explained Variance (%)': explained_variance_ratio
})

# Displaying the explained variance to the user
tools.display_dataframe_to_user(name="Explained Variance of Each Principal Component", dataframe=explained_variance_df)
```

The result is in the table below which contains the first 10 eigenvalues and the corresponding percent of the explained variance. The eigenvalues are usually ordered in descending way:

Table 1

The first 10 eigenvalues of the covariance matrix ant there importance in the explanation of the variance in data

Order	Value of eigenvalue	Explained variance, %	Cumulative explained variance, %
1	10.27404491	21.85	21.85
2	3.589577401	7.63	29.48
3	2.973504444	6.32	35.80
4	2.286543124	4.86	40.66
5	2.150963809	4.57	45.24
6	1.84612014	3.93	49.16
7	1.81918762	3.87	53.03
8	1.583324077	3.37	56.40
9	1.337555732	2.84	59.24
10	1.151848884	2.45	61.69

The explained variance gives insight into how much information (or variance) each principal component (associated with each eigenvalue) captures from the dataset. Here's how to interpret the results:

- **Eigenvalue** - represents the amount of variance captured by the corresponding principal component (a direction in feature space). A higher eigenvalue indicates that the corresponding principal component captures a larger portion of the variance in the data.
- **Explained Variance (%)** - tells us the proportion of the total variance in the dataset that is explained by each principal component. For example, the first principal

component in your data captures 21.85% of the total variance, and the second component captures 7.63%.

According to the data we get the following interpretations of the data:

- **Reduction of the dimension**. The principal components with the highest explained variance are the most significant. If you're looking to reduce dimensionality, you might retain only the components that explain most of the variance. For example, the top 5 components in your case explain over 45% of the variance, so you could potentially reduce the dimensionality to 5 components while still preserving a significant amount of information.
- **Cumulative Variance**. You can sum the explained variance percentages to see how much of the total variance is captured by a given number of components. This helps to decide how many components to keep in a dimensionality reduction task. If you're satisfied with, say, 70% of the variance explained, you can retain as many components as it takes to reach that threshold. In the present case the first 14 features are responsible for the at least 70% of the variance, and first 6 features explains a bit more than 49% of the variance.
- **Insights into Data Structure**. The first few components represent the directions in your data that have the most variability. If the first few components explain most of the variance, it means your data has some underlying structure that can be described by fewer variables.

Let us visualize the cumulative variance and the explained variance by principal components:

```
# Re-importing the required pandas library
import pandas as pd

# Redefining the file path and reloading the data
file_path = 'DB_sondaj_pasageri_standardized_final.xlsx'

# Reload the dataset and compute the covariance matrix
data = pd.read_excel(file_path)
covariance_matrix = data.cov()

# Recalculate the eigenvalues and explained variance
eigenvalues, eigenvectors = np.linalg.eig(covariance_matrix)
total_variance = np.sum(eigenvalues)
explained_variance_ratio = [(i / total_variance) * 100 for i in eigenvalues]

# Plotting the explained variance
plt.figure(figsize=(10, 6))
plt.bar(range(1, len(explained_variance_ratio) + 1), explained_variance_ratio,
alpha=0.7, align='center', color='blue', label='Individual Explained Variance')
```

```
        plt.step(range(1, len(explained_variance_ratio) + 1),
np.cumsum(explained_variance_ratio), where='mid', color='red', label='Cumulative Explained
Variance')

        plt.xlabel('Principal Component')
        plt.ylabel('Explained Variance (%)')
        plt.title('Explained Variance by Principal Components')
        plt.legend(loc='best')
        plt.grid(True)
        plt.show()
```

The generated corresponding Figure 1 is:

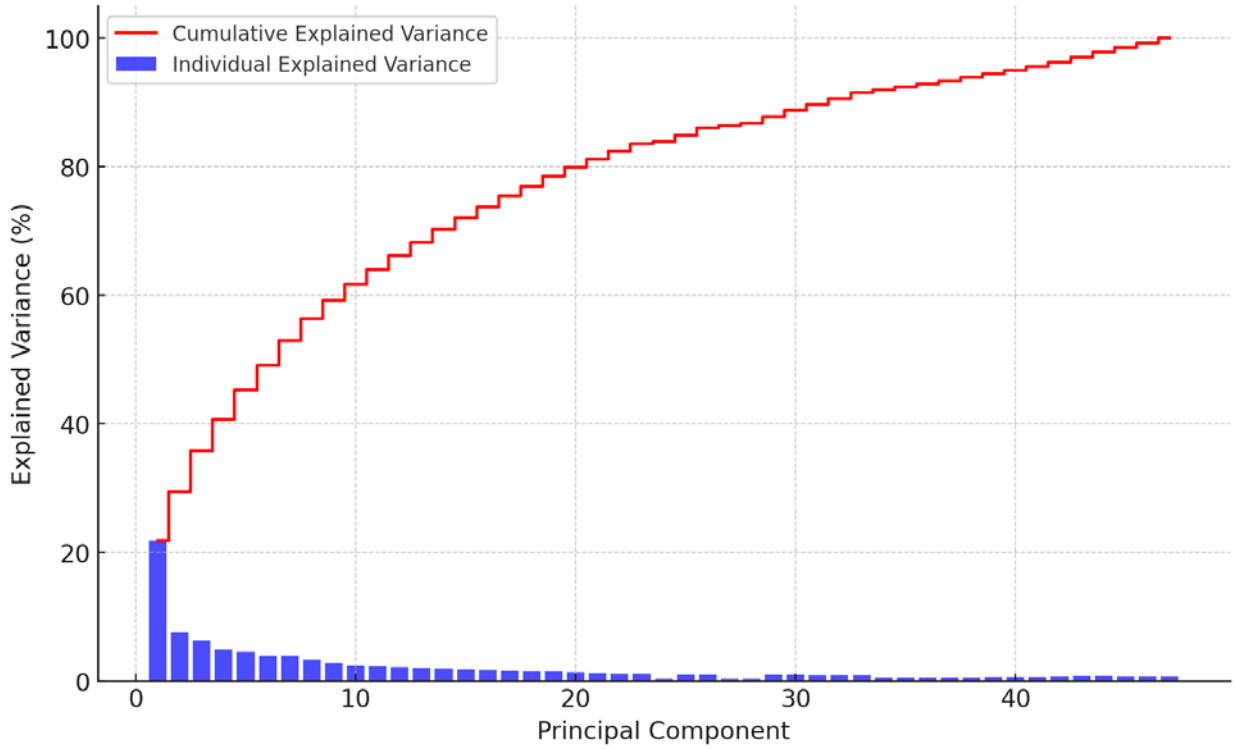

Figure 1. Explained Variance by Principal Components.

Now it is time to select the principal components and analyze them.

4.4 Selection of Principal Components

It is clear from the obtained data that the most important component is the first one which explains almost 21% of the variance, but it is not sufficient to explain the major change in variance. The first 5 principal components determines almost 50% of the variability in the variance. In the following we present the visualizations of the principal components. The next code uses a standard python module for data analysis.

4.5. Project data onto new feature space and interpretation of results

```
from sklearn.decomposition import PCA
```

```
        from sklearn.preprocessing import StandardScaler

        # Step 1: Standardize the data (as PCA requires standardized data)
        # Imputing missing values with the mean of each column
        data_filled = data.fillna(data.mean())

        # Standardizing the data after filling NaN values
        standardized_data_filled = scaler.fit_transform(data_filled)

        # Step 2: Perform PCA
        pca = PCA()
        pca_components = pca.fit_transform(standardized_data_filled)

        # Step 3: Capture the explained variance ratio
        explained_variance_ratio = pca.explained_variance_ratio_

        # Creating a DataFrame to show the principal components and explained variance
        pca_results_df = pd.DataFrame(pca_components, columns=[f'PC{i+1}' for i in
range(pca_components.shape[1])])

        # Adding explained variance information
        explained_variance_df = pd.DataFrame({
            'Principal Component': [f'PC{i+1}' for i in range(len(explained_variance_ratio))],
            'Explained Variance (%)': explained_variance_ratio * 100
        })

        # Displaying the PCA results to the user
        tools.display_dataframe_to_user(name="Principal Components",
dataframe=pca_results_df)
        tools.display_dataframe_to_user(name="Explained Variance per Principal
Component", dataframe=explained_variance_df)

        # Visualizing the first two principal components
        plt.figure(figsize=(10, 6))
        plt.scatter(pca_components[:, 0], pca_components[:, 1], alpha=0.7, edgecolors='k')
        plt.title('PCA: First Two Principal Components')
        plt.xlabel('Principal Component 1')
        plt.ylabel('Principal Component 2')
        plt.grid(True)
        plt.show()
```

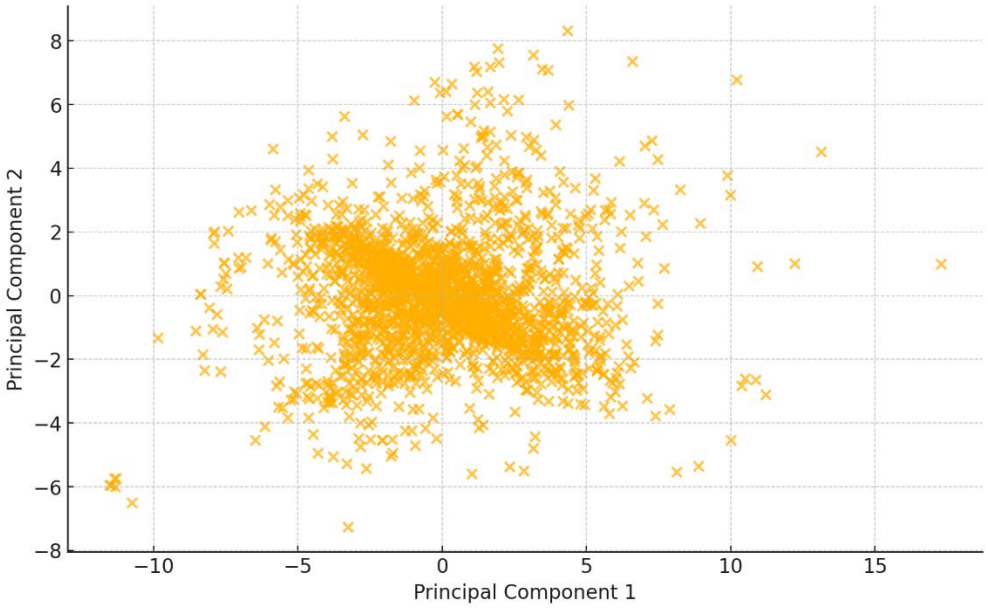

Figure 2. PCA – first two principal components.

The Figure 3 below shows the first 3 principal components.

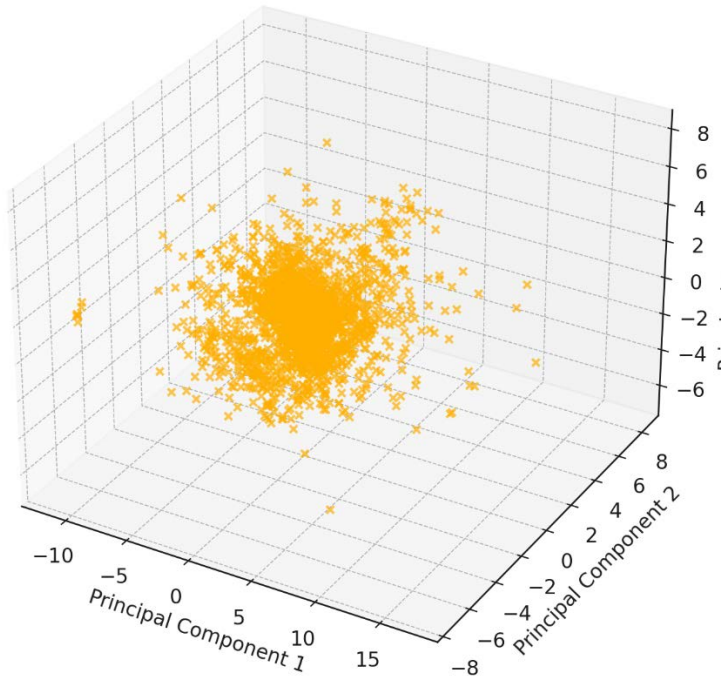

Figure 3. PCA – first three principal components

The Figure 3 above is obtained using the code:

```
from mpl_toolkits.mplot3d import Axes3D

# Visualizing the first three principal components in 3D
fig = plt.figure(figsize=(10, 8))
ax = fig.add_subplot(111, projection='3d')
```

```
        # Plotting the first three PCs
        ax.scatter(pca_components[:, 0], pca_components[:, 1], pca_components[:, 2],
alpha=0.7, edgecolors='k')

        # Setting labels and title
        ax.set_title('PCA: First Three Principal Components')
        ax.set_xlabel('Principal Component 1')
        ax.set_ylabel('Principal Component 2')
        ax.set_zlabel('Principal Component 3')

        plt.show()
```

In order to visualize the first 5 principal components we use slices, or different views, which are based on showing different important pairs of principal components. To get them use the code:

```
        # Visualizing the first five principal components in 2D scatter plots

        fig, axs = plt.subplots(2, 3, figsize=(15, 10))

        # Plotting the first five principal components pairwise
        pairs = [(0, 1), (0, 2), (0, 3), (1, 2), (1, 3), (2, 3)]
        for i, (pc1, pc2) in enumerate(pairs[:5]):
            row, col = divmod(i, 3)
            axs[row, col].scatter(pca_components[:, pc1], pca_components[:, pc2], alpha=0.7,
edgecolors='k')
            axs[row, col].set_xlabel(f'PC{pc1 + 1}')
            axs[row, col].set_ylabel(f'PC{pc2 + 1}')
            axs[row, col].grid(True)

        plt.suptitle('Scatter Plots of Top 5 Principal Components', fontsize=16)
        plt.tight_layout(rect=[0, 0, 1, 0.96])
        plt.show()
```

The result is in the Figure 4 below:

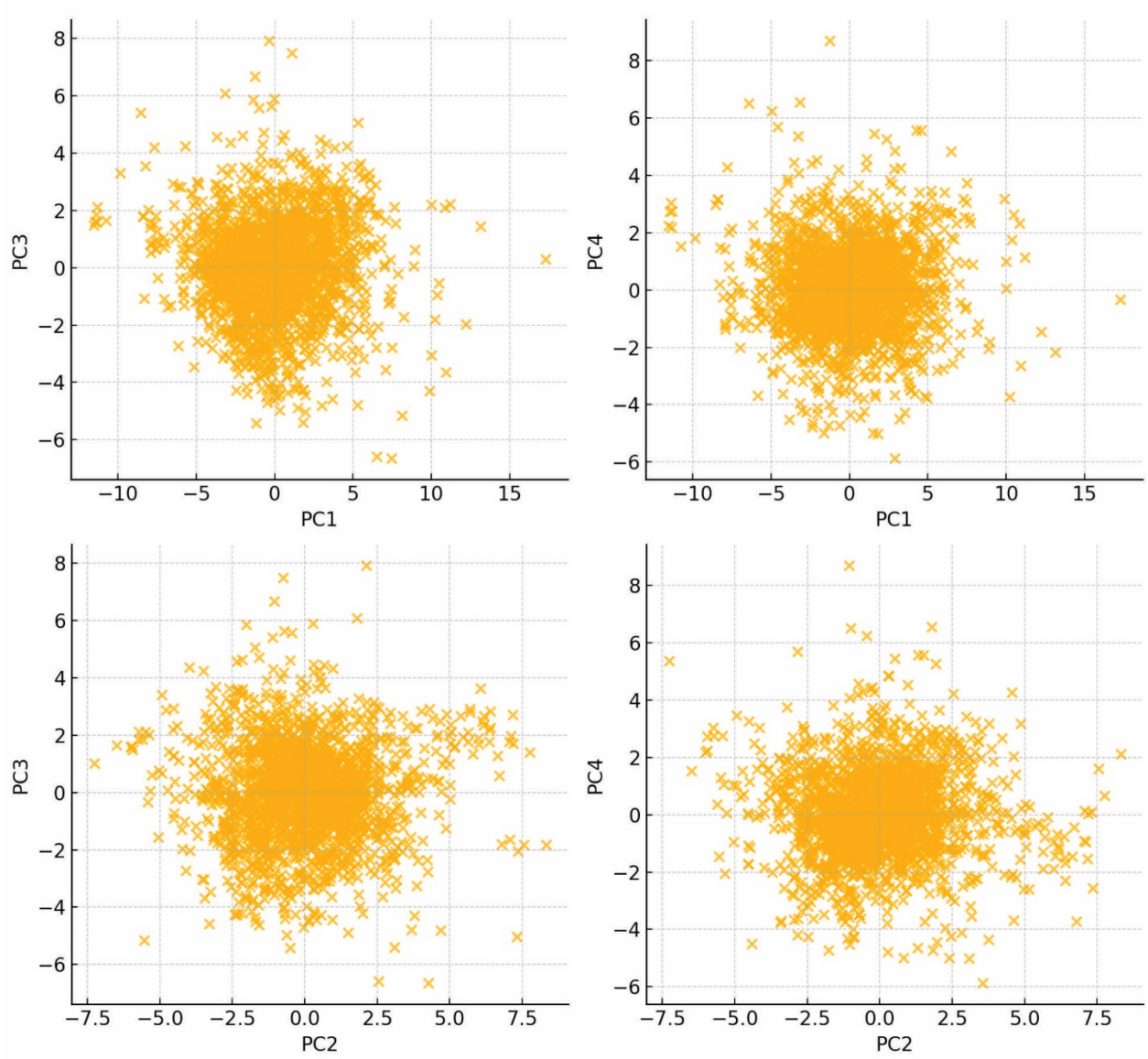

Figure 4. PCA – next two by two principal components

To determine the most important factors (or features) in the first three principal components, we need to analyze the **loading scores** or **eigenvectors** associated with each principal component. These loading scores show the contribution of each original feature to a principal component.

Let's extract the top contributing features for each of the first three principal components. I'll calculate and display the features with the highest loading scores for the first three principal components: PC1, PC2, and PC3.

```
# Extracting the eigenvectors (loadings) of the first 3 principal components
loading_scores = pd.DataFrame(pca.components_.T, columns=[f'PC{i+1}' for i in range(pca.n_components_)], index=data.columns)

# Getting the most important features (highest absolute loadings) for the first three principal components
top_features_pc1 = loading_scores['PC1'].abs().sort_values(ascending=False).head()
top_features_pc2 = loading_scores['PC2'].abs().sort_values(ascending=False).head()
```

```
top_features_pc3 = loading_scores['PC3'].abs().sort_values(ascending=False).head()

# Combining results into a single DataFrame for display
important_factors_df = pd.DataFrame({
    'PC1 Top Features': top_features_pc1.index,
    'PC1 Loading': top_features_pc1.values,
    'PC2 Top Features': top_features_pc2.index,
    'PC2 Loading': top_features_pc2.values,
    'PC3 Top Features': top_features_pc3.index,
    'PC3 Loading': top_features_pc3.values
})

# Display the important factors
tools.display_dataframe_to_user(name="Important Features in PC1, PC2, and PC3",
dataframe=important_factors_df)
```

The result is in the Table 2 below.

Table 2

Important features in first three principal components

No.	PC1 Top Features	PC1 Loading	PC2 Top Features	PC2 Loading	PC3 Top Features	PC3 Loading
1	Satisfaction with public transport stations in general	0.2248	Satisfaction with the minibus route network - general satisfaction	0.3383	Satisfaction with the trolleybus route network - general satisfaction	0.2590
2	General satisfaction with public transport in Chisinau	0.2232	Satisfaction with the minibus route network - time you spend approaching (leaving) a stopping point	0.3253	Available mobile apps	0.2590
3	Experience of being on public transport while traveling on the route you most often use - It is easy for you to get in and out of the public transport (applying physical force)	0.1939	Satisfaction with the minibus route network - the ability to get anywhere and at any time to any part of the city	0.3161	Given each of these aspects, how satisfied are you with providing information about the public transport timetable as a whole	0.2523

Continuation Table 2

4	Given each of these aspects, how satisfied are you with providing information about the public transport timetable as a whole	0.1904	Satisfaction with the minibus route network - number of available routes	0.3082	Information shown on electronic scoreboards at some stops about the time of arrival of public transport	0.2395
5	Satisfaction with public transport stations - possibility to sit	0.1902	Satisfaction with the minibus route network - distance to the nearest public transport stop	0.2778	Satisfaction with the trolleybus route network - distance to the nearest public transport stop	0.2375

We have identified the most important features for the first three principal components (PC1, PC2, and PC3). For each component, the features with the highest loading scores contribute the most to that principal component. Here are the top contributing factors for each:

PC1: Primarily influenced by general satisfaction factors related to transport stations and the ease of entry and exit during travel.

PC2: Heavily related to the satisfaction with microbus routes, including the availability of routes, travel time, and distance to stations.

PC3: Largely driven by satisfaction with trolleybus routes and available mobile applications, along with the availability of public information.

Let us also get a heatmap for the loading of the first 5 principal components. The color intensity indicates the contribution (positive or negative) of each feature to the respective principal component. This visualization helps to see which features strongly influence each component.

```
import seaborn as sns

# Plotting a heatmap of the loadings for the first 5 principal components
plt.figure(figsize=(12, 8))
sns.heatmap(loading_scores.iloc[:, :5], annot=True, cmap='coolwarm', center=0)
plt.title('Heatmap of Loadings for the First 5 Principal Components')
plt.xlabel('Principal Components')
plt.ylabel('Features')
plt.show()
```

The heating map is the presented in Picture 5.

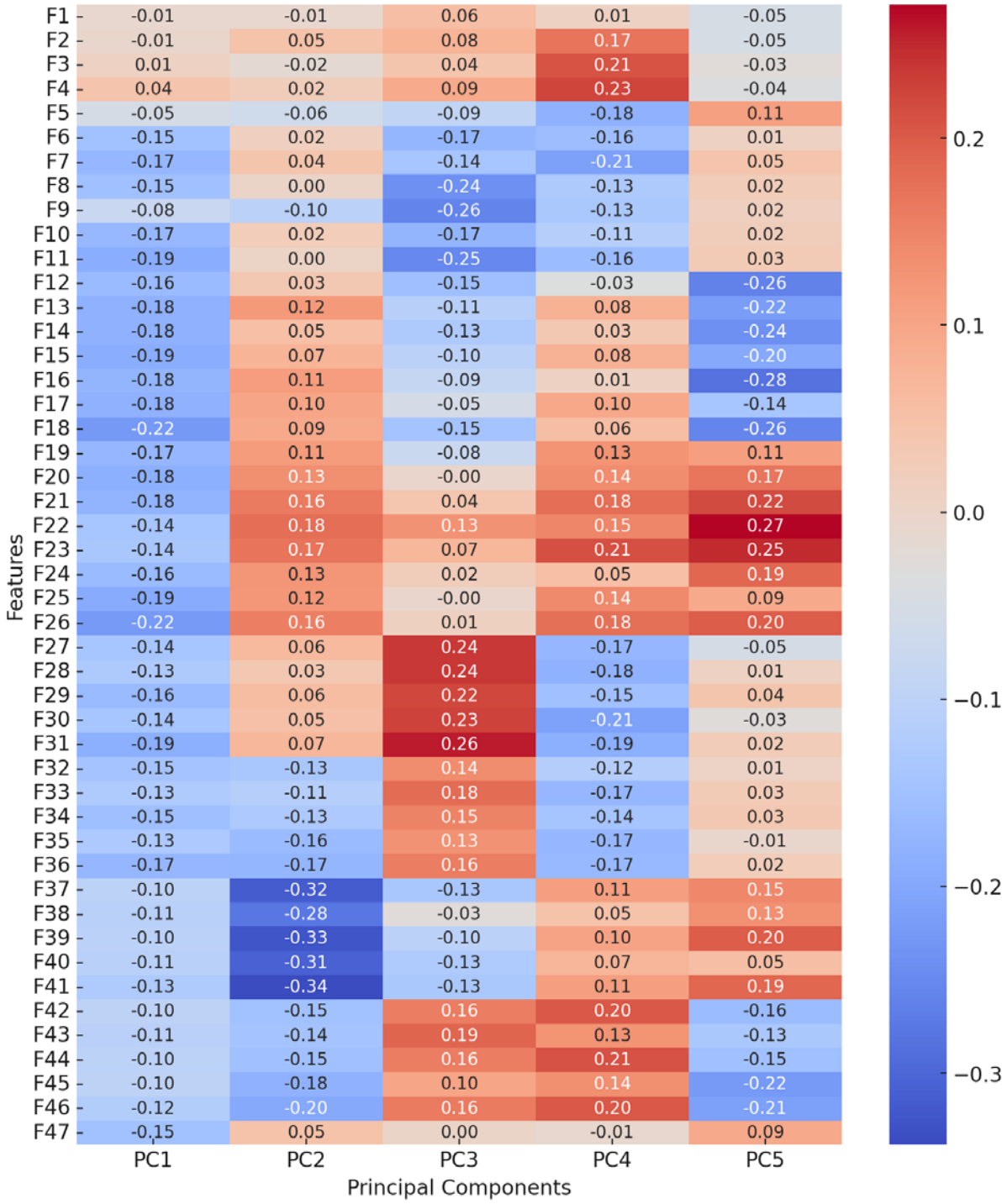

Figure 5. Heatmap of loadings for the first 5 principal components.

The features F1, ..., F47 are given in the next list:

- F1 = Gender of the responder
- F2 = Age of the respondent
- F3 = Do you live in Chisinau or in the suburbs.
- F4 = What mode of transport do you use most often to travel
- F5 = How often do you use public transport
- F6 = Availability of the correct public transport timetable at the stops
- F7 = Easy to read and understand a public transport timetable at stops

- F8 = Information shown on electronic scoreboards at some stops about the time of arrival of public transport
- F9 = Available mobile apps
- F10 = Actual compliance with established public transport timetable
- F11 = Given each of these aspects, how satisfied are you with providing information about the public transport timetable as a whole
- F12 = Satisfaction with public transport stations - lighting
- F13 = Satisfaction with public transport stations - cleanliness and the amount of garbage
- F14 = Satisfaction with public transport stations - the opportunity to hide from rain and wind
- F15 = Satisfaction with public transport stations - possibility to sit
- F16 = Satisfaction with public transport stations - pavement condition
- F17 = Satisfaction with public transport stations - congestion of passengers at a time when you usually drive
- F18 = Satisfaction with public transport stations in general
- F19 = Experience of being on public transport while traveling on the route you most often use - cabin occupancy
- F20 = Experience of being on public transport while traveling on the route you most often use - softness of public transport travel
- F21 = Experience of being on public transport while traveling on the route you most often use - comfort inside the cabin
- F22 = Experience of being on public transport while traveling on the route you most often use - temperature inside the cabin in winter
- F23 = Experience of being on public transport while traveling on the route you most often use - temperature inside the cabin in summer
- F24 = Experience of being on public transport while traveling on the route you most often use - quality and level of illumination of the cabin
- F25 = Experience of being on public transport while traveling on the route you most often use - It is easy for you to get in and out of the public transport (applying physical force)
- F26 = Satisfaction with the experience of being in public transport cabin in general
- F27 = Satisfaction with the trolleybus route network - the ability to get anywhere and at any time to any part of the city
- F28 = Satisfaction with the trolleybus route network - distance to the nearest public transport stop
- F29 = Satisfaction with the trolleybus route network - time you spend approaching (leaving) a stopping point
- F30 = Satisfaction with the trolleybus route network - number of available routes
- F31 = Satisfaction with the trolleybus route network - general satisfaction
- F32 = Satisfaction with the city bus route network - the ability to get anywhere and at any time to any part of the city
- F33 = Satisfaction with the city bus route network - distance to the nearest public transport stop

- F34 = Satisfaction with the city bus route network - time you spend approaching (leaving) a stopping point
- F35 = Satisfaction with the city bus route network - number of available routes
- F36 = Satisfaction with the city bus route network - general satisfaction
- F37 = Satisfaction with the minibus route network - the ability to get anywhere and at any time to any part of the city
- F38 = Satisfaction with the minibus route network - distance to the nearest public transport stop
- F39 = Satisfaction with the minibus route network - time you spend approaching (leaving) a stopping point
- F40 = Satisfaction with the minibus route network - number of available routes
- F41 = Satisfaction with the minibus route network - general satisfaction
- F42 = Satisfaction with the suburban bus route network - the ability to get anywhere and at any time to any part of the city
- F43 = Satisfaction with the suburban bus route network - distance to the nearest public transport stop
- F44 = Satisfaction with the suburban bus route network - time you spend approaching (leaving) a stopping point
- F45 = Satisfaction with the suburban bus route network - number of available routes
- F46 = Satisfaction with the suburban bus route network - general satisfaction
- F47 = General satisfaction with public transport in Chisinau

It follows from the heatmap that (see PC2) some data related to microbuses have great negative impact, the accessibility and the diversity of trolleybus routes have a positive impact (PC3). The PC1 shows that all factors have a light negative impact on general satisfaction, while other principal components have higher diversity in negative and positive perception.

5. Conclusions

The results shows that there are no unique set of factors which has a high influence on the general satisfaction of the users of the public transport in in the municipality of Chisinau. At the same time the PCA method helps to identify among the 47 factors under consideration the mixtures that have a significant impact on general satisfaction. These mixtures are collected in first 5 identified principal components. This can help de decision factors in the administration of the municipality to consider the most adequate policies in order to increase the general satisfaction of the users.

The conducted case study shows that the first principal component is responsible for about 20% of the users identified satisfaction. At the same time the first principal component has a weight as the sum of the next three principal components. Since the first 5-6 principle components explains about 50% in the variance of the level of satisfaction of the users we can conclude that almost all examined factors are relatively important, and the general satisfaction of the users depends on all of them, so this implies an action polity regarding almost all of them.

At the same time the analysis of the first principal component (Table 2) tell us that the factors that are relatively important in this component are:

- satisfaction with public transport stations in general;
- satisfaction with the experience of being in public transport cabin in general;
- experience of being on public transport while traveling on the route you most often use - it is easy for you to get in and out of the public transport (applying physical force);
- given each of these aspects, how satisfied are you with providing information about the public transport timetable as a whole;
- satisfaction with public transport stations - possibility to sit.

On the other hand, the same Table 2 and Figure 5 the second principal component have brought to light the general insatisfaction with any aspect related to minibuses:

- satisfaction with the minibus route network - general satisfaction;
- satisfaction with the minibus route network - time you spend approaching (leaving) a stopping point;
- satisfaction with the minibus route network - the ability to get anywhere and at any time to any part of the city;
- satisfaction with the minibus route network - number of available routes;
- satisfaction with the suburban bus route network - distance to the nearest public transport stop.

The third principal component shows us that in general, travelers are satisfied with the trolleybus network, the distance to the trolleybus stations, the level of information through mobile applications and other information sources.

Conflicts of interest: The authors declare no conflict of interests.

Acknowledgments: The work carried out by Rusu Andrei was partially supported within the Institutional Project 011301 "Computer Science Systems based on Artificial Intelligence" (strategic priority "V. Innovative technologies, sustainable energy, digitalization"; strategic direction "Innovative technologies and products; Information and communication technology and digital development"; carried out at State University of Moldova, Vladimir Andrunachievici Institute of Mathematics and Computer Science).

References

1. Ballon, H.; Jackson, K. T. *Robert Moses and the modern city: the transformation of New York*. W.W. Norton & Co, NY, SUA, 2007, 336 p.
2. Wardrop, J.G. *Some Theoretical Aspects of Road Traffic Research*. Institution of Civil Engineers, Northwestern University, 1952, 54 p.
3. Vuchic, V. *Transportation for Livable Cities*. Taylor and Francis, Milton, UK, 2017, 376 p.
4. Spirin, I. V., *Organization and management of passenger transportation*. Academy, Moscow, 2020, 398 p. [in Russian].
5. "Regulations on road transport of passengers and luggage on the territory of Chisinau municipality." approved by the decision of the Chisinau Municipal Council no. 4/22 of May 5, 2023. [in Romanian].
6. Rotaru, I.; Ceban,V. Quality of public transport services in Chisinau. *Journal of Engineering Science* 2024, 31(2), pp. 7–16, doi: 10.52326/jes.utm.2024.31(2).01.
7. Pearson, K. LIII. On lines and planes of closest fit to systems of points in space. *The London, Edinburgh, and Dublin philosophical magazine and journal of science* 1901, 2(11), pp. 559–572.
8. Hotelling, H. Analysis of a complex of statistical variables into principal components. *Journal of educational psychology* 1933, 24(6), pp. 417-441, doi: https://doi.org/10.1037/h0071325.

9. Jolliffe, I. T. *Principal component analysis for special types of data*. pp.338–72. Springer Series in Statistics. New York: Springer-Verlag, 2002. https://doi.org/10.1007/0-387-22440-8_13.
10. Greenacre, M.P.; Groenen, J. F.; Hastie, T.; D'Enza, A. I.; Markos, A.; Tuzhilina, E. Principal component analysis. *Nature Reviews Methods Primers* 2022, 2(1), 100, doi: 10.1038/s43586-022-00184-w.
11. Wold, S.; Esbensen, K.; Geladi, P. Principal component analysis. *Chemometrics and intelligent laboratory systems*, 1987, 2(1–3), pp. 37–52.
12. Bro, R.; Smilde, A. K. Principal component analysis. *Analytical methods* 2014, 6(9), pp. 2812–2831.
13. Abdi, H.; Williams, L. J. Principal component analysis. *Wiley interdisciplinary reviews: computational statistics* 2010, 2(4), pp. 433–459.
14. Jolliffe, I. T.; Cadima, J. Principal component analysis: a review and recent developments. *Philosophical transactions of the royal society A: Mathematical, Physical and Engineering Sciences* 2016, 374, 2065.
15. Rotaru, I. *Survey on the satisfaction of public transport users in Chisinau municipality*. Nov. 28, 2022. [Excel]. Available online: https://docs.google.com/spreadsheets/d/1m0An_EEqww6dfLvN9Ts0GnVn58zweFYY/edit?usp=drive_link&ouid=110108346911593091702&rtpof=true&sd=true (accessed on 12.10.2024).
16. Strang, G. *Introduction to Linear Algebra*. Wellesley-Cambridge Press, Massachusetts, SUA, 2023, 440 p.

Citation: Rotaru, I.; Rusu, A. Measuring passenger satisfaction in urban public transport in Chisinau. *Journal of Engineering Science* 2024, XXXI (4), pp. 33-54. https://doi.org/10.52326/jes.utm.2024.31(3).03.

Submission of manuscripts: jes@meridian.utm.md

Journal of Engineering Science *Vol. XXXI, no. 4 (2024), pp. 55 - 72*
Fascicle *Industrial Engineering* *ISSN 2587-3474*
Topic *Electrical Engineering and Power Electronics* *eISSN 2587-3482*

https://doi.org/10.52326/jes.utm.2024.31(4).04
UDC 621.365.5:004.94:663.93

IMPLEMENTATION OF INDUCTIVE PROCESSES IN GENERAL-PURPOSE EQUIPMENT TO ENHANCE HEAT TRANSFER PROCEDURES

Adrian Turcanu*, ORCID: 0009-0009-3482-4503,
Ilie Nucă, ORCID: 0000-0001-7750-4846

Technical University of Moldova, 168 Stefan cel Mare Blvd., Chisinau, Republic of Moldova
*Corresponding author: Adrian Țurcanu, *turcanu.adrian@eie.utm.md*

Received: 11. 12. 2024
Accepted: 12. 23. 2024

Abstract. The paper explores the energy efficiency of general-purpose installations, particularly the equipment used in espresso coffee production, and the unique functions of hydraulic systems. By applying eco-design principles and innovative, efficient solutions, the negative impact on the environment can be significantly reduced, transforming citizens into eco-consumers. The study aimed to explore ways to decrease energy consumption in hydraulic systems of standard installations, particularly in heat transfer processes in solids and liquids, which account for up to 97% of energy consumption in such installations. An innovative solution is presented that converts electric energy into heat in liquids using inductive heat transfer. The instant heating inductive boiler, based on inductive heat transfer phenomena, eliminates the convective and conductive heat transfer losses associated with the operation of the boiler with the resistive heating element. The design methodology for dimensioning this type of equipment is provided, and the simulation model for necessary verifications in MatLab Simscape is created. With its practical benefits, the new inductive boiler reduces the preheating period to 7.5 s compared to the 90 s of systems with resistive heating elements, thereby eliminating the need to keep the coffee machine at operating temperatures during breaks and providing a reliable solution for energy efficiency.

Keywords: *coffee machines, inductive heating boiler, hydraulic systems, design methodology, simulation.*

Rezumat. Lucrarea se referă la instalații de uz general, în special la echipamentele pentru procesul de producere al cafelei espresso, precum și la particularitățile funcțiilor sistemului hidraulic. Prin aplicarea principiilor de proiectare ecologică și a soluțiilor inovatoare și eficiente, impactul negativ asupra mediului poate fi redus semnificativ, transformând cetățenii în eco-consumatori. Studiul și-a propus să exploreze modalități de reducere a consumului de energie în sistemele hidraulice ale instalațiilor standard, în special în procesele de transfer de căldură în corpuri solide și lichide, care reprezintă până la 97% din consumul de energie în astfel de instalații. Lucrarea prezintă o soluție inovatoare pentru transformarea energiei electrice în căldură în lichide folosind transferul inductiv de căldură. Boilerul inductiv inovator de tip instant se bazează pe fenomene de transfer termic inductiv și elimină pierderile de transfer de căldură convective și conductive asociate funcționării

cazanului cu elementul de încălzire rezistiv. Este prezentată metodologia de proiectare a acestui tip de echipament, iar modelul de simulare pentru verificările necesare a fost creat și rulat în MatLab Simscape. Cu avantajele sale practice, noul cazan inductiv reduce perioada de preîncălzire la 7,5 s comparativ cu 90 s de sisteme cu elemente de încălzire rezistive, eliminând astfel necesitatea de a menține aparatul de cafea la temperaturi de funcționare în timpul pauzelor și oferind o soluție fiabilă pentru eficiență energetică.

Cuvinte cheie: *aparat de cafea, boiler de încălzire inductiv, sisteme hidraulice, metodologie de proiectare, simulare.*

1. Introduction

The scientific and engineering part of our society seeks new ways to quantify and minimize products' adverse environmental impact. Creating energy-efficient and less harmful products encourages consumers to be eco-conscious, enhancing our well-being.

Reducing energy consumption in technological processes and its impact on the environment aligns with the Environmental Strategy. for 2014-2023 approved by Government Decision nr. 301 of 24.04.2014 and Government Decision nr. 102 of 05.02.2013 on the Republic of Moldova Energy Strategy until 2030, both for industrial use and domestic needs [1-3].

The study refers to standard equipment, especially coffee machines. For most people, every morning starts with a delicious cup of coffee or some other type of beverage and finding a solution that would increase the efficiency of every coffee machine or kettle will reduce electricity consumption considerably.

The work aims to analyze the power consumption of a super-automated coffee maker and develop a solution that implements inductive heat transfer and considerably improves its efficiency.

2. Synthesis of construction principles and aspects of operation of electromechanical systems of conventional coffee machine

2.1. Espresso extraction process

Espresso, a popular coffee brewing method, has its origins in the 19th-century Italian Industrial Revolution. This method involves extracting coffee under high pressure in under 30 s, resulting in significantly improved quality. Through numerous experiments, the Italian Espresso National Institute has established a set of precise technical parameters for producing certified Italian Espresso, which are meticulously preserved [4].

The manufacturers are considering the finest tuning of all the parameters described above, which should be considered during the expresso extraction in modern equipment, depending on the necessary class and the production productivity.

As mentioned in the paper's introduction, the present study focuses on the super-automated category of coffee machines and provides a detailed description of these Electromechanical Systems (EMS).

2.2. Description of the electromechanical system in modern devices

Super-automated coffee machines are the most advanced and sophisticated. During the espresso extraction process, the machine's electromechanical system must perform several actions: grind the coffee beans to the required size, measure the right amount of coffee for a cup, pump water through the heating system into the preparation unit to raise the water temperature from about 10˚C to 95˚C, and dispense espresso and steam as needed. Considering all the steps the system must perform and the raw materials for brewing coffee,

the system contains several subsystems operated by the control system. Figure 1 shows the diagram of such an EMS in which the control unit is performing the necessary steps of the production process through three subsystems [5-7].

- **Grinding system**. The coffee beans are received in the grinder, which is tuned for a proper coffee fraction for the best performance of the present hydraulic subsystem. The dozing step follows the grinding process. The necessary amount of coffee is ground using one of the two well-known methods: time- and volume-based.
- **Hydraulic system.** During the grinding process, the hydraulic subsystem prepares for the extraction process, which will be performed as soon as the grinding is finished. The components of this system will vary depending on the type of unit. In this case, the system is based on instant heating boilers, which are the most efficient ones due to the amount of water that is heated. The system is designed to instantly heat the water as low as 10°C to the operating temperature for the extraction. To produce hot water and steam for milk frothy, the number of instant boilers could be more significant than one and depends on the machine's performance.
- **Extraction system.** The final subprocess is the extraction itself. The coffee machine performs the extraction based on the brewing unit type of system. The central role played by the brewing unit is designed to perform all the expresso extraction steps done by a barista operating a professional, high-performance coffee maker. The ground coffee is moved into the extraction chamber, tampered with by the preset force, the espresso is extracted, and the processed coffee is thrown into the garbage.

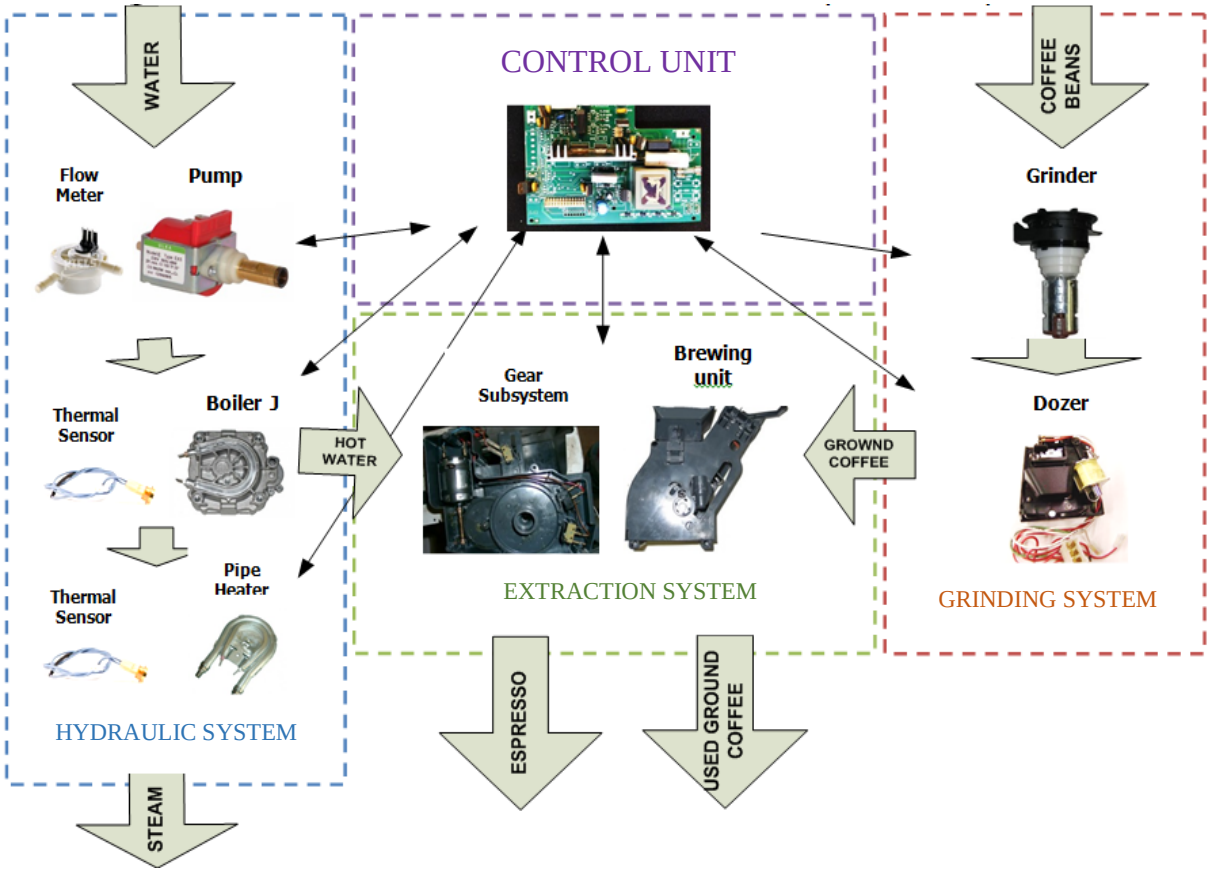

Figure 1. Diagram of the super-automatic electromechanical system of the SAECO ROYAL series [7].

An assessment is essential for understanding the energy usage of an electromechanical system. The analysis should cover the information that needs to be examined for this goal.

The energy consumption data collected in previous research revealed that about 99% of the total energy consumption belongs to the hydraulic system, with 97% for heating water and 2% for pumping it. This information guided the research to streamline the coffee extraction process and optimize the operation of the hydraulic system. An instant boiler with an inductive heating process must be designed and implemented to lower energy consumption and increase efficiency [8].

3. Dimensioning of the inductive heater

3.1. Input data for the calculations

To perform the necessary calculation, a set of internal data was needed, which is presented in Table 1 below.

Table 1

Input data for calculations of the power required to heat water

Parameter Value	Parameter Name
$\theta_i = 10^{\circ}C$	- initial water temperature at the inlet to the heater
$\theta_f = 95^{\circ}C$	- required temperature at the outlet of the heater
$\gamma_{ap} = 997\frac{kg}{m^3}$	- water density
$\gamma_{ot} = 7860\frac{kg}{m^3}$	- iron density
$c_{ap} = 4180\frac{J}{kg \cdot K}$	- thermal mass capacity (specific heat) of water
$c_{al} = 900\frac{J}{kg \cdot K}$	- mass thermal capacity (specific heat) of aluminum
$c_{ot} = 459.8\frac{J}{kg \cdot K}$	- mass heat capacity (specific heat) of iron
$q_{ap} = 3.06 \cdot 10^{-6}\frac{m^3}{s}$	- the required flow of water
$t_{h.ap} = 60s$	- the heating time of the required volume of water passed through the heater

An important aspect to consider was the enthalpy and the total volume of steel required to ensure that.

3.2. The calculus of the inductive heating boiler [9-11]

The calculus for the power required to heat the water, Eq. (1)

$$P_{i.ap} = q_{ap} \cdot c_{ap} \cdot \gamma_{ap} \cdot \left(\theta_f - \theta_i\right), [W] \quad (1)$$

The dimensions of the workpiece (ferromagnetic lamb with water pipe in it) were determined and specified.

- *The surface temperature of the heating part was calculated*.

For this calculation, the acuity of the thermal chain in a heat exchanger that has the following forms was considered. The heat transfer process in the resistive heater in the SAECO boiler was regarded as in the inductive heater calculations, Eq. (2)

$$\theta_{si} = \frac{P_{i.ao}}{m_{i.saeco} \cdot c_{al}} \cdot t_{h.ap} + \theta_i, [K] \tag{2}$$

- *The coefficient of convective heat transfer was calculated.*

Considering the parameters of the SAECO ROYAL resistive heater and the material from which it was made (aluminum), the convective heat transfer coefficient was determined geometrically based on its thermal transfer process, Eq. (3)

$$h_c = \frac{P_{i.r}}{\pi \cdot d_{c.ap.i.r} \cdot l_{c.ap.i.r} \cdot \left(\theta_f - \theta_i\right)}, \left[\frac{W}{m^2 \cdot K}\right] \tag{3}$$

where: $l_{c.ap.i.r}$ - the length of the water channel in the resistive heater; $d_{c.ap.i.r}$ - diameter of water channel in resistive heater; $P_{i.r}$ - active power of the resistive heater.

- *The mass of the workpiece of the inductive heater was calculated, Eq. (4)*

$$m_{i.i.ot} = \frac{P_{i.ap}}{\theta_{si} \cdot c_{ot}} \cdot t_{h.ap}, [kg] \tag{4}$$

- *The volume of steel required in the workpiece was calculated to ensure optimal conductions of heat transfer, Eq. (5)*

$$V_{n.ot} = \frac{m_{i.i.ot}}{\gamma_{ot}}, \left[m^3\right] \tag{5}$$

- *The area of the required surface area of the water channel was calculated, Eq. (6)*

$$S_{c.ap.nec} = \frac{P_{i.ap}}{h_c \cdot \left(\theta_f - \theta_i\right)}, [mm^2] \tag{6}$$

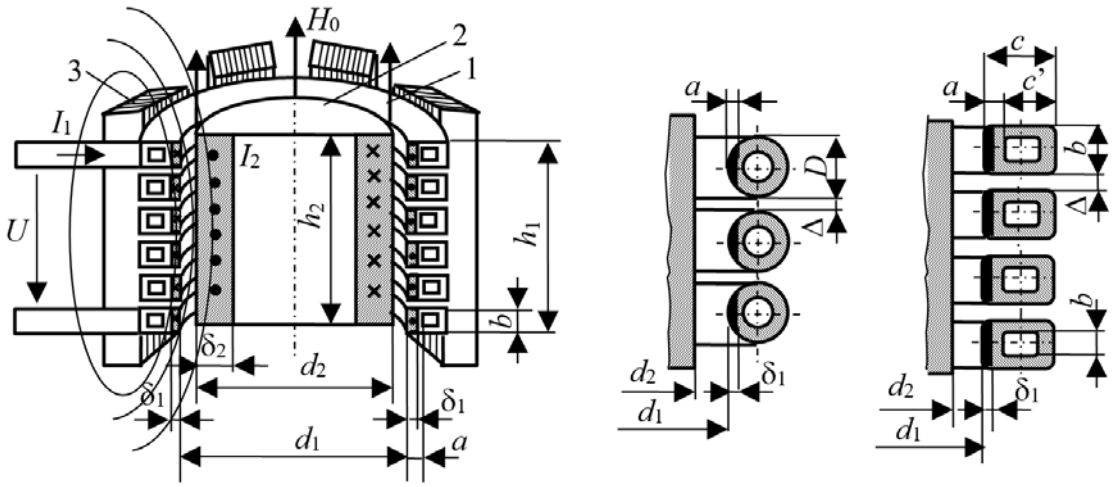

Figure 2. The dimensions of the inductor and the workpiece [9]: 1 - inductor; 2 - heating body; 3 - electromagnetic screen made of sheet metal package.

- *The length of the water pipe to provide the required surface area was calculated, Eq. (7)*

$$L_{c.ap.calc} = \frac{S_{c.ap.nec}}{\pi \cdot d_{c.ap.i.i}}, [mm] \tag{7}$$

where: $d_{c.ap.i.i}$ - diameter of the water channel of the inductive heater.

The calculation steps described above resulted in the necessary dimensions of the water channel, and the shape and form of the workpiece and the inductor were calculated according to the parameters shown in the figure below.

The sizing of the workpiece and water channel resulted in the workpiece being obtained and realized in SolidWorks, represented in Figure 3. It was used for further simulations.

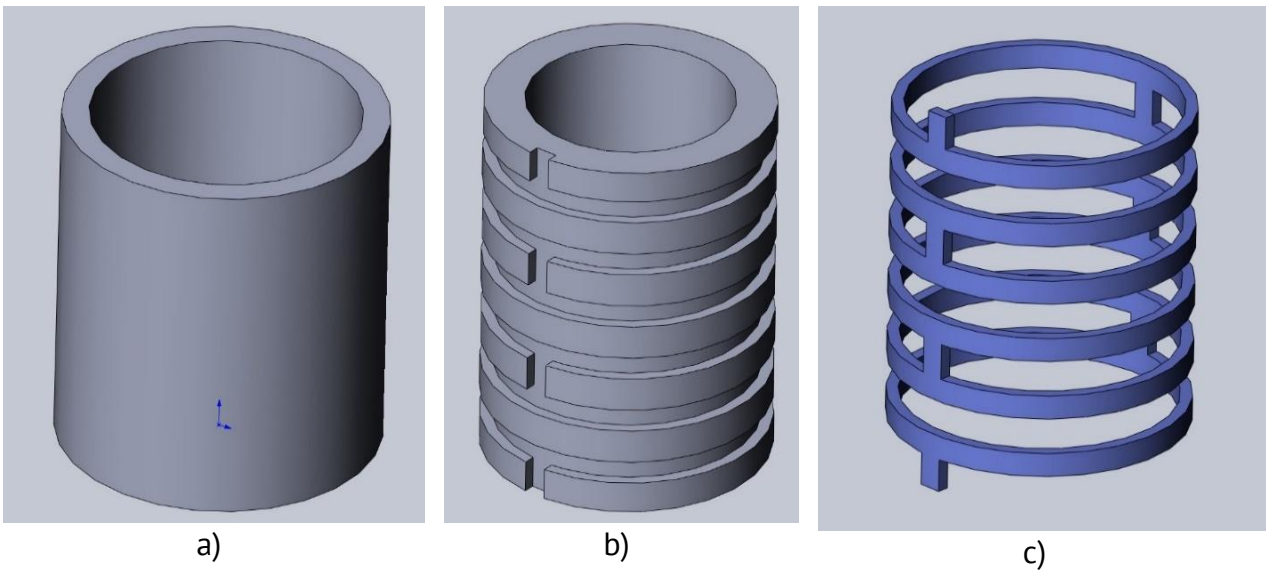

a) b) c)

Figure 3. 3D representation of workpiece components at dimensioned inductive heater made in SolidWorks: a) outer cylinder; b) inner cylinder; c) the shape of the obtained water channel.

The calculus of the electric parameters of the inductor and the workpiece

Considering the dimensions of the workpiece shown in Figure 4, i.e. the distance from the boundary with the fluid to the outer wall of the workpiece is 5 mm, select the operating frequency of the inductor at a value that will not allow the depth of penetration to exceed 0.5 mm.

- *The penetration depth in the inductor at 20°C, Eq. (8)*

$$\delta_{1.20C}(f) = \sqrt{\frac{2 \cdot \rho_{cup.20C}}{2 \cdot \pi \cdot f \cdot f_0 \cdot \mu_{cup}}}, [mm] \tag{8}$$

- *The penetration depth in the workpiece at 20°C, Eq. (9)*

$$\delta_{2.20C}(f) = \sqrt{\frac{2 \cdot \rho_{ot.20C}}{2 \cdot \pi \cdot f \cdot f_0 \cdot \mu_{ot}}}, [mm] \tag{9}$$

- *The penetration depth in the workpiece at 150°C, Eq. (10)*

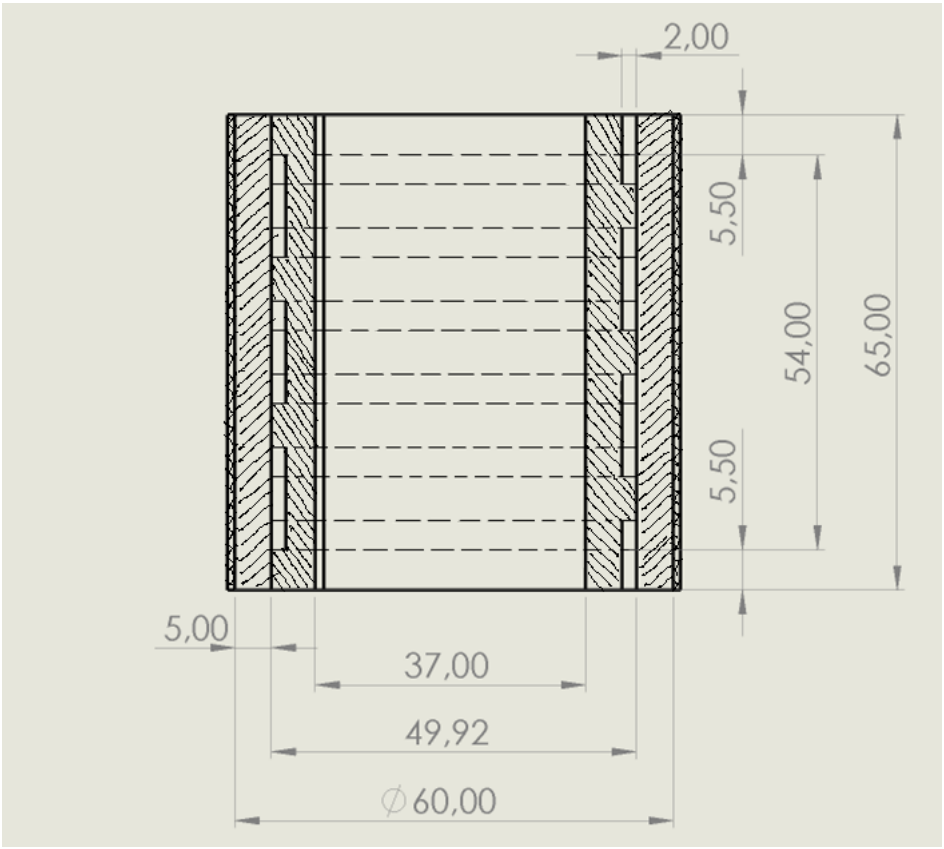

Figure 4. View of inductive heater made in SolidWorks.

Figure 5 shows the calculation and construction of the characteristic δ(f) for the inductor and the workpiece.

Figure 5. Dependence of penetration depth on the inductor supply frequency.

$$\delta_{2.150C}(f)=\sqrt{\frac{2\cdot\rho_{ot.150C}}{2\cdot\pi\cdot f\cdot f_0\cdot\mu_{ot}}},[mm] \tag{10}$$

● *We determine the thickness of the spiral wall according to the following recommendations a= (1.2, ... 2), Eq. (11).*

For the heater's operation, components F (corresponding to active power) and G (corresponding to reactive power) of the total energy absorbed at the body's surface shall be equal, and ε=a/δ shall be less than or equal to 1.57. The lower ε, the more efficient the power transfer will be. Penetration is minimal for ε=1.57.

$$a_1=1.57\cdot\delta_1,[mm] \tag{11}$$

● *The parameters of the inductor were calculated.*

To determine the inductor parameters, the number of turns (N) was determined. Then, the parameters for a single turn were selected, considering the turns linked in parallel. The internal resistance and reactance of the single-turn inductor were calculated with Eq. (12) using the given relationship, with a filling factor of g_u=0.8.

$$R_{1.1}=\rho_{cup.20C}\cdot\frac{\pi\cdot d_1}{h_1\cdot\delta_1\cdot g_u},[\Omega];\ X_{1.1}=R_{1.1} \tag{12}$$

● *The related resistance and reactance of the load, if we have Kr2=Kx2=1 and the number of turns N=N0=1, were calculated with the formulas in Eq. (13).*

$$R_2'=N_0^2\cdot\rho_{ot.20C}\cdot\frac{\pi\cdot d_2}{h_2\cdot\delta_2}\cdot K_{r2},[\Omega];\ X_2'=R'$$
$$R_2=\rho_{ot.20C}\cdot\frac{\pi\cdot d_2}{h_2\cdot\delta_2}\cdot K_{r2},[\Omega] \tag{13}$$

● *Air reactance was calculated with the formulas in Eq. (14).*

$$X_{II}=\frac{2\cdot f_{ind}\cdot\mu_0\cdot\left(\frac{\pi\cdot d_1^2}{4\cdot h_1}\cdot\alpha_1-\varsigma\cdot\frac{\pi\cdot d_2^2}{4\cdot h_2}\cdot\alpha_2\right)+X_{1.1}}{p^2},[\Omega]$$
$$where:\varsigma=\left(\frac{\alpha_m}{\alpha_1}\right)^2=0.94;\ p=\varsigma=0.94;\ \mu_0=4\cdot10^{-7}\frac{H}{m} \tag{14}$$

● *Parameters of the inductor system were determined with Eq. (15).*

$$R_1=R_{1.1}+\varsigma\cdot R_2;\ X_1=X_{1.1}+\varsigma\cdot\left(X_2-X_{II}\right),[\Omega] \tag{15}$$

Determination of the power absorbed by the inductor.

The necessary calculations are presented below

● *Determination of inductor electrical efficiency with Eq. (16)*

$$\eta_e=\frac{\varsigma\cdot R_2}{R_1} \tag{16}$$

- *Determination of inductor power factor with Eq. (17)*

$$\cos\varphi = \frac{R_1}{\sqrt{R_1^2 + X_1^2}} \tag{17}$$

- *Calculation of power converted into heat for heating the workpiece with Eq. (18).*

$$P_{2.ot} = \frac{m_{ot} \cdot c_{p.ot} \cdot 100K}{\eta_t}, [W] \tag{18}$$

- *Determination of active power absorbed from the network without reactive power compensation with Eq. (19).*

$$P_{in} = \frac{P_2 + P_{2.ot}}{\eta_e}, [W] \tag{19}$$

- *Determination of the apparent power of the inductive heater with Eq. (20).*

$$S_{in} = \frac{P_{in}}{\cos\varphi}, [VA] \tag{20}$$

- *Determination of inductor's required salination value with Eq. (21)*

$$NI_1 = \sqrt{\frac{P_{in}}{R_1 \cdot \eta_e}}, [A \cdot sp] \tag{21}$$

- *Determination of inductor supply voltage with Eq. (22)*

$$U_{in} = N_i \cdot \frac{S_{in}}{NI_1}, [V] \tag{22}$$

- *Determination of the inductive heater supply current with Eq. (23)*

$$I_1 = \frac{NI_1}{N_i} = 177.39[A] \tag{23}$$

As a result of the dimensioning, the inductive heater (Figure 6) containing the inductor (8) was obtained, which consists of 7 turns made of a copper tube, parameters of which are dimensioned to conduct the current of over 178 A with a frequency of about 100 kHz. The inductor is wrapped around the workpiece, which consists of two pieces in the form of tubular rings made of represented ferromagnetic material: outer cylinder (5) and inner cylinder (7).

On the outside of the inner tubular ring, cuts of such shape and length are made so that when assembling these tubular rings, a channel is obtained for the passage of the fluid to be heated. The shape of the channel obtained in the figure is represented by (6). To ensure much higher flow rates and temperatures of the heated fluid than those dimensioned, both in the hot water generation regime of about 90 °C and the steam generation regime of 120 °C, the inductor can be forcibly cooled by pumping a caloportor agent inside the copper tube, thus ensuring the stability of the heater. To avoid short circuits, the inductor is isolated from the workpiece using an insulator (4) with high thermal resistance, and its turns are removed from each other. To reduce magnetic field losses outside the inductor, sheets of electrical steel (9) are added and kept spaced away from the inductor utilizing side shields (3).

These shields position both the sheets of the magnetic circuit and the working core. To decrease heat losses in the environment, the inductive heater is also provided with thermal protection made by thermal protection elements (1) and (2) of the heater made of a material with high thermal resistance and low thermal conductivity coefficient [13, 15].

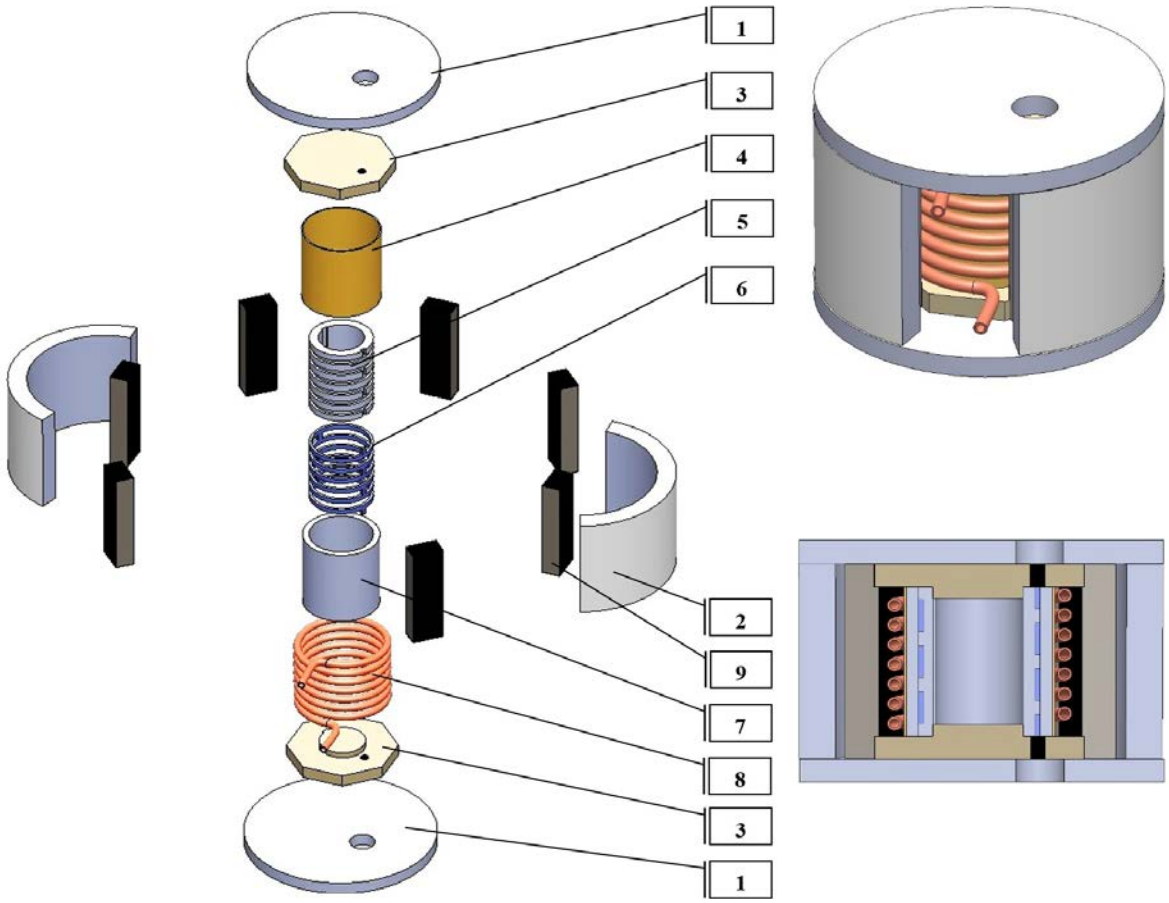

Figure 6. The final representation of the inductive heater with all parts included [13].
1,2-thermal protection elements; 3-side positioning shields; 4-insulator;
5-outer cylinder; 6-the profile of the water channel; 7-inner cylinder;
8-inductor; 9-sheets of electrical steel.

4. Simulations of the inductive heater in MatLab Simscape

The results that have been obtained need to be simulated, and for that purpose, the MatLab Simscape library was considered. The simulations will determine if the designed inductive boiler meets the necessary characteristics, the most important of which is the preheating time. To maximize the efficiency of the new boiler, it is essential to get the preheating time to be less than 8 seconds. Such a short time would make the preheating time so insignificant that the coffee machine would have enough time to get the hydraulic system ready for work within the grinding and dozing phases of the production process [14-16].

Figure 7 presents the simulation diagram constructed in MatLab Simscape.

The simulation diagram contains two subsystems: one is the inductor modeling subsystem, and the other is the workpiece modeling subsystem. These subsystems relate to each other using the magnetic field (Figure 8 a, b). The same diagram has a thermal liquid settings block that is used to specify the water properties in various thermal conditions, the water reservoir for modeling the water source that is pushed through the hydraulic system by the armature vibrating pump.

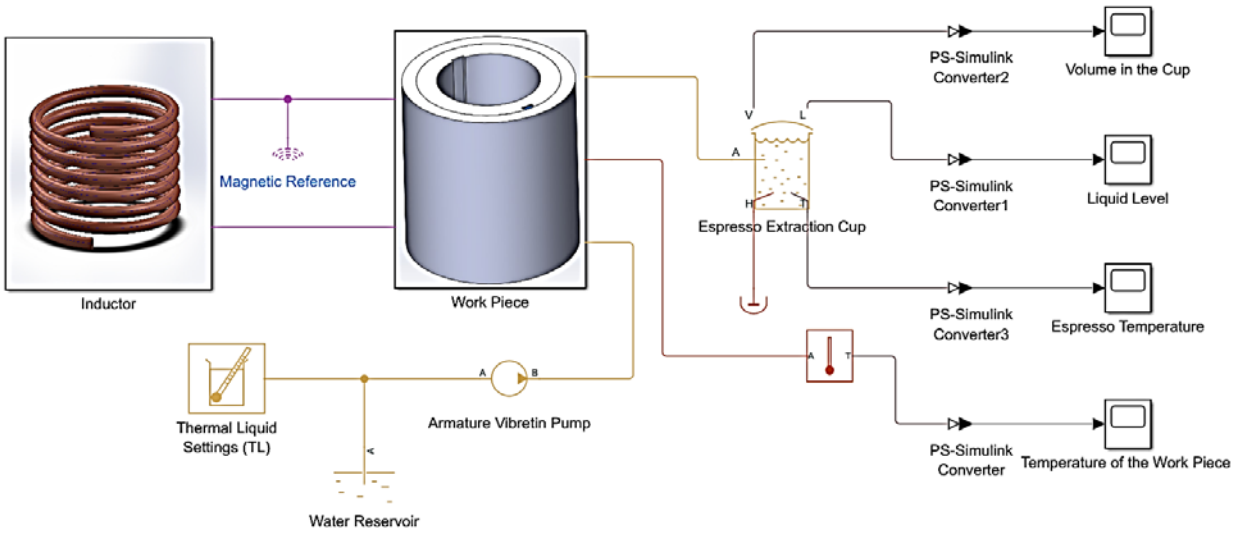

Figure 7. The simulation diagram of the inductive heating boiler.

The pump forces the water through the workpiece of the induction heating boiler, and the boiler's output relates to a block that simulates the espresso extraction cup. This block has several ports beside port A for the hydraulic connection. Some of the ports are the V port – which is for measuring the volume of the water in the cup; the L port - which is for measuring the level of the liquid in the cup; and the T port - which is for measuring the temperature of the liquid in the cup. The H port in this diagram simulates the heat losses from that container.

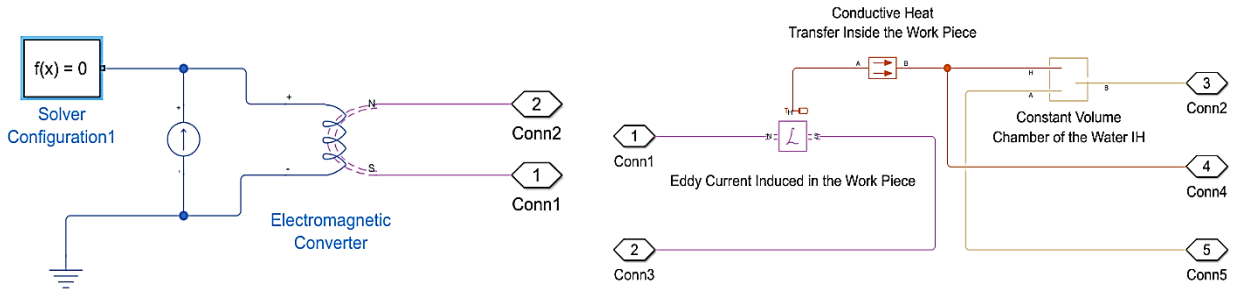

a) b)

Figure 8. The MatLab Simscape model subsystems:
a) inductor module; b) workpiece module.

Figure 9a shows the diagram for simulating the inductor module. It includes a current source block where the operating current and frequency are specified. The inductor block has all the necessary settings for correct operation. The workpiece diagram, presented in Figure 9b, consists of three blocks.

The "Eddy Current Induced in the Workpiece" block models the induced current that generates heat based on the workpiece's set parameters. The "Conductive Heat Transfer Inside the Workpiece" block simulates the process of conductive heat transfer, with parameters set for the layer. The inductor is designed to induce a current field in a minimal depth to achieve a high current density, resulting in a preheating time of under 8 s. Heat transfer from the induced current layer to the water takes some time. The "Constant Volume Chamber of the Water" block represents the water in the inductive heating boiler. Figure 10

below presents the simulation results with the inductor current set to 177 A and the frequency set to 100 kHz.

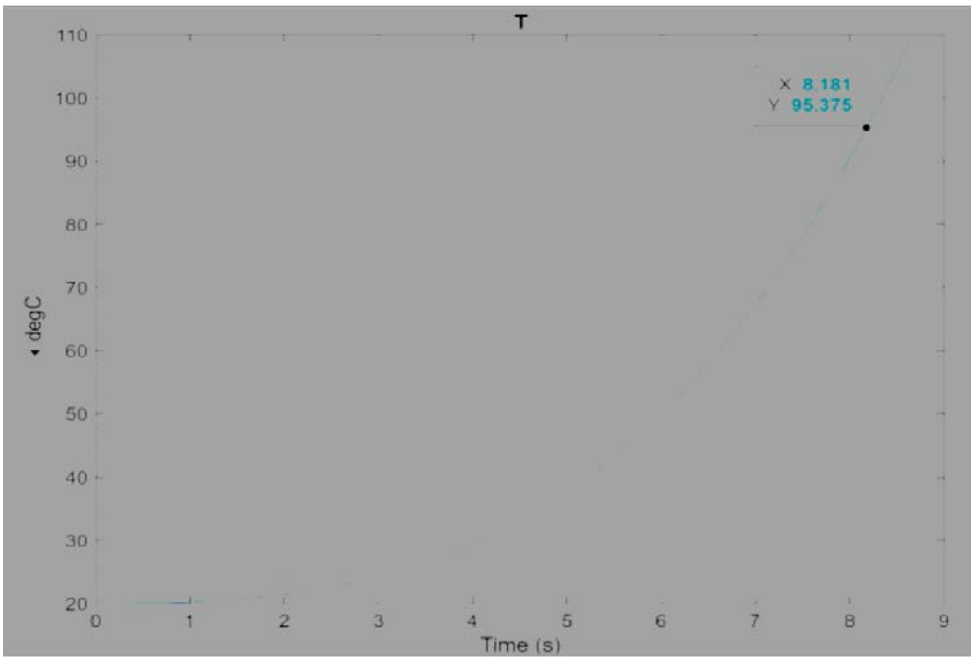

Figure 9. The evolution of the temperature in the inductive heating boiler workpiece with inductor parameters at 177 A and 100 kHz.

It becomes evident that the set of parameters with the current at 177 A and the frequency at 100 kHz gets to the necessary temperature level in 8.3 s The preheating time has to be shortened, and to do that, the following simulation will be performed with the current at 200 A, and the frequency remains constant. The results of that simulation are represented in Figure 10 below.

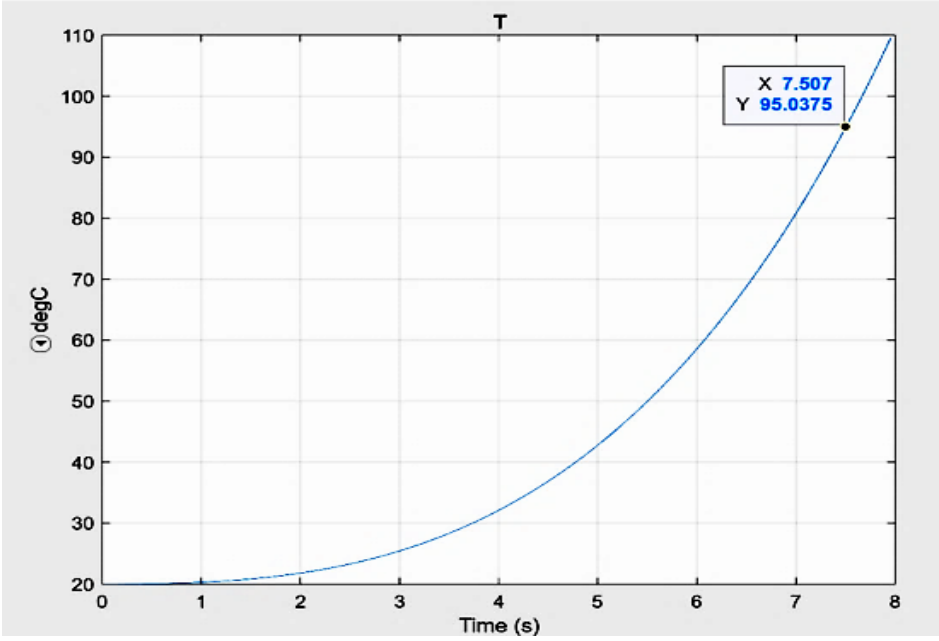

Figure 10. The evolution of the temperature in the inductive heating boiler workpiece with inductor parameters at 200A and 100kHz.

This time, the necessary time was achieved, and the preheating process was finished in 7.5 s with the water temperature as high as 95 °C.

5. Comparative analysis of energy consumption between resistive and inductive heaters

To carry out the analysis of the impact of innovations on the performance parameters of the coffee machine, the research will be divided into two parts as follows:

- *Determination of energy losses in the operation of resistive boilers* – At this stage, the consumption and energy losses in the operation of the resistive heater will be analyzed, and all phases of the operation process of such boilers will be considered. These include pre-heating, extraction process, and keeping the boiler at an optimal temperature during the waiting period for the next extraction step.

- *Energy consumption analysis for both the resistive and inductive heaters* – here, the performance of the two types of boilers will be analyzed, given the different times of thermodynamic processes, which are motivated by various physical processes, on which the operation of the respective types of boilers is based.

5.1. Determination of energy losses in the operation of resistive boilers

The determination of energy losses in the operation of the resistive heater will be carried out by numerical research, and the energy consumption used to pre-heat the respective boiler will be analyzed. For this, SAECO's resistive boiler will be considered. The required active power calculated for the preheating process of this boiler, having as input quantities the mass of the boiler, the mass thermal capacity of the boiler material, the temperature gradient of that process at which the active power required to heat the water inside the boiler during preheating will be gathered. The Eq. (24) determines the active power to pre-heat the resistive boiler.

$$P_{i.ap.al}=\frac{m_{ap.iboiler}\cdot c_{ap}\cdot\left(\theta_f-\theta_i\right)}{90}+\frac{m_{i.saeco}\cdot c_{al}\cdot\left(\theta_f-\theta_i\right)}{90},[W] \tag{24}$$

The energy losses in the operation of the resistive heater are determined with Eq. (25)

$$P_{losses}=\frac{P_{i.ap.al}}{P_n}\cdot 100-100=-28.63\% \tag{25}$$

As can be seen from the above calculations, the resistive heater consumes about 29% more power than is required for the components subjected to heating, which proves that even during the lifetime of a boiler of this type, the energy consumption will be even higher.

5.2. Energy consumption analysis for both the resistive and inductive heaters

To capitalize on the impact of innovations on the performance parameters of the coffee machine, namely, to analyze the energy consumption in the operation process of the inductive boiler and compare it with the resistive boiler, a production process of a street trade point with an 8-hour work schedule and average productivity of 100 servings of coffee bean drinks will be analyzed. Considering that the basis of all coffee bean drinks is the portion of coffee with espresso extraction and to simplify the calculation process, these portions of drinks produced during a workday mentioned above will be equated to 100 servings of espresso. Table 2 provides input data for the performance analysis of the boilers concerned.

Table 2

Input data for the analysis of boiler performance compared

Parameter value	Explanation of the parament
$N_{p.zi.} = 100\ [extrac.]$	- Number of servings produced during a working day
$D_{zi} = 8\ [h]$	- Length of the working day
$P_{ii.i} = 1090\ [W]$	- Power consumed by the resistive heater
$P_{ii.i} = 1900\ [W]$	- Power consumed by the inductive heater in the heating process
$P_{ii.ex} = 740\ [W]$	- Power consumed by the inductive heater in the extraction process

- *The calculation of the total time of the extraction cycle by considering and evenly distributing the rest time on all extractions with Eq. (26).*

$$if:$$

$$N_{p.houe} = \frac{N_{p.day}}{D_{day}} \approx 12\left[extr./h\right]$$

$$then:$$

$$T_{c.pc} = \frac{3600}{N_{p.hour}} = 300[\mathrm{s}] \qquad (26)$$

- *Calculation of the power consumption of the appliance in which the resistive heater is used*

Figure 11 below shows the histogram of the distribution of the total energy consumption of the resistive heater for an extraction process, including pauses.

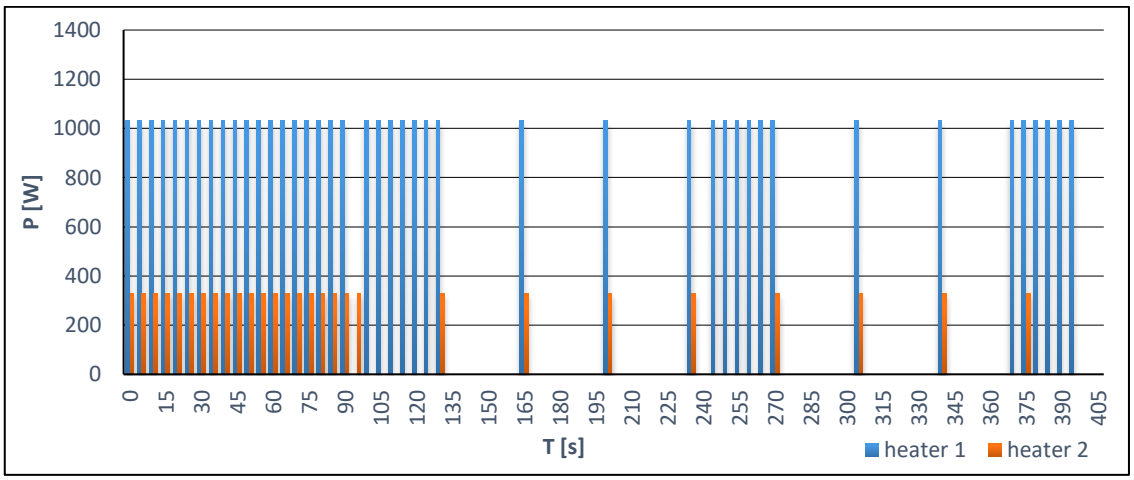

Figure 11. Histogram of the distribution of the total energy consumption of the resistive heater for an extraction process, including pause.

(Elaborated by the author).

As can be seen from the histogram built on the experimentally collected database, in the first 90 seconds, the boiler preheats, after which the first extraction process takes place. During the break, the boiler must maintain its temperature; for these reasons, it needs to be periodically replenished. It was noted that in 300 s, such connections were 8.

- *Calculation of total energy consumption for an extraction process, including pause, is done with Eq. (27)*

$$W_{day.ir} = \frac{\left(P_{preinc.ir} + P_{extr.ir} + 8 \cdot P_{ment.ir}\right) \cdot D_{zi} \cdot N_{p.hour}}{1000}, [Wh] \quad (27)$$

- *Calculation of the cost of electricity consumed in a month using the resistive heater, and the electricity price is calculated with Eq. (28).*

$$E_{month.ir} = W_{day.ir} \cdot p_{ee} \cdot 31 [MDL] \quad (28)$$

- *Calculation of the energy consumption of the appliance in which the inductive heater is used.*

Figure 12 shows the histogram of the distribution of total energy consumption when operating the coffee maker using the inductive heater.

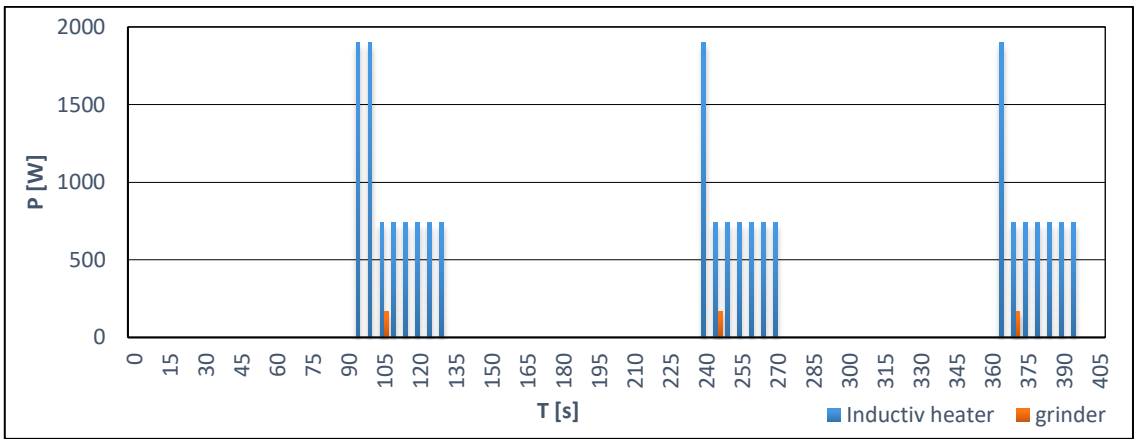

Figure 12. Histogram of the power consumption distribution of the inductive heater for an extraction process including pause

(Elaborated by the author).

As can be seen from the histogram built on the collected database, the preheating process of the inductive boiler takes only 8 s with a consumption of 1900 W, and extraction requires a consumption of 740 W for 28 s. Due to the performance of the inductive boiler, during the break, it is not necessary to maintain the temperature of the boiler, and its thermal protection gives us the possibility to reduce the time of returning the boiler to the optimum temperature at the next extraction by heating it only for 2 s instead of 7.5.

- *Calculation of energy consumption for an extraction process, including pause using an inductive boiler, is done with Eq. (29).*

$$W_{day.ii} = \frac{\left(P_{preheat.ii} + P_{extr.ii} + P_{re-heating.ii}\right) \cdot D_{zi} \cdot N_{p.hour}}{1000}, [Wh] \quad (29)$$

- *Calculation of the cost of electricity consumed in a month using the inductive heater is done with Eq. (30)*

$$E_{month.ii} = W_{day.ii} \cdot p_{ee} \cdot 31 [MDL] \quad (30)$$

- *Comparison of electricity consumption between the two types of heaters is calculated with Eq. (31).*

$$E_{-\%month} = \frac{E_{month.ii}}{E_{month.ir}} \cdot 100 - 100\% = -55.48\% \quad (31)$$

The implementation of the inductive heater at the selling points of the itinerant trade with coffee drinks will increase energy efficiency by over 55%, and this number will vary with respect to the change in workload.

6. Discussion regarding the results

As a result of the research, a prototype of the induction heater was manufactured and patented. Figure 13a represents the inner cylinder of the induction heater that was made according to the developed model, and in Figure 13b shows the assembled and polished workpiece with the inductor wrapped around the assembly

a) b)

Figure 13. The inductive heater assembly without magnetic circuit and thermal protection: a) inner cylinder; b) part condition after assembly and machining.

The experiments performed with the prototyped boiler above lacked the external magnetic circuit components and thermal protection, which will be added to the heater as soon as they are manufactured. But even in this condition, performance-wise, the pre-heating time stays within the necessary limits of up to 8 s, which is much better than the 90 s of conventional, resistive heaters.

The roughness of the water channels of the inner cylinder and the sharp edges between the horizontal and vertical ones play an important role in enhancing heat transfer by increasing the turbulent flow of the heated fluid. Therefore, the workpiece was polished only externally.

Considering the total mass of the innovative heater, which consists of about 700 g of metal, acts as a very good heat accumulator. After adding the external thermal protection elements, the thermal stability of the whole assembly will increase considerably. The power consumption of the inductive heater during the pre-heating time is double that of the resistive one. Still, the increased thermal stability of the first will result in a pre-heating time of just 1-2 s after a production pause of 30 minutes. These peculiarities in the functioning of the innovative heater, together with inductive processes will result in an increased efficiency of up to 55% in some scenarios.

There is potential even for future improvements. One such improvement could be using the inductor tube as a part of the fluid pre-heating element by pumping it through the inductor. It would permit better control of the inductor temperature, but, at the same time, a significant challenge that should be dealt with is the current leakage from the inductor into the fluid. Another possibility for improvement is the usage of space inside the inductive heater, which could benefit some production processes in the SEM of coffee makers or other devices.

Conclusions

- ✔ The hydraulic systems of general-purpose installations, such as coffee machines, account for up to 97% of energy consumption in heat transfer processes in solids and liquids.
- ✔ The design methodology of the inductive instant boiler was presented.
- ✔ The simulation model was created in MatLab Simscape, which was used for parameter verification.
- ✔ The innovative inductive heating boiler reaches the operating temperature in 7.5^{th} s.
- ✔ The optimal operating parameters of the heater are 200 A of current and a frequency of 100 kHz.
- ✔ The developed inductive heater increases the efficiency of coffee machines by about 29%, at the same time, their use in trade with coffee bean beverages as a finished product considering the schedule of a working day and the time required for the process of pre-heating and maintaining the appliance at the working parameters of the boiler (working temperature of the boiler) eliminated ensures an increase in efficiency of over 55%.

References

1. Directive 2009/125/EC of the European Parliament and of the Council, of 21 October 2009, establishing a framework for setting ecodesign requirements for energy-related products. Available online: https://eur-lex.europa.eu/legal-content/RO/TXT/PDF/?uri=CELEX:32009L0125&from=FR (accessed on 3 April 2019).
2. Directive 2012/27/EU of the European Parliament and of the Council of 25 October 2012 on energy efficiency, amending Directives 2009/125/EC and 2010/30/EU and repealing Directives 2004/8/EC and 2006/32/ Available online:https://eur-lex.europa.eu/legal-content/RO/TXT/PDF/?uri=CELEX:32012L0027&from=LV (accessed on 3 April 2019).
3. GD no. 750 of 13.06.2016 for the approval of the regulations on ecodesign requirements applicable to energy-related products. [in Romanian] Available online: http://lex.justice.md/index.php?action=view&view=doc&lang=1&id=365482 (accessed on 3 April 2019).
4. Certified Italian Espresso and Cappuccino. Available online: http://www.espressoitaliano.org/files/File/istituzionale_inei_hq_en.pdf (accessed on 10 April 2020).
5. Saeco technical support. Available online: www.saeco.co.uk/espresso-machine-support (accessed on 10 March 2022).
6. Ultraflex Power Technologies, support tehnic-theoretic, A Comparison of Efficiency and Power Consumption for Induction Heating versus other Heating Methods Efficiency of Induction Heating, Ultraflex Power Technologies. Available online: https://ultraflexpower.com/learn-about-induction-heating/efficiency-of-induction-heating (accessed on 10 November 2021).
7. Turcanu, A.; Nuca I. Modernization of the Grinding System of the Automated Coffee Machine. In: *National Conference of Electric Actions, CNAE-2014*, 28-29 September 2014, 21, pp. 251-262.
8. Turcanu, A. Methods of streamlining technological processes in usual installations. In: *Technical-scientific conference of students, master's and doctoral students*, 26-29 March 2019, Chisinau, 2019, 1, pp. 111-114 [in Romanian].
9. Golovanov, N.; Şora, I. Electrothermia şi electrotecnologie. Technical Bucharest, Bucarest, Romania, 2007, 2, 422 p. [in Romanian].
10. Manolea, G. Electromechanical Drives. Universitaria, Craiova, Romania, 2008, 174 p. [in Romanian].

11. Vedavarz, A. Handbook of Heating Ventilation and Air Conditioning for Design and Implementation. Industrial Press Inc., New York, SUA, 2007, 1080 p.
12. Nuca, I. Electric Drives, Course Notes. Available online: http://elearning.utm.md/moodle/course/view.php?id=68 (accessed on 15 October 2023) [in Romanian].
13. Turcanu, A. Inductive heater. Short-term patent 1617. BOPI 2022, 4, pp. 54-55 [in Romanian].
14. Ivanov, S. Modeling and simulation; electromechanical systems, environmental processes. Universitaria, Craiova, Romania, 2007, 203 p. [in Romanian].
15. Nuca, I. Mathematical Modeling of Electromechanical Systems, Course Notes. Available online: http://elearning.utm.md/moodle/course/view.php?id=67 (accessed on 30 March 2024) [in Romanian].
16. MathWorks help and support center. Available online: https://www.mathworks.com/help/matlab/index.html?s_tid=CRUX_lftnav (accessed on 30 March 2024).

Citation: Turcanu, A.; Nucă, I. Implementation of inductive processes in general-purpose equipment to enhance heat transfer procedures. *Journal of Engineering Science* 2024, XXXI (4), pp. 55-72. https://doi.org/10.52326/jes.utm.2024.31(3).01.

Submission of manuscripts: jes@meridian.utm.md

Journal of Engineering Science *Vol. XXXI, no. 4 (2024), pp. 73 - 83*
Fascicle *Electronics and Computer Science* *ISSN 2587-3474*
Topic *Electronics and Communication* *eISSN 2587-3482*

https://doi.org/10.52326/jes.utm.2024.31(4).05
UDC 681.586:629.783:004.8

ARCHITECTURE OF THE SPACE RADIATION SENSOR SATELLITE MODULE BASED ON ARTIFICIAL INTELLIGENCE

Nicolae Secrieru [1]*, ORCID: 0000-0002-9168-6049,
Viorel Carbune [1], ORCID: 0000-0002-1556-4453,
Tudor Zadorojneac [1], ORCID: 0000-0002-4079-252X,
Vladimir Melnic [1], ORCID: 0000-0003-4180-3654,
Mihai Ivanovici [2], ORCID: 0000-0002-0803-2918,
Andrei Bertescu [2], ORCID: 0009-0004-7464-0075,
Stefan Popa [2], ORCID: 0000-0001-9275-4536,
Artur Kazak [2], ORCID: 0000-0002-1463-9089

[1] *Technical University of Moldova, 168, Ștefan cel Mare Blvd., Chișinau, Republic of Moldova*
[2] *Transilvania University of Brasov, Brașov, Romania*
* Corresponding author: Nicolae Secrieru, *nicolae.secrieru@cnts.utm.md*

Received: 10. 05. 2024
Accepted: 11. 12. 2024

Abstract. This paper is dedicated to the study of the cosmic radiation and its effects on electronics, as well as methods to measure it in order to aid the elaboration of the architecture of the satellite module with space radiation sensors for classification and real-time analysis of cosmic radiation-induced fault patterns and state predictions the of electronic systems embedded in satellites. The architecture of the satellite module with an intelligent radiation sensor based on an FPGA device is proposed, which will include as radiation sensing elements arrays of various types of electronic memories (on semiconductors), both within the circuit and external nearby this circuit. A significant part of the FPGA circuit configuration consists in the development of acquisition, processing and communication procedures using structures with majoritz voting to exclude the influence of spatial radiation.

Keywords: *space radiation sensor, satellite module, artificial intelligence.*

Rezumat. Această lucrare este dedicată studiului radiației cosmice și efectelor acesteia asupra electronicii, precum și modalităților de măsurare a acesteia pentru a ajuta la dezvoltarea arhitecturii modulului satelit cu senzori de radiație spațială pentru clasificarea și analiza în timp real a tiparelor de defecțiuni induse de radiația cosmică și predicția stării sistemelor electronice încorporate în sateliți. Este propusă arhitectura modulului satelit cu senzorul inteligent de radiație bazat pe un circuit de tip FPGA, care va include ca elemente de detectare a radiației rețele de diferite tipuri de memorii electronice (pe semiconductori), atât în interiorul circuitului, cât și în exteriorul apropiat al acestuia. O latură semnificativă a configurării circuitului FPGA constă în realizarea procedurilor de achiziție, procesare și comunicare utilizând structuri cu vot majoritar pentru a exclude influența radiației spațiale.

Cuvinte-cheie: *senzor de radiație spațială, modul satelit, inteligență artificială.*

1. Introduction

Space radiation poses a significant threat to the electronic components of satellites in Earth orbit and spacecrafts on planetary missions. The particles in the cosmic space are the high-energy electrons, protons, alpha particles and cosmic rays. Space radiation can lead to disruptions and temporary malfunctions in integrated circuits, including memory components. While the natural space environment does not have high level dose pulses, electronic systems exposed to space radiation can accumulate a large sum dose of electrons and protons over many years [1,2].

The radiation effects caused by high-energy particles in space are mainly determined by the ionization process, in which high level energy particles generate electron and hole pairs (e-h) as they pass through the equipment.

In complement to generating electron and hole (e-h) pairs, radiation can cause deformation damage in the atomic semiconducter lattice by breaking atomic bonds and forming so-called recombination centers and centers by accretion. Both damage mechanisms can lead to decreased electronic scattering. The X-rays and gamma rays are the main ionizing electromagnetic radiations. The ionizing radiation consists of light uncharged particles (neutrons), light charged particles (electrons, protons), alpha and beta particles and heavy charged particles (heavy ions) of chemical elements such as iron, bromine, krypton, xenon. Gamma rays and X-rays cause damage similar to that caused by light-charged particles because their main effect is the interaction of charge with the atomic structure of the material. Neutrons are uncharged and interact primarily with the atomic nuclei, causing damage in the atomic lattice of the material [1,3,4].

Therefore, the development of space radiation sensor based on artificial intelligence would give the possibility to more adequately assess the state of space weather and will give the possibility to mitigate its negative effects.

2. Space Radiation Measurement Approaches

The purpose of the research is to analyze the deviations of sensor parameters over time and as a function of the accumulated spatial radiation dose. It is known that the absorbed radiation dose refers to the amount of radiation energy delivered per unit mass of material. This is usually measured in rad (absorbed radiation dose) or in international units such as Gray or mGy (milliGray = 1/1000 Gray).

At the current stage there are a variety of methods and means of radiation measurement [1], but semiconductor based detectors are preferred due to the principle of radiation responsiveness, mass and energy consumed. The radiation reaction occurs when a particle imposes energy on a semiconductor detector or semiconductor junction, resulting in an equal number of electrons and holes being created along the particle's path within a few picoseconds. The detector is designed to ensure that an electric field is present throughout the active volume, causing the charge carriers to experience electrostatic forces that drive them in opposite directions. Therefore, the movement of these electrons and holes generates a current that continues until the carriers are collected at the boundaries of the active volume of the semiconductor material.

Taking into account the effects of radiation on semiconductors, in this paper we will focus on semiconductor-based sensors.

3. Architecture of the space radiation sensor satellite module

The architecture of a prototype satellite module is proposed with the objectives to verify the value of a demonstration mission, which are of great interest both locally and internationally: to assess the feasibility of using a radiation sensor based on artificial intelligence and realized with Commercial-off-the-shelf components. At the core of this module is a Field Programmable Gate Arrays (FPGA) device circuit [5-9], in which several Single-Event Upset (SEU) detector arrays are embedded in the silicon area/surface of the circuit. The FPGA device will be configured with a custom design aimed at detecting SEUs and then clustering and classifying the patterns using an AI model. The device will be hosted on an auxiliary printed circuit board interfaced to the Onboard Computer's (OBC) main board through a connector. The four objectives of the AI-based hardware Cosmic Radiation Sensor (AICoRS) system are: i) evaluating the feasibility of using an FPGA device as a cosmic radiation sensor, ii) measuring and classifying the cosmic radiation patterns, iii) evaluating the effectiveness of SEU mitigating mechanisms (e.g. triple modular redundancy (TMR), error correction code and iv) evaluating the feasibility of using such a modern, low-cost general-purpose FPGA device for space applications. Based on the AMD FPGA the proposed system will contain: the FPGA device, voltage regulators for ensuring the required supply voltages, total and per voltage level current monitors for measuring the power draw, low-jitter oscillators for supplying clock signals, non-volatile flash memories for storing the FPGA configuration files, the necessary voltage levels converters for the data signals between the OBC and the FPGA and ICs for control (e.g. reset, enable/disable, configuration modes). All these devices contribute to the power draw. The board should support in-space FPGA reconfigurability. More details on the composition and functioning of this core are presented in [10].

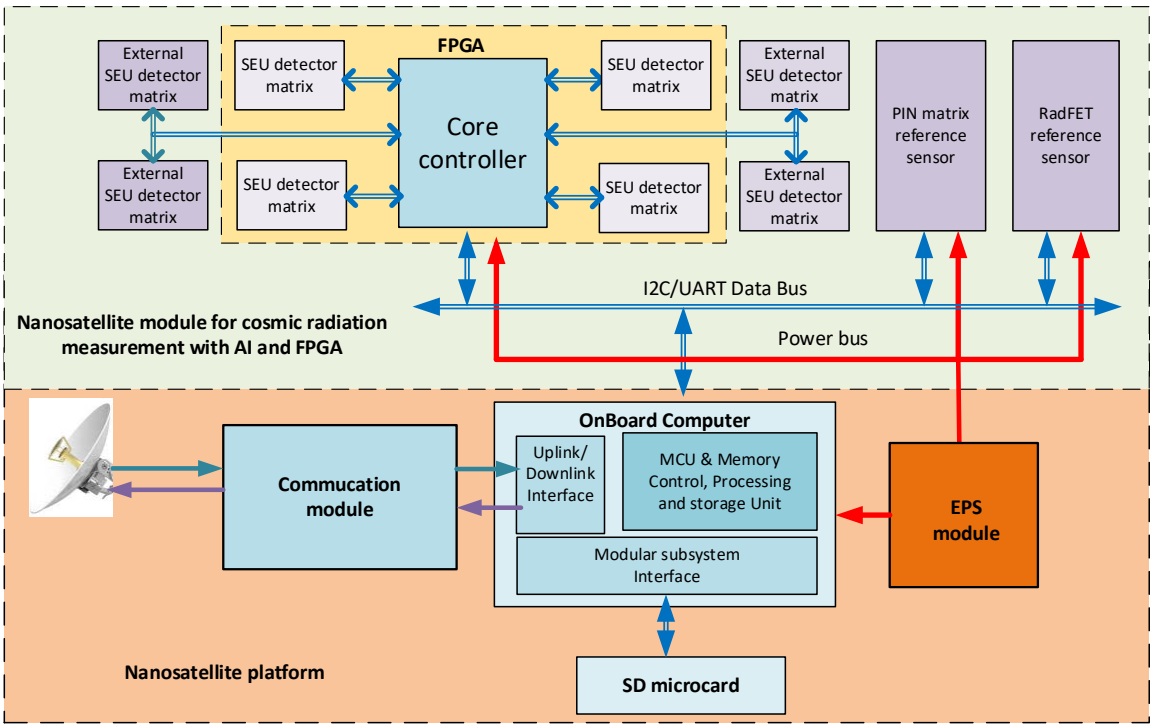

Figure 1. The functional schema of the space radiation sensor satellite module.

This core will be realized separately as a space radiation sensor with artificial intelligence properties. This satellite module has not only the technological demonstration

mission, but also the test/verification mission for training the artificial neural network. For this purpose, reference radiation sensors are proposed to accumulate veridical information of the types and intensities of spatial radiation, which will be further characterized.

4. Reference Sensors External to the FPGA

In order to propose solutions for External Sensors to the FPGA and other Reference Sensors a number of dosimetry methods have been considered, but we have limited ourselves to those based on [1-4,9,11]:

- memory dosimetry - single events cause bit flips/changes in memory - the accumulated number of errors reflects the absorbed dose;
- PIN diodes - voltage change before and during irradiation;
- RadFET transistors - p-MOS transistor threshold voltage shift indicates irradiation.

Memory dosimetry. After analyzing the reaction of various types of memory to radiation, it has been found that emerging resistance-shifting memory technologies such as Magnetoresistive random-access memory, Resistive random-access memory (ReRAM), Conductive bridging random access memory (CBRAM) and Phase-change random-access memory (PCRAM) (as known under typical names) are relatively insensitive to ionizing radiation, single event effects (SEE) and displacement damage, since there is no direct relation of interaction between radiation and the storage mode. But when radiation induced errors may arise, they are most common is the result of an interaction with the decoding unit or supporting peripheral circuitry. [2,9].

Therefore, as an external SEU detection to the FPGA it is proposed nonvolatile memory (NVM) arrays, which are less tolerant, i.e., more sensitive to cosmic radiation. There memories are usually arranged in arrays that are read and written operations using orthogonal address lines (AL) and data lines (DL). However different array topologies are used for different memory device technologies. For instance, three terminal charge based devices such as embedded floating gate (EFG) or charge trapping memory (CTM) are applied in NAND and NOR flash topologies. [2-4, 9, 11]. For two-terminal resistive type memories are more often applied in the form of dynamic random access memory (DRAM-like) random access arrays, which allow separate read and write operations on discrete cells.

The operations "write" or "program", for charge based memories, indicate the injection of charge into the storage element (FG or capture layer), while "erase" usually refers to the process of removing the charge. Usually, these terms are used to indicate reading and writing to NVM-type memory, which depends on the technology discussed. The operations "set" and "reset", in the case of resistive memory (ReRAM) or phase-change memory (PCRAM) types, are commonly used to indicate writing a low or high resistance state, respectively, to the memory cell. Endurance is the number of times data can be written to an NVM cell before it begins to commit errors. Due to technology, NVMs typically have a small number of endurance cycles, whereas SRAMs and DRAMs can effectively change the memory state an unlimited number of times.

NVMs type memories are affected by cumulative exposure to cosmic radiation over time, including total ionizing dose (TID). The effects caused by a single transient impact of energetic particles, known as single event effects (SEE), are the result/impact of the memory exposure to cosmic radiation.

Total ionizing dose TIDs modify the state of charge storage elements by altering the charge levels stored in the cell. All modern NVM technologies require CMOS control circuits,

which are subject to threshold voltage shifts and sub-threshold leakage paths due to TID, which can cause read and write circuits to malfunction. More details about TID effects in electronics can be found in [2-4,9,11].

The displacement damage is caused by charged particles interacting with the electronic component structure and can also constantly modify the atomic structure. In such a case, some of the atoms that "constitute" one bit are delocalized, which can cause permanent memory lock or lack of functionality. It is often characterized by the flux of particles per unit area of the electronic component, presented as ion/cm^2 counts. In some cases atom delocalizations are also used to quantify deterioration. In NVMs most types of SEU are observed due to impact with heavy ions or high energy charged particles. Some of the usual events include non-permanent or soft errors known as single event errors (SEU), and also include single-bit errors (SBU) and multi-bit errors (MBU). One SBU event in an NVM memory cell refers to a change of state of a single bit due to a transient impact of a particle, usually due to charge accumulation, but in some cases it is possible for a charged particle to disturb the state of several bits in the NVM cell, in which case a MBU error occurs.

A single-event functional interrupt appears when the functionality of the memory controller circuitry, such as a microcontroller controlling the sequence of read and write operations, is affected by the impact of these particles. Table 1 shows the effects of TID and SEE on memories of different NVM memory types and their tolerance to cosmic radiation. [2].

Memories that are sensitive to relatively low radiation doses, are affected by the direct interaction of ionizing radiation with the stored charge. TID can cause bit-level perturbations at 10-50 krad (in Si semiconductor) and is largely unaffected by scaling. As multi-level cells and three-level cells (which store three bits per cell) become more common in scaled devices, these advanced cells are increasingly vulnerable to TID- and SEU-induced errors. Single-event disruptions easily occur in floating cells at Linear Energy Transfer (LET) values below 10 MeV*cm^2/mg. Floating-gate memory becomes more susceptible to bit perturbations with scaling as the stored charge for the expected state decreases. In contrast, advanced CTM-type memory is much more resistant, capable of withstanding TID levels between 300-500 krad (Si), with effective cross-sections for perturbation starting at a LET of approximately 20 MeV*cm^2/mg.

Taking into account the above, the reference radiation sensors are proposed in order to investigate the properties of the intelligent radiation sensor. Therefore, the properties and characteristics of two types of reference radiation sensors (RadFET and PIN diode array) are presented.

RadFET dosimetry. For a calibrated device to measure the accumulated radiation dose it was decided to use RadFET as the radiation dose sensing element. The most important advantages of RadFET-based dosimetry are [12,13]:

- sensor power can be completely switched off during irradiation (no power consumption and increased reliability); integrated measurement (particularly important for small doses);
- on-line, non-destructive reading and small size, on the other hand it has important drawbacks: low sensitivity at low radiation doses - requires sophisticated measurement setup and requires temperature compensation.

As a result of analyzing various satellite missions, we decided to take as a basis a sensor based on the RADFet effect, which can be read with time interval between readings can range from seconds

to some days. The RadFET sensor (Reader Circuit - RC) designed circuit to read radiation value is presented in Figure 2.

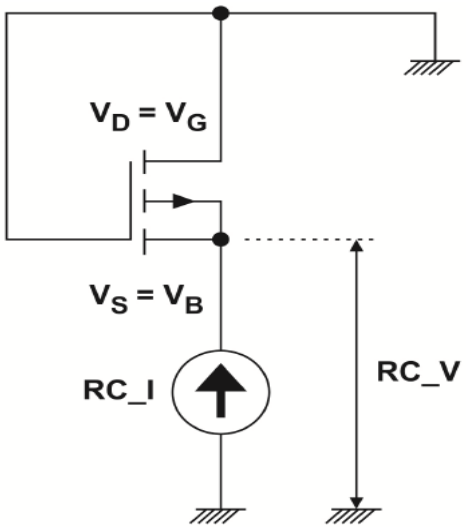

Figure 2. RadFET current measurement principle dependent on accumulated radiation dose [12,13].

The accumulated radiation dose is reflected by the readout current (RC_I) from the RADFET. But the current is measured indirectly, by measuring the source voltage (RC_V) - this voltage is called the "RC threshold voltage". For each RadFET element, there is the individual current-voltage (I-V) curve for the un-irradiated device, shown in Figure 3. In the given case the RC_I value was set above 10 μA for best temperature compensation.

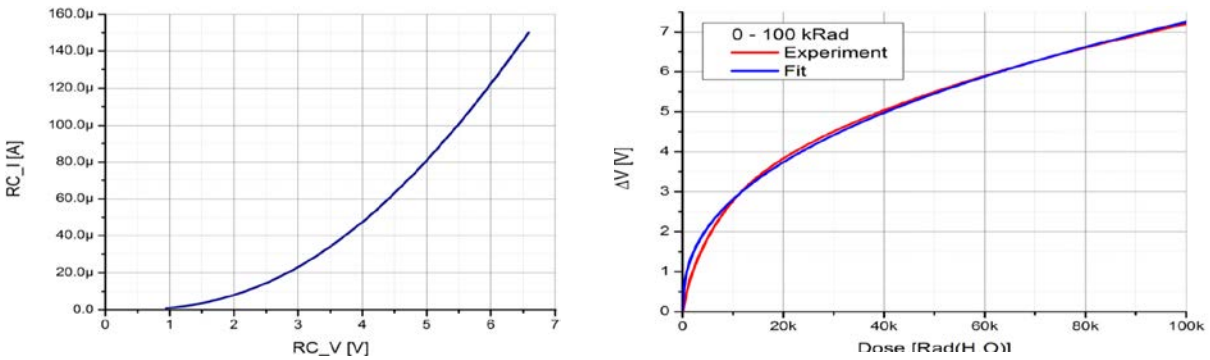

a) b)

Figure 3. RadFET characteristics: a) Pre-irradiation (I-V) curve measured at temperature 15 °C, b) curve of calibration during irradiation at normal temperature with gamma (Co-60) radiation source, dose rate ~50 Gy/h (5 krad/h) [12,13].

PIN-type diodes dosimetry. A positive-intrinsic-negative (PIN) diode has three layers, including an intrinsic layer sandwiched between the N- and P-type semiconductor crystal layers, with the specificity that the N-type layer is created when a pentavalent impurity is coated in the semiconductor region. In the P-type layer, a trivalent impurity is formed in the semiconductor region. The intermediate layer, called intrinsic, comprises an undoped semiconductor. The highly resistive intrinsic layer is positioned between the P and N regions and this intrinsic layer generates a strong electric field due to the movement of electrons and holes, causing the electric field to be directed from the N region to the P region. The strong

electric field allows the diode to respond to small signals. The operation of a PIN diode is determined by the structure of its three-layer semiconductor structure, which consists of a p-type layer, an intrinsic (undoped or lightly doped) layer, and an n-type (negative) layer. The intrinsic layer, which is crucial for its function, behaves as a variable resistor when a voltage is applied. Radiation affects the PIN diode by generating uniformly distributed electron-hole (e-h) pairs within the diode. At high dose rates, the separation of these charges reduces the internal electric field and results in prolonged storage of excess carriers [1].

After analyzing the characteristics of PIN-diode sensors, the AL53 was chosen due to its solid state sensor performance and ultra low power requirements, making it an ideal option for both cutting-edge designs and retrofitting existing systems [14]. This AL53 radiation sensor features a custom designed PIN diode and to prevent sensitivity to light is coated with a thin aluminum film. The sensor diagram includes an integrated pulse discriminator with a temperature compensating threshold level, providing a TTL level output signal (Figure 4a). The AL53 radiation sensor is capable of detecting alpha and beta particles, as well as gamma rays.

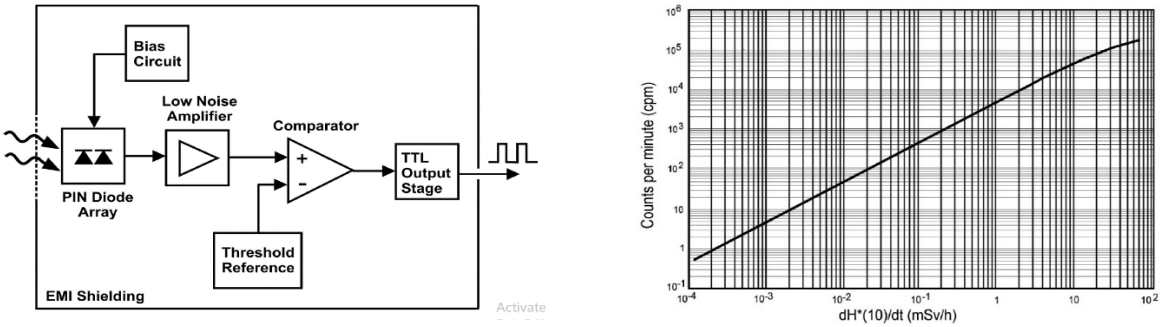

a) b)

Figure 4. AL53 PIN-diode [14]: a) Functional block diagram; b) curve of calibration during irradiation at normal at dH*(10)/dt - radiation dose rate for Cs-137 and Co-60 (mSv/h).

It should be noted an important side of these radiation sensors (RADFet and PIN-Diode) is that the former measures the cumulative dose, and the latter measures the current value of space radiation. These data we believe will be very useful for training of Artificial Neural Network.

Preliminary results

A preliminary FPGA design aimed at detecting SEUs and targeted at the AMD (Xilinx) UltraScale+ AU25P device is presented in [10]. It employs 100 blocks of SRAM (BRAMs) with a capacity of 36 Kb each, populated with a deterministic pattern of 1s and 0s that act as SEU detectors. Each such detector once triggered scans its memory content and can report and correct the encountered errors. The correct operation of the logic is insured by the TMR for all flip-flops (FFs) with separate replicas of the clock signal. The targeted AMD FPGA device was chosen based on its relatively low cost, available resources relative to the size and the implementation technology (i.e. the newest/smallest process for an FPGA-only AMD device – 16 nm). In [10] the design was analyzed regarding power consumption and real-time SEU detection capabilities. It was determined that a high clock signal frequency is unnecessary.

In the current work we analyze the same design but implemented on several other similar (in terms of resources, package footprint size and price) AMD FPGAs including one from the previous generation (using a 28 nm process) that is cheaper than the one used in

[10] while having comparable resources. The resources, package footprint size, resources and price for 10 devices are detailed in Table 2. The Look-Up Tables (LUTs) are all 6-bit, Ultra RAMs (URAMs) are block of SRAM 4K × 72 bits each (i.e. 288 Kb = 8 times larger than one BRAM) while each Digital Signal Processing (DSP) slice has a dedicated 25×18 bit two's complement multiplier and a 48-bit accumulator. The older XC7A200T device is potentially the most compact (i.e. 19×19 mm), and contains 65 more BRAMs than the AU25P device used in [10] while containing slightly less FFs and LUTs. However, it has significantly less DSPs that can be employed for the AI model.

Table 2

Comparative analysis of similar AMD FPGAs (in terms of resources, package footprint size and price)

Family	Device	Size	FFs	LUTs	BRAMs	URAM	DSPs	Approx. Price (x10)
Artix-7	**XC7A200T**	19×19 23×23 27×27	269200	134600	365	0	740	$3900
Artix UltraScale+	**AU20P**	23×23	218000	109000	200	0	900	$5900
Artix UltraScale+	**AU25P**	23×23	282000	141000	300	0	1200	$7000
Kintex UltraScale+	**KU3P**	23×23	325440	162720	360	48	1368	$22900
Kintex UltraScale+	**KU5P**	23×23	433920	216960	480	64	1824	$31000

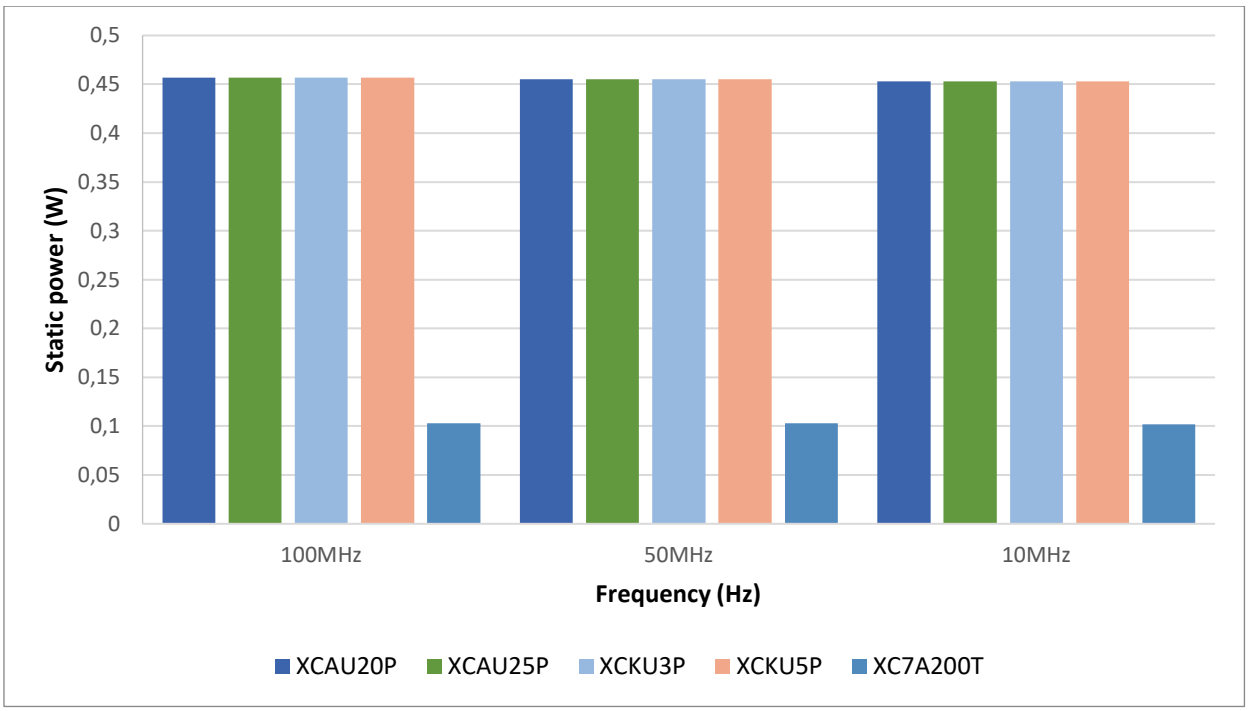

Figure 5. The static power consumptions for the five considered AMD FPGAs.

Like in [10] we targeted 3 frequencies for the clock signals: 10, 50 and 100 MHz. The static, dynamic and total (i.e. static plus dynamic) power consumptions are listed in Figures 5, 6 and 7, respectively. Even though the same tool is used (i.e. AMD Vivado 2024.1) with the

same constraints, design and settings, the much lower static power draw of the older XC7A200T device makes it the most energy-efficient device from the selected ones. This trend remains when estimating the power consumption using the signals toggling rates extracted from simulations.

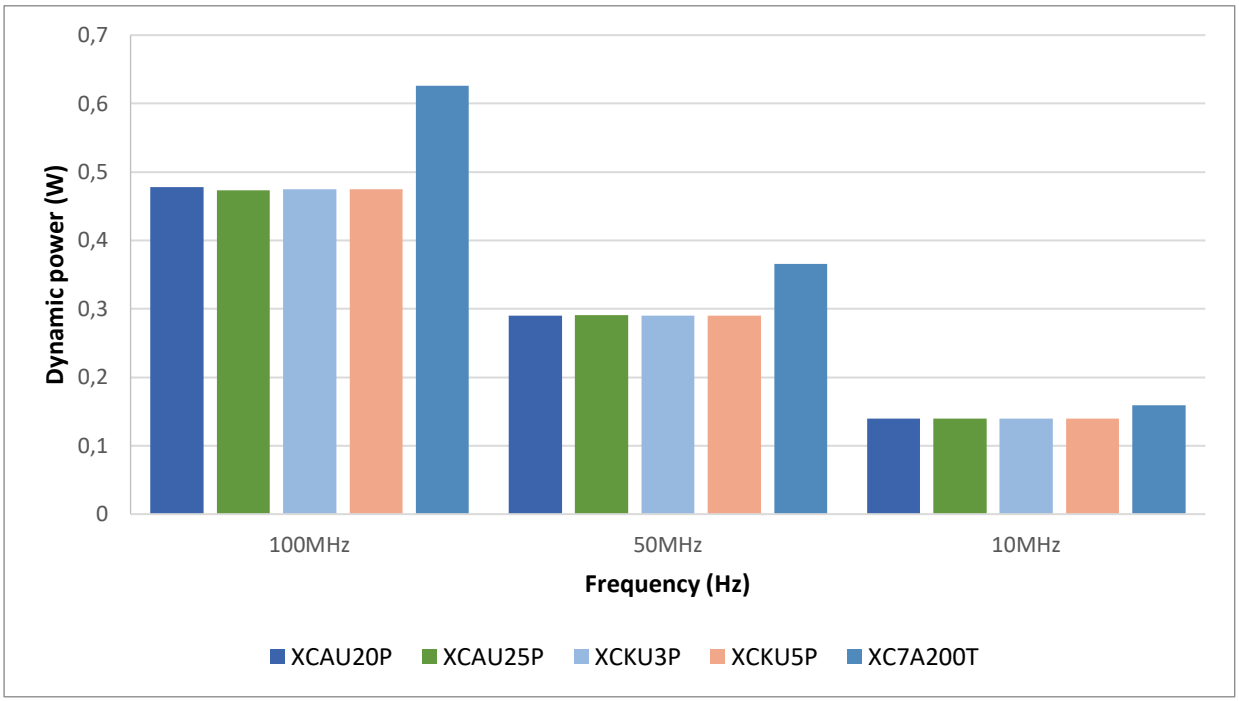

Figure 6. The dynamic power consumptions for the five considered AMD FPGAs.

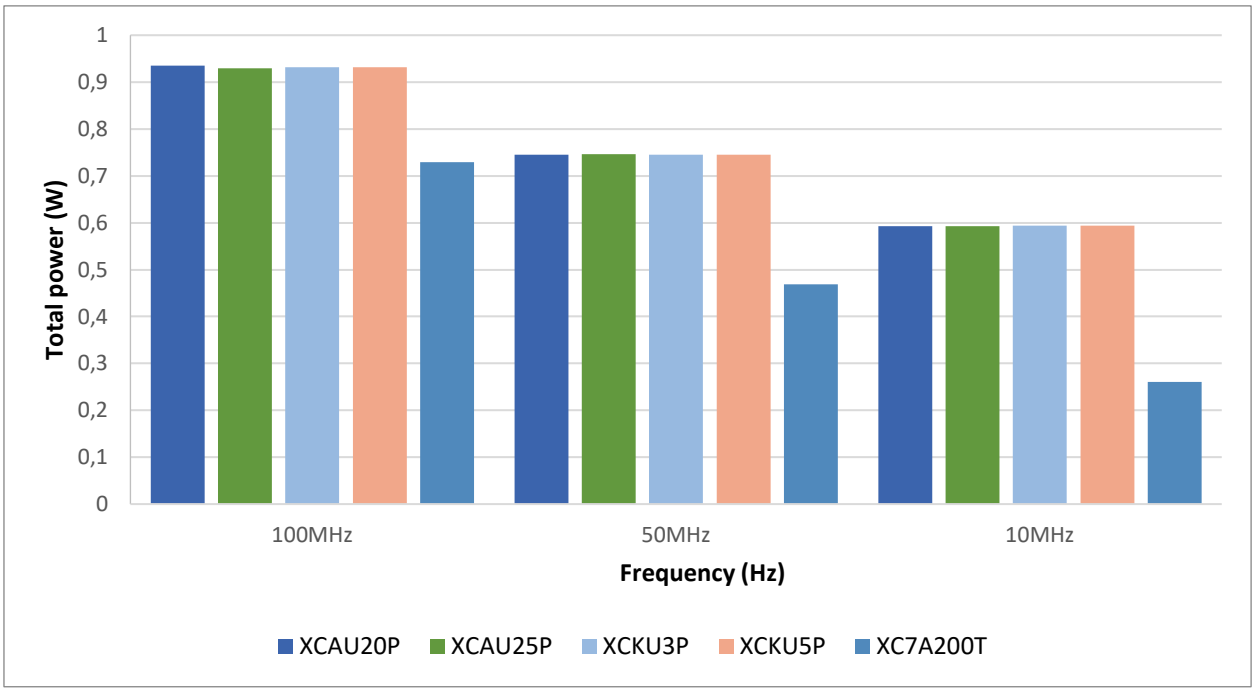

Figure 7. The total power consumptions for the five considered AMD FPGAs.

In this preliminary analysis for choosing the FPGA device we also consider the sensibility of the device to nuclear radiation. In [15] the determined BRAM cross-sections for the Artix-7 and the UltraScale+ FPGA families are 6.32×10^{-15} cm^2/bit and 9.82×10^{-16} cm^2/bit. These amounts are determined from LANSCE (Los Alamos Neutron Science Center) beam

testing. The older XC7A200T device is one order of magniture more susceptiple to nuclear radiation compared to the UltraScale+ devices which is advantageous in our case.

Considering all these characteristics, the AMD Artix-7 XC7A200T FPGA device was selected, which is the most energy efficient among the selected ones, and this trend is maintained when estimating the power consumption using the switching rates of the signals extracted from the simulations with back-to-back scanning (see Figures 5, 6 and 7).

Conclusion

In this paper, a study of the types of cosmic radiation and its effects on electronic circuits has been carried out. Particular attention has been paid to the methods of measuring cosmic radiation in order to design a smart sensor. The architecture of the satellite module with the smart radiation sensor based on an FPGA circuits was proposed, which includes radiation sensing elements, arrays of different types of electronic memories (on semiconductors), both inside and outside the circuit, which wll classify and analyze in real time the fault patterns induced by cosmic radiation and predict the state of the electronic systems embedded in satellites.

In order to exclude the influence of space radiation on the FPGA core it is proposed to realize acquisition, processing and communication procedures using TMR. The FPGA device was selected, which is the most energy efficient from the considered ones energy efficient The FPGA device was selected based on its estimated power draw, avaible resources, total cross section to maximize its susceptibly to radiation and price.

Acknowledgment

This work was funded by the Romanian Ministry of Research, Innovation and Digitalization, project PN-IV-P8-8.3-ROMD-2023-0068 entitled ”Artificial Intelligence-enabled Hardware Cosmic Radiation Sensor for Space Applications (AICoRS)”, contract no. 2ROMD/01.06.2024.

Conflicts of Interest: The author declares no conflict of interest.

Reference

1. Knoll, G.F. *Radiation Detection and Measurement*. John Wiley&Sons, NJ, SUA, 2000, p. 816.
2. Marinella, M. J. Radiation Effects in Advanced and Emerging Nonvolatile Memories. In: *IEEE Transactions on Nuclear Science* 2021, 68(5), pp. 28.
3. Verrelli, E.; Tsoukalas, D. Radiation Hardness of Flash and Nanoparticle Memories. *InTech* 2011, pp. 210-240.
4. Taggart, J.L. Ionizing radiation effects on nonvolatile memory properties of programmable metallization cells. *IEEE Transactions on Nuclear Science* 2014, 61 (6), pp. 2985–2990.
5. Wirthlin, M. High-Reliability FPGA-Based Systems: Space, High-Energy Physics, and Beyond. *Proceedings of the IEEE*, 2015, 103(3), pp. 379–389.
6. Wu, R.X.; Guo, J.; Du, J.; Li, J. Accelerating neural network inference on fpga-based platforms—a survey. *Electronics*, 2021, 10(9), 1025.
7. AMD. XQR Space-Grade Kintex™ UltraScale™ and Space Heritage. 2023, Available online: https://www.xilinx.com/publications/solution-briefs/xilinx-space-solution-brief.pdf (accessed on 06.06.2024).
8. Parkes, S. SpaceWire User’s Guide. Available online: https://www.star-dundee.com/wp-content/star_uploads/general/SpaceWire-Users-Guide.pdf (accessed on 07.06.2024).
9. Popa, S.; Martoiu, S.; Ivanovici, M. Study of the ATLAS new small wheel read-out controller ASIC in a neutron irradiation environment. Journal of Instrumentation 2020, 15(10), P10023.

10. Popa, S.; Kazak, A.; Dinu, A.; Ivanovici, M.; Secrieru, N.; Carbune, V.; Melnic, V. Architecture and Design Choices for an AI-enabled FPGA-based Cosmic Radiation Sensor. In: The paper of the ISTEC-2024 16th International Symposium on Electronics and Telecommunications (ISETC), Timisoara, November 6-7, 2024, p. 4.
11. Gerardin, S.; Paccagnella, A. Present and future non-volatile memories for space. IEEE Trans. Nuclear Science 2010, 57(6), pp. 3016–3039.
12. Varadis. Radfet, radiation detection sensors and dosimetry systems, 2024. Available online: https://www.varadis.com/products/ (accessed on 06.07.2024).
13. Bostan, V.; Bostan, I.; Ilco, V.; Melnic, V.; Martîniuc, A.; Vărzaru, V.; Secrieru, N.; Guţu, M.; Verjbiţki, V.; Magariu, N.; Lupan, O. KiboCUBE Program: the challenges and experience of the Technical University of Moldova on the development of nanosatellites. Bons Offices, Chisinau, RM, 2022, 259 p. ISBN 978-9975-166-65-2.
14. Teviso. Alpha Particle Sensor AL53. 2023. Available online: https://www.teviso.com/file/pdf/al53-data-specification.pdf (accessed on 07.06.2024).
15. AMD. Device Reliability Report. 2024. Available online: https://docs.amd.com/r/en-US/ug116/The-Reliability-Program UG116 (v10.18), (accessed on 07.06.2024).

Citation: Secrieru, N.; Cărbune, V.; Zadorojneac, T.; Melnic, V.; Bertescu A.; Ivanovici, M.; Popa, Ş.; Kazak, A. Architecture of the space radiation sensor satellite module based on artificial intelligence. *Journal of Engineering Science* 2024, XXXI (4), pp. 73-83. https://doi.org/10.52326/jes.utm.2024.31(3).01.

Submission of manuscripts: jes@meridian.utm.md

Journal of Engineering Science *Vol. XXXI, no. 4 (2024), pp. 84 - 94*
Fascicle *Electronics and Computer Science* *ISSN 2587-3474*
Topic *Electronics and Communication* *eISSN 2587-3482*

https://doi.org/10.52326/jes.utm.2024.31(4).06
UDC 004.522:811.135.1:621.865.8

ANALYSIS AND EVALUATION OF ROMANIAN VOICE COMMANDS FOR THE CONTROL OF MECHATRONIC SYSTEMS

Olesea Borozan *, ORCID: 0000-0003-1091-5506

Technical University of Moldova, 168 Ștefan cel Mare Blvd., Chisinau, Republic of Moldova
* Corresponding author: Olesea Borozan, *olesea.borozan@ia.utm.md*

Received: 10. 22. 2024
Accepted: 12. 05. 2024

Abstract. This paper focuses on the analysis and evaluation of voice commands for controlling mechatronic systems in exceptional situations. It highlights the role and benefits of mechatronic devices in modern society, emphasizing their use across various fields, from industrial process automation and infrastructure to consumer electronics and energy. Significant benefits of these devices, such as comfort, efficiency, and technological innovation, are outlined, along with the risks associated with their use, including short circuits and electro-mechanical failures. The research is directed towards integrating voice emotion recognition technologies into the control systems of household appliances to handle exceptional situations. Emotion recognition from speech, based on artificial intelligence and voice signal processing, is described as an interdisciplinary approach that combines audio processing, voice feature extraction, and machine learning. The objectives include developing effective techniques and methods to classify emotions and ensure the safe operation of devices. Research results show the potential of these techniques and technologies to transform interactions with mechatronic systems, offering innovative solutions for enhancing performance and reducing the risks associated with complex activities. The study opens new directions for integrating artificial intelligence into production processes and creating safer, more intuitive working environments.

Keywords: *industrial processes, robotic systems, human-machine interaction, natural language processing, voice recognition, emotional voice control, exceptional situations, neural network, emergency intervention.*

Rezumat. Lucrarea este axată pe analiza și evaluarea comenzilor vocale pentru controlul sistemelor mecatronice în situații excepționale. Sunt subliniate rolul și beneficiile dispozitivelor mecatronice în societatea modernă, subliniind utilizarea acestora în diverse domenii, de la automatizarea proceselor industriale și infrastructură până la electronica de consum și energetică. S-au scos în evidență beneficiile semnificative ale acestor dispozitive, precum confortul, eficiența și inovația tehnologică, dar și riscurile asociate exploatării lor, inclusiv scurtcircuitele și defectele electro-mecanice. Cercetările sunt orientate pe integrarea tehnologiilor de recunoaștere a emoțiilor vocale în sistemele de control ale dispozitivelor electrocasnice pentru a gestiona situațiile excepționale. Recunoașterea emoțiilor din vorbire,

bazată pe inteligență artificială și prelucrarea semnalelor vocale, este descrisă ca o abordare interdisciplinară care combină procesarea audio, extragerea de caracteristici vocale și învățarea automată. Obiectivele includ dezvoltarea unor tehnici și metode eficiente care să clasifice emoțiile și să asigure funcționarea dispozitivelor în regimuri sigure. Rezultatele cercetării arată potențialul acestor tehnici și tehnologii de a transforma interacțiunea cu sistemele mecatronice, oferind soluții inovatoare pentru îmbunătățirea performanței și reducerea riscurilor asociate activităților complexe. Studiul deschide noi direcții pentru integrarea inteligenței artificiale în procesele de producție și pentru crearea unor medii de lucru mai sigure și mai intuitive.

Cuvinte-cheie: *proces industrial, sistem robotic, interacțiune om-mașină, procesarea limbajului natural, recunoașterea vorbirii, control emoțional vocal, situații excepționale, rețea neuronală, intervenții de urgență.*

1. Introduction

Modern society cannot be imagined without the presence of various electro-mechanical devices, which serve to automate different fields of human activities. These devices are found everywhere: in systems for the automation of technological, industrial, and robotic processes [1]; in transportation and infrastructure to ensure the functionality of vehicles and transport systems [2]; in medical equipment to provide precise and efficient diagnosis and treatment [3]; in consumer electronics represented by household appliances [4]; in energy and environmental sectors, where they are used for the production and distribution of energy, as well as in environmental protection equipment [5], and so on.

Household appliances (such as electric and gas stoves, coffee makers, vacuum cleaners, blenders, irons, water heaters, etc.) play a particularly significant role in modern society, as they are omnipresent in their operation and bring a range of benefits and conveniences. These devices use electrical and mechanical technology to perform various household functions, transforming people's lifestyles into one of maximum comfort and efficiency. Some of the most important benefits offered by these appliances include comfort and efficiency, time and energy savings, connectivity and automation, diversity, and innovation. Through continuous innovation and technological development, these devices have secured a dominant place in modern society [6].

Alongside the benefits brought by household appliances, these devices can also pose certain risks to human life and health, such as fires and short circuits, electric shocks, explosions, mechanical failures, etc. All of these risks can be prevented by following proper usage and maintenance guidelines. However, during the operation of household appliances, exceptional situations may arise in which these devices can negatively impact health or present a risk to human life [6, 7]. In such cases, it is essential to have mechanisms in place to intervene in their operation by stopping or switching them to a maximum safety mode.

It is evident that emerging situations trigger an immediate response in the human body through emotions, including vocal emotions, which can be identified and used for emergency interventions in the functionality of household appliances. Emotions play a significant role in the communication process. They influence voice tone, speech rate, intonation, and other aspects of verbal expression. Tone and intonation can convey emotions such as happiness and joy, as well as fear, anxiety, or sadness. Negative emotions can also

impact the rhythm and speed of word pronunciation, making speech unclear or difficult to identify [8].

Speech emotion processing and recognition [9–12] is an interdisciplinary field of research focused on identifying and interpreting the feelings and emotional states expressed in a person's vocal discourse. In the first stage, the vocal signal is processed to eliminate noise and extract relevant features. This process may include signal filtering, sound level normalization, and segmenting the speech into analysis intervals. In the second step, vocal signal features are extracted to capture emotion-related information, including fundamental frequency, intensity, rhythm, pitch, pauses, and other aspects of voice modulation. In the third step, the extracted features are used to build emotion recognition models, which can be based on machine learning techniques such as neural networks, support vector machines, or supervised learning algorithms. These models are trained on a dataset labeled with emotions to learn the characteristic patterns of various emotional states. In the fourth step, the emotion recognition models are evaluated using separate datasets and adjusted according to their performance. This evaluation and adjustment process may involve optimizing model parameters or applying performance enhancement techniques, such as adding supplementary features or using natural language processing techniques [13,14].

Speech emotion processing and recognition is a rapidly evolving field of research that involves a wide range of techniques, technologies, and methods to identify and interpret emotions expressed in human vocal discourse. These technologies have the potential to significantly enhance human-machine interaction and contribute to the development of more responsive and intuitive systems. Speech emotion recognition has a wide array of practical applications in fields such as voice-assisted technology, speech recognition technology, discourse analysis, mental health, and human-machine interaction [15,16].

This paper presents the results of research conducted in the design of control systems for electro-mechanical devices based on vocal emotions in emergency situations. The research objectives are focused on: developing a mechanism for identifying and analyzing vocal emotions that will highlight vocal characteristics according to emotional state in emergency situations; developing a model and algorithm for emotion recognition and classification in emergency contexts, based on vocal signal processing and artificial intelligence; integrating emotions into the control systems of household electro-mechanical devices; selecting and justifying keywords expressed in exceptional situations; and evaluating and validating the results.

2. Statement of the Research Problem

The objectives of the conducted research are aimed at identifying technical and technological solutions that will enable the integration, identification, interpretation, and utilization of vocal emotions in the control process of electro-mechanical devices, particularly household appliances, in exceptional or emergency situations to enhance their effectiveness and safety. By identifying and interpreting emotions expressed in the user's vocal discourse, the devices are programmed to respond appropriately to manage crisis situations or prevent potential risks. Thus, an innovative approach is proposed to improve the performance and safety of electro-mechanical devices, enhancing their functionality and response in emergency situations, critical conditions, or under stress.

In line with the defined objectives, the focus of this work is the development of advanced vocal emotion recognition technology and its integration into the control systems

of electro-mechanical devices, particularly ubiquitous household appliances, with the aim of enabling more intuitive and efficient interactions between the user and the device.

3. Synthesis Functional Diagram of the Control System

The functional diagram for controlling electro-mechanical devices in exceptional situations based on vocal emotions is presented in Figure 1. The functional diagram includes the following components:

User – the person using the electro-mechanical system, who in normal operation can engage in discussions without emotions, but in emergency situations pronounces specific words related to the exceptional situation that will trigger the device to switch to a heightened safety mode. ***MK*** – microphone for perceiving sound waves and converting them into electrical signals. ***AM –*** amplifier of the electrical signals. ***Filter*** – a filter to exclude noise from the electrical signals caused by sounds generated by the user. ***ADC*** – Analog-to-Digital Converter synchronized with the frequency of the sound waves generated by the user. ***ANN*** – Artificial Neural Network adjusted to identify words and vocal emotions, generating control signals for the operational mode of the electro-mechanical device. ***EMD*** – Electro-mechanical device equipped with a safety system based on vocal emotions.

This diagram highlights the integrated flow of components that work together to analyze vocal emotions and adjust the device's operation accordingly to ensure safety in critical situations.

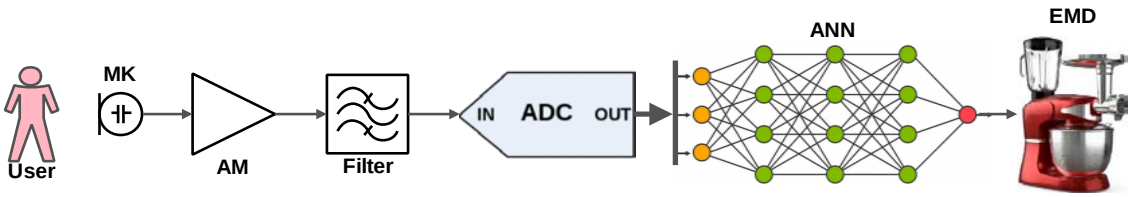

Figure 1. The functional diagram of the emotional voice control system.

4. Analysis and Evaluation of Words Pronounced by Humans in Exceptional Situations

Emotions in speech are pivotal in human communication, significantly shaping how messages are conveyed and understood. They add depth and context to words, influencing their interpretation by the receiver, whether it's another human, a machine, or an AI-powered robot. Emotions enrich spoken language, offering nuanced meanings and facilitating more effective interactions. By studying how emotions are expressed, perceived, and interpreted in speech, several critical scenarios and implications can be identified for enhancing human-to-human and human-machine communication:

The tone of voice can convey a range of emotions, such as joy, anger, fear, or dread, significantly impacting how the message is received. The speaker's emotional state influences the listener's perception and interpretation of the message, adding layers of meaning beyond the words themselves.

A message delivered with enthusiasm, happiness, or joy can elicit a positive response, whereas one expressed with sadness or disappointment is more likely to evoke feelings of compassion and empathy.

A tone that is aggressive or defensive can strain relationships, whereas a supportive tone has the potential to deepen emotional bonds and foster stronger connections.

Speech infused with emotions can be a powerful tool to influence or persuade the recipient's decision-making process.

- In human interactions, emotions conveyed through speech enrich communication by adding depth and nuance, enabling a more precise understanding and interpretation. This dynamic can also extend to interactions between humans and machines, as well as machines and humans.

The studies referenced in sources [17-22] explore the expression of emotional words by humans in exceptional circumstances. These emotions are categorized into various types, including joy, sadness, fear, suffering, panic, anger, frustration, admiration, or astonishment. In scenarios of human-machine communication during exceptional situations, emotional words typically associated with fear, suffering, or panic are especially identifiable.

Assessing emotional words spoken by individuals in exceptional circumstances is a nuanced and subjective endeavor. However, various methods can be employed to better understand and interpret their emotional resonance across different contexts. These methods include [23]: Lexical Analysis, Vocal Tone Analysis, Intuition and Empathy, Context Analysis.

To identify the key words pronounced by humans in various exceptional situations, a survey was conducted with multiple-choice selection, involving a sample of over 150 participants. For evaluation, emotional situations were simulated: "***Spaimă***" (Fear), "***Suferință***" (Suffering), "***Furie***" (Anger), "***Frică***" (Terror), "***Alarmă***" (Alarm) and "***Surpriză"*** (Surprise)**.** Words were proposed for evaluation that had a higher probability of being pronounced in various exceptional situations: "***Start***", "***Stop***", "***Ajutor***", "***A-a-u-u-u***", "***Help***" and "***SOS***". The results of the survey are presented in Table 1.

Table 1

The results of human-pronounced keyword evaluation in exceptional situations

	Start	Stop	Ajutor	A-a-u-u-u	Help	SOS	Total	%, max.*
Spaimă	17	49	48	25	29	20	188	26.06
Suferintă	12	30	30	71	31	9	183	38.80
Furie	20	89	15	17	12	9	162	54.94
Frică	12	33	57	20	35	24	181	31.49
Alarmă	35	52	23	11	22	38	181	28.73
Surpriză	84	15	9	42	4	7	161	52.17
Total	180	268	182	186	133	107		
%, max.*	46.67	33.21	31.32	38.17	26.32	35.51		

Note: % max. - maximum value obtained as a result of the survey.

Thus, based on the analysis of the survey results, we can conclude that:

- The word "***Start***" it is pronounced 84 times in emotional situations of "***Surpriză***", which constitutes 46.67%.
- The word "***Stop***" it is pronounced 89 times in emotional situations of "***Furie***", which accounts for 33.21%, and 52 times in emotional situations of "***Alarmă***", which accounts for 19.40%, and 49 times in emotional situations of "***Spaimă***", which accounts for 18.28%.
- The word "***Ajutor***" is pronounced 57 times in emotional situations of "***Frică***", which constitutes 31.32%, and 48 times in emotional situations of "***Spaimă***", which constitutes 26.37%.
- The word "***A-a-u-u-u***" is pronounced 71 times in emotional situations of "***Suferință***", which constitutes 38.17%, and 42 times in emotional situations of "***Surpriza***", which constitutes 22.58%.

- The word "***Help"*** is pronounced 35 times in emotional situations of "***Frică***", which constitutes 26.32%, and 31 times in emotional situations of "***Suferință***", which constitutes 23.30%.
- The word ***"SOS***" is pronounced 38 times in emotional situations of "***Alarmă",*** which constitutes 35.51%, and 24 times in emotional situations of "***Frică***", which constitutes 22.43%.
- In an emotional state of "***Spaimă***", the word ***"Stop"*** is pronounced 49 times, which constitutes 26.06%.
- In an emotional state of "***Suferință***", the word "***A-a-u-u-u"*** is pronounced 71 times, which constitutes 38.80%.
- In an emotional state of "***Furie***", the word "***Stop"*** is pronounced 89 times, which constitutes 54.94%.
- In an emotional state of ***"Frică***", the word "***Ajutor"*** is pronounced 57 times, which constitutes 31.49%.
- In an emotional state of ***"Alarmă",*** the word ***"Stop"*** is pronounced 52 times, which constitutes 28.73%.
- In an emotional state of ***"Surpriză***", the word ***"Start"*** is pronounced 84 times, which constitutes 52.17%.

As a result of the survey analysis, it can be concluded that to intervene in exceptional situations during the operation of an electro-mechanical system, the key words ***„Stop"*** and ***„Ajutor"*** specific to the Romanian language can be used.

5. Spectral Analysis of Waveform (Sound) of the Selected Keywords

For the spectral analysis of the selected key words for commands with mechatronic systems in exceptional situations, a software product was developed in Python using the TensorFlow and Keras libraries.

Spectral analysis of sound is the process of decomposing the sound signal, generated by a human, into its frequency components. It is performed to visualize and analyze the frequency and intensity spectrum of the signal. This analysis allows distinguishing between sounds generated by the human in normal and emotional states, thereby enabling the identification of the operator's emotional state.

The spectral analysis algorithm involves the following steps:

Capturing the sound signal, which involves acquiring the sound using a microphone (see Figure 1).

The transformation of the signal into the frequency domain. The sound signal is passed through a transformation algorithm, such as the Fourier Transform, which decomposes it into sinusoidal components at different frequencies.

Visualization of the spectrum. The frequency and intensity spectrum is visualized in the form of a spectrogram. This is a graph that shows the intensity of the signal as a function of frequency and time.

Spectrum analysis. The spectrum is analyzed to identify the signal's characteristics, such as the fundamental frequency (pitch), harmonics, and vocal formants.

Interpretation of the results. The results of the spectral analysis are interpreted to gain a deeper understanding of the signal and its acoustic characteristics. This may involve identifying patterns or anomalies in the spectrum and evaluating their impact on the signal, ultimately identifying the emotional state of the individual.

Therefore, spectral analysis of sound allows for the understanding of the characteristics of the audio signal and the evaluation of its impact in various contexts, providing an effective way to investigate and interpret the information present in sound signals.

In Figure 2, the results of processing and analyzing the sound generated for the word ***"Ajutor"*** in a neutral (non-emotional) state are presented: a) Waveform of the original Sound; b) Waveform after processing with Librosa library from Python; c) spectrogram Frequency-Amplitude; d) Log-Mel Spectrogram Time-Power-Frequency.

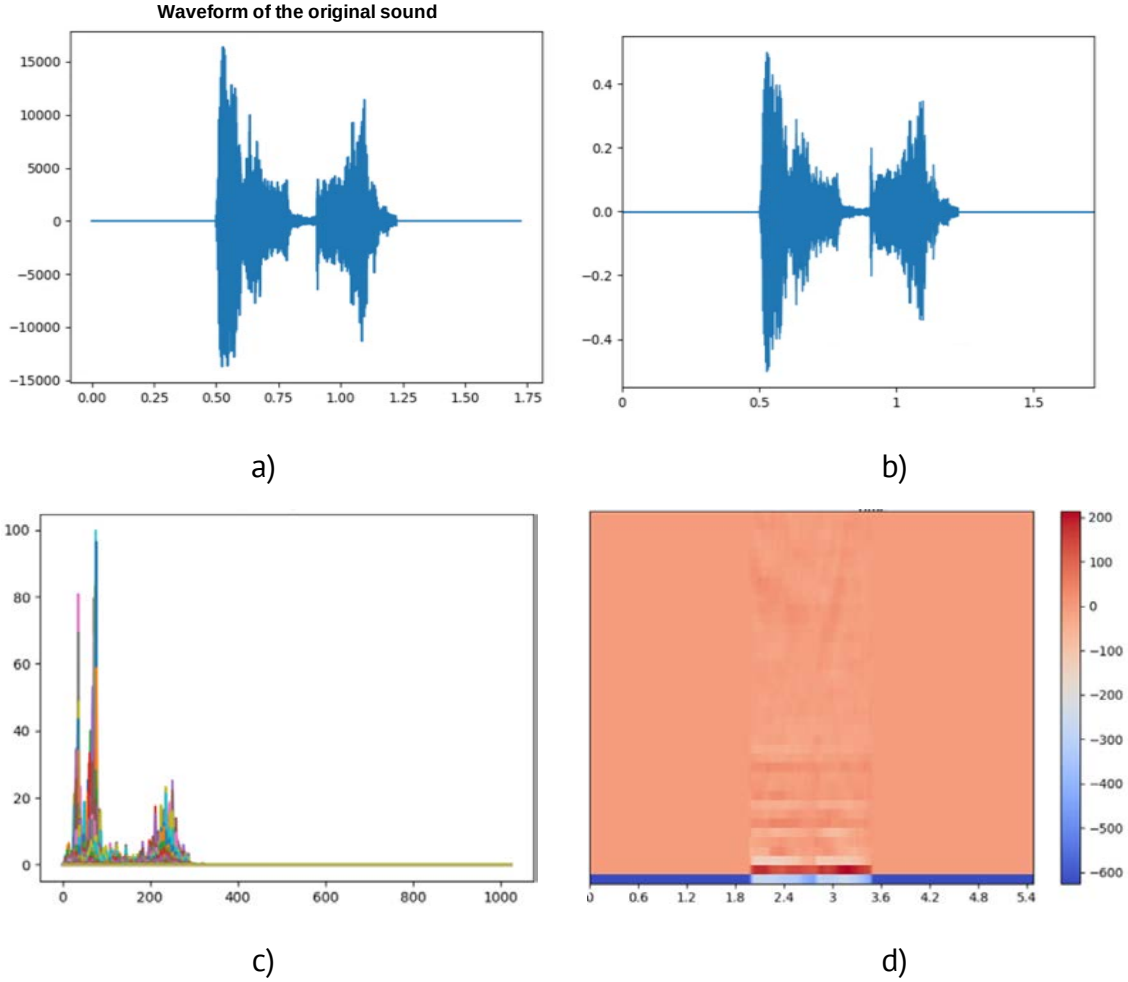

Figure 2. The results of processing and analyzing the sound generated for the word *"Ajutor"*: a) Waveform of the original Sound; b) Waveform after processing with Librosa library from Python; c) spectrogram Frequency-Amplitude; d) Log-Mel Spectrogram Time-Power-Frequency.

In Figure 3, the results of processing and analyzing the sound generated for the word ***"Ajutor"*** in an emotional state of fear are presented: a) Waveform of the original Sound; b) Waveform after processing with Librosa library from Python; c) spectrogram Frequency-Amplitude; d) Log-Mel Spectrogram Time-Power-Frequency.

The comparative analysis of the diagrams shows a significant difference between the normal and emotional states of the human when pronouncing the word ***"Ajutor",*** thus allowing the identification of the emotional state, which will lead to initiating the procedure for switching the mechatronic system to a maximum safety mode.

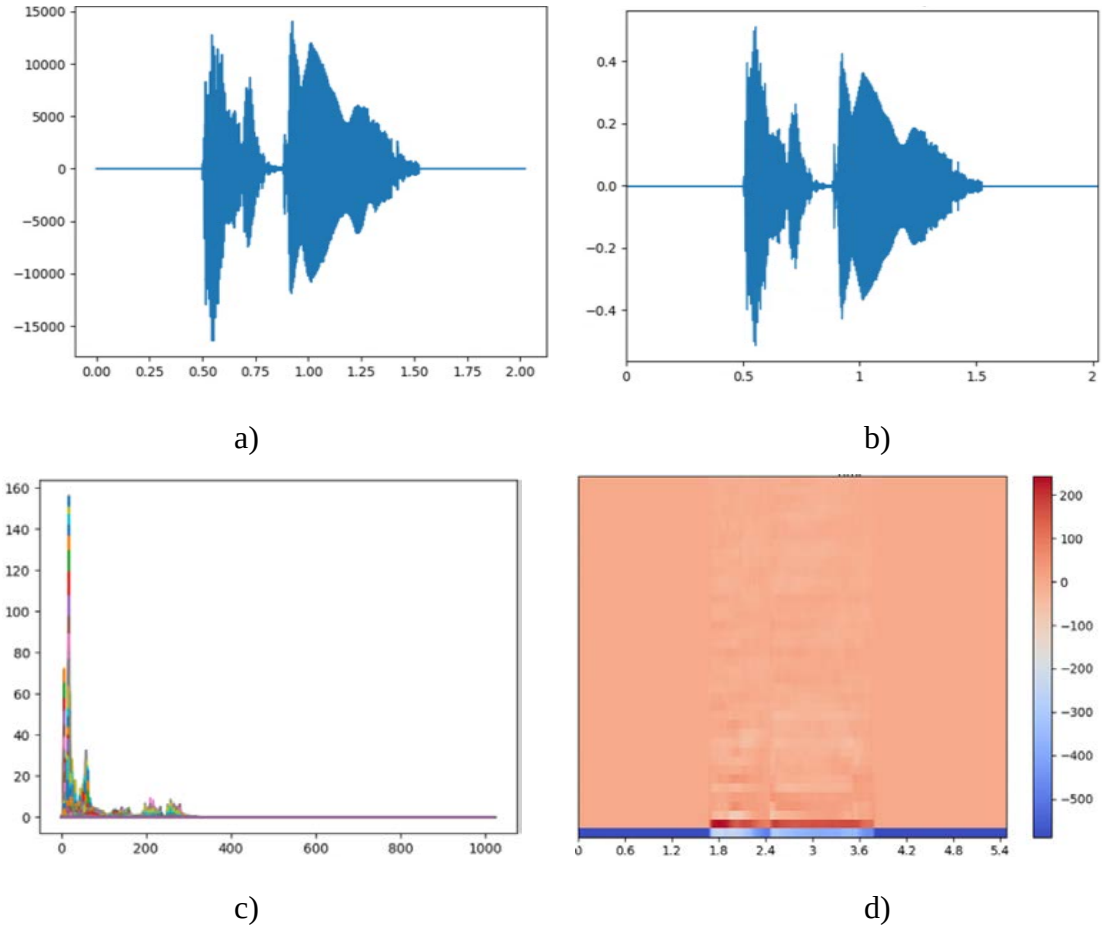

Figure 3. The results of processing and analyzing the sound generated for the word "*Ajutor*" in an emotional state of fear: a) Waveform of the original Sound; b) Waveform after processing with Librosa library from Python; c) spectrogram Frequency-Amplitude; d) Log-Mel Spectrogram Time-Power-Frequency.

In Figure 4, the results of processing and analyzing the sound generated for the word "***Stop***" in a neutral (non-emotional) state are presented): a) Waveform of the original Sound; b) Waveform after processing with Librosa library from Python; c) spectrogram Frequency-Amplitude; d) Log-Mel Spectrogram Time-Power-Frequency.

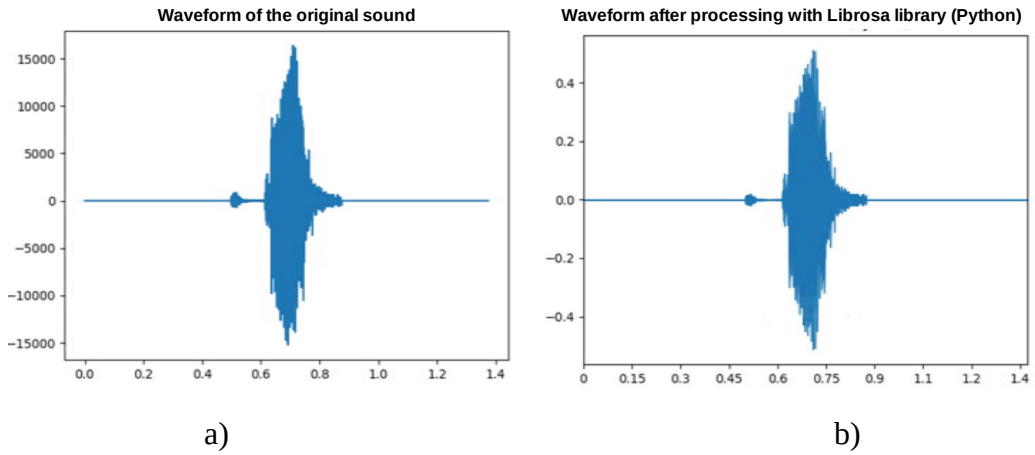

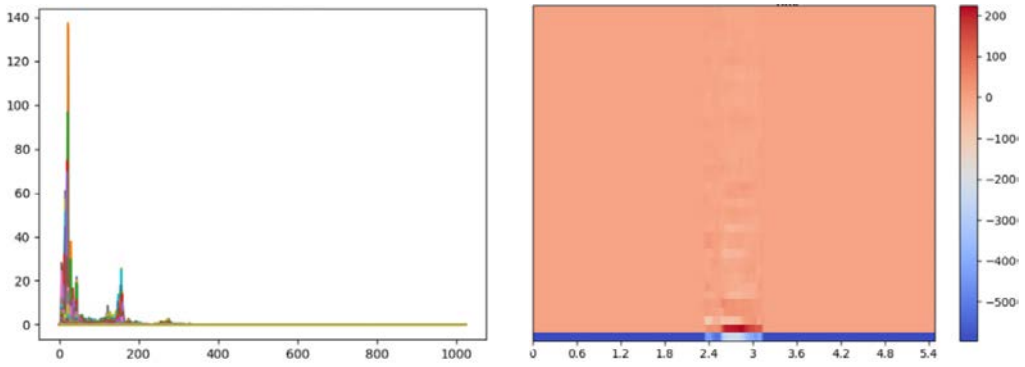

c) d)

Figure 4. The results of processing and analyzing the sound generated for the word *"Stop"*:): a) Waveform of the original Sound; b) Waveform after processing with Librosa library from Python; c) spectrogram Frequency-Amplitude; d) Log-Mel Spectrogram Time-Power-Frequency.

In Figure 5, the results of processing and analyzing the sound generated for the word ***"Stop"*** in an emotional state of fear are presented: a) Waveform of the original Sound; b) Waveform after processing with Librosa library from Python; c) spectrogram Frequency-Amplitude; d) Log-Mel Spectrogram Time-Power-Frequency.

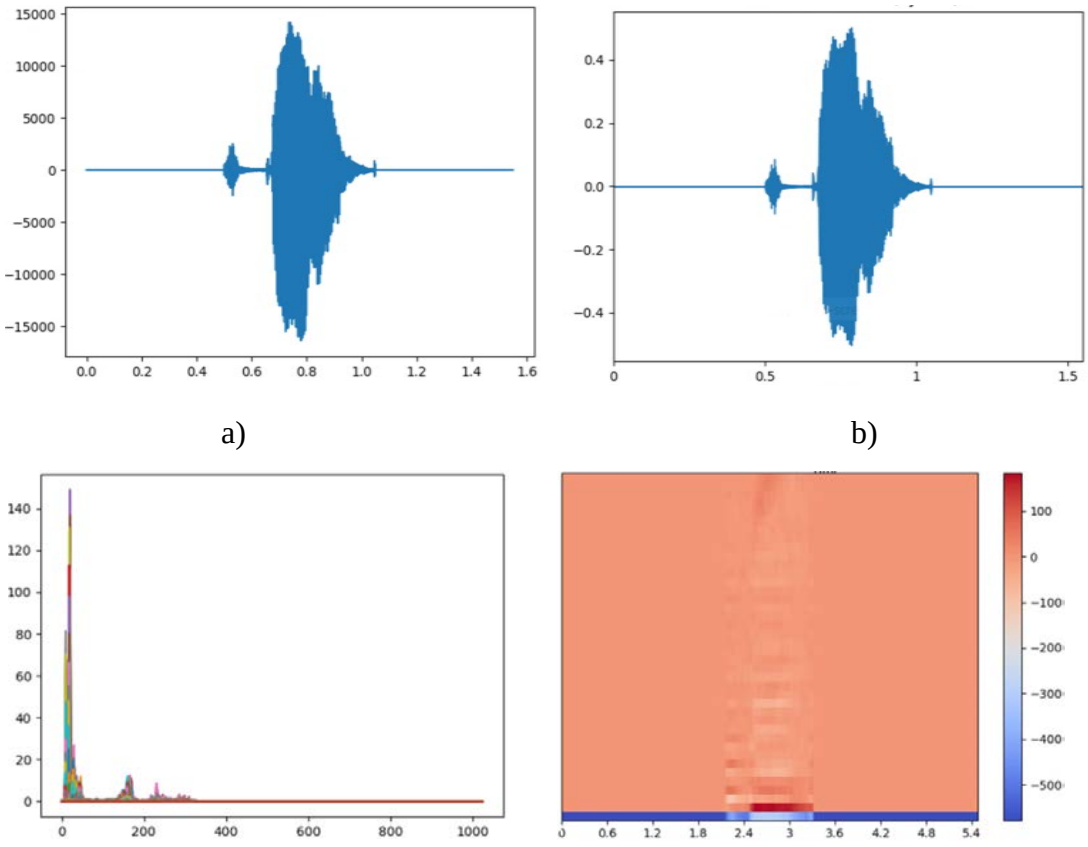

a) b)

c) d)

Figure 5. The results of processing and analyzing the sound generated for the word *"Stop"* in an emotional state of fear: a) Waveform of the original Sound; b) Waveform after processing with Librosa library from Python; c) spectrogram Frequency-Amplitude; d) Log-Mel Spectrogram Time-Power-Frequency.

The comparative analysis of the diagrams in Figure 4 and Figure 5 shows a significant difference between the normal state and the emotional state of the human when pronouncing the word "***Stop***", thus offering the possibility to identify the emotional state that will trigger the procedure to transition the mechatronic system into a maximum safety mode or stop its operation.

6. Conclusions

This paper addresses a current interdisciplinary topic focused on the integration of voice emotion recognition technologies into the control systems of mechatronic devices, particularly household appliances. In the context of a society increasingly dependent on technology, the proposed approach aims to enhance safety, efficiency, and human-machine interaction by using emotions as a significant input in exceptional situations.

The defined objectives of the research highlight the relevance and potential of implementing these techniques and technologies across various fields, from household mechatronic systems to more complex industrial robotic systems. The identification and use of vocal emotions in device control meet the emerging needs for safety and personalization in the use of household appliances. The importance of advanced artificial intelligence algorithms and neural networks for emotion recognition, optimizing human-device interaction, and reducing risks in critical situations is emphasized.

Integrating voice emotion recognition techniques and technologies into mechatronic devices can redefine safety and comfort standards, with significant implications for their design and use in the near future. The study thus contributes to technological progress and the development of innovative solutions, tailored to a constantly evolving modern society.

For the future, research is planned for the design and implementation of speech emotion processing and identification models using reconfigurable Field-Programmable Gate Array (FPGA) devices, which will significantly reduce costs and system complexity, facilitating widespread adoption.

Acknowledgments: The research conducted in this paper is part of the doctoral thesis topic. The analysis and evaluation of the key words selected for the study were carried out with the technical and technological support provided by the Department of Computer Science and Systems Engineering, Technical University of Moldova.

Conflicts of Interest: The author declares no conflict of interest.

References

1. Aswani, T.B.; Kewalramani, K.; Malekar, N. Industrial Robotics. *International Research Journal of Engineering and Technology* 2020, 7(8), pp. 2329-2332. ISSN: 2395-0056.
2. Rizzoni, G.; Kearns, J. *Principles and Applications of Electrical Engineering*. McGraw-Hill, NY, SUA, 2022, 992 p. ISBN: 978-126-025-804-2.
3. Chapman, S.J. *Electric Machinery Fundamentals*, McGraw-Hill, 5th Edition, New York, NY., USA, 2012, 680 p. ISBN: 978-0-07-352954-7.
4. Dagostino, F.; Wujek, J. *Mecanical and Electrical Systems in Architecture, Engineering and Construction*, Pearson, 5th Edition, Upper Saddle River, New Jersey, USA, 2009, 960 p. ISBN: 978-013-500-004-5.
5. Melkebeek, J.A. *Electrical Machines and Drives*. *Fundamentals and Advanced Modelling*. Springer, Cham, Switzerland, 2018, 733 p. ISSN: 1860-4676, DOI: 10.1007/978-3-319-72730-1.
6. Wilson, C.; Hargreaves, T.; Hauxwell-Baldwin, R. Benefits and Risks of Smart Home Technologies. *Energy Policy* 2017, 103, pp. 72-83. DOI: 10.1016/j.enpol.2016.12.047.

7. Saleheen, R. U.; Farhan, A.; Ramesha, N. Z.; Tasnim, R.; Erin, M. T. U. R.; Shahria, S. Emerging Applications of Mechatronics. In: *Mechatronics: Fundamentals and Applications*, Springer Nature Singapore, Singapore, 2024, pp. 143-160. DOI: 10.1007/978-981-97-7117-2_7.
8. Monisha, S.T.A.; Sultana, S.; A Review of the Advancement in Speech Emotion Recognition for Indo-Aryan and Dravidian Languages. *Advances in Human-Computer Interaction* 2022, 9602429. DOI: 10.1155/2022/9602429.
9. Lopes, N.; Perkusich, M.; Lima, C. A Review of Emotion Recognition in Speech. *Journal of Information and Data Management* 2019, 10(4), pp. 222-234.
10. Zhang, Z.; Zhao, Y.; Liu, Z. A survey on deep learning for speech emotion recognition. *ACM Computing Surveys* (*CSUR*) 2019, 52(3), pp. 1-33.
11. Ververidis, D.; Kotropoulos, C. Emotional speech recognition: resources, features, and methods. *Speech Communication* 2006; 48(9), pp. 1162-1181.
12. Cowie, R.; Douglas-Cowie, E.; Tsapatsoulis, N.; Votsis, G.; Kollias, S.; Fellenz, W.; Taylor, J. G. Emotion recognition in human-computer interaction. *IEEE signal processing magazine* 2001, 18(1), pp. 32-80.
13. Borozan, O.; Ababii, C.; Roșca, N.; Lungu. I. The Use of Emotions in Speech to Control Exceptional Situation in Robotic Systems. In: *Proceedings of the XVI International Scientific and Practical Conference „Information Technologies and Automation-2023"*, Odessa, Ukraine, October 19-20, 2023, pp. 313-315.
14. Borozan, O. Safety System for Robotic Processes Based on Voice Emotion Recognition. In: *Proceedings of the Workshop on Intelligent Information Systems, WIIS-2023*, Chisinau, Republic of Moldova, October 19-21, 2023, pp. 55-61.
15. Borozan, O.; Turcan, A.; Ababii, C.; Lasco, V.; Struna, V. Speech Processing System for Emergency Management, In: *Proceedings of the International Scientific Conference on Mathematics & IT: Research and Education, MITRE-2023*, Chisinau, Republic of Moldova, 26-29 June, 2023, pp. 75.
16. Ababii, V.; Sudacevschi, V.; Borozan, O.; Fratavchan, V. Decision making system based on voice-emotional commands, In: *Proceedings of the International Scientific and Practical Internet Conference on "Informatics and Computer Technics Problems", PICT-2022*, 10-13 November, 2022, pp. 69-74.
17. Kuhn, L.K., Emotion recognition in human face and voice. PhD thesis, London, 2014; p. 261.
18. Ozseven, T. A novel feature selection method for speech emotion recognition. *Applied Acoustics* 2019, 146, pp. 320-326.
19. Bhardwaj, P.; Debbarma, S. A Study of Methods Involved in Voice Emotion. *International Journal of Advanced Research in Computer and Communication Engineering* 2014, 3(2), pp. 5517-5521.
20. Byun, S.W.; Lee, S.P. A Study on a Speech Emotion Recognition System with Effective Acoustic Features Using Deep Learning Algorithms. *Applied Sciences* 2021, 11(4), 1890.
21. Joshi, A.; Kaur, R. A Study of Speech Emotion Recognition Methods. *IJCSMC* 2013, 2(4), pp. 28 – 31.
22. Kerkeni, L.; Serrestou, Y.; Mbarki, M.; Raoof K.; Mahjoub, M. Speech Emotion Recognition: Methods and Cases Study. In: *Proceedings of the 10th International Conference on Agents and Artificial Intelligence, ICAART 2018,* Funchal, Madeira, Portugal, 24-26 January, 2018, 2, pp. 175-182.
23. Borozan, O. Emotional words uttered in exceptional circumstances, State, achievements and prospects of information systems and technologies. In: *Proceedings of the XXIV All-Ukrainian Scientific and Technical Conference of Young Scientists, Postgraduate Students, and Students* Odessa, Ukraine, April 18-19, 2024; pp. 328-329.

Citation: Borozan, O. Analysis and evaluation of Romanian voice commands for the control of mechatronic systems. *Journal of Engineering Science* 2024, XXXI (4), pp. 84-94. https://doi.org/10.52326/jes.utm.2024.31(3).01.

Submission of manuscripts: jes@meridian.utm.md

Journal of Engineering Science *Vol. XXXI, no. 3 (2024), pp. 95 - 104*
Fascicle *Electronics and Computer Science* *ISSN 2587-3474*
Topic *Biomedical Engineering* *eISSN 2587-3482*

https://doi.org/10.52326/jes.utm.2024.31(4).07
UDC 616.127-005.8:004.94

EXPLORING THE HUMAN CIRCULATORY SYSTEM THROUGH SYSTEM DYNAMICS: A MODEL-BASED APPROACH

Victor Iapăscurtă[1,2], ORCID: 0000-0002-4540-7045

[1] *Technical University of Moldova, 168 Stefan cel Mare Blvd., Chisinau, Republic of Moldova*
[2] *N. Testemitanu University of Medicine and Pharmacy, 165 Stefan cel Mare Blvd., Chisinau, Republic of Moldova*
*Corresponding author: Victor Iapăscurtă, *victor.iapascurta@doctorat.utm.md*

Received: 11. 20. 2024
Accepted: 12. 18. 2024

Abstract. System dynamics is a robust methodology for understanding the behavior of complex systems over time. By employing feedback loops, stocks, flows, and time delays, this approach provides a comprehensive framework for simulating and analyzing dynamic systems. The application of system dynamics to the human circulatory system presents numerous possibilities, benefits, and practical applications that can significantly enhance our understanding and management of cardiovascular health. This article details experimental results from modeling myocardial infarction conditions using a six-compartment model developed in the NetLogo integrated development environment, incorporating BehaviorSpace for extensive simulations. For result analysis, specialized packages in R, Python, and Wolfram Mathematica were utilized to ensure rigorous data interpretation. The results demonstrate promising fidelity when compared to existing literature and real-time patient data, indicating the model's potential for clinical applications. By illustrating the interactions within the circulatory system, this research not only contributes to theoretical knowledge but also offers practical insights into disease management and intervention strategies, paving the way for improved cardiovascular health outcomes.

Keywords: *system dynamics modeling; circulatory system; myocardial infarction; integrated development environment.*

Rezumat: Dinamica sistemului este o metodologie robustă pentru înțelegerea comportamentului sistemelor complexe în timp. Utilizând bucle de feedback, stocuri, fluxuri și întârzieri, această abordare oferă un cadru cuprinzător pentru simularea și analiza sistemelor dinamice. Aplicarea dinamicii sistemului la sistemul circulator uman prezintă numeroase posibilități, beneficii și aplicații practice care ne pot îmbunătăți în mod semnificativ înțelegerea și gestionarea sănătății cardiovasculare. Acest articol detaliază rezultatele experimentale din modelarea condițiilor de infarct miocardic folosind un model cu șase compartimente dezvoltat în mediul de dezvoltare integrat NetLogo, încorporând BehaviorSpace pentru simulări extinse. Pentru analiza rezultatelor, au fost utilizate pachete specializate în R, Python și Wolfram Mathematica pentru a asigura o interpretare riguroasă a datelor. Rezultatele demonstrează o fidelitate promițătoare în comparație cu literatura

existentă și cu datele în timp real ale pacientului, indicând potențialul modelului pentru aplicații clinice. Prin ilustrarea interacțiunilor din cadrul sistemului circulator, această cercetare nu numai că contribuie la cunoștințe teoretice, ci oferă și perspective practice asupra managementului bolii și strategiilor de intervenție, deschizând calea pentru îmbunătățirea rezultatelor sănătății cardiovasculare.

Cuvinte cheie: *modelarea dinamicii sistemului; sistemul circulator; infarct miocardic; mediu de dezvoltare integrat.*

1. Introduction

The human circulatory system is a complex network of interacting components, including the heart, blood vessels, and blood, responsible for maintaining physiological homeostasis [1]. Understanding its dynamics is crucial for diagnosing and treating cardiovascular diseases, which remain the leading causes of morbidity and mortality worldwide [2]. Traditional approaches to studying the circulatory system often rely on static models that fail to capture the intricate feedback loops and time-dependent interactions inherent in human physiology. In response to these limitations, researchers have increasingly turned to system dynamics modeling (SDM), a powerful method for simulating complex systems over time [3,4].

System dynamics offers a comprehensive framework for analyzing the circulatory system by utilizing stocks, flows, and feedback loops to represent physiological processes. This approach allows for exploring various scenarios, such as the impact of lifestyle changes, medication, or surgical interventions on cardiovascular health. Recent advances in computing power and data acquisition technologies, such as wearable devices and high-resolution imaging, have further enhanced the potential of system dynamics models. These innovations enable real-time data integration, allowing for continuous validation and refinement of models, thereby improving their accuracy and practical applicability.

A particularly promising development in this field is the emergence of personalized models [5]. By incorporating patient-specific data, these models account for individual variability in anatomy, physiology, and risk factors, offering tailored insights into disease progression and treatment outcomes. For instance, patient-specific hemodynamic models can simulate blood flow dynamics using patient data, providing valuable information for surgical planning and risk assessment. Similarly, personalized models of cardiac function can predict responses to therapies, aiding in managing conditions such as heart failure and hypertension.

Moreover, integrating machine learning techniques with system dynamics modeling has opened new avenues for enhancing predictive capabilities. By learning from vast datasets, these hybrid models can identify patterns and refine simulations, leading to more precise predictions of cardiovascular events. This synergy between system dynamics and machine learning represents a significant leap toward the realization of personalized medicine in cardiovascular care.

In this article, we explore the current status and recent advances in system dynamics modeling of the circulatory system, focusing on personalized approaches. The paper discusses the methodologies employed, the challenges encountered, and the transformative potential these models hold for improving patient outcomes and advancing cardiovascular research.

2. Materials and Methods

The NetLogo integrated development environment (IDE) [6] is used for system dynamics modeling. Data analysis is performed using specialized packages [7-10] in R programming language [11], Python [12], and, to a lesser extent, Wolfram Mathematica [13].

3. Aspects Important for System Dynamics Modeling of the Circulatory System

3.1. Basic components and mathematical aspects behind SDM

A. *Basic Components*

1. Stocks and Flows

- Stocks represent accumulations (e.g., blood volume).
- Flows are rates of change affecting stocks (e.g., blood flow rate).

2. Feedback Loops

- Positive Feedback: Enhances changes (e.g., increased heart rate).
- Negative Feedback: Stabilizes the system (e.g., blood pressure regulation).

B. Main Mathematical Equations

a. Stock and Flow Equations

- Change in Blood Volume (*V*)

$$\frac{dV}{dt} = Q_{in} - Q_{out}, \tag{1}$$

where Q_{in} is the rate of blood entering the system and Q_{out} is the rate of blood leaving the system.

- Cardiac Output (*CO*)

$$CO = HR \times SV, \tag{2}$$

where HR is the heart rate (beats/minute), and SV is the stroke volume (mL).

b. Feedback Loop Equations

- Blood Pressure (BP) Regulation

$$BP = TPR \times CO, \tag{3}$$

where TPR denotes total peripheral vascular resistance (mmHg·s/mL), and CO is cardiac output (L/min).

- Baroreceptor Reflex: Adjusts heart rate and vessel diameter in response to changes in blood pressure, modeled by:

$$HR = f(BP_{setpoint} - BP), \tag{4}$$

where HR denotes heart rate, BP - blood pressure (mmHg), and f represents the response function of the baroreceptor.

C. Simulation and Analysis

- Differential Equations: Used to simulate changes over time.
- Numerical Methods: Employed to solve these equations and analyze system behavior.

By formulating these equations, system dynamics models capture the interplay between different physiological components, allowing for the simulation and analysis of the circulatory system's behavior under various conditions.

3.2. Possibilities, Benefits, and Potential Practical Applications of the SDM Approach

A. Possibilities

The human circulatory system is a complex network that involves the heart, blood vessels, and blood. It is characterized by numerous interactions and feedback loops, making it an ideal candidate for system dynamics modeling. Researchers can simulate various physiological and pathological conditions, such as hypertension, heart failure, and atherosclerosis, by creating a system dynamics model of the circulatory system.

This approach allows for exploring how different variables interact over time, such as blood pressure, heart rate, and blood volume. It enables testing hypotheses regarding the impact of lifestyle changes, medications, or surgical interventions on cardiovascular health. Moreover, such models can be adapted to simulate individual patient scenarios, offering personalized insights into disease progression and treatment outcomes.

B. Benefits

One of the primary benefits of using system dynamics for modeling the circulatory system is the ability to visualize and understand complex interactions that are not immediately apparent. This holistic approach facilitates the identification of key leverage points where interventions can be most effective.

Additionally, system dynamics models can serve as valuable educational tools. Medical students and healthcare professionals can better understand cardiovascular physiology and pathology by simulating different scenarios. These models can also be used to communicate complex concepts to patients, improving their understanding and engagement in their care.

System dynamics models can also predict interventions' long-term outcomes, aiding healthcare providers' decision-making processes. Clinicians can optimize therapeutic strategies and improve patient outcomes by simulating patient responses to different treatments.

C. Practical Applications

In practice, system dynamics models of the circulatory system can be used to inform public health strategies. For instance, by modeling the population-level impacts of lifestyle changes or public health interventions, policymakers can make informed decisions about resource allocation and health promotion initiatives.

In clinical settings, these models can support the development of decision-support systems that assist clinicians in diagnosing and managing cardiovascular diseases. Such models can provide dynamic risk assessments and personalized treatment recommendations by integrating real-time patient data.

Furthermore, pharmaceutical companies can use system dynamics models to simulate the effects of new drugs on the circulatory system, thereby streamlining the drug development process and reducing costs associated with clinical trials.

3.3. Integrating SDM of the Circulatory System with Real-Time Data

Integrating system dynamics models of the circulatory system with real-time patient data can enhance their accuracy and applicability. The following presents vital components for doing this.

A. Data integration techniques

1. Data Acquisition: Using wearable devices and sensors to continuously monitor patient metrics such as heart rate, blood pressure, and oxygen levels. These devices can transmit data wirelessly to a centralized system.
2. Data Processing: Implementing algorithms to clean and preprocess the incoming data, ensuring accuracy and consistency. This step is crucial for real-time analysis.
3. Model Adaptation: Using real-time data to update the model parameters dynamically. Machine learning techniques can adjust model variables based on the latest data, ensuring the model remains relevant to the patient's condition.

B. Technical Infrastructure

1. Cloud Computing: Utilizing cloud platforms for data storage and processing can provide the computational power to handle large volumes of real-time data and complex simulations.
2. Application programming interfaces (APIs) and Interoperability: Developing APIs to facilitate seamless data exchange between monitoring devices, electronic health records (EHRs), and the system dynamics model. Ensuring interoperability among different systems is critical.

C. Real-Time Feedback and Decision Support

1. Dashboard Visualization: Creating intuitive dashboards that display real-time model outputs and patient data, allowing healthcare providers to monitor patient status effectively.
2. Alerts and Notifications: Setting up automated alerts for healthcare providers if the model predicts potential adverse events or deviations from expected health patterns.
3. Personalized Treatment Adjustments: Using the insights gained from the model to tailor treatment plans on the fly, optimizing medication dosages or recommending lifestyle changes based on current data.

D. Challenges and Considerations

1. Data Privacy and Security: Ensuring compliance with regulations like HIPAA [14] by implementing robust encryption and access controls to protect patient data.
2. Model Validation: Continuously validating and refining models with new data to maintain accuracy and reliability.
3. User Training: Providing training for healthcare providers to interpret model outputs and integrate them into clinical decision-making effectively.

By effectively integrating real-time patient data, system dynamics models of the circulatory system can become powerful tools for personalized healthcare, improving patient outcomes and optimizing treatment strategies.

4. Experimental Results

The research the current paper is based on is at its preclinical stage. Thus, although it is taking care of the aspects to be considered at more advanced stages (e.g., integration with real-time patient data), it focuses primarily on essential modeling aspects at the current stage. Figure 1 presents the system dynamic scheme (NetLogo SDM). The squares represent the model's six compartments (i.e., stocks), including the heart chambers and arterial and venous segments of the circulatory system. The diamond structures denote various parameters of the model (over 30 in number), and thin arrows indicate influences or interactions. The thick arrows illustrate the flows. Behind each influence/interaction are mathematical equations, some of which have been described in previous sections.

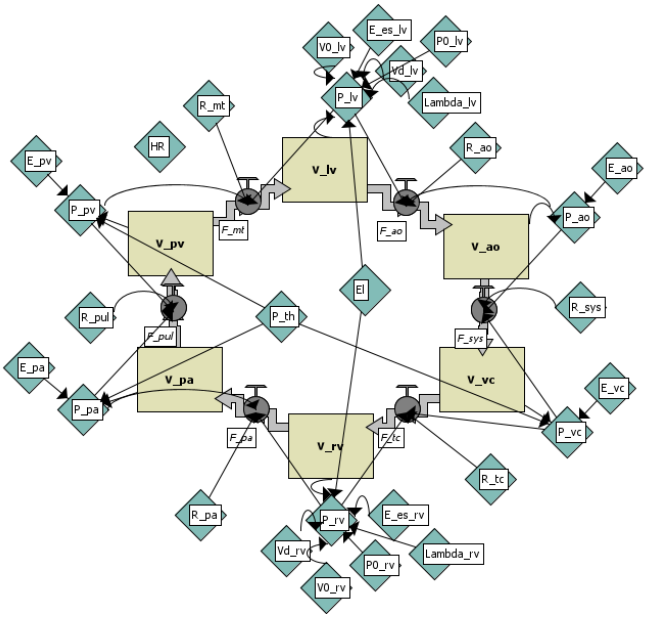

Figure 1. The system dynamic scheme for the created model. Squares represent stocks and diamonds denote other parameters. Capital letters point to a certain parameter: V – volume, E– elastance of different compartments of the system (for ventricles – end systolic elastance), Lambda - the curvature of end-diastolic pressure-volume relationship function, V0 – zero-pressure volume and P0 – zero-volume pressure, P – pressure, F – flow, R – resistance, El – time-varying elastance, HR – heart rate. Subscripts denote specific compartments of the circulatory system: ao – aorta, vc – vena cava, sys – systemic circulation, tc – tricuspid valve, rv – right ventricle, pa – pulmonary artery, pv – pulmonary veins, th – intrathoracic, mt – mitral valve.

Figure 2 illustrates the model's user interface. The sliders on the bottom are used to adjust model parameters.

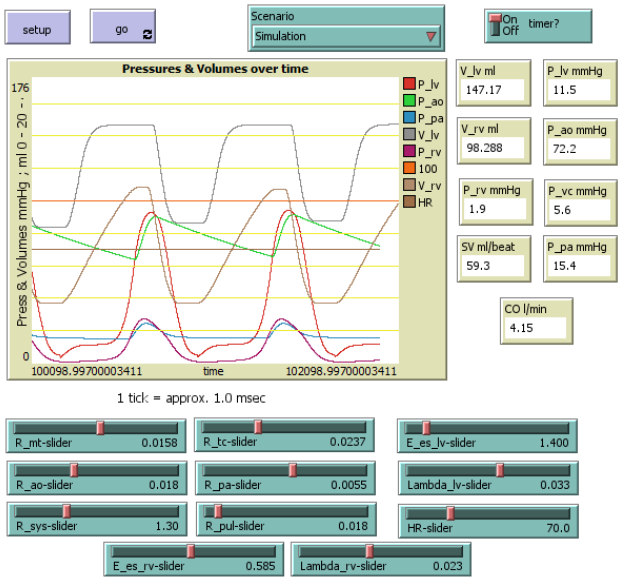

Figure 2. The appearance of the model's user interface. Capital letters denote different physiological parameters: V – volume, P – pressure, SV - stroke volume, CO – cardiac output, R – resistance, E– elastance, Lambda – a function influencing myocardial contractility, HR – heart rate. Subscripts denote specific compartments of the circulatory system (e.g., ao – aorta, lv – left ventricle, etc., as in Figure 1).

The monitors on the right continuously communicate the numerical values of particular model outputs (e.g., volumes in different compartments of the system as well as pressures: left and right ventricles, aorta, and pulmonary artery) along with the stroke volumes and cardiac output of both parts of the heart. The plotting area on the left shows the dynamics in time for the mentioned physiological parameters.

Figure 3 shows the pressure-volume loop of a patient with a simulated myocardial infarction (green color for the left ventricle and yellow for the right ventricle). It can be noticed that they shrink with the institution of the infarction.

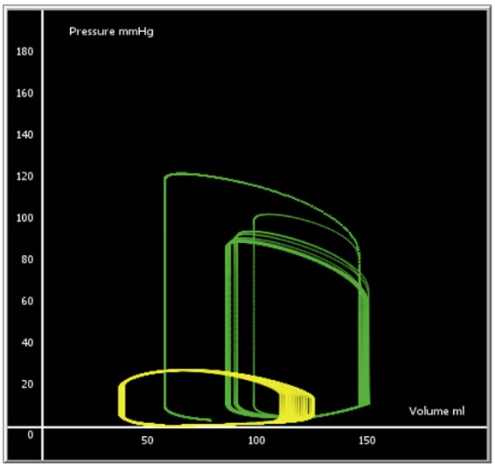

Figure 3. The pressure-volume loop in a patient with a simulated myocardial infarction. Green color denotes left ventricle and yellow color – right ventricle.

Table 1 denotes the time-varying values of six physiological parameters during the simulation.

Table 1

A small portion of the simulation results

Left ventricle pressure (mm Hg)	Left ventricle output (L/min)	Right ventricle output (L/min)	Right ventricle volume (mL)	Aortic pressure (mm Hg)	Vena Cava pressure (mm Hg)
69.24	4.14	4.14	96.68	91.25	4.81
70.32	4.14	4.14	96.54	91.20	4.81
71.42	4.14	4.14	96.36	91.16	4.81
72.52	4.14	4.14	96.13	91.11	4.81
73.65	4.14	4.14	95.87	91.07	4.81
74.78	4.14	4.14	95.58	91.02	4.81
75.93	4.14	4.14	95.26	90.97	4.81
77.09	4.14	4.14	94.92	90.93	4.81
78.26	4.14	4.14	94.54	90.88	4.82
79.45	4.14	4.14	94.15	90.84	4.82

Most of the physiological parameters shown in Table 1 have a clinical equivalent, which may be of importance when integrating the model in a clinical setting.

Numerical data generated by simulations can be analyzed from different perspectives using methods of various degrees of sophistication appropriate for multimodal/multivariate time series. Figure 4 illustrates the perspective based on Kolmogorov-Chaitin (KC) complexity [15-17] estimated in a case of simulated myocardial infarction (MI).

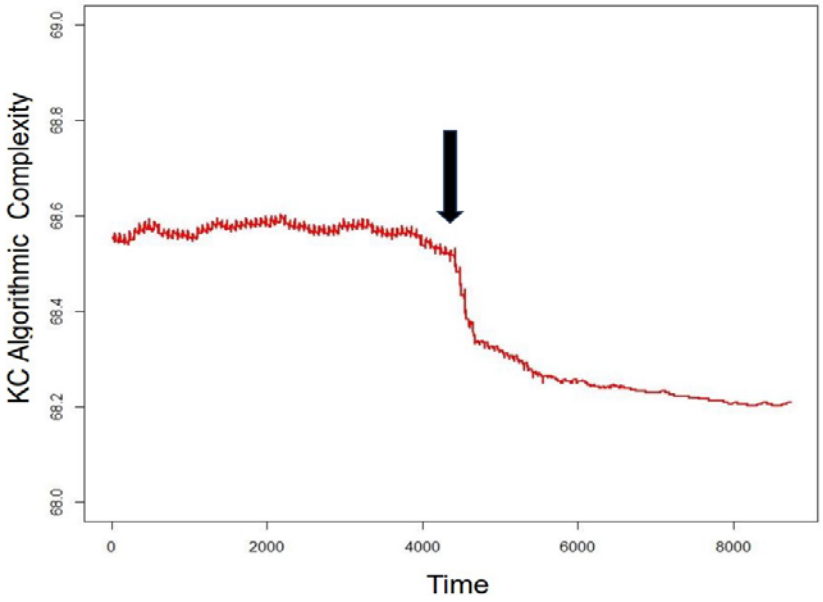

Figure 4. Kolmogorov-Chaitin complexity over time for a simulated case of myocardial infarction. The black arrow denotes the occurrence of myocardial infarction.

For estimation, values of twelve model parameters over time were used. The black arrow denotes the time moment when MI occurred. An evident drop in the KC complexity can be noticed with the institution of MI. This is just an example of a less traditional metric for tracking the overall dynamics of a system (e.g., the circulatory system), but the researcher evidently can use metrics and analysis methods that suit his research goals the best.

5. Discussion

This research builds on an earlier work [18,19] focused on a simpler (i.e., three compartments) similar model. While the previous model let the researcher control 4 model parameters (i.e., volume status, arterial vascular resistance, myocardial contractility, and vascular elastance), the current model has an extended set of controllable parameters, denoted by the sliders in Figure 2 (e.g., concerning all four heart chambers, valves, systemic and pulmonary circulations). This is expected to provide more detailed simulations.

Experiments were performed in NetLogo IDE BehaviorSpace, a software tool integrated with NetLogo that allows researchers to conduct experiments with models providing numerical data to be analyzed. Table 1 in the previous section presents a small portion of such data. The volume of the data can be much larger depending on the experiment duration and the number of parameters set to be monitored. Selecting parameters equivalent to those in a clinical setting can leverage the integration of SDM with real-time patient data.

Concerning a potential future integration of SDM with real-time patient data, there are several aspects to be considered and, when necessary, solved:

Real-Time Data Acquisition

Wearable Devices: Utilizing devices to continuously monitor heart rate, blood pressure, and ECG data.

Data Connectivity: Ensuring seamless data flow from devices to the model for real-time updates.

Data Processing and Management

Data Cleaning: Implementing algorithms to filter and preprocess incoming data for accuracy.

Dynamic Model Updating: Using real-time data to adjust model parameters dynamically, improving precision.

Clinical Decision Support

Risk Assessment: Developing tools to assess patient risk in real-time, providing alerts for potential complications.

Personalized Intervention: Tailoring treatment recommendations based on individual patient data and model predictions.

Privacy and Security

Data Protection: Ensuring compliance with data privacy regulations by implementing robust encryption and security measures.

The SDM, including myocardial infarction, can become a valuable tool for understanding disease dynamics and supporting personalized patient care by focusing on these aspects.

6. Conclusions

Applying system dynamics to the human circulatory system presents a promising approach for advancing cardiovascular research and healthcare. These models offer significant insights into disease mechanisms, treatment effects, and public health strategies by capturing the complexity of physiological interactions. As technology advances and more data becomes available, the potential for system dynamics modeling in cardiovascular health will continue to grow, ultimately contributing to improved patient outcomes and more efficient healthcare systems.

Conflicts of Interest: The author declares no conflict of interest.

References

1. Hall, J.; Hall, M. Guyton and Hall Textbook of Medical Physiology. Elsevier, Philadelphia, SUA, 2021, 1152 p.
2. World Health Organization/Cardiovascular diseases. Available online: https://www.who.int/health-topics/cardiovascular-diseases#tab=tab_1 (accessed on 18.11.2024).
3. Frolov, S.V.; Sindeev, S.V.; Lischouk, V.A.; Gazizova, D.Sh.; Liepsch, D.; Balasso, A. A lumped parameter model of cardiovascular system with pulsating heart for diagnostic studies. J. Mech. Med. Biol. 2017, 17(5),1750056.
4. Ježeka, F.; Kulhánekb, T.; Kaleckýa, K.; Kofránek, J. Lumped models of the cardiovascular system of various complexity. J. Appl. Biomed. 2017, 37, pp. 666-678.
5. Garber, L.; Khodaei, S.; Keshavarz-Motamed, Z. The critical role of lumped parameter models in patient-specific cardiovascular simulations. *Arch. Computat. Methods Eng.* 2022, 29, pp. 2977–3000.
6. Wilensky, U. NetLogo. Center for Connected Learning and Computer-Based Modeling, Northwestern University, Evanston, IL. Dec 12, 2018. Available online: ccl.northwestern.edu/netlogo/index.shtml (accessed on 15.11.2024).
7. Zeileis, A.; Grothendieck, G. Zoo:S3Infrastructure for regular and irregular time series. J. Stat. Softw. 2005, 14(6), pp.1-27. https://doi.org/10.18637/jss.v014.i06.
8. Wickham, H.; François, R.; Henry, L.; Müller, K.; Vaughan, D. dplyr: A Grammar of Data Manipulation. R package version 1.1.4. Available online: https://github.com/tidyverse/dplyr, https://dplyr.tidyverse.org (accessed on 18.11.2024).

9. Web Application Framework for R — shiny-package. Available online: https://shiny.posit.co/r/reference/shiny/1.4.0/shiny-package.html (accessed on 18.11.2024).
10. Gauvrit, N.; Singmann, H.; Soler-Toscano, F.; Zenil, H. Algorithmic complexity for psychology: A user-friendly implementation of the coding theorem method. Behav. Res. Methods 2015, 48, pp. 1–16.
11. R Core Team. R: A language and environment for statistical computing. R Foundation for Statistical Computing, Vienna, Austria, 2021. Available online: https://www.R-project.org/(accessed on 18.11.2024).
12. Van Rossum, G.; Drake, F.L. Python 3 Reference Manual. CreateSpace, Scotts Valley, CA, 2009, 242 p.
13. ISBN:978-1-4414-1269-0.
14. Wolfram Research, Inc., Mathematica, Version 14.1, Champaign, IL, 2024. Available online: https://support.wolfram.com/41360 (accessed on 20.11.2024).
15. Health Insurance Portability and Accountability Act. Available online: https://www.hhs.gov/hipaa/index.html, (accessed on 18.11.2024).
16. Kolmogorov, A.N. Three approaches to the quantitative definition of information. Probl. Inf. Transm. 1965, 1, pp. 1–7.
17. Iapascurta, V. Estimation of Kolmogorov-Chaitin Complexity on Continuous Biomedical Data for Machine Learning Purposes. In: Intelligent and Fuzzy Systems INFUS 2024. Lecture Notes in Networks and Systems, Springer, Cham., 2024, 1090, pp 60–67.
18. Zenil, H. A review of methods for estimating algorithmic complexity: options, challenges, and new directions. Entropy 2020, 22(6), 612.
19. Iapascurta, V. Cardiac_output-Simple_Model_01_01, NetLogo Modeling Commons. Available online: www.modelingcommons.org/browse/one_model/5361 (accessed on 18.11.2024).
20. Iapăscurtă, V. Netlogo integrated development environment for modeling physiological processes. In: The Technical Scientific Conference of Undergraduate, Master, PhD students, Technical University of Moldova, Chișinău, Moldova, March 27-29, 2024, 2, pp. 992-995.

Citation: Iapăscurtă, V. Exploring the human circulatory system through system dynamics: a model-based approach. *Journal of Engineering Science* 2024, XXXI (4), pp. 95-104. https://doi.org/10.52326/jes.utm.2024.31(3).01.

Submission of manuscripts: jes@meridian.utm.md

Journal of Engineering Science *Vol. XXXI, no. 4 (2024), pp. 105 - 123*
Fascicle *Electronics and Computer Science* *ISSN 2587-3474*
Topic *Computers and Information Technology* *eISSN 2587-3482*

https://doi.org/10.52326/jes.utm.2024.31(4).08
UDC 004.4:519.8:657.4

MEASURING THE IMPACT OF MOBILE APPLICATIONS

Vasile Nastas [1], ORCID: 0000-0003-2374-4611,
Ion Bolun [2*], ORCID ID: 0000-0003-1961-7310

[1] *Code Parts SRL, 5 Ion Neculce Str., Chisinau, Republic of Moldova*
[2] *Technical University of Moldova, 168 Stefan cel Mare Blvd., Chisinau, Republic of Moldova*
*Corresponding author: Ion Bolun, *ion.bolun@isa.utm.md*

Received: 10. 15. 2024
Accepted: 11. 24. 2024

Abstract. Although mobile devices have widespread popularity, allowing, for example, companies to innovate, streamline operations, and maintain a competitive advantage in a rapidly evolving market, the economic impact of using mobile applications (apps) is less researched. In an attempt to improve the state of affairs in the field, this paper provides a classification (based on business domains) and defines models for calculating the costs of developing and using mobile apps in various situations. To evaluate the economic impact of mobile apps, the opportunity of use is argued and the mathematical expressions for calculating the quantitative indices, Net Present Value, Profitability and Internal Rate of Return, eventually in conjunction with the Equivalent Annual Value method, are determined for 12 specific cases of development and use of mobile apps. Also, multiple qualitative indices for measuring the impact of mobile apps are succinctly characterized and systematized. In confirmation of the significant economic and social impact of mobile apps, three implementations of them in various fields are described.

Keywords: *classification, mobile application costs, mobile application system, qualitative indices, quantitative indices, use cases.*

Rezumat. Deși dispozitivele mobile se bucură de o largă popularitate, permițând, de exemplu, companiilor să inoveze, să eficientizeze operațiunile și să mențină un avantaj competitiv pe o piață în evoluție rapidă, impactul economic al utilizării aplicațiilor mobile este mai puțin cercetat. În încercarea de a îmbunătăți starea de lucruri în domeniu, această lucrare oferă o clasificare (pe baza domeniilor de afaceri) și definește modele de calculare a costurilor de dezvoltare și utilizare a aplicațiilor mobile în diferite situații. Pentru evaluarea impactului economic al aplicațiilor mobile, se argumentează oportunitatea utilizării și se determină expresiile matematice pentru calcularea indicilor cantitativi, Valoarea Actuală Netă, Profitabilitatea și Rata Internă de Rentabilitate, eventual împreună cu metoda Valorii Anuale Echivalente, pentru 12 cazuri specifice de dezvoltare și utilizare a aplicațiilor mobile. De asemenea, mai mulți indici calitativi pentru măsurarea impactului aplicațiilor mobile sunt succint caracterizați și sistematizați. Pentru a confirma impactul economic și social semnificativ al aplicațiilor mobile, sunt descrise trei implementări ale acestora în diverse domenii.

Cuvinte cheie: *clasificare, costuri cu aplicațiile mobile, sistem de aplicații mobile, indici calitativi, indici cantitativi, cazuri de utilizare.*

1. Introduction

Today's business environment is complex and competitive. Organizations, day by day, are increasingly forced to adjust their affairs and be more agile. To compete with the market, each company does research, development and improvement over their business model on a regular basis. This represents a lot of data to be collected and processed; therefore, they strongly rely on Information and Communication Technologies (ICT) support. Nowadays, there are over 5.44 billion ICT users out of 8.17 billion global population [1]. Combining business and technology, companies grow faster and plan more effective business strategies. Among these strategies and opportunities an important role belongs to mobile applications (apps), the use of which grows in a fast linear progression [2]. These apps enable businesses to innovate, streamline operations, and maintain a competitive edge in a rapidly evolving market.

One of the most tangible values of mobile apps is their ability to enhance customer engagement. According to eMarketer [3], "in 2023, the average U.S. adult spent over four hours per day on mobile devices, with nearly 90% of that time spent on apps". An Adobe survey [4] revealed that "companies utilizing mobile apps for internal operations reported a 44% increase in employees' productivity". According to IBM [5], "90% of the world's data has been created in the last two years alone, with much of it generated by mobile devices".

Statistics predicts [6] that the number of smartphone users worldwide is expected to reach 7.33 billion by 2025, providing businesses with unprecedented access to global consumers. Oberlo reported [7] that "mobile commerce is projected to account for 63% of all e-commerce sales by 2028". A study by Business Insider [8] "found that 78% of mobile searches for local business information result in a purchase". According to Statista Market Insights, mobile POS payments apps have revolutionized the financial services industry; such payments projected to surpass US$12.5 trillion globally in 2025 [9].

However, the development of mobile apps involves expenses, often significant. Since financial resources, and not only, are limited, it is important to make such expenses more efficient. But for this, it is required to estimate the impact of mobile apps on various activities, which in turn involves rigorous measurements of some respective indices. Despite their significance, measuring the impact of mobile applications present a unique set of challenges, unlike traditional ICT projects where outcomes can be directly observed or quantified, the benefits of mobile apps often manifest in intangible ways. At the same time, there are still no well-defined rigorous methods for this purpose.

Considering the importance and widespread use of mobile apps, the main objective of this paper is to explore reasonable methodologies for measuring the impact of mobile apps. The focus will be on identifying key metrics, selecting appropriate approaches, and addressing common challenges associated with impact measurement.

2. Materials, methodology and methods

2.1. Methodologies used to evaluate the mobile applications impact

The subject regarding the impact of mobile apps was explored and researched by P. Karami [10], I.M. Tactuk, N. Munaiah, and A. Meneely [11], A. Holden [12], H. Heflin, J. Shewmaker, and J. Nguyen [13], K. Hahn [14], A.R. Altaleb [15], etc. Most researchers address qualitative impact and conduct analyses through survey method [13], interview method [14,15] or scoring method [16].

At the same time, mostly all mentioned authors and others touch the topic of mobile apps by solving a specific problem. They took a targeted use case related to a mobile app and how it can solve a business issue. But there is no in-depth study described on the impact of mobile apps themselves. Parts of research, such as measurable quantitative impact that could help businesses improve their activities usually are missing. They do not generalize a global formulation of the problem and propose generic solutions for measuring the impact. Here comes the biggest challenge, most organizations want to enter this environment and achieve new results, but there is poor research and it is not clearly understood what impact mobile applications specifically will bring to businesses.

Measuring the impact of a mobile app can be complex and multi-dimensional, due to the intangible nature of many benefits that it brings, such as enhanced customer experience or improved decision-making capabilities. The specific criteria or indices used depend on the context and goals of what is being measured. These are needed for every business to understand the value of their investment and present informative reports to investors or stakeholders. To determine what indices to choose for evaluating the impact of mobile application on a specific business affair, it is needed to determine, first of all, what type of impact is expected to achieve.

2.2. Mobile applications classification based on business domains

The most popular mobile stores worldwide are Google Play Store and Apple App Store. It can be observed that there are a lot of mobile app categories on each store, namely:

1. Google Play Store has 3805891 applications available for download [17], where:
   a. 96.98% applications are for free (3686297 apps).
   b. 3.02% applications are paid (114929 apps).
2. Apple App Store has 1807268 applications available for download [18], where:
   a. 87.89% applications are for free (1588326 apps).
   b. 12.11% applications are paid (218942 apps).

The number of available mobile apps on each store depends on many factors as: selected countries, selected category, review process that approves or rejects depending on compliance, and other local or store restrictions. The mobile stores specify a lot of categories in order to define what type of application is more appropriate to one of their categories, what policies and regulations (depending on the countries selected for distribution) they should apply and to let the auditory or users that download the app to understand what type of application they are downloading. On both, Google Play Store and Apple App Store, there are a lot of categories and classifications. Putting aside the mobile store app categories and business domains classifications, the mobile applications under different business activities groups could be classified into the following categories:

1. E-commerce and Retail Applications.
2. Banking and Finance Applications.
3. Healthcare and Fitness Applications.
4. Entertainment and Media Applications.
5. Educational and Learning Applications.
6. Productivity and Business Management Applications.
7. Travel and Hospitality Applications.
8. Social Networking and Communication Applications.
9. Real Estate and Property Management Applications.

10. Food Delivery and Restaurant Applications.
11. Utilities and others.

The main idea is not to target the mobile application type itself, but to go over the main purpose and scope of the application for the end users.

2.3. General indices for measuring the impact

When companies analyze what criteria to consider regarding the impact of mobile applications over their activity, in most of the cases they look over quantitative indices. But sometimes qualitative indices also play an important role.

Quantitative indices

Mobile apps are IT applications. A decision of investment in an IT project (i-project) is usually made based on efficiency criteria/indices. For the assessment of economic efficiency of investment projects, in various sources is recommended to use such quantitative indices as: profit, profit rate [19], payback period (PP), net present value (NPV) [20], profitability index (PI) [19], internal rate of return (IRR) [19,20], return on investment (ROI) [19,21], adjusted expenditure [21], total costs of ownership [22] and so on.

The known theoretical results do not give an unambiguous answer on preferences of using, in concrete situations, the indices for the estimation of efficiency of investment in i-projects.

The most synthetic index of the efficiency of economic activity of an economic agent as a whole is considered the profit rate [19]. In methodological recommendations [20], the basic indices for estimating the economic efficiency of investment projects are: net value, NPV, IRR, ROI, PP and indices that characterize the financial state of the enterprise participating in the project. The World Bank's financial criteria for choosing an investment project are: PP, NPV, discount rate, IRR, and PI [23].

The comparative analysis carried out in [24,25] of the 16 indices for i-projects, the income from the implementation of which can be estimated with reasonable efforts, led to the reduction of the number of core indices from 16 to 3, namely: NPV, IRR and PI, eventually in conjunction with the equivalent annual value (EAV) method. It is proved that for such i-projects the solution, obtained by using any of the other 13 indices, coincides with the solution, obtained by using one or more of the three indices mentioned above. At the same time the NPV, IRR and PI indices form a Pareto set. Thus, not taking any of them into account can lead to unsuccessful decisions.

A key role in calculating the **Net Present Value** is played by the choice of the discount rate d, which must consider the significance of risks and the decrease in the value of money in the future. Let I_{it} are investments and CF_{it} are cash flows in year t related to the mobile application i. Then NPV index for the mobile app i, i.e. NPV_i, is determined as [21]:

$$NPV_i = \sum_{t=1}^{L_i} \frac{CF_{it}}{(1+d)^t} = \sum_{t=1}^{L_i} \frac{P_{it} + AA_{it} - I_{it}}{(1+d)^t}, i = \overline{1,n}, \quad (1)$$

where: n is the total number of considered mobile apps, I_i – total investment with the project, L_i – the duration of the project, P_{it} – the profit and AA_{it} – the amortization in year t with refer to mobile app i. For the NPV calculation, the rate d usually used is equal to the WACC (weighted average cost of capital) value [26] or the historical average returns of a similar project.

Usually, contributions from a product appear only after all the investments in it have been appropriated. If the investment takes more than one year, then the expression (1) can be presented in the form

$$\mathrm{NPV}_i = -\sum_{t=1}^{\tau_i} \frac{I_{it}}{(1+d)^t} + \sum_{t=\tau_i+1}^{L_i} \frac{P_{it} + \mathrm{AA}_{it}}{(1+d)^t} = \sum_{t=\tau_i+1}^{L_i} \frac{\mathrm{CF}_{it}}{(1+d)^t} - I_i\,, i = \overline{1,n}, \tag{2}$$

where: $L_i = \tau_i + D_i$, τ_i is the duration of the acquisition of investments (own development) and D_i is the duration of the use of mobile application *i*.

The **Internal Rate of Return** [21] of a project shows the rate at which investments in the project pay off, i.e. the present value of investments is zero. So, taking into account (2), the IRR for mobile application *i*, i.e. IRR_i, is determined by solving the equation [21]:

$$-\sum_{t=1}^{\tau_i} \frac{I_{it}}{(1+\mathrm{IRR})^t} + \sum_{t=\tau_i+1}^{L_i} \frac{P_{it} + \mathrm{AA}_{it}}{(1+\mathrm{IRR})^t} = \sum_{t=\tau_i+1}^{L_i} \frac{\mathrm{CF}_{it}}{(1+\mathrm{IRR})^t} - I_i = 0, i = \overline{1,n}. \tag{3}$$

The **Profitability Index** for the mobile application *i*, i.e. PI_i, is calculated by dividing the present value of future cash flows generated by the mobile application by the initial investment required [24]:

$$\mathrm{PI}_i = 1 + \frac{\mathrm{NPV}_i}{I_i}, i = \overline{1,n}. \tag{4}$$

The **Equivalent Annual Value method** is used for the appropriate comparison of projects with different lifetimes [27]. It puts in an adequate correspondence to the updated summary value over a period of time of an index of a value over a shorter period, e.g. one year, thus allowing comparative analysis of projects with different lifetimes of their products. For the index XX, which characterizes a certain absolute value for the entire period *D*, the equivalent annual value will be noted EAXX and is determined as

$$\mathrm{EAXX} = \mathrm{CRF} \times \mathrm{XX}, \tag{5}$$

where:

$$\mathrm{CRF} = \left[\sum_{t=1}^{D} \frac{1}{(1+d)^t}\right]^{-1} = \frac{d(1+d)^D}{(1+d)^D - 1}. \tag{6}$$

So, one has:

$$\mathrm{EANPV} = \mathrm{CRF} \times \mathrm{NPV}; \tag{7}$$

$$\mathrm{EAPI} = \mathrm{CRF} \times \mathrm{PI}. \tag{8}$$

Qualitative indices [28]

Qualitative indices for mobile apps provide subjective yet vital measurements for assessing the overall user experience, ethical standing, and emotional engagement of an app. These indices help evaluate aspects that are difficult to quantify but essential for a comprehensive understanding of an app's impact on its users and how much users are engaged with it. Among the most common group of such indices are Acquisition, Engagement, Monetization and Retention.

The **Acquisition indices group** is mainly composed from user acquisition, traffic acquisition and user acquisition cohorts. *User acquisition* refers to the process of tracking how new users are brought to a mobile app. The most common user acquisition indices are: New users, Session duration, Screen session, and Conversion.

Traffic acquisition focuses on understanding how users arrive at a mobile app and the quality of traffic driven from various sources. Key components of traffic acquisition include Channels, Search traffic, Direct traffic, Social traffic, and Referral traffic.

User acquisition cohorts refer to a specific feature that groups users based on common characteristics, particularly when they acquired or started using a mobile app. Key elements of user acquisition cohorts in Google Analytics include Cohort definition, Cohort metrics, Behavioral patterns, and Comparing acquisition channels.

The **Engagement indices group** is mainly composed from events and screens. *Engagement events* are specific actions or interactions that users take within a mobile app, providing deeper insights into user behavior beyond basic metrics like screen views or session duration. Key aspects of engagement events include Event categories, Event actions, Tracking engagement metrics, and Custom event tracking.

Screens refers to a report that provides insights into how users navigate and interact with the various screens within a mobile app. Key elements of the "Pages and Screens" report include: Screenviews, Average time on screen, Screen pathing, User interaction on screens, and Conversion tracking.

The **Monetization indices group** is mainly composed from Purchase journey, Checkout journey and In-app purchase. The *Purchase journey* refers to the path a user takes from their initial interaction with a website or app to the final step of completing a purchase. By understanding how users move through each stage of this journey, businesses can tailor their strategies to meet customer needs at every point, from acquisition to checkout and beyond.

The *Checkout journey* refers to the steps a user takes once he decides to make a purchase and proceed to the checkout process. Understanding the checkout journey enables businesses to identify bottlenecks, reduce misunderstandings, and enhance the user experience, ultimately leading to higher conversion rates and more completed purchases.

By tracking *In-app purchase* (IAP) businesses can gain valuable insights into user behavior, optimize their monetization strategies, and enhance the overall performance of their mobile app. This data enables informed decision-making that drives higher revenue and improves user satisfaction with IAP.

The **Retention indices** group refers to the tracking and measurement of how frequently users return to a website or mobile app over time. Key aspects of retention tracking include User retention rates, Cohort analysis for retention, Active users, Churn rate, and Retention by device or platform.

3. Results and discussions

From many points of view, mobile apps can suit different business and no business activities in many aspects, but besides need and opportunities, it is required to understand the costs of buying or developing from scratch such mobile apps. These costs are taken into account by NPV, IRR, and PI indices.

3.1. Evaluate development cost of a mobile application

Developing a mobile app is nothing different than developing any other type of software solution, basically all of them share mostly the same Software Development Life Cycle (SDLC), just each so called target platform (web, desktop, mobile) has its own specifics or narrow. Taking into consideration SDLC and understanding that a person cannot cover complete all or several roles according to its effect over the performance, most economic

agents prefer Agile methodologies for delivering software solutions over traditional ones as Waterfall, due to many reasons regarding delivery time, costs and change requests from the product owner [29]. In order to handle a single mobile app with a set of features based on Agile framework, it is required an agile team that at least would consist of a group of employees (by categories):

1. Software engineers that will deal with mobile development.
2. Designers that will deal with the user experience and user interface.
3. Quality assurance engineers that will deal with testing phase of the application.
4. Managers that will handle the team, be responsible for the requirement and deliveries.

From business and costs point of view the agile methodology, in order to calculate the costs for delivering a mobile app, will require the following characteristics:

H_k- total number of hours spent by employees of category *k*, $k = \overline{1,4}$;

R_k- rate per hour for an employee of category *k*, $k = \overline{1,4}$;

M - miscellaneous costs, such as licensing, 3rd party services, etc.

The costs of a mobile app i will be marked as C_i, $i = \overline{1,n}$, where *n* is the number of mobile apps. Considering the costs with employees, the mobile app *i* costs are determined as

$$C_i = \sum_{k=1}^{4} H_{ki} R_k + M_i, i = \overline{1,n}, \quad (9)$$

where: H_{ki} is the number of hours spent by employees of category *k* to develop the mobile app *i*.

As any other software product, besides the first phase of development and delivery, it also could have new development phases and maintenance. Here comes the specific software development that was discussed above, people and organizations in average keep their mobile devices for a period between 2-4 years, afterwards replace them with newer ones because of better hardware capabilities, battery life and support of new version of mobile operating systems (OS). This replacement can be observed with fast adoption of updates for OS for iOS [30] and Android [31] devices on a global level. Due to many technical and legal reasons, with each OS update over the mobile device, come a lot of changes like new features for users and developers to implement, deprecated features in previous OS versions, new security updates and restrictions by the OS, etc.

Going over the mentioned adoption and changes, will be considered the total required investments as well for maintaining a mobile app that will be marked E. The mobile apps investments, during maintenance period for E consist from minor development and update distribution. These investments are mostly required because people are used to do regular mobile OS updates [30,31] and mobile app market stores might require applying several changes within the mobile app, otherwise it can be blocked or removed completely from their marketplace. Most private organization offer different types of maintenance packages, like on-demand, monthly, yearly or specific number of hours. These costs are covered separately and on beneficiary wish. In other words, if the beneficiary will need maintenance, then it will have to support these costs. These are several conclusions, recommendations regarding going for or no maintenance:

1. If the beneficiary does not have in mind to change the mobile devices and use it only internally for a long period of time (at least 5-7 years), then he doesn't need the maintenance part.

2. The maintenance part for mobile apps consists mainly in updates within the code and submitting to the distribution layer new mobile apps versions. Mobile OS updates are coming around every year and their major transition takes around another year.

3. The maintenance costs are evaluated around 20% of the initial core development of the mobile apps [32].

4. If the development phase of a mobile app passes a certain period of time and it's near the release of new versions of OS, then the beneficiary should take the maintenance part in order to continue further with mobile stores permissions.

Considering that mobile app delivery consists in most cases by covering two platforms (Android & iOS), these can be analyzed in many use cases, because not every mobile app is designed only for public use and covering both platforms. These use cases are the following:

- mobile apps for internal use only (Cases):
  a) develop and use only an Android or an iOS mobile app;
  b) develop and use both an Android and an iOS mobile app;
- mobile apps for external use (Cases):
  c) develop and distribute only an Android or an iOS mobile app;
  d) develop and distribute both an Android and an iOS mobile app;
- mobile apps for internal and external use (Cases):
  e) develop, internal use and distribute only an Android or an iOS mobile app;
  f) develop, internal use and distribute both an Android and an iOS mobile app.

Cases (a)-(f) look similar, but in real life the costs are different. Each of Cases (a)-(f) will be analyzed separately.

Case a. *Develop and internal use only an Android or an iOS mobile app*

For internal use it is required to develop and, also, to cover the maintenance costs of a mobile application *i*. The maintenance costs, considered equal with an Android and with an iOS mobile app and marked E_i, is around 20% of the initial development [32]. So, taking into account (9), one has

$$E_i = 0.2\sum_{k=1}^{4} H_{ki}R_k\,, i = \overline{1,n}. \tag{10}$$

Thus, the total costs for a beneficiary with the development (see (9)) and maintenance (see (10)) of a mobile app *i* for internal use is determined as

$$C_i + E_i = \sum_{k=1}^{4} H_{ki}R_k + M_i + 0.2\sum_{k=1}^{4} H_{ki}R_k = 1.2\sum_{k=1}^{4} H_{ki}R_k + M_i, i = \overline{1,n}. \tag{11}$$

Case b. *Develop and internal use both an Android and an iOS mobile app*

To develop, maintain and internal using both an Android and an iOS mobile app, it is needed doubling costs for one of them. Taking into account (3), the total costs for a beneficiary with the development and maintenance of an Android and an iOS mobile app *i* for internal use is determined as

$$2(C_i + E_i) = 2.4\sum_{k=1}^{4} H_{ki}R_k + 2M_i, i = \overline{1,n}. \tag{12}$$

Case c. *Develop and distribute only an Android or an iOS mobile app*

In this case will be supported the same costs for development and maintenance determined according to formula (11) as in case (a), the only difference is that the Android distribution to mass public will require to pay many mobile store accounts, when with regard to the iOS distribution to mass public will require to pay only one mobile store account. Distributing an Android mobile app can be done only by manually sharing the .apk file or other free distribution service like Firebase App Distribution [33]. If to compare the distribution of an Android app with the one of an iOS app, we will have a lot more options where we can distribute it, not only for Europe or United States users, but as well for those which live in the Asia. Here is a list of places and prices that apply for publishing on their stores [28]:

1. Google Play Store (25 USD one-time payment).
2. Amazon AppStore (free distribution).
3. Samsung Galaxy Store (free distribution).
4. Huawei AppGallery (free distribution).
5. F-droid (free distribution).
6. Oppo App Market (free distribution).
7. Xiaomi Mi Store (free distribution), etc.

Most of Android mobile app stores have free distribution option to mass public or at least require a small and symbolic fee in order to use their platform. So, the total costs for a developer to develop, maintain and distribute an Android mobile application *i* (Case c.1), based on (11), is determined as:

$$C_i + E_i + \sum_{s=1}^{S} C_{si} = 1.2 \sum_{k=1}^{4} H_{ki} R_k + \sum_{s=1}^{S} C_{si} + M_i, i = \overline{1,n}, \quad (13)$$

where: $C_{si} \geq 0$ are Android mobile app store *s* costs for the mobile app *i,* and $S \geqslant 1$ is the number of Android mobile app stores to be supported.

At the moment, in order to distribute an iOS mobile app is necessary to have an Apple Developer Account due to OS restrictions and certificates released by Apple for their devices, so additionally to this will be added the costs of the developer platform. Distribution policy and restrictions enforce to have additional 99 USD per year costs [34]. So, the total costs for a developer to develop, maintain and distribute an iOS mobile app *i* (Case c.2), based on (11), is determined as

$$C_i + E_i + C_{\mathrm{O}i} = 1.2 \sum_{k=1}^{4} H_{ki} R_k + C_{\mathrm{O}i} + M_i, i = \overline{1,n}, \quad (14)$$

where: $C_{\mathrm{O}i} \geq 0$ are iOS mobile app store costs for the mobile app *i*.

At the same time, when sailing a product its price is equal to costs with it multiplied by (1 + established profit rate). Let established profit rate be marked as PR. Usually, $d \leqslant \mathrm{PR} \leqslant 0.2$.

So, for a purchaser, the price I_i (investment) for an Android or an iOS mobile app *i* (Case c.3), taking into account (11), is determined as:

$$I_i = (C_i + E_i)(1 + \mathrm{PR}) = (1 + \mathrm{PR}) \left(1.2 \sum_{k=1}^{4} H_{ki} R_k + M_i \right), i = \overline{1,n}. \quad (15)$$

Case d. *Develop and distribute both an Android and an iOS mobile app*

For a developer (Case d.1), to develop, maintain and distribute both an Android and an iOS mobile app needs total costs determined by summing the costs according to formulas (13) and (14), that is:

$$C_i + E_i + \sum_{s=1}^{S} C_{si} + C_i + E_i + C_{Oi} = 2.4 \sum_{k=1}^{4} H_{ki} R_k + \sum_{s=1}^{S} C_{si} + C_{Oi} + 2M_i, i = \overline{1,n}. \quad (16)$$

Evidently, for a purchaser, the price I_i (investment) for an Android or an iOS mobile app *i* (Case d.2) is determined according to (15).

Case e. *Develop, internal use and distribute only an Android or an iOS mobile application*

In this case, the costs with a mobile app *i* supported by a developer are the same as in Cases c.1 and c.2, that is they are determined according to (13), for an Android mobile app (Case e.1), and - according to (14), for an iOS mobile app (Case e.2). Of course, in both cases, the respective cash flows, including the estimated profit, are different being higher than in Cases c.1 and c.2.

At the same time, for a purchaser (Case e.3) the price for a mobile app *i* is the same as in Case c.3, i.e. it is determined according to (15).

Case f. *Develop, internal use and distribute both an Android and an iOS mobile app*

In a similar mode, the costs with a mobile app *i* supported by a developer (Case f.1) are the same as in Case d.1, that is they are determined according to (16). Of course, the respective cash flows, including the estimated profit, are different being higher than in Cases c.1, c.2, d.1, e.1, and e.2.

Also, as in Cases d.2 and e.3, for a purchaser (Case f.2) the price for a mobile app *i* is the same as in Case c.3, i.e. it is determined according to (15).

Resuming on Cases (a)-(f), for a developer one can conclude that by total costs with a mobile application the relations among the cases are

$$\text{(a)} \leqslant \text{c.2} = \text{e.2} \leqslant \text{c.1} = \text{e.1} \leqslant \text{(b)} \leqslant \text{d.1} = \text{f.1}, \quad (17)$$

and by total profit on a mobile application the relations usually are:

$$\text{f.1} \geqslant \text{d.1} \geqslant \text{e.1} \geqslant \text{c.1} \geqslant \text{e.2} \geqslant \text{c.2} \geqslant \text{(a)} \geqslant \text{(b)}. \quad (18)$$

In its turn, for a purchaser the price for a mobile application *i* is the same in all cases, i.e. Cases c.3, d.2, e.3, and f.2, and is determined according to (15).

Cases (a)-(f) show how costs can vary depending on the requirement if it is of internal, of external or both of internal and external usage. If to take a look over device adoptions statistics analyzed by Andrew Buck on MobiLoud [35], one has the device adoption by zone shown in Table 1.

Table 1

Mobile device adoptions statistics [35]

Zone\Platform	iOS	Android	Other
North America	58%	41%	1%
Europe	33%	66%	1%
Asia	20%	79%	1%
Africa	13%	85%	2%
South America	16%	84%	0%

From the current values, one can observe and conclude that Case (b) would be relevant only for North America and Europe zones and there is a big chance that it won't be reasonable to invest because iOS mobile devices produced by Apple have a pricing model higher than any other Android mobile device produced by other companies.

After determining the development costs or required investment for a mobile app, it is important to understand and choose right quantitative indices for measuring their impact.

3.2. Quantitative indices for measuring the impact by use cases

In possible impact of the use of mobile apps, measured by NPV, IRR, and PI indices, each of Cases (a)-(f), described in Section 3.1, will be concretized separately for one beneficiary and one (Android or iOS, scenario {j = 1, n = 1}) or two (Android and iOS, scenario {j = 1, n = 2}) mobile apps. To scenario {j = 1, n = 1}, for a developer correspond Cases (a), c.1, c.2, e.1, and e.2 and for a purchaser - Cases c.3, d.2, e.3, and f.2. At the same time, to scenario {j = 1, n = 2}, for a developer correspond Cases (b), d.1, and f.1, and for a purchaser - there are no such cases. Knowing the expressions of quantitative indices for these scenarios, it is easy to determine the corresponding expressions for other scenarios, too.

In all examined below cases, it will be considered the mobile app i and the C_i cost is determined according to (9).

Net Present Value by use cases

Taking into account the costs for each of Cases (a)-(f), the NPV is determined according to formula (2), where:

- for a purchaser (Cases c.3, d.2, e.3, and f.2) occurs $\tau_i = 0$. Thus, one has:

$$\mathrm{NPV}_i = \sum_{t=1}^{D_i} \frac{P_{it} + \mathrm{AA}_{it}}{(1+d)^t} - I_i, \tag{19}$$

where: I_i is determined according to (15);

- for a developer in Case (a), occurs $I_i = C_i$. So, is obtained

$$\mathrm{NPV}_i = \sum_{t=\tau_i+1}^{L_i} \frac{P_{it} + \mathrm{AA}_{it}}{(1+d)^t} - C_i = \sum_{t=\tau_i+1}^{L_i} \frac{P_{it} + \mathrm{AA}_{it}}{(1+d)^t} - \sum_{k=1}^{4} H_{ki} R_k - M_i; \tag{20}$$

- for a developer in Cases c.1 and e.1, occurs $I_i = C_i + \sum_{s=1}^{S} C_{si}$. Thus, is obtained

$$\begin{aligned} \mathrm{NPV}_i = & \sum_{t=\tau_i+1}^{L_i} \frac{P_{it} + \mathrm{AA}_{it}}{(1+d)^t} - C_i - \sum_{s=1}^{S} C_{si} = \\ & = \sum_{t=\tau_i+1}^{L_i} \frac{P_{it} + \mathrm{AA}_{it}}{(1+d)^t} - \sum_{k=1}^{4} H_{ki} R_k - \sum_{s=1}^{S} C_{si} - M_i; \end{aligned} \tag{21}$$

- for a developer in Cases c.2 and e.2, occurs $I_i = C_i + C_{\mathrm{O}i}$. So, finally, is obtained

$$\mathrm{NPV}_i = \sum_{t=\tau_i+1}^{L_i} \frac{P_{it} + \mathrm{AA}_{it}}{(1+d)^t} - C_i - C_{\mathrm{O}i} == \sum_{t=\tau_i+1}^{L_i} \frac{P_{it} + \mathrm{AA}_{it}}{(1+d)^t} - \sum_{k=1}^{4} H_{ki} R_k - C_{\mathrm{O}i} - M_i; \tag{22}$$

- for a developer in Case (b), occurs $I_i = 2C_i$. Thus, is obtained

$$\mathrm{NPV}_i = \sum_{t=\tau_i+1}^{L_i} \frac{P_{it} + \mathrm{AA}_{it}}{(1+d)^t} - 2C_i = \sum_{t=\tau_i+1}^{L_i} \frac{P_{it} + \mathrm{AA}_{it}}{(1+d)^t} - 2\left(\sum_{k=1}^{4} H_{ki} R_k - M_i\right); \tag{23}$$

- for a developer in Cases d.1 and f.1, occurs $I_i = 2C_i + C_{Oi} + \sum_{s=1}^{S} C_{si}$. So, is obtained

$$\begin{aligned} \text{NPV}_i = &\sum_{t=\tau_i+1}^{L_i} \frac{P_{it} + \text{AA}_{it}}{(1+d)^t} - 2C_i - C_{Oi} - \sum_{s=1}^{S} C_{si} = \\ &= \sum_{t=\tau_i+1}^{L_i} \frac{P_{it} + \text{AA}_{it}}{(1+d)^t} - 2\left(\sum_{k=1}^{4} H_{ki}R_k - M_i\right) - C_{Oi} - \sum_{s=1}^{S} C_{si}. \end{aligned} \tag{24}$$

Internal Rate of Return by use cases

In general case, the value of the IRR for mobile app *i* is determined by solving the equation (3). In a similar mode, by use cases, taking into account relationships (3) and (19)-(24), the value of IRR for mobile app *i* is determined:

- for a purchaser (Cases c.3, d.2, e.3, and f.2), because $\tau_i = 0$, by solving the equation

$$\sum_{t=1}^{D_i} \frac{P_{it} + \text{AA}_{it}}{(1+\text{IRR})^t} - I_i = 0, \tag{25}$$

where I_i is determined according to (15);

- for a developer in Case (a), because $I_i = C_i$, by solving the equation

$$\sum_{t=\tau_i+1}^{L_i} \frac{P_{it} + \text{AA}_{it}}{(1+\text{IRR})^t} - C_i = \sum_{t=\tau_i+1}^{L_i} \frac{P_{it} + \text{AA}_{it}}{(1+\text{IRR})^t} - \sum_{k=1}^{4} H_{ki}R_k - M_i = 0; \tag{26}$$

- for a developer in Cases c.1 and e.1, because $I_i = C_i + \sum_{s=1}^{S} C_{si}$, by solving the equation

$$\begin{aligned} &\sum_{t=\tau_i+1}^{L_i} \frac{P_{it} + \text{AA}_{it}}{(1+\text{IRR})^t} - C_i - \sum_{s=1}^{S} C_{si} = \\ &= \sum_{t=\tau_i+1}^{L_i} \frac{P_{it} + \text{AA}_{it}}{(1+\text{IRR})^t} - \sum_{k=1}^{4} H_{ki}R_k - \sum_{s=1}^{S} C_{si} - M_i = 0; \end{aligned} \tag{27}$$

- for a developer in Cases c.2 and e.2, because $I_i = C_i + C_{Oi}$, by solving the equation

$$\sum_{t=\tau_i+1}^{L_i} \frac{P_{it} + \text{AA}_{it}}{(1+\text{IRR})^t} - C_i - C_{Oi} = \sum_{t=\tau_i+1}^{L_i} \frac{P_{it} + \text{AA}_{it}}{(1+\text{IRR})^t} - \sum_{k=1}^{4} H_{ki}R_k - C_{Oi} - M_i = 0; \tag{28}$$

- for a developer in Case (b), because $I_i = 2C_i$, by solving the equation

$$\sum_{t=\tau_i+1}^{L_i} \frac{P_{it} + \text{AA}_{it}}{(1+\text{IRR})^t} - 2C_i = \sum_{t=\tau_i+1}^{L_i} \frac{P_{it} + \text{AA}_{it}}{(1+\text{IRR})^t} - 2\left(\sum_{k=1}^{4} H_{ki}R_k - M_i\right) = 0; \tag{29}$$

- for a developer in Cases d.1 and f.1, because $I_i = 2C_i + C_{Oi} + \sum_{s=1}^{S} C_{si}$, by solving the equation

$$\begin{aligned} &\sum_{t=\tau_i+1}^{L_i} \frac{P_{it} + \text{AA}_{it}}{(1+\text{IRR})^t} - 2C_i - C_{Oi} - \sum_{s=1}^{S} C_{si} = \\ &= \sum_{t=\tau_i+1}^{L_i} \frac{P_{it} + \text{AA}_{it}}{(1+\text{IRR})^t} - 2\left(\sum_{k=1}^{4} H_{ki}R_k - M_i\right) - C_{Oi} - \sum_{s=1}^{S} C_{si} = 0. \end{aligned} \tag{30}$$

Profitability Index by use cases

Taking into account the costs for each of Cases (a)-(f), the PI is determined according to formula (4), where:

- for a purchaser (Cases c.3, d.2, e.3, and f.2), occurs $\tau_i = 0$. Thus, one has

$$\mathrm{PI}_i = \frac{1}{I_i}\sum_{t=1}^{D_i}\frac{P_{it}+\mathrm{AA}_{it}}{(1+d)^t}, \tag{31}$$

where I_i is determined according to (15);

- for a developer in Case (a), occurs $I_i = C_i$. So, is obtained

$$\mathrm{PI}_i = \sum_{t=\tau_i+1}^{L_i}\frac{P_{it}+\mathrm{AA}_{it}}{(1+d)^t}\Bigg/\left(\sum_{k=1}^{4}H_{ki}R_k - M_i\right); \tag{32}$$

- for a developer in Cases c.1 and e.1, occurs $I_i = C_i + \sum_{s=1}^{S} C_{si}$. Thus, one has

$$\mathrm{PI}_i = \sum_{t=\tau_i+1}^{L_i}\frac{P_{it}+\mathrm{AA}_{it}}{(1+d)^t}\Bigg/\left(\sum_{k=1}^{4}H_{ki}R_k - \sum_{s=1}^{S}C_{si} - M_i\right); \tag{33}$$

- for a developer in Cases c.2 and e.2, occurs $I_i = C_i + C_{\mathrm{O}i}$. So, is obtained

$$\mathrm{PI}_i = \sum_{t=\tau_i+1}^{L_i}\frac{P_{it}+\mathrm{AA}_{it}}{(1+d)^t}\Bigg/\left(\sum_{k=1}^{4}H_{ki}R_k - C_{Oi} - M_i\right); \tag{34}$$

- for a developer in Case (b), occurs $I_i = 2C_i$. Thus, one has

$$\mathrm{PI}_i = \sum_{t=\tau_i+1}^{L_i}\frac{P_{it}+\mathrm{AA}_{it}}{(1+d)^t}\Bigg/2\left(\sum_{k=1}^{4}H_{ki}R_k - M_i\right); \tag{35}$$

- for a developer in Cases d.1 and f.1, occurs $I_i = 2C_i + C_{\mathrm{O}i} + \sum_{s=1}^{S} C_{si}$. So, is obtained

$$\mathrm{PI}_i = \sum_{t=\tau_i+1}^{L_i}\frac{P_{it}+\mathrm{AA}_{it}}{(1+d)^t}\Bigg/\left[2\left(\sum_{k=1}^{4}H_{ki}R_k - M_i\right) - C_{\mathrm{O}i} - \sum_{s=1}^{S}C_{si}\right]. \tag{36}$$

Equivalent Annual Net Present Value by use cases

With refer to the EANPV, based on formulas (6) and (7) and taking into account the formulas for NPV in each of Cases (a)-(f), one has

$$\begin{aligned}\mathrm{EANPV}_i = \frac{d(1+d)^{L_i}}{(1+d)^{L_i}-1}\left[\sum_{t=\tau_i+1}^{L_i}\frac{P_{it}+\mathrm{AA}_{it}}{(1+d)^t} - \sum_{t=1}^{\tau_i}\frac{I_{it}}{(1+d)^t}\right] = \\ = \frac{d(1+d)^{L_i}}{(1+d)^{L_i}-1}\left[\sum_{t=\tau_i+1}^{L_i}\frac{\mathrm{CF}_{it}}{(1+d)^t} - I_i\right],\end{aligned} \tag{37}$$

where:

- for a purchaser (Cases c.3, d.2, e.3, and f.2), occurs $\tau_i = 0$. Thus, one has

$$\mathrm{EANPV}_i = \frac{d(1+d)^{D_i}}{(1+d)^{D_i}-1}\left[\sum_{t=1}^{D_i}\frac{P_{it}+\mathrm{AA}_{it}}{(1+d)^t} - I_i\right], \tag{38}$$

where I_i is determined according to (2.7);

- for a developer in Case (a), occurs $I_i = C_i$. So, is obtained

$$\text{EANPV}_i = \frac{d(1+d)^{L_i}}{(1+d)^{L_i}-1}\left[\sum_{t=\tau_i+1}^{L_i}\frac{P_{it}+\text{AA}_{it}}{(1+d)^t} - \sum_{k=1}^{4} H_{ki}R_k - M_i\right]; \quad (39)$$

- for a developer in Cases c.1 and e.1, occurs $I_i = C_i + \sum_{s=1}^{S} C_{si}$. Thus, is obtained

$$\text{EANPV}_i = \frac{d(1+d)^{L_i}}{(1+d)^{L_i}-1}\left[\sum_{t=\tau_i+1}^{L_i}\frac{P_{it}+\text{AA}_{it}}{(1+d)^t} - \sum_{k=1}^{4} H_{ki}R_k - \sum_{s=1}^{S} C_{si} - M_i\right]; \quad (40)$$

- for a developer in Cases c.2 and e.2, occurs $I_i = C_i + C_{\text{O}i}$. So, is obtained

$$\text{EANPV}_i = \frac{d(1+d)^{L_i}}{(1+d)^{L_i}-1}\left[\sum_{t=\tau_i+1}^{L_i}\frac{P_{it}+\text{AA}_{it}}{(1+d)^t} - \sum_{k=1}^{4} H_{ki}R_k - C_{\text{O}i} - M_i\right]; \quad (41)$$

- for a developer in Case (b), occurs $I_i = 2C_i$. Thus, is obtained

$$\text{EANPV}_i = \frac{d(1+d)^{L_i}}{(1+d)^{L_i}-1}\left[\sum_{t=\tau_i+1}^{L_i}\frac{P_{it}+\text{AA}_{it}}{(1+d)^t} - 2\left(\sum_{k=1}^{4} H_{ki}R_k - M_i\right)\right]; \quad (42)$$

- for a developer in Cases d.1 and f.1, occurs $I_i = 2C_i + C_{\text{O}i} + \sum_{s=1}^{S} C_{si}$. So, is obtained

$$\text{EANPV}_i = \frac{d(1+d)^{L_i}}{(1+d)^{L_i}-1}\left[\sum_{t=\tau_i+1}^{L_i}\frac{P_{it}+\text{AA}_{it}}{(1+d)^t} - 2\left(\sum_{k=1}^{4} H_{ki}R_k - M_i\right) - C_{\text{O}i} - \sum_{s=1}^{S} C_{si}\right]. \quad (43)$$

Equivalent Annual Profitability Index by use cases

Regarding the EAPI index, based on formulas (6) and (7) and taking into account the formulas for Profitability Index in each of Cases (a)-(f), one has

$$\text{EAPI}_i = \text{CRF}\cdot\text{PI}_i = \frac{d(1+d)^{L_i}}{(1+d)^{L_i}-1}\left(1+\frac{\text{NPV}_i}{I_i}\right), \quad (44)$$

where:

- for a purchaser (Cases c.3, d.2, e.3, and f.2), occurs $\tau_i = 0$. Thus, one has

$$\text{EAPI}_i = \frac{d(1+d)^{D_i}}{I_i[(1+d)^{D_i}-1]}\sum_{t=1}^{D_i}\frac{P_{it}+\text{AA}_{it}}{(1+d)^t}, \quad (45)$$

where I_i is determined according to (15);

- for a developer in Case (a), occurs $I_i = C_i$. So, is obtained

$$\text{EAPI}_i = \frac{d(1+d)^{L_i}}{(1+d)^{L_i}-1}\sum_{t=\tau_i+1}^{L_i}\frac{P_{it}+\text{AA}_{it}}{(1+d)^t}\Bigg/\left(\sum_{k=1}^{4} H_{ki}R_k - M_i\right); \quad (46)$$

- for a developer in Cases c.1 and e.1, occurs $I_i = C_i + \sum_{s=1}^{S} C_{si}$. Thus, one has

$$\text{EAPI}_i = \frac{d(1+d)^{L_i}}{(1+d)^{L_i}-1}\sum_{t=\tau_i+1}^{L_i}\frac{P_{it}+\text{AA}_{it}}{(1+d)^t}\Bigg/\left(\sum_{k=1}^{4} H_{ki}R_k - \sum_{s=1}^{S} C_{si} - M_i\right); \quad (47)$$

- for a developer in Cases c.2 and e.2, occurs $I_i = C_i + C_{\text{O}i}$. So, is obtained

$$\text{EAPI}_i = \frac{d(1+d)^{L_i}}{(1+d)^{L_i}-1}\sum_{t=\tau_i+1}^{L_i}\frac{P_{it}+\text{AA}_{it}}{(1+d)^t}\Bigg/\left(\sum_{k=1}^{4}H_{ki}R_k - C_{\text{O}i} - M_i\right); \quad (48)$$

- for a developer in Case (b), occurs $I_i = 2C_i$. Thus, one has

$$\text{EAPI}_i = \frac{d(1+d)^{L_i}}{(1+d)^{L_i}-1}\sum_{t=\tau_i+1}^{L_i}\frac{P_{it}+\text{AA}_{it}}{(1+d)^t}\Bigg/2\left(\sum_{k=1}^{4}H_{ki}R_k - M_i\right); \quad (49)$$

- for a developer in Cases d.1 and f.1, occurs $I_i = 2C_i + C_{\text{O}i} + \sum_{s=1}^{S} C_{si}$. So, is obtained

$$\text{EAPI}_i = \frac{d(1+d)^{L_i}}{(1+d)^{L_i}-1}\sum_{t=\tau_i+1}^{L_i}\frac{P_{it}+\text{AA}_{it}}{(1+d)^t}\Bigg/\left[2\left(\sum_{k=1}^{4}H_{ki}R_k - M_i\right) - C_{Oi} - \sum_{s=1}^{S}C_{si}\right]. \quad (50)$$

3.3. Some of implemented use cases

IMNA Solutions use case

IMNA Solutions (IMNA) [36] is a technology company that specializes in developing innovative solutions aimed at enhancing healthcare delivery and patient management. One of the flagship products developed by IMNA is a comprehensive patient management platform that enables healthcare providers to monitor patient progress in real-time. Among the most critical problems that IMNA observed while discussing with different healthcare institutions were:

1. Data inconsistency from different patients, doctors, records, etc.
2. Communication issues between patients and doctors.
3. Patients often do not update their medical data.
4. Patients and doctors are not updated in real-time with all the events that are happening.
5. Patients are often dropping trials and do not complete medical questionnaires.

Mobile apps were one of the proposed solutions. Using native mobile frameworks, because of security, data privacy, and smart device connectivity issues, mobile apps were discussed, developed, and finally delivered. After their implementation, the following results were obtained:

1. Clinical institutions started to receive more accurate data from patients and the smart devices that were worn.
2. The communication issues between doctor and patients started to disappear. They became more often and more proactive, this part was sensed the most during the COVID-19 period.
3. Patients began to complete more often medical questionnaires and reach the end of medical trials, including:
   1) according to reports from Nasus Pharma [28], after using IMNA mobile apps, one of their last medical trials out of 1000 people it ended with 100% user engagement - a significant increase from the previously achieved maximum of 72%;
   2) according to reports from RambamHealth [28], after using IMNA mobile applications, one of their latest medical studies of 200 people ended with 98.5% user engagement - a significant increase from the previously achieved maximum of 67%.

To determine the economic impact, in Table 2, summary data obtained by IMNA are systematized.

Table 2

IMNA Solutions Cash flows for mobile apps in the 2019-2022 years [28]

Year	Income, USD	Costs, USD	Cash flows, USD
2019	97,400	133,900	-36,500
2020	98,800	130,100	-31,300
2021	284,000	141,800	142,200
2022	484,000	253,700	230,300

From Table 2, a trend of rapid growth in Cash flows can be observed, exceeding 230 thousand USD in 2022, over 1.6 times more than in 2021.

Securer use case

Securer [37] is an infrastructure for digitizing investors, assets, companies and funds ecosystems. Securer faced the following issues: 1) finding new auditory; 2) finding new communication and engagement channels; 3) to do more marketing and gain more attraction; 4) automate the Know Your Customer (KYC) process.

As a solution, the development of a mobile app was proposed. Using hybrid approach, because of planned and limited budget, the mobile app was developed and delivered. After implementing the mobile app, Securer received more insights about their products and services, raised the number of active users by 12%, achieves new engagement channel for further research, and obtains a proof of concept of mobile KYC [28].

VentureRocket use case

VentureRocket [38] is a comprehensive platform designed to streamline and enhance the processes of fundraising, investment management, and collaboration within the startup ecosystem. Aimed at entrepreneurs, investors, and accelerators, VentureRocket provides a robust digital infrastructure that facilitates the growth and development of early-stage companies by connecting them with the resources, capital, and networks they need to succeed.

VentureRocket was trying to extend their user engagement channels and reach new leads and users for their platform by: 1) finding new auditory; 2) finding new communication and engagement channels; 3) increase their reputation and branding; 4) secure their data against different potential issues.

In order to check and investigate a new communication channel and source of new users, the development of a mobile app was proposed. Using hybrid approach because of limited available developer resources during that period of time, the mobile app was developed and delivered. After implementing the mobile app with biometric verification layer, VentureRocket received more insights about their products and service, raised the number of active users by 9%, and achieved new engagement channel for further research [28].

4. Conclusions

The widespread use of mobile devices requires streamlining the development and use of mobile apps. In this context, it is imminent to evaluate the impact of mobile apps on business activities in particular and on the quality of life in general. Unfortunately, the

information, research and analytical data regarding the quantitative economic impact of mobile apps is poor.

In this paper, an attempt is made to improve the situation in the field. To this end, taking into account the categories of mobile apps in the Google Play Store and Apple App Store and the statistical classification of economic activities, a classification of mobile apps is proposed. This can help organizations promote and generate new types of income.

From the multitude of indices used to assess the economic efficiency of IT investment projects, the NPV, IRR and PI indices are selected, eventually in conjunction with the EAV method. These three indices form a Pareto set; the use of each of them, depending on the case, may lead to a different solution. Several qualitative indices have also been systematized to measure the impact of mobile apps.

To calculate the NPV, IRR and PI indices, the costs with mobile applications are essential. For this reason, six base cases were defined, and afterwards 12 sub-cases (more precisely, two base cases and 10 sub-cases) were defined and for each of them the respective formulas were obtained. Subsequently, based on these, the final formulas for calculating the NPV, IRR, PI, EANPV and EAPI indices were obtained for each of the 12 sub-cases.

Moreover, concrete calculations were performed regarding the impact of mobile applications developed and implemented within the companies IMNA Solutions, Securer and VentureRocket. These implementations confirmed the significant economic and social impact of mobile apps.

Conflicts of Interest: The authors declare no conflict of interest.

References

1. Petrosyan, A. Number of internet and social media users worldwide as of July 2024. Aug 19, 2024. Available online: https://www.statista.com/statistics/617136/digital-population-worldwide/ (accessed on 24.08.2024).
2. Laricchia, F. Global smartphone penetration rate as share of population from *2016 to 2023*. May 8, 2024. Available online: https://www.statista.com/statistics/203734/global-smartphone-penetration-per-capita-since-2005/ (accessed on 11.05.2024).
3. Wurmser, Y. Time Spent With Connected Devices 2023. Jun 12, 2023. Available online https://www.emarketer.com/content/ connected-device-time-spent-2023 (accessed on 16.08.2023).
4. Four Advantages of a Planned Approach TO DIGITAL MATURITY 2015. Adobe Inc., July 2015. Available online: https://landing.adobe.com/dam/downloads/whitepapers/192320.en.digital-marketing-survey-report.pdf (accessed on 12.01.2022).
5. Chari, B. Industry leaders are migrating to DataStage on Cloud Pak for Data. Shouldn't you?. September 30, 2020. Available online: https://www.ibm.com/blog/industry-leaders-are-migrating-to-datastage-on-cloud-pak-for-data-shouldnt-you/ (accessed on 12.10.2021).
6. Taylor, P. Forecast number of mobile users worldwide from 2020 to 2025. November 16, 2023. Available online: https://www.statista.com/statistics/218984/number-of-global-mobile-users-since-2010/ (accessed on 24.12.2023).
7. Mobile commerce growth (2017–2028). Oberlo. Available online: https://www.oberlo.com/statistics/mobile-commerce-sales (accessed on 23.06.2023).
8. Sterling, G. Study: 78 Percent Of Local-Mobile Searches Result In Offline Purchases. April 9, 2014. Available online: https://searchengineland.com/study-78-percent-local-mobile-searches-result-offline-purchases-188660 (accessed on 19.08.2022).
9. Mobile POS Payments – Worldwide. Statista Market Insights, September 2024. Available online: https://www.statista.com/ outlook/fmo/digital-payments/mobile-pos-payments/worldwide (accessed on 22.09.2024).
10. Karami, P. *Empirical evaluation of the impact of mobile development frameworks on the application source code quality*. Montreal: École de technologie supérieure, 2023, 117 p. Available online: https://espace.etsmtl.ca/id/eprint/3209/1/ KARAMI_Parsa.pdf (accessed on 13.03.2023).

11. Tactuk, I. M.; Munaiah, N.; Meneely, A. The Impact of Cross-Platform Development Approaches for Mobile Applications from the User's Perspective, WAMA 2016. In: *Proceedings of the International Workshop on App Market Analytics, co-located with FSE* 2016. 2016, pp. 43-49.
12. Holden, A. Mobile learning and teacher quality: Assessing the impact of a mobile application on the positive psychology and professional practice of Panamanian teachers. University of Cambridge, 2021. Available online: https://www.repository.cam.ac.uk/bitstreams/51960eab-13b2-4f86-8dcf-e23b1f3646b0/download (accessed on 24.08.2021).
13. Heflin, H.; Shewmaker, J.; Nguyen, J. Impact of mobile technology on student attitudes, engagement and learning. *Computers & Education* 2017, 107, pp. 91-99. ISSN 0360-1315.
14. Hahn, K. Critical investigation of the mobile information technology expert's perspective on the impact of the mobile application development within the German financial market and service industry (PhD thesis). Edinburgh Napier University, May 31, 2017. Available online: https://www.napier.ac.uk/research-and-innovation/research-search/outputs/ critical-investigation-of-the-mobile-information-technology-experts-perspective-on-the (accessed on 27.08.2021).
15. Altaleb, A.R. An industrial study of effort estimation in mobile app development using agile processes. 2020. Available online: https://search.ebscohost.com/login.aspx?direct=true&db=ddu&AN=ddu.oai.ethos.bl.uk.827146&site=ehost-live (accessed on 26.02.2021).
16. Hoos, E.; Gröger, C.; Kramer, S.; Mitschang, B. Improving Business Processes through Mobile Apps. In: *16th International Conference on Enterprise Information Systems* (ICEIS), SciTePress, 2014, pp. 71-82.
17. Google Play Statistics and Trends *2024*. 42 matters, April 2024. Available online: https://42matters.com/google-play-statistics-and-trends (accessed on 11.07.2024).
18. Apple App Store Statistics and Trends 2024. 42 matters, April 2024. Available online: https://42matters.com/google-play-statistics-and-trends (accessed on 11.07.2024).
19. Romanu, I.; Vasilescu, I. *Economic Efficiency of Investments and of Fixed Capital*. Didactic and Pedagogical Publishing House, Bucharest, Romania, 1993, 301 p. [in Romanian].
20. Kossov, V.V.; Livshits, V.N.; Shahnazarov, A.G. *Methodical recommendations for evaluating the effectiveness of investment projects*. Economica, Moscow, 2000, 325 p. [in Russian].
21. Albu, S., Capsîzu, V., Albu, I. *Efficiency of Investment*. CEP USM, Chisinau, RM, 2005, 138 p. [in Romanian].
22. Ellram, L.M. A Taxonomy og Total Cost of Ownership Models. *Journal of Business Logistics* 1994, 15(1), pp. 171-191. ISSN 0735-3766.
23. Botnari, N. *Enterprise Finance*. Central Printing House, Chisinau, RM, 2006, 240 p. [in Romanian].
24. Bolun, I. On criteria to be used by mission of projects. *Economica* 2017, 102(4), pp. 135-148. ISSN 1810-9136.
25. Bolun, I. Aspects of selecting investment I-projects. *Competitiveness and innovation in the knowledge economy* 2018, 5, pp. 7-12.
26. *Costs of Capital by Industry Sector - NYU Stern*. New York: Stern School of Business at New York University. Available online: https://people.stern.nyu.edu/adamodar/New_Home_Page/datafile/ wacc.htm (accessed on 18.01.2022).
27. Edge, C. G.; Irvine, V. B. *A Practical Approach to the Appraisal of Capital Expenditures*. Society of Management Accountants of Canada, (2nd ed.), Hamilton, Canada, 1981, 283 p.
28. Nastas, V. Impact of mobile applications on business affairs (PhD thesis). ASEM, Chisinau, RM, 2024, 189 p. [in Romanian].
29. Shankarmani, R.; Pawar, R.; Mantha, S.S. Agile Methodology Adoption: Benefits and Constraints. *International Journal of Computer Applications* 2012, 58, pp. 31-37. ISSN 0975-8887.
30. iOS Adoption. StatCounter 1999-2024. Available online: https://gs.statcounter.com/os-version-market-share/ios/mobile-tablet/ worldwide (accessed on 14.07.2023).
31. Android Adoption. StatCounter 1999-2024. Available online: https://gs.statcounter.com/os-version-market-share/android/mobile-tablet/worldwide (accessed on 16.07.2023).
32. Woods, S. An introduction to maintenance costs for custom software. July 20, 2019. Available online: https://westarete.com/ insights/maintenance-costs-for-custom-software/ (accessed on 18.03.2020).
33. Firebase App Distribution. Google Inc. Available online: https://firebase.google.com/docs/app-distribution/get-set-up-as-a-tester?platform=android (accessed on 09.03.2023).
34. Google Play Store Fee Account. Google Inc. Available online: https://support.google.com/ googleplay/android-developer/answer/ 6112435?hl=en#zippy=%2Cstep-accept-the-developer-distribution-agreement%2Cstep-pay-registration-fee (accessed on 22.04.2023).

35. Buck, A. Android vs iOS Market Share: Most Popular Mobile OS in 2024. Available online: https://www.mobiloud.com/ blog/android-vs-ios-market-share (accessed on 08.09.2024).
36. IMNA Solutions. Available online: https://imnasol.com/ (accessed on 19.02.2022).
37. Securer. Available online: https://securer.io (accessed on 22.02.2021).
38. VentureRocket. Available online: https://venturerocket.network/ (accessed on 21.05.2021).

Citation: Nastas, V.; Bolun, I. Measuring the impact of mobile applications. *Journal of Engineering Science* 2024, XXXI (4), pp. 105-123. https://doi.org/10.52326/jes.utm.2024.31(3).01.

Submission of manuscripts: jes@meridian.utm.md

Journal of Engineering Science *Vol. XXXI, no. 4 (2024), pp. 124 - 141*
Fascicle *Electronics and Computer Science* *ISSN 2587-3474*
Topic *Computers and Information Technology* *eISSN 2587-3482*

https://doi.org/10.52326/jes.utm.2024.31(4).09
UDC 681.515:004.4:621.865.8

CASCADE CONTROL ALGORITHM OF THE ROBOTIC ARM'S SERVOMOTOR

Dumitru Moraru *, ORCID: 0000-0001-8957-6046,
Ion Fiodorov, ORCID: 0000-0003-0938-3442,
Bartolomeu Izvoreanu, ORCID: 0000-0001-9886-5878,
Irina Cojuhari, ORCID: 0000-0003-2248-1338

Technical University of Moldova, 168 Stefan cel Mare Blvd., Chisinau, Republic of Moldova
* Corresponding author: Dumitru Moraru, dumitru.moraru@ati.utm.md

Received: 12. 02. 2024
Accepted: 12. 28. 2024

Abstract. In this paper, there have been synthesized the control algorithms in cascade control systems. The control object is the robotic arm which is actuated by a servo motor presented as an automatic cascade control system which is consisting of two loops. The use of multiple loops is justified by the fact that with a single loop, only one parameter of the servo motor is controlled, which leads to a decrease in the reliability of the automatic system. A case study was carried out for a direct current electric motor, where proportional (P), proportional-integral (PI), and proportional-integral-derivative (PID) control algorithms were used, with P and PI applied to the inner loop, and P, PI, and PID to the outer loop. The system was simulated with the synthesized algorithms and the results were analyzed, it was established that the system has robustness and high performance for the case of using maximum stability degree method with iterations.

Keywords: *maximum stability degree method with iterations, proportional-integral-derivative controller, automatic control system, cascade control systems.*

Rezumat. În lucrare sunt sintetizați algoritmii din cadrul sistemelor de reglare în cascadă. Obiectul de reglare este brațul robotic acționat de un servomotor, prezentat ca un sistem automat de reglare în cascadă format din două bucle. Utilizarea mai multor bucle este argumentată de faptul că, într-un sistem cu o singură buclă, doar un singur parametru al servomotorului poate fi reglat, ceea ce duce la o scădere a fiabilității sistemului automat. A fost realizat un studiu de caz pentru un motor electric de curent continuu, unde au fost utilizați algoritmi de reglare proporțional (P), proporțional-integrativ (PI) și proporțional-integrativ-derivativ (PID), cu P și PI aplicate pentru bucla interioară și P, PI și PID pentru bucla exterioară. Sistemul a fost simulat utilizând algoritmii sintetizați, iar rezultatele au fost analizate, stabilindu-se că sistemul are robustețe și performanțe ridicate în cazul utilizării metodei gradului maxim de stabilitate cu iterații.

Cuvinte cheie: *metoda gradului maximal de stabilitate cu iterații, regulator proporțional-integrativ-derivativ, sistem de reglare automat, sistem de reglare în cascadă.*

1. Introduction

In recent decades, robots have passed a fast way in their evolution, one of the main stages being the emergence of soft (flexible) robots. For actions such as grasping and manipulating with objects, soft (flexible) robots realize much better with the passive adaptation required due to unpredictability and changing environmental conditions. In other words, while a rigid robot must be programmed in advance to capture an object, a soft robot can do it on its own due to passive adaptation [1-3].

Although soft robotics technology has evolved in terms of mobility, tactile perception is much more important for extending the manipulative capabilities of robots [4].

Tactile perception in robotics often faces problems of non-linearity, low receptor density and/or lack of modularity, which prevents the adoption of a single solution. Distributed data arrays obtained by tactile sensors address the low-density problem to some extent, but they are usually limited to flexible boards or soft sensors with strongly non-linear characteristics. Currently, the main challenge in this field lies in the development of sensor models that can provide high-precision information for closed-loop control [1-5].

At the same time, the perception of touching the object by the robot can be realized by following the parameters of the execution element, such as voltage, current of direct current (DC) motors, servomotors etc. [5-8].

The servomotor is a commonly used as actuator element in the construction of robotic arms due to its ability to provide precise positioning of the position of the arm or part of the robot. A servo motor is a type of electric motor specifically designed to provide precise positioning in a mechanical system. The field of use includes: robotic arms, robots, computer numerical control (CNC) machines, aircraft, automobiles, industrial equipment, medicine etc. [7, 8].

2. Problem formulation

Given the mathematical model of a DC servomotor with permanent magnets, it is described the second order with astatism transfer function [9-13]:

$$H_M(s) = \frac{k}{s(T_m T_e s^2 + T_m s + 1)}, \quad (1)$$

where: k is transfer coefficient, T_m – electromechanical time constant, T_e – electrical time constant.

In order to verify the hypothesis, that a single control loop of the servo output shaft angle is not enough, a DC motor model with known parameters was used:

Maximum rotor voltage $U_r = 6$ V.

Power $P = 0.46$ W.

Nominal rotations $n_n = 2850$ rpm.

Rotor current $I_r = 0.076$ A.

Engine torque $M_m = 0.0016$ Nm.

The active resistance of the rotor $R = 7.9$ Ω.

The moment of inertia of the motor $J_m = 0.91 \cdot 10^{-7}$ kgm^2.

The transfer coefficient k represents the rotor voltage - angular speed of the motor and is calculated based on the technical data by the expression:

$$k = \frac{1}{k_e} = \frac{n}{U_r - \alpha R I_r} = \frac{2850}{6 - 1.2 \cdot 7.9 \cdot 0.076} = 539.77 \text{ (rpm/V)}.$$

It is calculated the coefficient k_e by the relation:

$$k_e = \frac{1}{k} = \frac{1}{539.77} = 0.00185.$$

The electromechanical time constant is calculated according to the relationship:

$$T_m = \frac{1}{9.55}\frac{J\alpha R}{k_m k_e} = \frac{1}{9.55}\frac{0.91\cdot10^{-7}\cdot1.2\cdot7.9}{0.0176\cdot0.00185} = 0.00277 \text{ s.}$$

The coefficient k_m it is calculated by the expression:

$$k_m = \frac{k_e}{0.105} = \frac{0.00185}{0.105} = 0.0176.$$

Inductance with $\beta = 0.3$ and $p = 2$ poles it is calculated by the relations:

$$L = \frac{30}{\pi}\beta\frac{U_r}{pnI_R} = \frac{30}{3.14}0.3\frac{6}{2\cdot2850\cdot0.076} = 0.03969 \text{ H.}$$

The electrical time constant T_e is calculated by the relation:

$$T_e = \frac{L}{R} = \frac{0.03968}{7.9} = 0.00502 \text{ s.}$$

The coefficients are introduced in (1) and it is obtained the motor transfer function:

$$H_M(s) = \frac{k}{T_m T_e s^2 + T_m s + 1} = \frac{539.77}{0.00277\cdot0.00502 s^2 + 0.00277 s + 1} = \\ = \frac{539.77}{1.39\cdot10^{-5} s^2 + 0.00277 s + 1}.$$

In the motor coil the current changes according to the equivalent transfer function of a simple inductor [8]:

$$H_I(s) = \frac{U_{\text{int}}}{Ls + R} = \frac{4.5}{0.003968 s + 7.9}, \quad (2)$$

where: $H_I(s)$ is the transfer function of the current change in the motor coil (rotor), U_{int} – the voltage applied to the coil which must not exceed the maximum admissible voltage (6 V) for the supply, L – the inductance of the coil and R – the resistance of the coil.

Due to the fact that astatism is present in the system (which occurs because the rotations of the DC motor need to be converted into angular displacement) the P controller was chosen as a simple solution and closer to the real object that was tuned using parametric optimization.

As mentioned above, the motor supply voltage is 4.5 V, from this reason a saturation element with limits between -4.5 and +4.5 V was introduced in the structural block diagram of the system (Figure 1) [14].

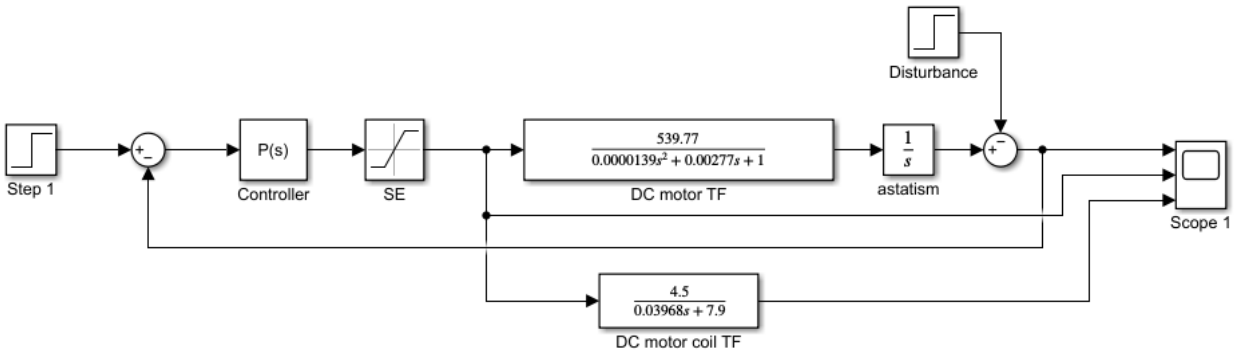

Figure 1. Structural block scheme of the automatic control system with one loop.

Figure 2 depicts the index step response of the automatic control system (curve 1), the voltage applied to the motor generated by the controller P (curve 2) and the variation of the current in the motor coil (curve 3).

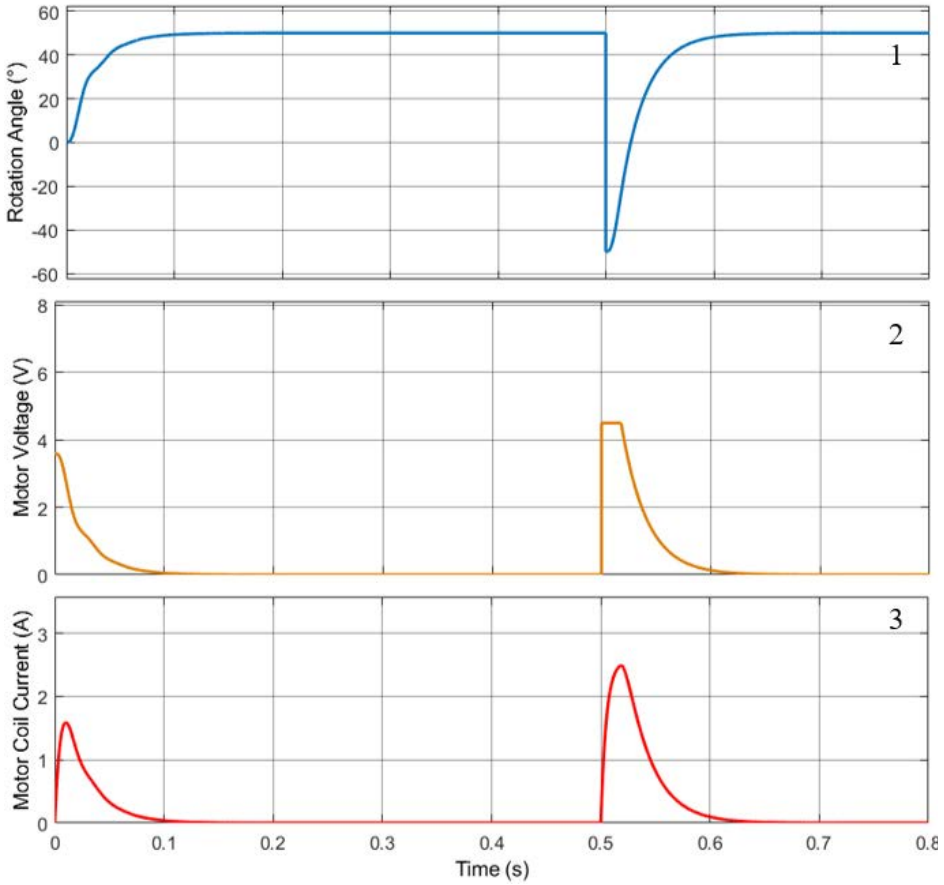

Figure 2. The response of the control system to the step signal with the application of the disturbance.

Analyzing the curves from Figure 2, can be observed that a sudden increase the current in the motor coil, both when the system is started and when the load disturbance is applied at 0.5 s from start-up. According to the technical data of the motor, the maximum current of the motor coil is 0.076 A, and on the transient process a peak of about 2 A is observed at system start-up and about 2.5 A at the moment of applying the disturbance, which is approximate 33 times greater the rated current. The duration for which the current exceeding the allowed limit is approximately 0.1 s for the case of applying the load disturbance, during which the power transistors fail to dissipate the amount of heat dissipate and often go out of commission, motor coils usually hold up because they have a greater ability to dissipate power on itself.

In order to make the control of the servomotors more efficient, the system with two loops is proposed to use. The inner loop performs the control of the motor coil current, and the outer loop control the rotation angle of the servo motor.

3. Synthesis automatic control algorithms for system with two control loops

Cascade control structures are used for control fast and slow processes with or without time delay. The presence of many time constants in the transfer function of the fixed part makes it difficult to use some typical control algorithms, which impose the compensation of these time constants, by control algorithms containing several first-degree binomials. There are given difficulties in the tuning of such control algorithms, taking into account the negative effect that derivative components have on the system response (amplification of

noises) it is recommended to use cascade control structures. The structural block scheme of the two-loop automatic control system with servomotor is represented in Figure 3 [15-23].

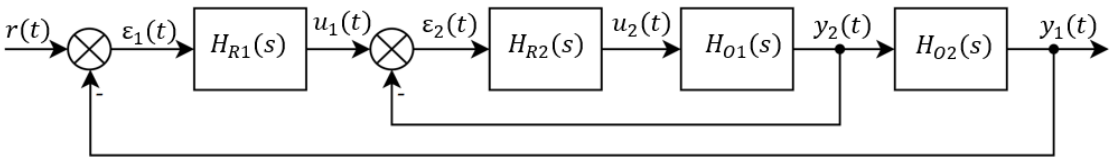

Figure 3. Structural block –scheme of the two-loop automatic control system.

Tuning the controllers in cascade control systems is done from the inner loop and then it is performed in the outer loop.

Figure 4 presents the structural block scheme of the DC motor for controlling the rotation angle.

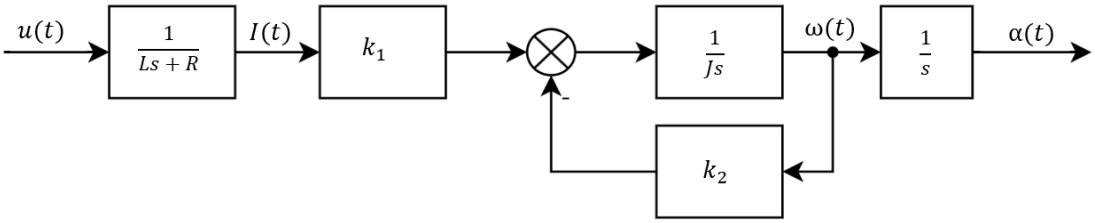

Figure 4. Structural block scheme of the DC motor.

In Figure 4, the following notations are used: $u(t)$ is the command signal (supply voltage), $\frac{1}{Ls+R}$ – the transfer function of the electromechanical component (coil) of the motor, k_1– the torque coefficient of the motor, $\frac{1}{Js}$ – the transfer function of the mechanical component of the engine, k_2 – the viscous friction force coefficient, $\omega(t)$ – the angular speed of the rotor and $\alpha(t)$ – the rotation angle of the rotor shaft.

According to the structural block scheme of the DC motor, the expressions for the parts $H_{01}(s)$ and $H_{02}(s)$ of the control object are following:

$$H_{01}(s) = \frac{k_2}{Ls+R} = \frac{539.77}{0.03968s+7.9}, \quad (3)$$

$$H_{02}(s) = \frac{\frac{1}{Js}}{1+\frac{1}{Js}k_3}\frac{1}{s} = \frac{1}{Js+k_3}\frac{1}{s} = \frac{1}{0.91\cdot10^{-7}s^2+0.002s}, \quad (4)$$

A. Tuning the controller in the inner loop

In the inner loop, it is recommended to use controllers with a simpler structure than in the outer one. Next, the synthesis of the P and PI controllers are presented according to the maximum stability degree method (MSD). PD and PID controllers cannot be tuned by the MSD method, because according to the methodology of the MSD method, the order of the characteristic equation of the closed loop system must be greater than or equal to the number of tuned parameters [24,25].

It is considered the inner loop represented in Figure 5.

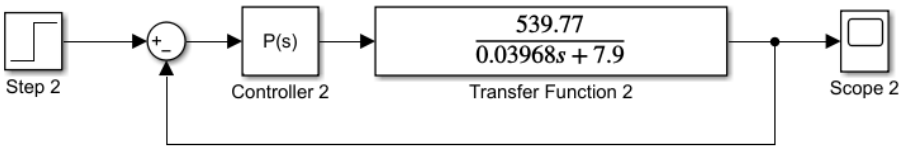

Figure 5. Structural block scheme of the inner loop.

The procedure of tuning P and PI controllers consists from following steps:

1. It is chosen one of the desired control laws.

2. The transfer function of the closed loop system with the chosen control algorithm is obtained.

3. The characteristic equation of the closed loop is obtained.

4. The substitution $p = -J$ in the characteristic equation is done.

5. Derivation on variable J of the characteristic equation from point 4 is performed a number of times equal to the number of tuning parameters.

6. From the equation obtained in point 5, its roots are determined, which represent the degrees of stability of the designed automatic system, and the value of the optimal degree J_{opt} is the smallest real root, or the real part of the complex root.

7. Using J_{opt} and the algebraic equations obtained in step 5, the parameter values of the chosen control laws are calculated.

8. The performance of the designed automatic control system is verified by computer simulation [24,25].

If the system performance is not satisfied by the analytical calculations, it is recommended to use the maximum stability degree method with iterations (MSDI), which consists in determining the analytical expressions of the tuning parameters, that depend on the object's parameters that are known and stability degree parameter, that is unknown and there are obtained the dependencies $k_p = f_p(J)$, $k_i = f_i(J)$.

At the variation of the stability degree J from for the P and PI control algorithms and the sets of values are chosen from the obtained curves of the tuning parameters P and I $J_i - k_{pi}$, k_{ii}. Next, the automatic control system with the chosen control algorithm is simulated on the computer and there are obtained the transient responses, after which the highest possible performance of the system is determined, which would satisfy the imposed performance of the automatic control system.

If the performances of the system are satisfied, the synthesis procedure is finished, or otherwise, the procedure starts from the beginning with another type of control law or another tuning method.

For the calculation of the tuning parameters of the typical P and PI controllers transfer function (3) is presented in a generalized form:

$$H_{01}(s) = \frac{539.77}{0.03968s+7.9} = \frac{k_2}{a_0 s+\mathrm{a}_1}, \tag{5}$$

where $k_2 = 539.77$ is transfer coefficient, and the generic coefficients of the control object are $a_0 = 0.03968$, that represents the time constant of the process and $a_1 = 7.9$.

Synthesis the P controller in the inner loop

The transfer function of inner closed loop with P controller is presented:

$$H_0 = \frac{H_R(s)H_{01}(s)}{1+H_R(s)H_{01}(s)} = \frac{k_{p2}k_2}{a_0 s+a_1+k_{p2}k} = \frac{B(s)}{A(s)}, \tag{6}$$

where k_{p2} is tuning parameter of the P controller.

The characteristic equation $A(s)$ of the inner loop is:

$$A(s) = a_0 s + a_1 + k_{p2}k = \frac{a_0 s+a_1}{k_2} + k_{p2} = 0. \tag{7}$$

According to the algorithm of maximum stability degree method, it is done the substitution $s=-J$ and it is obtained the expression:

$$A(-J) = \frac{-a_0 J + a_1}{k_2} + k_{p2} = 0. \quad (8)$$

For determining the tuning parameter of the P controller by the MSDI method from expression (8) it is obtained the relation:

$$k_{p2} = \frac{a_0 J - a_1}{k_2} = \frac{0.03968J - 7.9}{539.77}. \quad (9)$$

The variation of J from 0 to 300 means investigating the system's performance at different levels of stability. Figure 6 illustrates the dependency of P controller parameter k_{p2} on the stability degree J.

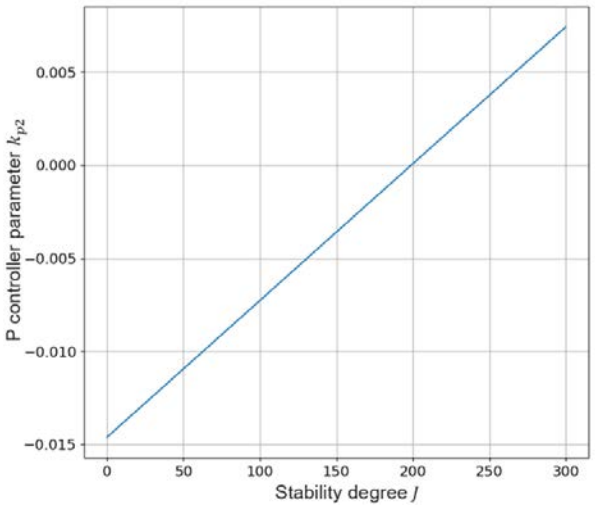

Figure 6. Dependence $\boldsymbol{k_{p2} = f_{p2}(J)}$.

From sets of obtained values $k_{p2} = f_{p2}(J)$, the values that provide the best performance for the automatic control system are selected. Figure 7 depict the transient responses of the system corresponding to different selected values of k_{p2}.

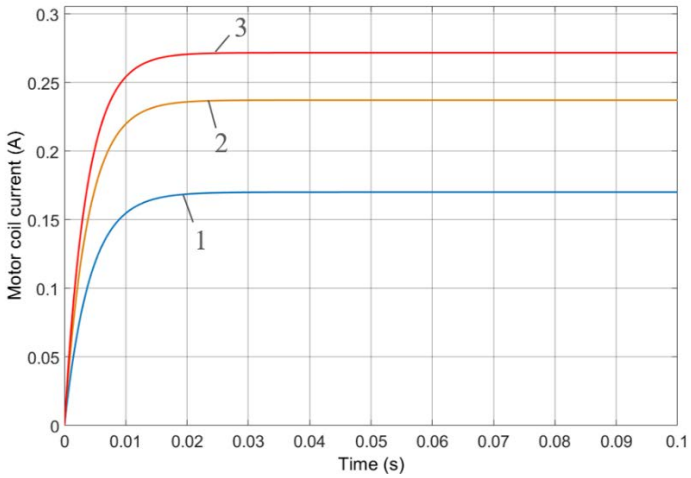

Figure 7. The step response of the inner loop with P controller.
Note: *the transient responses labeled 1, 2 and 3 correspond to the No. iter. listed in Table 1.*

In Table 1, there are presented the performances of the automatic control system of the DC motor coil current with P controller.

In the case of the P controller, the steady-state error is high, because P controller cannot be used in the inner loop.

Table 1

Tuning parameters and performances of the automatic control system with P controller

No. iter.	J	k_{p2}	t_r (s)	σ (%)	t_s (s)	n
1	240	0.003	0.0088	-	0.012	-
2	261	0.00455	0.0095	-	0.011	-
3	273.5	0.00546	0.0091	-	0.011	-

Note: J – stability degree, k_{p2} – P controller parameter, t_r – rise time, σ – overshoot, t_s – settling time, n – number of deviations from the set value.

Synthesis of the PI controller in the inner loop

It is determinate the transfer function of the inner loop with PI controller:

$$H_{0i} = \frac{H_R(s)H_{01}(s)}{1+H_R(s)H_{01}(s)} = \frac{(k_{p2}s+k_{i2})k_2}{a_0s^2+a_1s+(k_{p2}s+k_{i2})k_2} = \frac{B(s)}{A(s)}, \quad (10)$$

where k_{p2}, k_{i2} are tuning parameters of the PI controller.

The characteristic equation $A(s)$ of the system is following:

$$A(s) = s(a_0s + a_1) + (k_{p2}s + k_{i2})k_2 = \frac{a_0s^2+a_1s}{k_2} + k_{p2}s + k_{i2} = 0. \quad (11)$$

According to the algorithm of the MSDI method, it is done the substitution $s = -J$ in expression (11) and after some transformation it is obtained:

$$A(-J) = \frac{a_0J^2-a_1J}{k_2} - k_{p2}J + k_{i2} = 0. \quad (12)$$

In the case of using PI controller, it is necessary to derive equation (12) on the variable J once and there are obtained the expressions:

$$k_{p2} = \frac{2a_0J-a_1}{k_2} = \frac{0.07936J-7.9}{539.77}, \quad (13)$$

$$k_{i2} = \frac{-a_0J^2+a_1J}{k_2} + k_{p2}J = \frac{-0.03968J^2+7.9J}{539.77} + k_{p2}J. \quad (14)$$

At the variation the stability degree value J from 0 to 100, there are calculated and constructed the curves $k_{p2} = f_{p2}(J)$ și $k_{i2} = f_{i2}(J)$ for control algorithm PI (Figure 8).

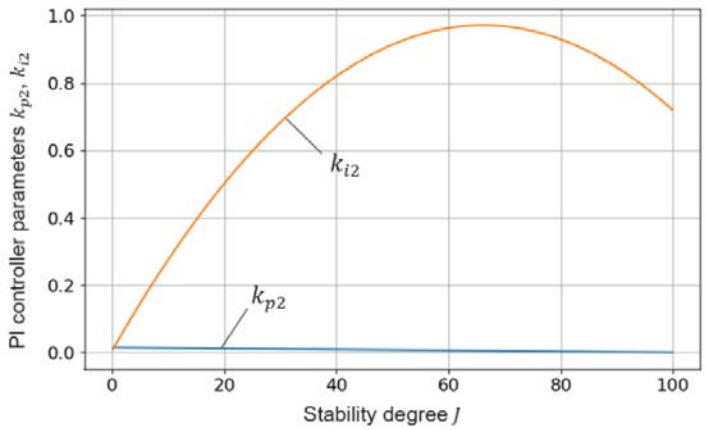

Figure 8. Dependencies $k_{p2} = f_{p2}(J)$ and $k_{i2} = f_{i2}(J)$.

In the Figure 9, there are presented the transient responses of the system for the different values of the k_{p2} and k_{i2}.

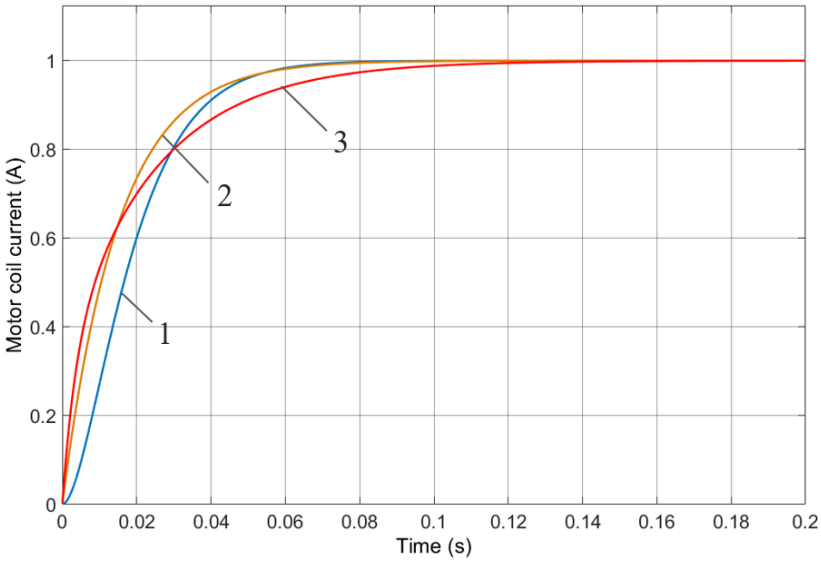

Figure 9. The step response of the inner loop with PI controller.
Note: *the transient responses labeled 1, 2 and 3 correspond to the No. iter. listed in Table 2.*

In Table 2, there are presented the performances of the automatic current control system of the DC motor with PI controller.

In the case of use the PI controller in the inner loop, there are obtained the good performances and the best was obtained for the 3rd iteration from Table 2.

Table 2

Tuning parameters and performances of the automatic control system with PI controller

No. iter.	J	k_{p2}	k_{i2}	T_{i2} (s)	t_r (s)	σ (%)	t_s (s)	n
1	40.5	0.00868	0.8237	1.214	0.041	-	0.047	-
2	66.3	0.00489	0.9713	1.029	0.043	-	0.045	-
3	98.7	0.00012	0.7407	1.35	0.063	-	0.064	-

Note: J – stability degree, k_{p2} – P controller parameter, k_{i2} – I controller parameter, T_{i2} – oscillation period of the I component of controller, t_r – rise time, σ – overshoot, t_s – settling time, n – number of deviations from the set value.

B. Tuning controller in the outer loop

For tuning the controller in the outer loop, it is necessary to calculate the transfer function of the fixed part, which is the product of the transfer function of the closed system $H_0(s)$ from the inner loop $H_{0i}(s)$ and the transfer function of the mechanical component $H_{02}(s)$ of the DC motor. In the inner loop, the PI controller will be used because, following its tuning, the best results were obtained (Table 2, iteration 3).

$$H_0(s) = H_{0i}(s)H_{02}(s) = \frac{(k_{p2}s+k_{i2})k_2}{a_0s^2+a_1s+(k_{p2}s+k_{i2})k_2}\frac{1}{a_2s^2+a_3s} = \frac{c_0s+c_1}{d_0s^4+d_1s^3+d_2s^2+d_3s}, \quad (15)$$

where $c_0 = k_2k_{p2} = 3.9996$, $c_1 = k_2k_{i2} = 892.77$, $d_0 = a_0a_2 = 3{,}61 \cdot 10^{-9}$, $d_1 = a_0a_3 + a_1a_2 + a_2k_{p2}k_2 = 8.044 \cdot 10^{-5}$, $d_2 = a_1a_3 + a_2k_{i2}k_2 + a_3k_{p2}k_2 = 0.0328$ and $d_3 = a_3k_{i2}k_2 = 1.7855$.

The mathematical model of the control object is with advance first-order, inertia third order and astatism. The structural block scheme of the outer loop of the automatic control system is presented in Figure 10.

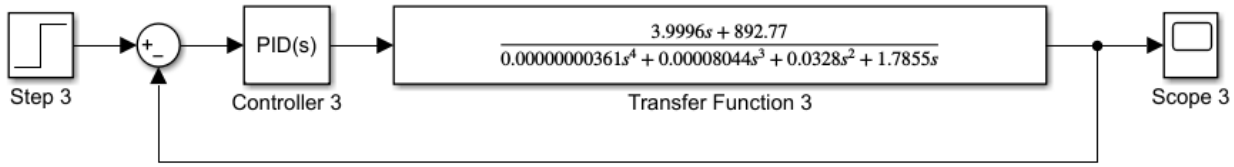

Figure 10. Structural block scheme of the outer loop.

The transfer function of the closed loop system is presented in the following form:

$$H_0(s) = \frac{H_d(s)}{1+H_d(s)} = \frac{H_R(s)H_{PF}(s)}{1+H_R(s)H_{PF}(s)} = \frac{H_R(s)(c_0s+c_1)}{d_0s^4+d_1s^3+d_2s^2+d_3s+H_R(s)(c_0s+c_1)} = \frac{B(s)}{A(s)}, \quad (16)$$

where $H_d(s) = H_R(s)H_{PF}(s)$ is the transfer function of the open loop system, $H_R(s)$ – transfer function of the controller, where $A(s)$ and $B(s)$ – the system polynomials.

Next, it is presented the procedures for tuning P, PI and PID controllers to the model of object (15).

Synthesis of the P controller in the outer loop

The characteristic equation $A(s)$ of the automatic control system is:

$$A(s) = d_0s^4 + d_1s^3 + d_2s^2 + d_3s + k_{p1}(c_0s + c_1) = 0, \quad (17)$$

where k_{p1} is a tuning parameter of P controller.

According to the algorithm of the MSDI method, it is done the substitution $s = -J$ and after some transformation it is obtained:

$$A(-J) = \frac{d_0J^4-d_1J^3+d_2J^2-d_3J}{c_1-c_0J} + k_{p1} = 0. \quad (18)$$

In the case of using P controller, it is necessary to derive equation (18) on the variable J once and the following expression is obtained:

$$\dot{D}(-J) = \frac{-3d_0c_0J^4+J^3(4d_0c_1+2d_1c_0)-J^2(3d_1c_1+d_2c_0)+2d_2c_1J-d_3c_1}{(c_1-c_0J)^2} = 0. \quad (19)$$

The value of the stability degree J_{opt} is the smallest positive root of the equation:

$$-3d_0c_0J^4 + J^3(4d_0c_1 + 2d_1c_0) - J^2(3d_1c_1 + d_2c_0) + 2d_2c_1J - d_3c_1 = 0. \quad (20)$$

For determination the tuning parameter of P controller from expression (18) there is used the following relationship:

$$k_{p1} = \frac{-d_0J^4+d_1J^3-d_2J^2+d_3J}{c_1-c_0J} = \frac{3.61\cdot10^{-9}J^4+8.044\cdot10^{-5}J^3-0.0328J^2+1.7855J}{892.77-3.9996J}. \quad (21)$$

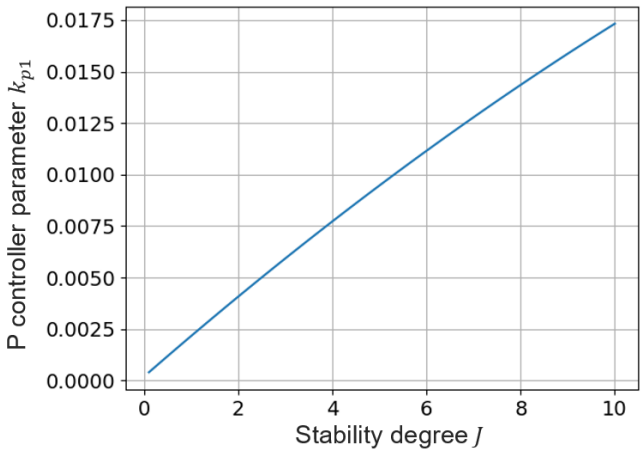

Figure 11. Dependence $\boldsymbol{k_{p1} = f_{p1}(J)}$.

At the variation the stability degree J from 0 to 10, there are calculated and constructed the curves $k_{p1} = f_{p1}(J)$ for the P control algorithm (Figure 11).

In Figure 12, the transient responses of the automatic control system with a P controller in the outer loop are presented for different values of k_{p1}, showing the rotation angle of the servomotor's output shaft.

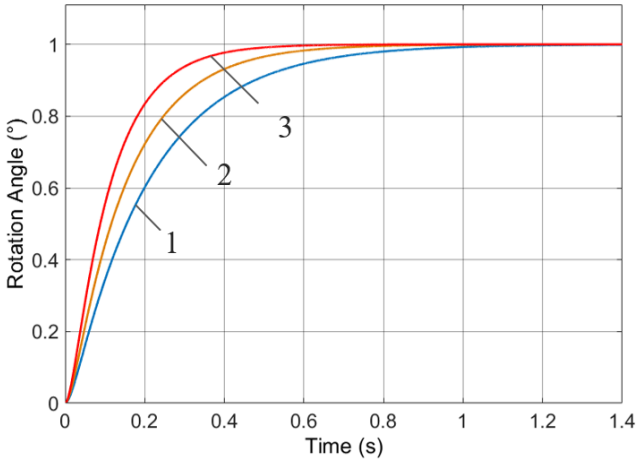

Figure 12. The step response of the outer loop with P controller

Note: *the transient responses labeled 1, 2 and 3 correspond to the No. iter. listed in Table 3.*

Table 3 represents the performance of the automatic control system for controlling the angle of rotation of the servomotor's output shaft with a P controller.

Table 3

Tuning parameters and performances of the automatic control system with P controller

No. iter.	J	k_{p1}	t_r (s)	σ (%)	t_s (s)	n
1	5.0	0.0093	0.579	-	0.615	-
2	7.0	0.0126	0.417	-	0.447	-
3	10.0	0.0175	0.297	-	0.321	-

Note: J – stability degree, k_{p1} – P controller parameter, t_r – rise time, σ – overshoot, t_s – settling time, n – number of deviations from the set value.

In the case of the system with P controller in the outer loop, there are obtained the good performances, due to the astatism existing in the object, and the steady-state error is zero (Table 3, iteration 3).

Synthesis of the PI controller in the outer loop

The characteristic equation $A(s)$ of the automatic control system with PI controller is following:

$$A(s) = d_0 s^5 + d_1 s^4 + d_2 s^3 + d_3 s^2 + (k_{p1} s + k_{i1})(c_0 s + c_1) = 0, \quad (22)$$

where k_{p1}, k_{i1} are tuning parameters of PI controller.

According to the algorithm of the MSDI method, it is done the substitution $s = -J$ and after some transformation it is obtained:

$$A(-J) = \frac{-d_0 J^5 + d_1 J^4 - d_2 J^3 + d_3 J^2}{c_1 - c_0 J} - k_{p1} J + k_{i1} = 0. \quad (23)$$

In the case of using PI controller, it is necessary to derive equation (23) on the variable J twise and it is obtained the expression:

$$\ddot{A}(-J) = \frac{d_0J^6 - d_1J^5 + d_2J^4 - d_3J^3 + d_4J^2 - d_5J + d_6}{(c_1 - c_0J)^4} = 0, \quad (24)$$

where: $d_0 = 12d_0c_0^3$, $d_1 = 42d_0c_0^2c_1 + 6d_1c_0^3$, $d_2 = 50d_0c_0c_1^2 + 22d_1c_0^2c_1 + 2d_2c_0^3$, $d_3 = 20d_0c_1^3 + 28d_1c_0c_1^2 + 8d_2c_0^2c_1$, $d_4 = 12d_1c_1^3 + 12d_2c_0c_1^2$, $d_5 = 6d_2c_1^3 + 2d_3c_0c_1^2$, $d_6 = 2d_3c_1^3$.

The value of the stability degree J_{opt} is the smallest positive root of the equation:

$$d_0J^6 - d_1J^5 + d_2J^4 - d_3J^3 + d_4J^2 - d_5J + d_6 = 0. \quad (25)$$

For determining the tuning parameters of the PI controller there are used the following relationships:

$$k_{p1} = \frac{4d_0c_0J^5 - J^4(5d_0c_1 + 3d_1c_0) + J^3(4d_1c_1 + 2d_2c_0) - J^2(3d_2c_1 + d_3c_0) + 2d_3c_1J}{(c_1 - c_0J)^2} =$$
$$= \frac{5.77 \cdot 10^{-8}J^5 - 0.000981J^4 + 0.4783J^3 - 71.1021J^2 + 3188.2215J}{(892.77 - 3.9996J)^2}, \quad (26)$$

$$k_{i1} = \frac{d_0J^5 - d_1J^4 + d_2J^3 - d_3J^2}{c_1 - c_0J} + k_{p1}J =$$
$$= \frac{3.61 \cdot 10^{-9}J^5 - 8.044 \cdot 10^{-5}J^4 + 0.0328J^3 - 1.7855J^2}{892.77 - 3.9996J} + k_{p1}J. \quad (27)$$

At the variation the stability degree J from 0 to 10, there are calculated and constructed the curves $k_{p1} = f_{p1}(J)$ and $k_{i1} = f_{i1}(J)$ for the PI control algorithm (Figure 13).

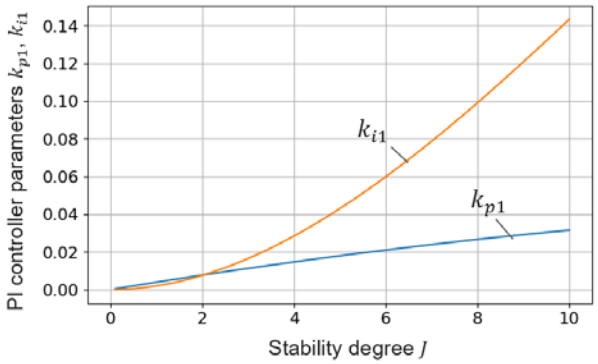

Figure 13. Dependence $\boldsymbol{k_{p1} = f_{p1}(J)}$ and $\boldsymbol{k_{i1} = f_{i1}(J)}$.

In Figure 14 are presented the transient responses of the automatic control system for the different values of k_{p1} and k_{i1}.

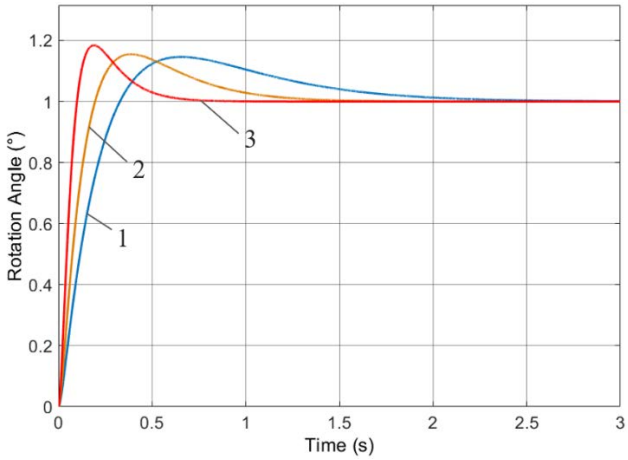

Figure 14. Transient response of the automatic control system with PI controller.

Note: *the transient responses labeled 1, 2 and 3 correspond to the No. iter. listed in Table 4.*

In Table 4 are presented the performance of the automatic control system for controlling the angle of rotation of the servo motor with a PI controller.

Table 4

Tuning parameters and performances of the automatic control system with PI controller

No. iter.	J	k_{p1}	k_{i1}	T_{i1} (s)	t_r (s)	σ (%)	t_s (s)	n
1	3.0	0.01152	0.017	58.82	0.26	14.5	1.4	1
2	5.0	0.01867	0.0455	21.97	0.154	15.4	0.849	1
3	10.0	0.0347	0.1647	6.071	0.075	18.4	0.434	1

Note: J – stability degree, k_{p1} – P controller parameter, k_{i1} – I controller parameter, T_{i1} – oscillation period of the I component of controller, t_r – rise time, σ – overshoot, t_s – settling time, n – number of deviations from the set value.

In the case of the automatic control system with the PI controller in the outer loop, there are obtained the transient processes with overshoot, because of the presence of the astatism component in the system. The best performances were obtained for the 3rd iteration from Table 4.

Synthesis of the PID controller in the outer loop

The characteristic equation $A(s)$ of the automatic control system with PID controller is following:

$$A(s) = d_0 s^5 + d_1 s^4 + d_2 s^3 + d_3 s^2 + (k_{d1} s^2 + k_{p1} s + k_{i1})(c_0 s + c_1) = 0, \quad (28)$$

where k_{p1}, k_{i1}, k_{d1} are tuning parameters of PID controller.

According to the algorithm of the MSDI method, it is done the substitution $s = -J$ and after some transformation it is obtained:

$$A(-J) = \frac{-d_0 J^5 + d_1 J^4 - d_2 J^3 + d_3 J^2}{c_1 - c_0 J} + k_{d1} J^2 - k_{p1} J + k_{i1} = 0. \quad (29)$$

In the case of PID controller it is necessary to derive the expression (29) on the variable J by the three times and there is obtained the following expression:

$$\dddot{A}(-J) = \frac{dJ^9 - \mathrm{d}J^8 + d_2 J^7 - d_3 J^6 + d_4 J^5 - d_5 J^4 + d_6 J^3 - d_7 J^2 + d_8 J - d_9}{(c_1 - \mathrm{c}_0 J)^8} = 0, \quad (30)$$

where $d_0 = 24 d_0 c_0^7$, $d_1 = 186 d_0 c_0^6 c_1 + 6 d_1 c_0^7, d_2 = 624 d_0 c_0^5 c_1^2 + 48 d_1 c_0^6 c_1$, $d_3 = = 1176 d_0 c_0^4 c_1^3 + 168 d_1 c_0^5 c_1^2$, $d_4 = 1344 d_0 c_0^3 c_1^4 + 336 d_1 c_0^4 c_1^3$, $d_5 = 930 d_0 c_0^2 c_1^5 + +414 d_1 c_0^3 c_1^4 + 6 d_2 c_0^4 c_1^3 - 6 d_3 c_0^5 c_1^2$, $d_6 = 360 d_0 c_0 c_1^6 + 312 d_1 c_0^2 c_1^5 + 24 d_2 c_0^3 c_1^4 - 24 d_3 c_0^4 c_1^3$, $d_7 = 60 d_0 c_1^7 + 132 d_1 c_0 c_1^6 + 36 d_2 c_0^2 c_1^5 - 36 d_3 c_0^3 c_1^4$, $d_8 = 24 d_1 c_1^7 + 24 d_2 c_0 c_1^6 - 24 d_3 c_0^2 c_1^5$, $d_9 = 6 d_2 c_1^7 - 6 d_3 c_0 c_1^6$.

The optimal value of stability degree J_{opt} is the smallest positive root of the expression:

$$d_0 J^9 - \mathrm{d}_1 J^8 + d_2 J^7 - d_3 J^6 + d_4 J^5 - d_5 J^4 + d_6 J^3 - d_7 J^2 + d_8 J - d_9 = 0. \quad (31)$$

For the calculation tuning parameters of the PID controller there are used the relations:

$$k_p = \frac{4 d_0 c_0 J^5 - J^4 (5 d_0 c_1 + 3 d_1 c_0) + J^3 (4 d_1 c_1 + 2 d_2 c_0) - J^2 (3 d_2 c_1 + d_3 c_0) + 2 d_3 c_1 J}{(c_1 - \mathrm{c}_0 J)^2} + 2 k_{d1} J, \quad (32)$$

$$k_i = \frac{d_0 J^5 - d_1 J^4 + d_2 J^3 - d_3 J^2}{c_1 - c_0 J} - k_{d1} J^2 + k_{p1} J, \quad (33)$$

$$k_d = \frac{-g_0 J^6 + g_1 J^5 - g_2 J^4 + g_3 J^3 - g_4 J^2 + g_5 J - g_6}{2(c_1 - c_0 J)^4}, \quad (34)$$

where $g_0 = 12d_0c_0^3$, $g_1 = 42d_0c_0^2c_1 + 6d_1c_0^3$, $g_2 = 50d_0c_0c_1^2 + 22d_1c_0^2c_1 + 2d_2c_0^3$, $g_3 = 20d_0c_1^3 + 28d_1c_0c_1^2 + 8d_2c_0^2c_1$, $g_4 = 12d_1c_1^3 + 12d_2c_0c_1^2$, $g_5 = 6d_2c_1^3 + 2d_3c_0c_1^2$, $g_6 = 2d_3c_1^3$.

At the variation the stability degree value J from 0 to 50, there are calculated and constructed the curves $k_{p1} = f_{p1}(J)$ and $k_{d1} = f_{d1}(J)$ for control algorithm PID (Figure 15).

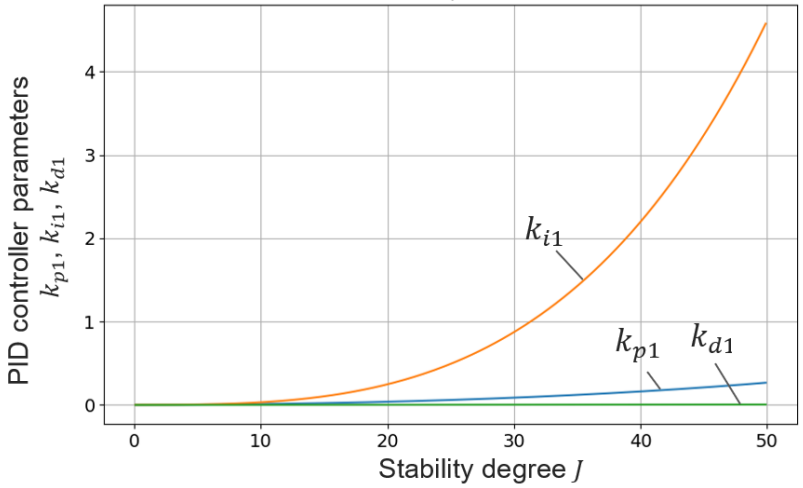

Figure 15. Dependencies $\boldsymbol{k_{p1} = f_{p1}(J)}$, $\boldsymbol{k_{i1} = f_{i1}(J)}$ and $\boldsymbol{k_{d1} = f_{d1}(J)}$.

In the Figure 16 there are presented the transient responses of the automatic control system for the different values of the tuning parameters k_{p1}, k_{i1} and k_{d1}.

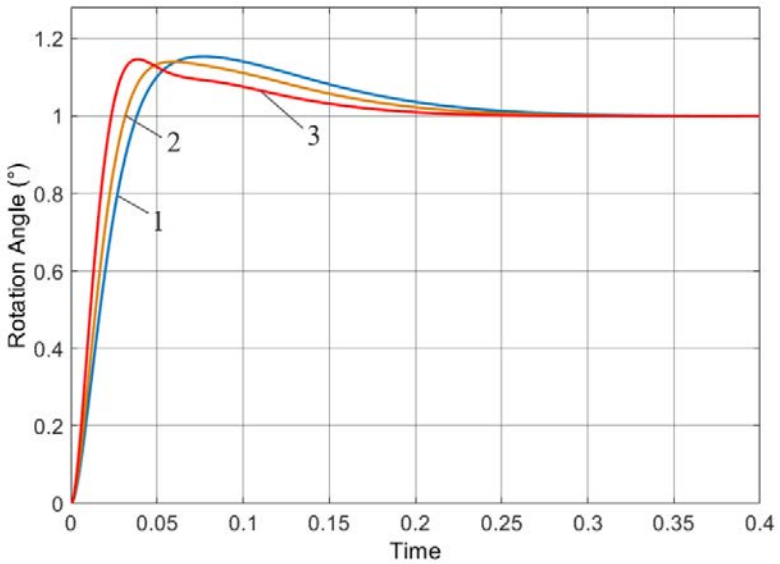

Figure 16. Transient responses of the automatic control system with PID controller.
Note: *the transient responses labeled 1, 2 and 3 correspond to the No. iter. listed in Table 5.*

In Table 5 there are presented the performances of the automatic servo motor rotation angle control system with the PID controller.

For the system with the PID controller in the outer loop, the best performances are presented in Table 5, iteration 3.

Table 5

Tuning parameters and performances of the automatic control system with PID controller

No. iter.	J	k_{p1}	k_{i1}	T_{i1} (s)	k_{d1} (s)	t_r (s)	σ (%)	t_s (s)	n
1	31.8	0.096	1.0387	0.962	0.00092	0.029	15.2	0.182	1
2	34.8	0.1171	1.3865	0.721	0.00123	0.024	14.0	0.158	1
3	40.0	0.1593	2.178	0.459	0.0018	0.017	14.6	0.126	1

Note: J – stability degree, k_{p1} – P controller parameter, k_{i1} – I controller parameter, T_{i1} – oscillation period of the I component of controller, k_{d1} – I controller parameter, t_r – rise time, σ – overshoot, t_s – settling time, n – number of deviations from the set value.

Tuning the controller in the outer loop using the polynomial method

In order to gain a better understanding of the results obtained from tuning the controller using the maximum stability degree method, the polynomial method was used in the outer loop of the DC motor drive system. The synthesis procedure of the control algorithm is reduced to the following steps:

1. The damping ratio is specified $\xi = 0.707$ and the settling time $t_r = 1$ s, and the natural frequency of the outer loop is determined using the following relation:

$$\omega = \frac{4}{\xi t_r} = \frac{4}{0.707 \cdot 1} = 5.658 \text{ s}^{-1}. \quad (35)$$

2. The dominant poles of the outer loop are determined using the following relation:

$$p_{1,2} = -\xi\omega \pm j\omega\sqrt{1-\xi^2} = -4 \pm j4. \quad (36)$$

3. According to the polynomial method, the transfer function of the fixed part (15) of degree $n = 4$ of the outer loop is represented in the form:

$$H_0(s) = \frac{c_0 s + c_1}{d_0 s^4 + d_1 s^3 + d_2 s^2 + d_3 s} = \frac{c_0 s + c_1}{s(d_0 s^3 + d_1 s^2 + d_2 s + d_3)} = \frac{C^-(s)C^+(s)}{D^-(s)D^+(s)}, \quad (37)$$

where: $C^-(s) = c_0 s + c_1$, $C^+(s) = 1$, $D^-(s) = d_0 s^3 + d_1 s^2 + d_2 s + d_3$, $D^+(s) = s$ and we denote the degrees of the respective polynomials: $n_{C^-} = 1$, $n_{C^+} = 0$, $n_{D^-} = 3$, $n_{D^+} = 1$.

4. The desired characteristic polynomial is constructed using the following relation:

$$P_d(s) = C^+(s)M(s) + D^+(s)N(s)s^r, \quad (38)$$

where: $M(s)$ and $N(s)$ are unknown polynomials that will be determined, and the component s^r introduces astatism (in this case, the degree of astatism is $r = 0$ because the astatism is contained in the fixed part).

The degrees of the polynomials are denoted $P_d(s)$, $M(s)$ and $N(s)$ n_P, n_M, n_N. The coefficients of the polynomials $M(s)$ and $N(s)$ are determined from the system of algebraic equations, which are obtained by equating the coefficients of the same powers on both sides of the polynomial equation (38).

5. The degree of the characteristic polynomial is determined $P_d(s)$ from the condition $n_P == n = 4$. For a simpler implementation of the control algorithm, the smallest values of the degrees n_M, n_N of the unknown polynomials are determined. It is assumed $n_M = 0$ and the degree of n_N is determined from the conditions:

$$n_P \leq n_M + n_N + 1, n_N = n_P - n_M - 1 = 4 - 0 - 1 = 3 \quad (39)$$

and to satisfy these conditions, the values of the unknown degrees are obtained $n_M = 0$ $n_N = 3$. The unknown polynomials are presented in the form:

$$M(s) = m_0, N(s) = n_0 s^3 + n_1 s^2 + n_2 s + n_3. \quad (40)$$

6. The desired characteristic polynomial of the outer loop is constructed using the following relation:

$$P_d(s) = C^+(s)M(s) + D^+(s)N(s) = 1 \cdot m_0 + s(n_0 s^3 + n_1 s^2 + n_2 s + n_3) = \\ = n_0 s^4 + n_1 s^3 + n_2 s^2 + n_3 s + m_0. \quad (41)$$

7. The characteristic polynomial of degree $n = 4$ is constructed based on the dominant poles:

$$P_{dd}(s) = (s + 4 - j4)(s + 4 - j4)(s + 30)^2 = s^4 + 68s^2 + +1412s + 9120s + 28800.$$

8. The polynomials $P_d(s) = P_{dd}(s)$ are equated, and the system of algebraic equations is constructed by equating the coefficients of the same powers of s on both sides:

$$n_0 s^4 + n_1 s^3 + n_2 s^2 + n_3 s + m_0 = s^4 + 68s^2 + +1412s + 9120s + 28800, \\ n_0 = 1, n_1 = 68, n_2 = 1412, n_3 = 9120, m_0 = 28800.$$

9. The transfer function of the controller is constructed using the following relation:

$$H_R(s) = \frac{Q(s)}{P(s)} = \frac{D^-(s)M(s)}{C^-(s)N(s)} = \frac{(d_0 s^3 + d_1 s^2 + d_2 s + d_3)m_0}{(c_0 s + c_1)(n_0 s^3 + n_1 s^2 + n_2 s + m_0)} = \frac{q_0 s^3 + q_1 s^2 + q_2 s + q_3}{p_0 s^4 + p_1 s^3 + p_2 s^2 + p_3 s + p_4} = \\ = \frac{0.000104 s^3 + 2.3167 s^2 + 944.64 s + 51422.4}{3.9996 s^4 + 1164.7428 s^3 + 66355.7952 s^2 + 1297067.592 s + 8142062.4}. \quad (42)$$

In Figure 17 are presented the transient responses of the automatic control system tuned using the polynomial method.

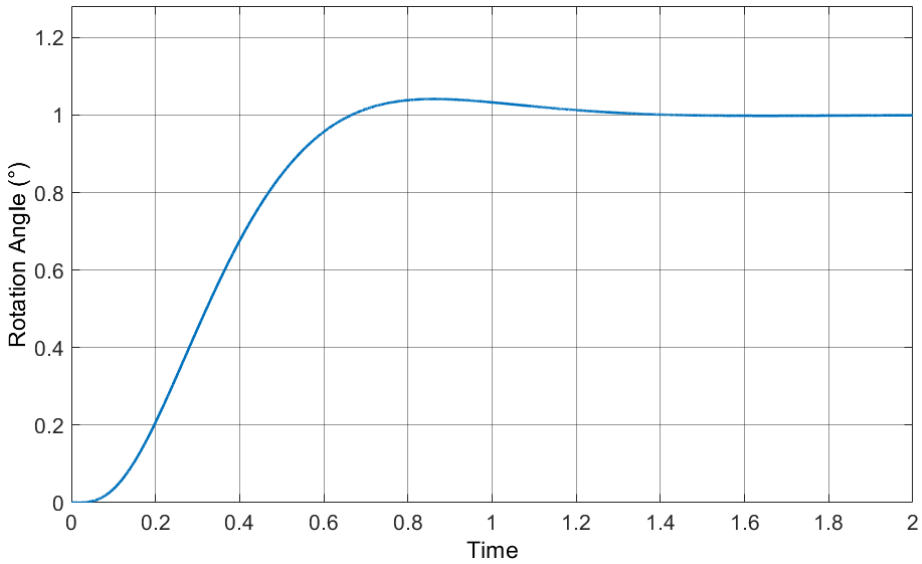

Figure 17. Transient response of the automatic control system tuned using the polynomial method.

As a result of the simulation, the following system performance was recorded: rise time $t_r = 0.58$ s, overshoot $d = 6.30$ %, settling time $t_s = 0.58$ s. and deviations $n = 1$ s.

4. Conclusions

This study demonstrated the design and implementation of a cascade control system for a DC servomotor used in robotic arm applications. The research focused on tuning and optimizing controllers for both the inner and outer control loops, using methods such as the Maximum Stability Degree with Iterations and the Polynomial method.

The proportional controller in the outer loop, combined with the inner loop P controller, exhibited the best overall performance in terms of rise time ($t_r = 0.297$) and settling time ($t_s = 0.321$ s). This configuration proved particularly effective for systems with astatism, offering rapid, and robust responses to both reference and disturbance signals.

The inner loop's performance with a PI controller demonstrated significant improvement in transient behavior, achieving better system stability and reduced steady-state error compared to the P controller.

The outer loop's use of PI and PID controllers achieved satisfactory results but introduced overshoots in transient responses due to the inherent characteristics of the system. Despite this, the PID controller yielded the most accurate positioning, making it suitable for applications requiring high precision.

The polynomial method was successfully applied to tune the controller in the outer loop, providing enhanced accuracy in system performance. This method offered flexibility in adjusting system dynamics, ensuring precise tuning for desired response characteristics.

The research highlights the practical benefits of implementing a cascade control system in robotic applications, demonstrating its ability to reject disturbances effectively. Although the current two-loop control system provides satisfactory performance in terms of stability and response time, further improvements can be achieved by introducing a third control loop to regulate the rotational speed of the motor. This additional loop would allow the output shaft angle of the servomotor to change at different speeds and minimize speed fluctuations caused by external disturbances or load variations.

Acknowledgments: This work was supported by the subproject 02.04.04 „Innovations in Biomedical Engineering: Advanced Technologies and Applications for Data Acquisition, Processing, and Analysis".

Conflicts of Interest: The authors declare no conflict of interest.

References

1. Wang, Y.; Wang, Y.; Mushtaq, R.; Wei, Q. Advancements in Soft Robotics: A Comprehensive Review on Actuation Methods, Materials, and Applications. *Polymers* 2024, 16(8), 1087.
2. Kim, S.; Laschi, C.; Trimmer, B. Soft robotics: a bioinspired evolution in robotics. *Trends Biotechnol*. 2013, 31(5), pp. 287-294.
3. Rus, D.; Tolley, M. T. Design, fabrication and control of soft robots. *Nature* 2015, 521, pp. 467-475.
4. Stavridis, S.; Falco, P.; Doulgeri, Z. Pick-and-place in dynamic environments with a mobile dual-arm robot equipped with distributed distance sensors. In: *IEEE-RAS 20th International Conference on Humanoid Robots (Humanoids)*. 2021, Munich, Germany, 19-21 July 2021.
5. Navarro, S.E.; Mühlbacher-Karrer, S.; Alagi, H.; Zangl, H.; Koyama, K.; Hein, B.; Duriez, C.; Smith, J. R. Proximity Perception in Human-Centered Robotics: A Survey on Sensing Systems and Applications. *IEEE Transactions on Robotics* 2022, 38(3), pp. 1599-1620.
6. Xie, D.; Chen, L.; Liu, L.; Chen, L.; Wang, H. Actuators and Sensors for Application in Agricultural Robots: A Review. *Machines* 2022, 10, 913.
7. Boussaada, D.; Chen, J.; Bonnet, C.; Niculescu, S.I.; Chen, J. PID control design for first-order delay systems via MID pole placement: Performance vs. robustness. *Automatica* 2022, 137, pp. 110-102.
8. Tarczewski, T.; Skiwski, M.; Niewiara, L.J.; Grzesiak, L.M. High-performance PMSM servo-drive with constrained state feedback position controller. *Bulletin of the polish academy of sciences technical sciences* 2018, 66(1), pp. 49-58.
9. Izvoreanu, B. The Iterative Algorithm of Tuning Controllers to the Model Object with Advance Delay and Inertia Second Order. In: *Proceedings of the 10-th International Conference on Development and Application Systems DAS-2010*. 22-24 May 2010, Suceava. pp. 111-115.
10. Kim, D. P. *Teoria avtomaticheskogo upravlenia*. T. 1. *Lineinye sistemy*. Fizmatlit, Moscow, 2003, 288 p.
11. Ким, D. P.; Dmitrieva, N. D. *Sbornik zadach po teorii avtomaticheskogo upravlenia. Lineinye sistemy*. Fizmatlit, Moskva, 2007, 167 p.

12. Izvoreanu, B. *Automation Systems Engineering. Course material.* Technique-TUM, Chisinau, RM, 2024, 337 p. [in Romanian].
13. Electrical4u: *RL circuit transfer function time constant*, © 2024 (accessed 05.06.2024). Available online: https://www.electrical4u.com/rl-circuit-transfer-function-time-constant-rl-circuit-as-filter/. (accessed on 02.11.2024).
14. Isd-Soft: *Tuning a PID regulator.* © 2023 (accessed 02.06.2024). Available online: https://isd-soft.com/tech_blog/tuning-pid-regulator/ (accessed on 05.11.2024).
15. Dumitrache, I. *Automatic control engineering.* Politehnica Press, Bucharest, Romania, 2016, 407 p. [in Romanian].
16. Ahmed, A.S.; Marzog, H.A.; Abdul-Rahaim, L. A. Design and implement of robotic arm and control of moving via IoT with Arduino ESP32. *International Journal of Electrical & Computer Engineering* 2021 11(5), pp. 101-110.
17. Mhawesh, M.A. Performance comparison between variants PID controllers and unity feedback control system for the response of the angular position of the DC motor. *International Journal of Electrical and Computer Engineering* 2021, 11(1), pp. 802-814.
18. Dewi, T.; Nurmaini, S.; Risma, P.; Oktarina, Y.; Roriz, M. Inverse kinematic analysis of 4 DOF pick and place arm robot manipulator using fuzzy logic controller. *International Journal of Electrical &Computer Engineering* 2020, 10(2), pp. 1376-1378.
19. Borase, R.P.; Maghade, D.K.; Sondkar, S.Y.; Pawar, S.N. A review of PID control, tuning methods and applications. *International Journal of Dynamics and Control* 2021, 9, pp. 818–827.
20. Chotikunnan, P.; Chotikunnan, R. Dual Design PID Controller for Robotic Manipulator Application. *Journal of Robotics and Control* 2023, 4(1), pp. 23-34.
21. Ma'arif, A.; Setiawan, N. R. Control of DC motor using integral state feedback and comparison with PID: simulation and Arduino implementation. *Journal of Robotics and Control (JRC)* 2021, 2(5), pp. 456-461.
22. Koca, Y.B.; Aslan, Y.; Gökçe, B. Speed Control Based PID Configuration of a DC Motor for An Unmanned Agricultural Vehicle. In: *8th International Conference on Electrical and Electronics Engineering (ICEEE)*. Antalya, Turkey, 09-11 April 2021. pp. 117-120.
23. Ramadhani, N.; Ma'arif, A.; Çakan, A. Implementation of PID Control for Angular Position Control of Dynamixel Servo Motor. *Control Systems and Optimization Letters* 2024, 2(1), pp 8-14.
24. Moraru, D. Tuning method of automatic controllers to object models with second order advance-delay and dead time. *Acta et Commentationes Exact and Natural Sciences* 2023, 2(16), pp. 78–88.
25. Zagarii, G. I., Shubladze, A. M. *Sintez sistem upravlenia na osnove kriteria maximalnoi stepeni ustoichivosti.* Energoatomizdat, Moskva, 1998, 198 s.

Citation: Moraru, D.; Fiodorov, I.; Izvoreanu, B.; Cojuhari, I. Cascade control algorithm of the robotic arm's servomotor. *Journal of Engineering Science* 2024, XXXI (4), pp. 124-141. https://doi.org/10.52326/jes.utm.2024.31(3).01.

Submission of manuscripts: jes@meridian.utm.md

Journal of Engineering Science *Vol. XXXI, no. 4 (2024), pp. 142 - 156*
Fascicle *Architecture, Civil Engineering and Environment* *ISSN 2587-3474*
Topic *Civil Engineering and Management* *eISSN 2587-3482*

https://doi.org/10.52326/jes.utm.2024.31(4).10
UDC 624.131.4:631.43(478)

SELECTION OF DESIGN VALUES FOR PHYSICAL-MECHANICAL PROPERTIES IN THE CONSTRUCTIONS ON COLLAPSIBLE SOILS

Vladimir Polcanov, ORCID: 0000-0001-8389-2128,
Alexandru Rascovoi, ORCID: 0009-0002-1074-2924,
Alexandru Cirlan *, ORCID: 0000-0003-4009-2790

Technical University of Moldova, Stefan cel Mare bd., 168, Chisinau, Moldova
* Corresponding author: Alexandru Cirlan, *alexandru.cirlan@cms.utm.md*

Received: 10. 25. 2024
Accepted: 11. 28. 2024

Abstract. The article substantiated the necessity of detailed geological-engineering surveys during the design and construction on collapsible soils. A landslide incident on the Cahul-Giurgiulești railway line at 74th km was highlighted. Among the main causes there were the soaking of collapsible soils and the development of suffusion processes. A brief historical overview of the study of collapsible soils in Republic of Moldova was provided. The results of theoretical and laboratory studies aimed at further revealing the nature of collapsible soils were presented. The impact of additional soil moisture on the values of physical-mechanical property characteristics was studied. Based on the moisture-density theory, the dependencies of strength on consistency were constructed. It was established that the decrease in the strength of collapsible loams over time might have been caused by the disruption of rigid cementation bonds of structural cohesion (C_c) and the reduction of hydrocolloid cohesion (Σ_w) under conditions of changes in the existing natural moisture regime (consistency) due to additional moisture from engineering activities and the rise of the groundwater level. Recommended design values for physical-mechanical characteristic parameters for construction projects were provided.

Keywords: *foundation, loess, landslide, strenght, soaking, reology.*

Rezumat. În articol a fost subliniată necesitatea efectuării unor investigații geologico-inginerești aprofundate pentru proiectarea și construcția pe pământuri sensibile la umezire. A fost menționat cazul de apariție a alunecării de teren pe un segment al drumului de cale ferată Cahul-Giurgiulești, km-ul 74. Printre principalele cauze au fost menționate anume umezirea pământurilor sensibile la umezire și dezvoltarea proceselor de sufoziune. A fost oferită o scurtă prezentare istorică a studiilor efectuate asupra pământurilor sensibile la umezire din Republica Moldova. Au fost prezentate rezultatele cercetărilor teoretice și celor de laborator, menite să aprofundeze înțelegerea naturii pământurilor sensibile la umezire. A fost studiată influența umezirii suplimentare a pământurilor asupra valorilor caracteristicilor fizico-mecanice ale acestora. Pe baza teoriei densității-umidității au fost construite dependențele rezistenței în funcție de consistență. S-a stabilit că scăderea rezistenței

argilelor sensibile la umezire în timp poate fi cauzată de distrugere legăturilor rigide ale coeziunii structurale (C_c) și de reducerea coeziunii de natură hydrocoloidală (Σ_w) în condițiile schimbării regimului natural de umiditate (consistență) din cauza umezirii suplimentare ca urmare a activităților inginerești și a creșterii nivelului apelor subterane. Au fost recomandate valori de calcul ale parametrilor caracteristicilor fizico-mecanice pentru proiectare.

Cuvinte cheie: *fundație, loess, alunecare de teren, rezistență, înmuiere, reologie*.

1. Introduction

The analysis of literary sources and expert studies has shown that construction on loess soils in the Republic of Moldova is generally carried out successfully. However, newly identified cases of deformation in several areas during field surveys have necessitated revisiting the peculiarities of design and construction on collapsible soils.

Figures 1 and 2 show photographic material reflecting the development of gully-landslide deformations in Chisinau, near the residential complex on Tudor Strisca Street 6. The deformations are occurring within the layer of collapsible loess. The gully extends up to 150m in length, with a width varying from 1.5 to 12m and a depth ranging from 1.0 to 5.7m.

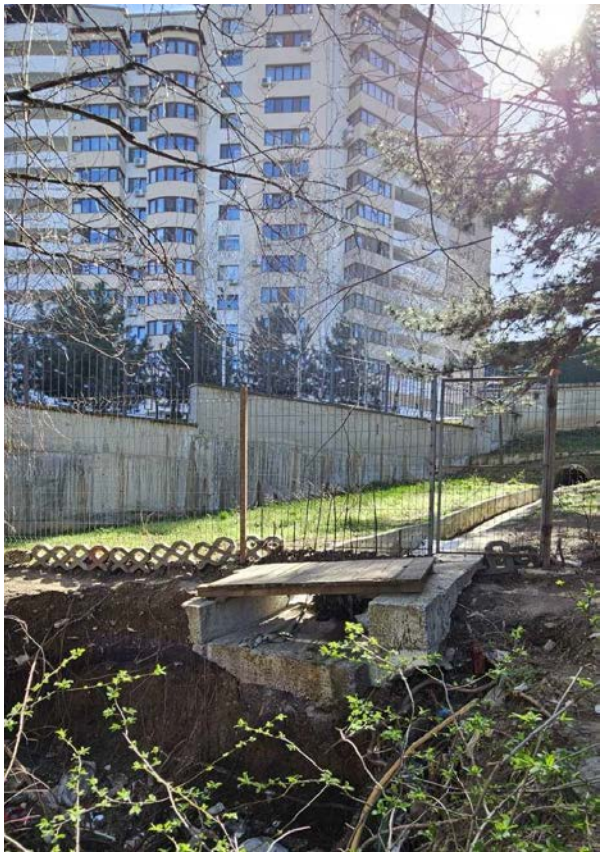

Figure 1. The damaged drainage ditch, which became the cause of the gully formation.
Photo by A. Cirlan, March 31, 2024.

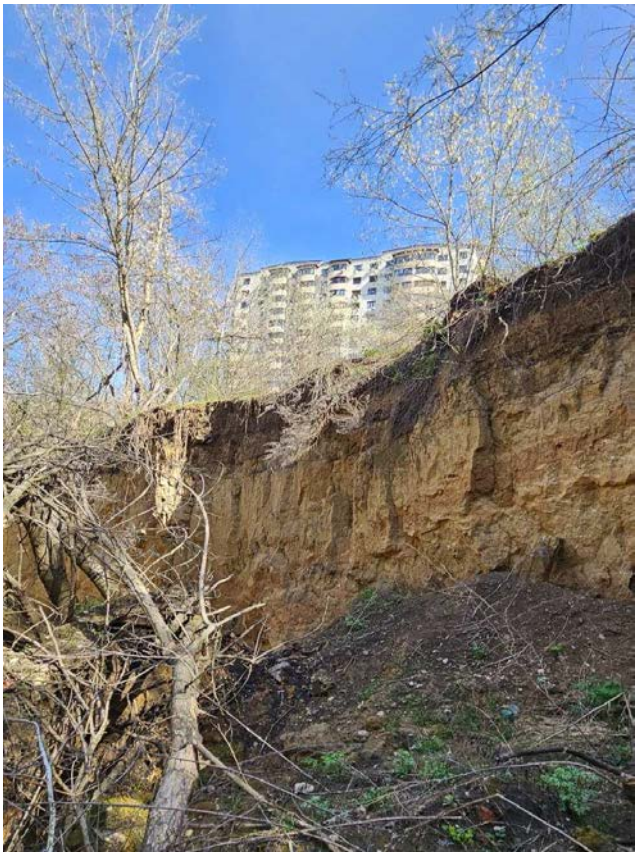

Figure 2. Gully-landslide deformations developing 150 m from the residential complex.
Photo by A. Cirlan, March 31, 2024.

The following case must unfortunately be classified as catastrophic. In the summer of 2022, a landslide occurred on the Cahul-Giurgiulesti railway line at 74th km near the Valeni village. The landslide extended approximately 300m along the railway line, with a width of 90-95m (see Figures 3 and 4).

The thickness of the landslide soils exceeds 30m. The slope and the floodplain area are composed of sandy loam soils. In the deformation zone, the soil profile includes collapsible sandy loams, loams, and water-saturated sand.

Significant difficulties arose during the construction of silos on the area adjacent to the port in Giurgiulesti. The foundation soils here consist of a substantial thickness (over 20m) of collapsible sandy loams and light loams. Undoubtedly, such cases cannot be overlooked.

Figure 3. Landslide deformations on a slope composed of collapsible soils.
Photo by C. Sherepera, 2022.

Figure 4. Displacement of the retaining wall due to the landslide process.
Photo by C. Sherepera,2022.

1.1. Brief Historical Overview

Detailed study of loess soils in Moldova began in the late 1950s. Among the earliest works was that of V.F. Kraev, which investigated the collapsible properties of the loess in the coastal area of the lower part of Transnistria (Administrative-Territorial Units of the Left Bank of the Dniester) [1].

In the early 1960s, the Institute of Geology and Geophysics of the Academy of Sciences of Moldova included a topic on the regional and comprehensive study of loess soils in its research plan. One of the sections was worked on by V.S. Goncharov during the period from 1963 to 1970 [2].

Based on the conducted research, a schematic map of the distribution and thickness of loess soils was created. It is important to note that the thickness of collapsible soils can vary from 1.0 to 25m. The loess cover of the lower part of Transnistria is found on all topographic elements: terraces, valley slopes, ravines, watersheds, and interfluves [2, pp. 19]. This fact is highly valuable as it allows for the differentiation of areas into Type I and II based on collapsibility, which forms the basis for the design of foundations for buildings and structures.

Based on research conducted from 1965 to 1975, G.E. Kostik completed a PhD thesis [3]. The work focused on predicting loess collapse using the method of engineering-geological analogies. G.E. Kostik posits that the extent of collapse should be considered as the sum of random variables, extrapolated within specific intervals of the soil layer or massive, and should also be treated as a random variable.

Based on the research conducted by G.E. Kostik, a methodology was developed that allows for determining the relative collapsibility of soils by evaluating just three indicators: moisture content, bulk density, and particle density.

According to the authors of the present work, the proposed methodology should be tested on a larger number of sites.

In the mid of 1970s, G.E. Kostik identified patterns of distribution, occurrence, and thickness of loess soils in Moldova [4]. This led to the development and implementation of modern methods for elimination of soil collapsibility, which significantly enhanced the safety of constructing buildings and structures on structurally unstable soils.

A significant event in the study of loess soils in Repubic of Moldova was the publication of the monograph by Yu.I. Olyanskiy in 1992 [5]. The results of Yu.I. Olyanskiy extensive research are essentially the first attempt to generalize existing data on loess soils in Moldova.

For designers, builders, and professionals in the agricultural sector, the most important fact is that "loess soils cover about 60% of the northern zone of the republic and over 90% of the southern zone, and are located in areas of intensive industrial and civil construction" [5, pp. 3]. Further research by Yu.I. Olyanskiy and his students focused on the patterns of subsidence development, forecasting loess area flooding, and post-collapse compaction issues [6-9].

In recent decades, the number of publications on the study of collapsible soils in Republic of Moldova and construction on these soils has decreased. It is surprising that research is now being conducted outside of Republic of Moldova [10-13].

Recent contributions include the works of A.D. Rascovoi [13, 14] and E.V. Shchekochikhina [15]. In particular, A.D. Rascovoi identified that for a long period, the study of collapsible soil properties was primarily conducted within the confines of major urban areas. Currently, new undeveloped territories are being explored, and construction is actively expanding in the southern regions of the republic. This situation underscores the need not only for theoretical research on loess soils within urbanized areas but also (which is most crucial) for obtaining calculated values of the physical-mechanical characteristics of soils for use in the design and construction on collapsible soils.

E.V. Shchekochikhina emphasizes the need to pay increased attention to factors that can impact the stability of structures during design and construction. One such factor is the co-occurrence of collapsible loess soils and the underlying Sarmatian clays. The impermeable properties of the clays contribute to the development of active groundwater conditions, resulting in the formation of a technogenic aquifer, the filtration of which leads to not only collapsible but also post-collapse deformations in the loess soils [15].

This has defined the main objective of the present study: to obtain new data characterizing the strength and deformation properties of loess soils for reliable design and safe construction on collapsible soils.

1.2. Research objectives

The chosen topic and the defined primary objective of this research required addressing the following tasks:

- to analyze previously published research on the study of the characteristics of collapsible soil properties occurring on the Republic of Moldova territory;
- to examine the physical-mechanical and rheological properties of loess soils in Republic of Moldova and their impact on the performance of the base of constructions;
- to determine the causes of potential strength reduction in collapsible soils;
- to determine the values of design strength indicators under varying conditions affecting the bases composed of collapsible soils.

2. Materials and Methods

This research is based on the following results:

- the analysis of numerous literature sources revealing the properties of collapsible soils in Republic of Moldova.
- field investigations, sampling of the necessary quantity of soil monoliths, and their subsequent study under laboratory conditions.
- determination of physical characteristics (according to standard methodologies);
- determination of strength and rheological characteristics of collapsible soils.

The experiments were carried out on direct shear devices. Samples with natural moisture content and those subjected to pre-soaking were tested. The results were processed using the moisture-density theory and the Maslov physico-technical creep theory [16].

Rheological characteristics such as structural cohesion (C_c), hydrocolloid cohesion (Σ_w), and creep threshold (τ_{lim}) were determined based on the results of shear tests on prepared surfaces. Long-term strength was determined through tests on prepared wetted surfaces. The results were processed according to the Coulomb-Mohr relationship.

In the overall scope of these studies, primary attention was given to the accurate determination of the physico-mechanical characteristics of soils with undisturbed structure and natural moisture content, as these indicators significantly influence further conclusions about soil properties.

Even slight disturbances in structure and moisture content lead to fundamental changes in strength and deformation characteristics. Therefore, in addition to soil monolith sampling during exploratory drilling, trenching was also conducted, with control samples taken in the form of monolith cubes, which were carefully sealed and tested in the geotechnical laboratory within a short time frame.

Additionally, supplementary control was carried out, based on field tests of soil samples using Litvinov's laboratory for accelerated testing of soil construction properties directly in natural conditions [17].

3. Results of the research

For reliable and efficient construction of buildings and structures in areas where structurally unstable soils are prevalent, the necessity of conducting fundamental research on their construction properties is beyond doubt. This is evidenced by the works of most scientists and researchers studying loess soils. The specific characteristics of such soils are determined by their structure, which depends on the conditions of the origin of the

formations, the subsequent process of compaction and transformation of accumulated sediments.

The key features of loess formations primarily include: the presence of vertically oriented macroporous channels, the ability to maintain a vertical slope of significant height, rapid solubility in water, and more. According to the widely recognized expert Yu.M. Abelev, it is precisely the macroporous structure that defines the deformation, strength, and filtration properties of loess formations [18].

When fully saturated with water, and even with minor moisture, the properties of loess formations change significantly. This implies that the safe performance of the base of structures could be compromised. This is clearly demonstrated by the aforementioned case of the loss of stability of the railway embankment on a section located on the western outskirts of the Văleni village in the Cahul district.

Field surveys and analysis of investigation materials conducted by the company "Intexnauca" revealed that the examined section of the railway track passes through a narrow floodplain of the Prut River. The Prut terrace rises 35m above the floodplain. The slopes are nearly vertical (see Fig. 3). The width of the floodplain over a distance of 300-320m is 10-14m. As a result of the landslide, the integrity of the railway track was completely disrupted. The topographic survey analysis showed that the displacement of the railway bed reached 4.5m. The lower retaining wall was displaced and overturned over a length of 25-30m. In the area of maximum deformations, the reinforcing slabs at the bottom of the slope were deformed (see Figure 4). One of the possible causes of the landslide process is attributed to the periodic changes in the water level of the Prut River and seasonal anomalies in precipitation, which contribute to the development of suffusion processes.

Within the framework of the ongoing scientific research, it was important to emphasize the following:

- the presence in the structure of the explored thickness of the slope (among other soils) of loess-like subsidence loams and sandy loams of solid consistency;
- the presence of a thin layer of soft to fluid-plastic loams and sandy loams;
- presence of interlayers of Sarmatian clay.

To quantitatively assess the physical and mechanical properties of loess soils in their natural deposition conditions on undeveloped areas and sites selected for construction in densely built-up areas, an analysis of geological maps and typical geological cross-sections was initially conducted, as well as a review of relevant literature sources. This analysis was based on the most significant works of V.S. Goncharov, G.E. Kostik, Yu.I. Olyanskiy, and other researchers.

The research work by E.V. Shchekochikhina [15] should be included among the latter. The author provided a detailed characterization of the composition and properties of the loess cover of the territory of Moldova. For general conclusions, E.V. Shchekochikhina used the results from over a thousand experiments conducted personally, as well as data previously obtained by various scientists and researchers.

When designing and constructing on collapsible soils, it is essential to first have the following data:

- thickness of the collapsible soil layer;
- soil density;
- values of collapsibility characteristics: initial collapsible moisture, relative collapsibility, initial collapsible pressure;

- values of strength characteristics: angle of internal friction and cohesion;
- values of deformation characteristics: compressibility coefficient, deformation modulus;
- values of the coefficient of filtration.

Undoubtedly, depending on the tasks to be solved, additional data may be required. According to the authors of this work, the least studied aspects are the strength and deformability characteristics of soils, which largely determine the stability of slopes, foundation sizes, dimensions of retaining structures, etc. Therefore, this work focuses primarily on the strength of collapsible soils and its potential change with additional moisture.

It should be noted that since shear resistance significantly depends on the granulometric composition, natural moisture content, and structural features of the soils, there is considerable variability in the results obtained for different types of loess soils.

For example, according to V.S. Goncharov, the angle of internal friction (φ) varies from 14° to 20°, and cohesion (C) ranges from 12 to 85kPa. For heavy loams, the most common values are: φ=17-20°, C=50-60kPa. For medium and light loams, respectively, φ=20-23°, C=20-40kPa.

Therefore, in studying strength issues, it was taken into account that disturbances in the natural equilibrium of the geological environment, including those caused by the saturation of the foundation and additional loads arising within construction sites, create new qualities and properties of the soils, consequently altering the bearing capacity of the foundations.

The experimental part of this work was conducted at the geotechnical laboratory "Ingeotehgrup."

The results are summarized in Tables 1-4. Graphical interpretation is presented in Figures 5-8.

Table 1

Strength property indicators of loams

Region of the Republic of Moldova	Range of strength variation τ_f (kPa), at pressure σ = 200kPa	Angle of internal friction φ (degrees)	Total cohesion C_w (kPa)	Structural cohesion C_c (kPa)	Hydro-colloidal cohesion Σ_w (kPa)
Northern	39 ÷ 222	11	60	40	20
Central	50 ÷ 375	14	120	60	60
Southern	20 ÷ 280	17	120	70	50

Based on the results presented in Table 1 and Fig. 5 the results show that in the investigated samples from the northern and central districts the values of structural and hydrocolloid cohesion are of practically the same proportions (50%). For the southern districts, structural cohesion bonds predominate in the total cohesion.

The maximum strength is characterized by the rocks of central and southern Moldova.

Processing of the experimental data showed that there is no systematic change of strength properties of the soils with depth. A significant scatter in the experimental determinations of strength properties was noted (Table 1, Fig. 5).

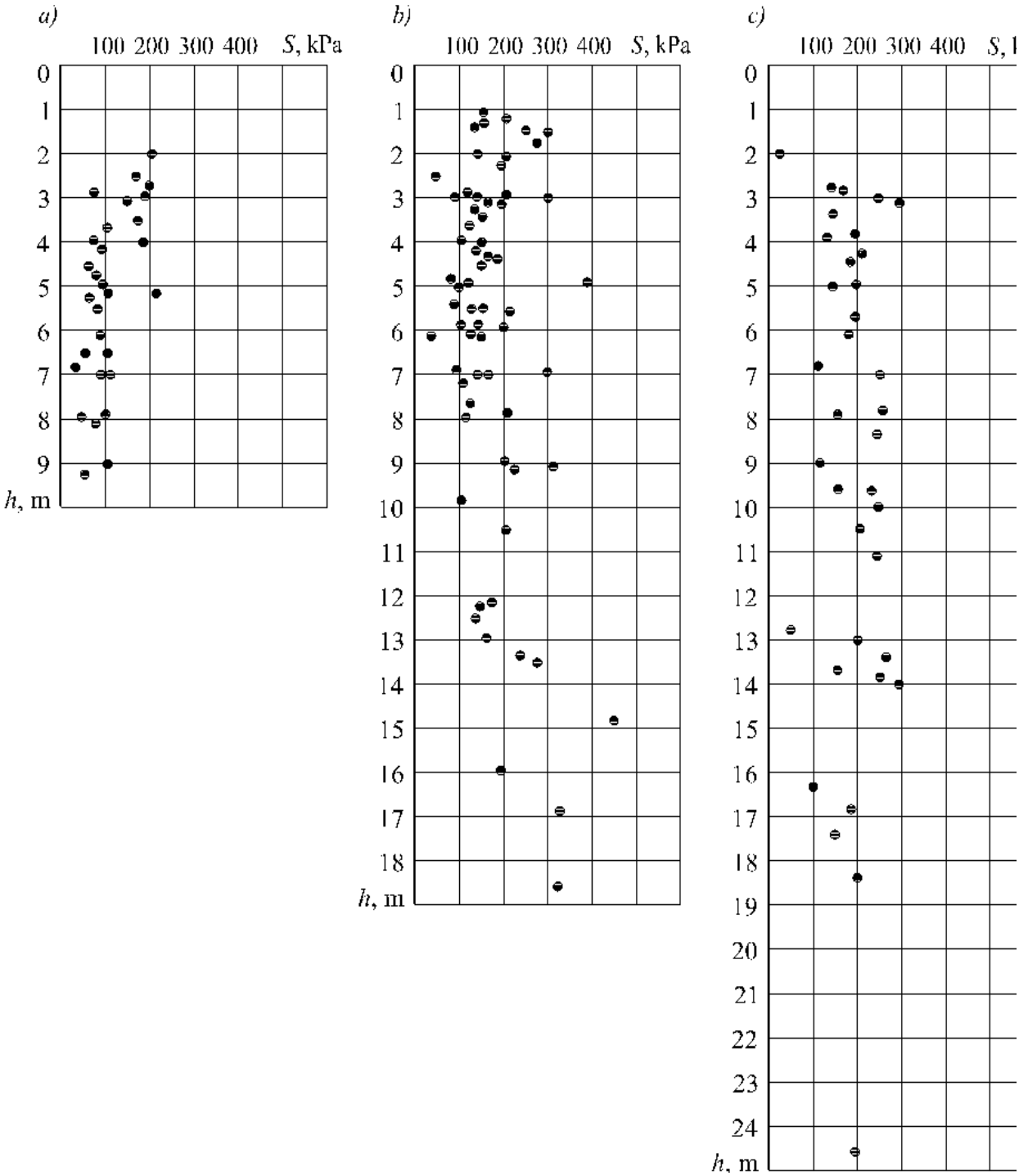

Figure 5. Scatter plots of strength (*S*) versus depth (*h*), for loams. Pressure *P*=200kPa: *a)* northern region; *b)* central region; *c)* southern region.

To identify the nature of the strength of the investigated soils, results from more than 750 shear tests of samples with natural and prepared shear surfaces were processed.

The equations characterizing the loams strength for different regions of Republic of Moldova, are expressed by the corresponding equations:

$$S_1=0{,}19\sigma+60\text{kPa} - \textit{for northern region;} \quad (1)$$

$$S_2=0{,}25\sigma+120\text{kPa} - \textit{for central region;} \quad (2)$$

$$S_3=0,30\sigma+120\text{kPa} - \textit{for southern region;} \quad (3)$$

where σ – the normal pressure to the shear plane.

Based on the results of shear tests on prepared surfaces, the total cohesion (C_w) was divided into two components: rigid structural cohesion (C_c) and hydrocolloid cohesion (Σ_w). This allowed for the derivation of equations characterizing the strength of the investigated soils at complete disruption of structural cohesion, based on the concept of prof. N.N. Maslov [17].

$$S_{rez1}=0,19\sigma+20\text{kPa} - \textit{for northern region;} \quad (4)$$

$$S_{rez2}=0,25\sigma+60\text{kPa} - \textit{for central region;} \quad (5)$$

$$S_{rez3}=0,30\sigma+50\text{kPa} - \textit{for southern region;} \quad (6)$$

To further investigate the potential reduction in strength with changes in consistency, shear tests on water-saturated soils were carried out, with special preparation of the samples and subsequent processing using the "density-moisture" method (Table 2, Figures 6-8).

Table 2

Indication of physical properties of the studied samples

Region of the Republic of Moldova	Particle density ρ_s (g/cm^3)	Density ρ (g/cm^3)	Moisture w (%)	Plasticity index I_P (fract. unit)	Consistency I_L (fract. unit)
Northern	2.69	$\frac{1.95}{1.65 \div 2.10}$	$\frac{25}{15 \div 40}$	$\frac{14}{7 \div 17}$	$\frac{0,2}{-0.5 \div 0.7}$
Central	2.72	$\frac{1.95}{1.5 \div 2.2}$	$\frac{15}{5 \div 25}$	$\frac{14}{10 \div 17}$	$\frac{0}{-0.5 \div 0.4}$
Southern	2.70	$\frac{2.00}{1.7 \div 2.2}$	$\frac{15}{5 \div 20}$	$\frac{10}{8 \div 17}$	$\frac{-0.1}{-0.6 \div 0.3}$

Additional moistening allowed to extend to a great extent the range of fluidity values, especially for samples taken in the northern districts of the republic: from I_L=-0.5 to I_L=+0.75 (Table 2). It was found that the influence of moistening is more pronounced in the consistency interval exceeding solid consistency (Figure 7). A detailed analysis of the physical properties of samples taken from the northern and central regions allowed for the processing of the overall sample.

As a result, dependencies of strength parameters on consistency were obtained (Figures 7-8), which can be used in the preliminary assessment stage when solving engineering problems.

Dependences presented in Figures 7-8 show that strength parameters: hydrocolloid cohesion (Σ_w) and angle of internal friction (φ_w) sharply decrease when subsidence soils are moistened.

The following averaged values can be used for design at the stage of preliminary calculations:

- for solid consistency: C_w=105kPa, Σ_w=48kPa, φ_w=15°;
- for tight plastic consistency: C_w=55kPa, Σ_w=23kPa, φ_w=8°.

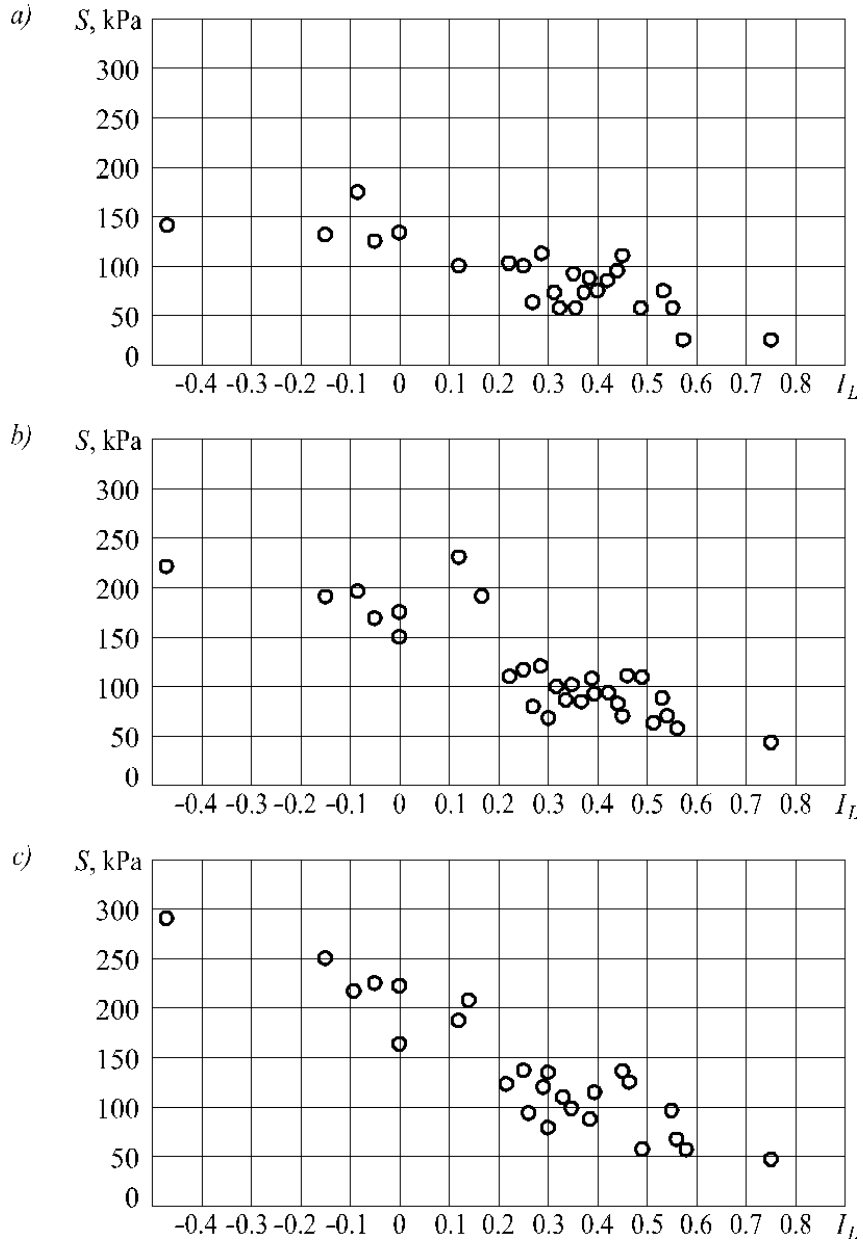

Figure 6. Scatter plots of strength (*S*) versus consistency (I_L), for loams at natural moisture and after additional moistening, Northern Region:
a) for *P*=100kPa; *b) P*=200kPa; *c) P*=300kPa.

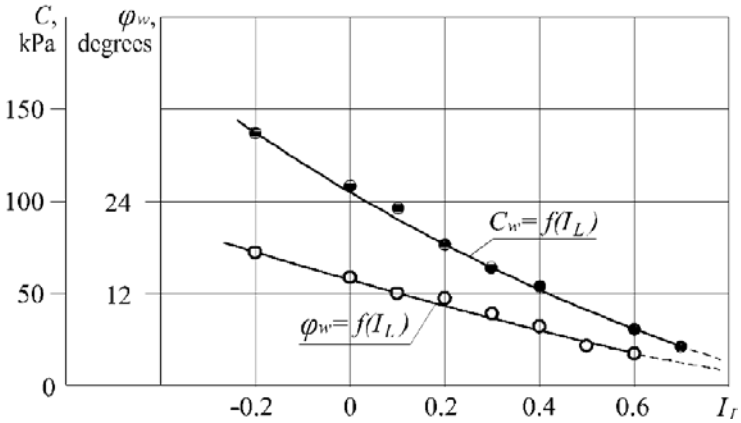

Figure 7. Dependence of total cohesion (*C*) and angle of internal friction (φ_w) on consistency (I_L), obtained using the „density-moisture" method for loams from North-Central region.

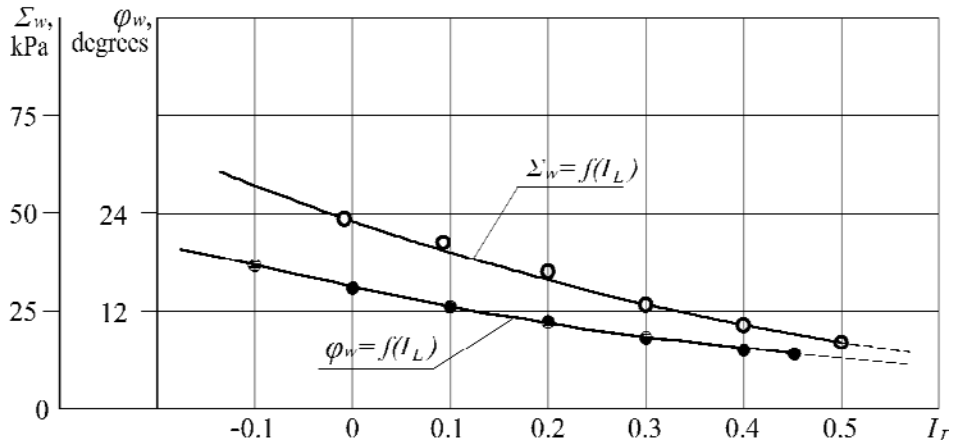

Figure 8. Dependence of hydrocolloidal cohesion (Σ_w) and angle of internal friction (φ_w) on consistency (I_L), for loams (overall sample).

According to the Maslov physico-technical creep theory [16], the main rheological characteristic of soil is the creep threshold τ_{lim}, which can be determined analytically using the formula:

$$\tau_{lim}=\sigma_n \cdot tg\varphi_w + C_c, \quad (7)$$

where: σ_n – normal stress, kPa; $tg\varphi_w$ – tangent of the true angle of internal friction; C_c – structural cohesion, kPa.

It should be noted that the results of experimental determination of creep threshold of loams from Republic of Moldova are practically absent. Some individual samples were tested in laboratories of Republic of Moldova, Dnipro and Odesa. However, these studies addressed specific isolated tasks, and there was no consensus on the methodology of tests.

In the context of this study, the value of structural cohesion (C_c) was determined based on the results of tests on soil samples with a prepared surface.

Based on the obtained dependencies, applied to the calculated consistency for the selected regions, the expressions for the creep threshold are as follows:

$$\tau_{lim1}=0.19\sigma+40\text{kPa} \text{ – } \textit{for northern region;} \quad (8)$$

$$\tau_{lim2}=0.25\sigma+60\text{kPa} \text{ – } \textit{for central region;} \quad (9)$$

$$\tau_{lim3}=0.30\sigma+70\text{kPa} \text{ – } \textit{for southern region;} \quad (10)$$

In the present research, reddish-brown loams were identified as a separate engineering-geological unit.

The laboratory studies focused on soil samples collected from the construction site of a residential complex on Testemitanu Street, Chisinau Municipality, and the slope of the M21 Brest-Chisinau-Poltava road excavation.

The results of these studies were summarized in Tables 3 and 4.

From Table 3, it is evident that at a depth of 6.0m, a weakened strength zone is clearly identified: the values of total cohesion are 2.6 times lower than at a depth of 1-3m. After moisture, cohesion may decrease by more than 6 times.

At the site along Testemitanu Street, a significant change in strength due to moisture is also observed: cohesion decreased by almost 3 times, and the internal friction angle by 1.3 times.

Table 3

Results of the research on the strength properties of reddish-brown loams Central region, section of the M21 Brest-Chisinau-Poltava road

Testing conditions	Depth of monolith sampling *h* (m)	Consistency I_L (fract. unit)		Strength parameters of samples tested for shear			
		natural	after moistening	at natural moisture content		after additional moistening	
				φ, degrees	*C*, kPa	*φ*, degrees	*C*, kPa
1*	1–3	-0.50	0.38	13	130	13	20
	6	-0.30	0.17	13	50	16	44
	7–15	-0.08	-	16	100	-	-
2*	1–3	-0.50	0.38	15	80	13	10
	6	-0.30	0.17	14	50	16	10
	7–15	-0.08	-	15	50	-	-
3*	1–3	not determined		13	30	9	10
	7–15	not determined		10	20	12	9

Note: 1* – shear of samples with natural structure, 2* – shear of samples with prepared surface, 3* – shear of samples with prepared moistened surface.

Table 4

Results of the research on the strength properties of reddish-brown loams Central region, section No. 2, Testemitanu Street, Chisinau Municipality

Testing conditions	Depth of monolith sampling *h* (m)	Consistency I_L (fract. unit)		Strength parameters of samples tested for shear			
		natural	after moistening	at natural moisture content		after additional moistening	
				φ, degrees	*C*, kPa	*φ*, degrees	*C*, kPa
1*	10.0	0.0	0.30	18	70	14	28
2*	10.0	0.0	0.30	16	30	12	20
3*	10.0	not determined		11	22	10	8

Note: 1* – shear of samples with natural structure, 2* – shear of samples with prepared surface, 3* – shear of samples with prepared moistened surface.

It is quite clear that the change in strength over time depends not only on the moisture regime (consistency) but also on the working conditions of the soil. In the absence of significant shear (tangential) stresses, in the conditions of soil consolidation under foundations, an improvement in strength characteristics can be expected. On slopes that have not yet reached limit of consolidation, tangential stresses may contribute to the development of creep processes. In the slopes of excavations and artificial structures, the processes of repeated soaking and drying will play a determining role.

Formation of loess soils took place in dry climate conditions with the predominance of physical weathering processes. As a result, these soils are highly sensitive to changes in physical-geographical conditions and geological environments. According to the figurative expression of M.P. Lysenko, loess soils are able to "adapt" to changes in the surrounding natural environment [19, p. 153].

This implies the necessity to take into account the influence on collapsible soils of some aspects of human engineering activities, first of all, the rise of groundwater level, which causes the change of the existing natural moisture regime.

4. Conclusions and Recommendations

Studies have shown that soils with collapsible properties cannot be considered reliable foundation for buildings and structures without the anthropogenic alteration of their primary structure.

The main cause of the change in the stress-strain state of the slope and the development of a landslide on the studied section of the Cahul-Giurgiulesti railway at 74th km was the additional wetting of the foundation soils, which manifested 15 years after construction due to post-collapse compaction associated with prolonged water filtration through the loess layer.

The results of the quantitative assessment of the physical-mechanical and collapsible characteristics of loess soils of Republic of Moldova, obtained by V.S. Goncharov, G.E. Kostik, and Y.I. Olyansky in the period from 1970 to 2000, need to be adjusted, as they do not take into account the changes in the natural-historical environment that have occurred over the past decades, caused by urbanization and construction in densely built-up areas.

The results of the study of loess soils in the area between the Prut and Dniester rivers, conducted by E.V. Shchekochikhina from 2011 to 2021, can be particularly valuable for design purposes. The collected factual material has shown that the issues related to studying the strength of loess soils are insufficiently covered. This fact limited the possibility of obtaining a representative sample based on previous investigations and has necessitated new research into the physical, strength, and rheological characteristics of these soils.

Based on Maslov "density-moisture" theory, the influence of moisture on the values of soil strength characteristics has been established, and dependencies of strength on consistency have been constructed. These derived dependencies can be used for the preliminary selection of design parameters that characterize the strength of collapsible loams.

From the conducted shear tests on samples with prepared surfaces and the established correlation dependencies, equations have been obtained that characterize the creep threshold of collapsible soils for the northern, central, and southern parts of the republic, respectively, as follows: $\tau_{lim1} = 0{,}19\sigma + 40$kPa; $\tau_{lim2} = 0{,}25\sigma + 60$kPa; $\tau_{lim3} = 0{,}30\sigma + 70$kPa.

It has been established that the reduction in the strength of collapsible loams over time can be attributed to the following reasons:

- the disruption of rigid cementitious bonds of structural cohesion (C_c) under conditions where the shear stresses arising in the soil exceed the creep threshold ($\tau > \tau_{lim}$).
- the decrease in hydrocolloidal cohesion (Σ_w) due to changes in the existing natural moisture regime (consistency) as a result of additional moisture infiltration caused by engineering activities, including the rise of the groundwater level.

New data have been obtained regarding the physical and strength properties of soils under natural deposition conditions and in densely built-up areas.

The results of these studies can be used for modelling the stress-strain state of foundations and building bases, as well as for assessing the stability of slopes and embankments of artificial structures.

Acknowledgements: The present research was conducted as part of the scientific research project *"020406. Models, systems, and technologies for energy efficiency, decarbonization, and digitalization of processes in energy, industry, construction, and transport"* under the supervision of Dr. Ilie Nucă, with participation of Department of Civil Engineering and Geodesy at the Technical University of Moldova.

Conflicts of Interest: The authors declare no conflict of interest.

References

1. Kraev, V.F. Prosadochnye svoystva lessovykh porod pravoberezhnoi chasti nizhnego Pridnestrov'ya [Collapsible properties of loess soils on the right-bank part of the lower part of Transnistria]. Publishing House of the Academy of Sciences of the Ukrainian SSR, Kiev, USSR. 1956, 148p. [in Russian]
2. Goncharov, V.S. Inzhenerno-geologicheskaya kharakteristika lessovogo pokrova nizhnego Pridnestrov'ya. Abstract of the cand. of geologico-mineralogical sciences dissertation, Odessa State University, Odessa, 1971, 2 2p.
3. Kostik, G.E. Prognoz prosadki lessovykh porod metodom inzhenerno-geologicheskikh analogiy. Abstract of cand. of geological and mineralogical sciences dissertation, Odessa State University, Odessa, 1975, 33 p.
4. Kostik, G.E. Opyt prognozirovaniya prosadki lessovykh porod metodom analogiy. Stiinta, Chisinau, USSR, 1978, 43p. [in Russian]
5. Olyansky, Y.I. Lessovye gruntы yugo-zapadnogo Prichernomorya. Stiinta, Chisinau, Republic of Moldova, 1992, 130p. [in Russian]
6. Olyansky, Y.I.; Perfilov, V.A.; Makhova, S.I.; Kuzmenko, I.Y.; Charykova, S.A. Prognoz podtopleniya urbanizirovannykh territoriy. *Geologija, geografija i globalinaja jenergija* 2013, 1 (48), pp. 119-129.
7. Olyansky, Y.I.; Charykova, S.A. Inzhenerno-geologicheskie problemy melioratsii yuzhnykh rayonav Moldovy. In: *Problems of decrease in natural hazards and risks, Proceedings of the International scientifically-practical conference "Georisk-2012"*, People Friendship University of Russia, Moscow, Russia, October 18-19, 2012, 1, pp. 192-197.
8. Bogomolov, A.N.; Olyansky, Y.I.; Charykova, S.A.; Kiseleva, O.V.; Tikhonova, T.M. Opyt prognoza podtopleniya lessovykh territoriy. In: *Problems of decrease in natural hazards and risks, Proceedings of the International scientifically-practical conference "Georisk-2012"*, People Friendship University of Russia, Moscow, Russia, October 18-19, 2012, 1, pp. 37-43.
9. Olyansky, Y.I.; Bogdevich, O.P.; Vovk, V.M. O dopolnitel'nom uplotnenii nekotorykh tipov lessovykh porod Moldavii pri filtratsii vody. *Izvestia of Academy of Sciences MSSR. Physics and Technology* 1991, 3(6), pp. 118-121.
10. Bogomolov, A.N.; Olyansky, Y.I.; Shchekochikhina, E.V.; Kuzmenko, I.Y.; Mozgunov, M.D.; Charykova, S.A. Osobennosti vozvedeniya zdaniy i sooruzheniy na lessovykh osnovaniyakh v Moldavii. *Bulletin of Perm National Research Polytechnic University. Construction and Architecture* 2017, 8 (1), pp.53-59.
11. Bogomolov, A.N.; Olyansky, Y.I.; Shchekochikhina, E.V.; Kuzmenko, I.Y. Osobennosti deformatsionnogo povedeniya zamedlenno-prosadchnykh lessovykh gruntov v osnovaniyakh inzhenernykh sooruzheniy pri tekhnogennom obvodnenii. *Vestnik PNIPU, Construction and Architecture* 2016, 7(3), pp.34-45.
12. Bogomolov, A.N.; Olyansky, Y.I.; Shchekochikhina, E.V.; Kuzmenko, I.Y.; Charykova, S.A. Osobennosti otsenki prosadochnykh svoystv lessovykh porod pri proektirovanii osnovaniy i fundamentov v tsentral'noy Moldavii. *Vestnik PNIPU, Construction and Architecture* 2016, 7(3), pp. 46-53.
13. Polcanov, V.; Rascovoi, A.; Polcanova, A. Sovremennye metody ustranenija prosadochnosti gruntov. Ocenka tehnicheskoj celesoobraznosti i jekonomicheskoj jeffektivnosti. Monograph. LAP LAMBERT Academic Publishing: Saarbrucken, Germany, 2019, 136 p. ISBN-13: 978-620-0-24793-3.
14. Rascovoi, A.; Polcanov, V. K voprosu izuchenija fiziko-mehanicheskih svojstv uplotnennyh prosadochnyh gruntov. In: *Probleme actuale ale urbanismului si amenajarii teritoriului., Proceedings of VIII International*

scientific and technical conference, Technical University of Moldova, Chisinau, Moldova, November 17-19, 2016, Tehnica-UTM: Chisinau, 2016. pp. 159-163.
15. Shchekochikhina, E.V. Inzhenerno-geologicheskoe obosnovanie stroitel''stva na territorijah sovmestnogo zaleganija lessovyh prosadochnyh i glinistyhnabuhajushhih porod. PhD. Geology and mineralogy thesis, Volgograd State Technological University, Volgograd, 2023, 342p.
16. Maslov, N.N. Fiziko-tehnicheskaja teorija polzuchesti glinistyh gruntov v praktike stroitel'stva. Stroyizdat, Moscow, USSR, 1984, 176 p.
17. Litvinov, I.M. Ukreplenie i uplotnenie prosadochnyh gruntov v zhilishhnom i promyshlennom stroitel'stve. Budivelnik, Kiev, USSR, 1977, 288p.
18. Abelev, Y.M., Abelev, M.Y. Osnovy proektirovanija i stroitel'stva na prosadochnyh makroporistyh gruntah. 3rd ed. Stroyizdat, Moscow, USSR, 1979, 271p.
19. Lysenko, M.P. Lessovye porody. Nedra, Leningrad, USSR, 1978, 208p.

Citation: Polcanov, V.; Rascovoi, A.; Cirlan, A. Selection of design values for physical-mechanical properties in the construction on collapsible soils. *Journal of Engineering Science* 2024, XXXI (4), pp. 142-156. https://doi.org/10.52326/jes.utm.2024.31(3).01.

Submission of manuscripts: jes@meridian.utm.md

Journal of Engineering Science *Vol. XXXI, no. 4 (2024), pp. 157 - 165*
Fascicle *Architecture, Civil Engineering and Environment* *ISSN 2587-3474*
Topic *Architecture, Urbanism and Cadaster* *eISSN 2587-3482*

https://doi.org/10.52326/jes.utm.2024.31(4).11
UDC 004.658.2:332(478-25)

ANALYSIS METHODOLOGY OF OPENSTREETMAP DATA COMPLETENESS (CASE STUDY: CHISINAU CITY)

Rodica Sîrbu *, ORCID: 0000-0001-7892-8747

Technical University of Moldova, 168 Ștefan cel Mare Blvd., Chisinau, Republic of Moldova
* Corresponding author: Rodica Sîrbu, *rodica.sirbu@icg.utm.md*

Received: 11. 26. 2024
Accepted: 12. 17. 2024

Abstract. In recent years, special attention has been paid to free and open geospatial data sources accessible to the whole world, which have benefits for all sectors of the national economy. Taking into account the interest in this topic, the article proposes a data completeness analysis for OpenStreetMap, that is based on crowd sourcing, compared to data sources available at the national level, such as statistical information from Public Institution Real Estate Cadastre registers or the Spatial Data Infrastructure of the Republic of Moldova (NSDI), Agency Geodesy, Cartography and Cadastre. Thus, a general methodology for completeness analysis framework is designed based on the characteristics of OSM data, since is a well-known standard. Secondly, an attempt was made to apply a quality assessment model for OSM data through three different quality elements: completeness, thematic accuracy and positional accuracy based on the visual and quantitative analyses taking into account the spatial data that already exists on national platforms. The Chisinau city was selected as a case study/area of interest, and the results of the presented research can subsequently be applied to the entire Republic of Moldova. Based on the analysis performed, it can conclude that spatial data sources, whether from official sources or those based on crowd sourcing, still need to be supplemented with both spatio-temporal and qualitative information.

Keywords: *volunteered geographic information, spatial data, Geographical Information Systems, OpenStreetMap, National Spatial Data Infrastructure.*

Rezumat. În ultimii ani s-a acordat o atenție deosebită surselor de date spațiale gratuite și deschise, accesibile tuturor, care au beneficii pentru toate sectoarele economiei naționale. Ținând cont de interesul deosebit față de această tematică, articolul propune o analiză a plenitudinii datelor spațiale de pe OpenStreetMap (OSM), care se bazează pe crowd sourcing, comparativ cu sursele de date disponibile la nivel național, precum informații statistice din registrele I.P. Cadastrul Bunurilor Imobile sau cele spațiale prezente Infrastructura de date a Republicii Moldova (INDS), Agenția Geodezie, Cartografie și Cadastru. Astfel, este concepută o metodologie generală pentru cadrul de analiză a plenitudinii pe baza caracteristicilor datelor OSM, deoarece sunt concepute în baza unui standard internațional. În al doilea rând, s-a încercat aplicarea unui model de evaluare a calității datelor OSM prin prisma a trei

elemente de calitate diferite: plenitudine, acuratețe tematică și acuratețe poziționlă pe baza analizelor vizuale și cantitative ținând cont de datele spațiale care există deja pe platformele naționale. Ca zonă interes a fost selectat orașul Chișinău, iar rezultatele cercetării prezentate pot fi ulterior aplicate pe întreg teritoriul Republicii Moldova. Pe baza analizei efectuate, se poate concluziona că sursele de date spațiale, fie din surse oficiale, fie cele bazate pe crowd sourcing, mai trebuie completate atât cu informații spațio-temporale, cât și calitative.

Cuvinte cheie: *informații geografice voluntare, date spațiale, Sisteme Informaționale Geografice, OpenStreetMap, Infrastructura națională de date spațiale*.

1. Introduction

For centuries, mapping of territory was carried out by state organizations. At first, military interests dominated, while in the 20th century, attention and application migrated to institutions responsible for land management, infrastructure planning or monitoring environmental components [1]. Meanwhile, Geographical Information Systems (GIS) have been used for decades, and currently they are no longer a tool used only by dedicated specialists, because the internet and web have significantly influenced the process of representing, searching, exploiting and use of geographic data. From the category of Web Mapping 2.0 applications, OSM remains to until today the best-known global geographic application project. OpenStreetMap Java Editor (JOSM) as a desktop application for editing OSM, being the most complex of the available editors today. The OSM project as a geographic application was initiated in 2004, for mapping the territory of Great Britain, and in 2006 the OpenStreetMap Foundation was founded for the development and distribution of free and open spatial data [2]. The geographical data in the OSM platform obtained according to the principle of "crowd-sourcing" is based on voluntary contributions of users to update the maps, which are subsequently accessible to the public as free and open data. At the same time, large companies such as Amazon, Apple, Facebook, Kaart and others contribute to improving the quality of OSM data [3]. Although Voluntary Geographic Information (VGI) has significantly improved the availability and use of geographic data, at the same time it has raised some reasonable concerns about their quality, reliability and overall value [4]. Although GIS experts have conducted research on the quality of OSM spatial data quality [5], it remains a current topic due to challenges related to the value of cartographic content, since the completeness of spatial information varies both at national and regional levels and also over time.

Currently, OSM data are most frequently used for urban infrastructure mapping [6,7], as they offer open access, global coverage, acceptable geo-precision, thematic and temporal plenitude [8] and are widely used by scientists and practitioners alike [9]. At the same time, national infrastructures are being developed all over the world with a multitude of reference data for different topics depending on state interest. But of course, the general users' interest in relation to spatial data is more focused on global sources because they are integrated into various common, well-known platforms with friendly and intuitive user interfaces, which is an additional reason to verify their quality.

2. Materials and methods

The initial materials used for the research were the specialized literature, the OSM and Geofabrik platforms, National Spatial Data Infrastructure (NSDI) of the Republic of Moldova, statistical data provided by the Public Institution Real Estate Cadastre. To assess the accuracy

of spatial data, a series of methods were used, from traditional ones, such as visual analysis, to the application of advanced processing tools in the specialized program. Some of the methods applied are strictly quantitative (Figure 1), while others are based only on visual observations taking into account the specifics of the information in the attribute tables or geometries. For all the processing described in this study, the specialized GIS software, free and open QGIS was used, as it represents a resource that can be accessible to all users.

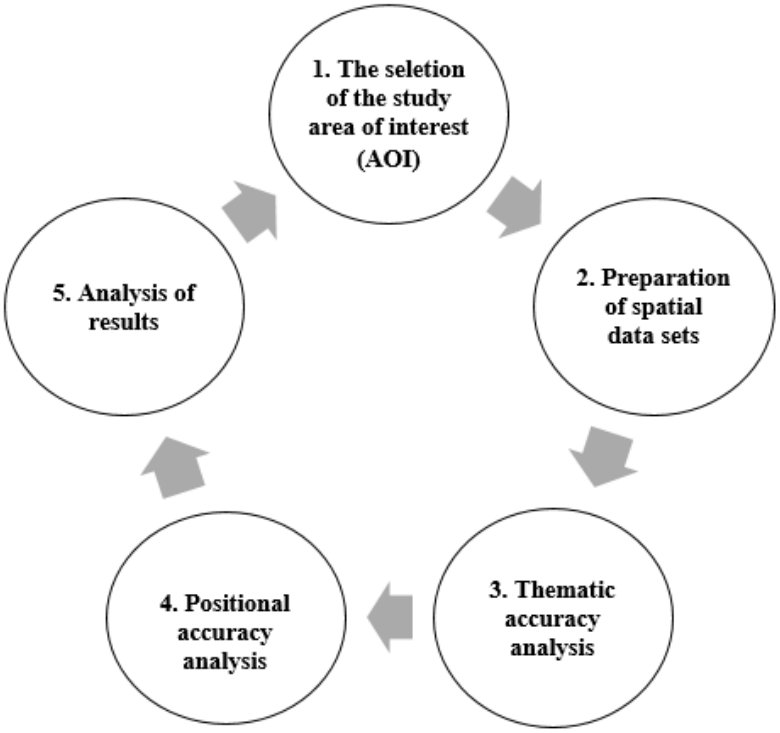

Figure 1. The methodology approached.

The Chisinau city, capital of the Republic of Moldova, was selected as the study area, which has an area of 122 km² [10] and a population of about 600 000 inhabitants [11]. Previous studies evaluated OSM in comparison with existing data to provide detailed information on selected cities [12], therefore, it is already an existing initial reference information. Since the method presented in the paper allows the assessment of positional accuracy and completeness of spatial data, therefore the analysis of previous literature focused mainly on these two aspects.

The process of preparing the spatial datasets had two objectives, namely firstly, the datasets must match each other in order to be able to compare them. Secondly, the datasets must be edited in such a way that they contain similar information, in order to facilitate the analysis procedure. As an element for the data analysis, the principle of completeness of information was used. Thus, the length and completeness of the name were analysed from the length or number of names of the tested dataset compared to the length or number of names of the reference dataset. The completeness of the spatial data was evaluated by comparing the OSM data with those accessed by the NSDI thematic geoportal and the data provided by the Public Institution Real Estate Cadastre. The thematic accuracy (accuracy of the name and classification) for the study area was analysed using the information from the attribute tables of the downloaded spatial data. The positional accuracy was determined by applying the query on OSM database or downloaded from Geofabrik [13], where a complete copy of the OSM database not older than one day is performed, and the instant download of

several existing datasets allows a more complex analysis, which enabled the selection and export of data categories for comparative analysis.

The OSM data were obtained using the QuickOSM plugin and through the query procedure were downloaded in shapefile format. For comparison, existing spatial data from the metadata of the NSDI platform of the Republic of Moldova were used. The GIS software used for the analysis was the free and open source QGIS, with the tools from the vector, plugin and geoprocessing tools on the menu bar.

3. Results

Large-scale projects, such as OSM, Wikimapia, GeoSam and others, provide access to spatial information for individual users, organizations and the scientific community without legal and economic restrictions, and among the most important benefits are minimal costs, accessibility, interoperability, data for less documented regions, etc. At the same time, these data are collected by users less experienced in GIS and consequently, the question arises regarding their quality. As is known, the methodology for analysing the quality of spatial data is very extensive, and through the existence of different standards and definitions, the following aspects can be considered [14]:

- ✓ Descent – refers to the way in which the dataset was collected and developed.
- ✓ Positional accuracy – evaluates the coordinates of an object (location).
- ✓ Attribute accuracy – objects in a geographic database are represented not only by their geometric shape but also by additional attributes, this measure evaluates how correct these values are.
- ✓ Logical consistency – topologically correctness and relationships that are encoded in the database.
- ✓ Completeness – coverage of objects existing in the real world.
- ✓ Semantic accuracy – links the way the object is integrated and represented in the database to its meaning and how it should be interpreted.
- ✓ Temporal quality – this is a measure of the validity of changes in the database in relation to real world changes and the rate of updates.

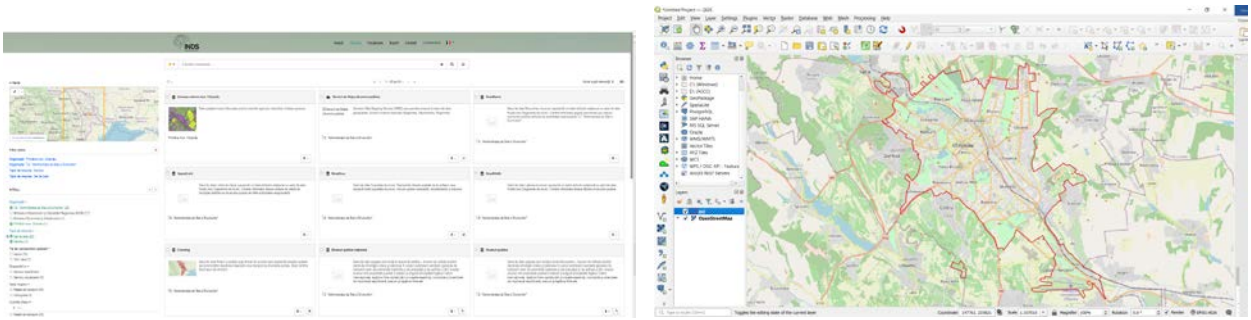

Figure 2. Selection of initial spatial data sets and delimitation of the AOI.

Thus, in order to proceed with the data analysis, existing metadata were identified using the filtering tool [15] through specific key words, identifying the required services or spatial data and as well the study area was delimited (Figure 2).

The next step was to install the QGIS plugin - QuickOSM, which made it easy to download and manage OSM data directly from the specialized software graphic user interface, without Overpass Turbo or other intermediary platforms. QuickOSM is a very useful tool for quickly downloading OSM data based on custom filters (Figure 3).

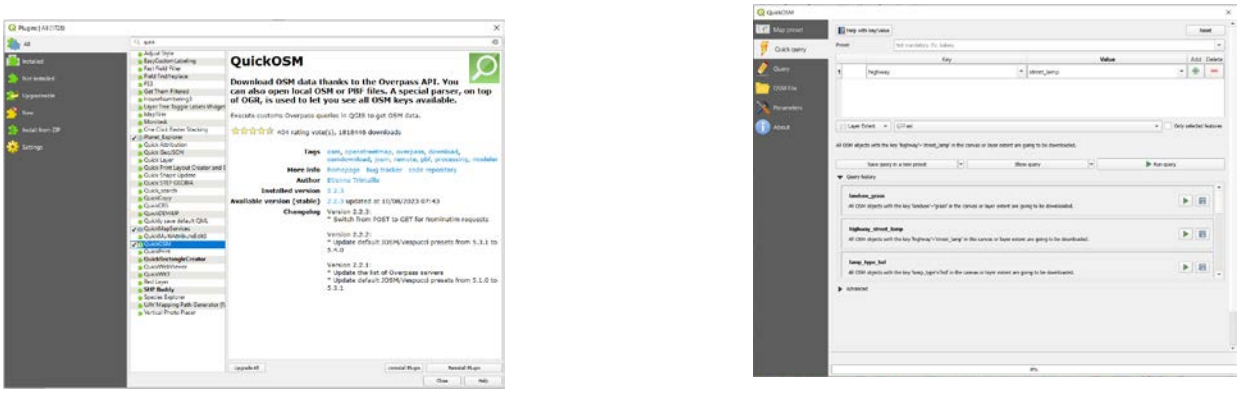

Figure 3. Installing the QuickOSM plugin and applying queries to OSM database.

As a result of the procedure for querying and downloading data from OSM (for example, street lighting), an information layer in vector format was obtained. To verify this data, other existing information layers at the national level were selected. For comparison, the metadata provided by the Chisinau City Hall and the metadata for the Linear Maps (Web Map Service (WMS) and Web Feature Service (WFS) allow viewing the base map - Base Map) 2017, for the territory of the Republic of Moldova, were selected. The linear map has approximately 90 layers with information about: administrative units, landscape, hydrography, buildings, roads, railways, utilities etc. The collection of objects was carried out based on orthoimages from 2016) which provide the possibility of accessing information through the WFS and WMS network services through specialized GIS programs.

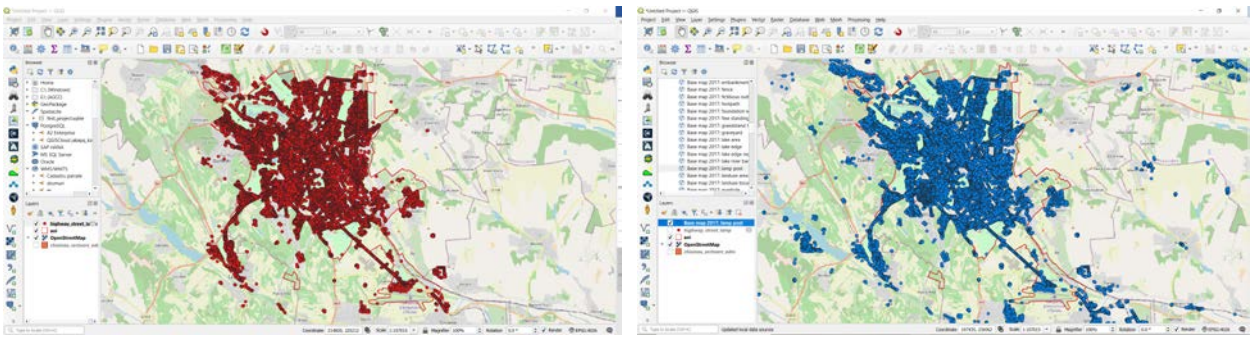

Figure 4. Analysis of SPATIAL datasets from OSM and Linear Maps.

In the city of Chisinau, sectors were identified where the OSM data (Figure 4) with greater coverage have a higher completeness than the official data existing on the NSDI or Geodata platform, or the State Geographic Information System at the local level for local public administration authorities (SIGSNL).

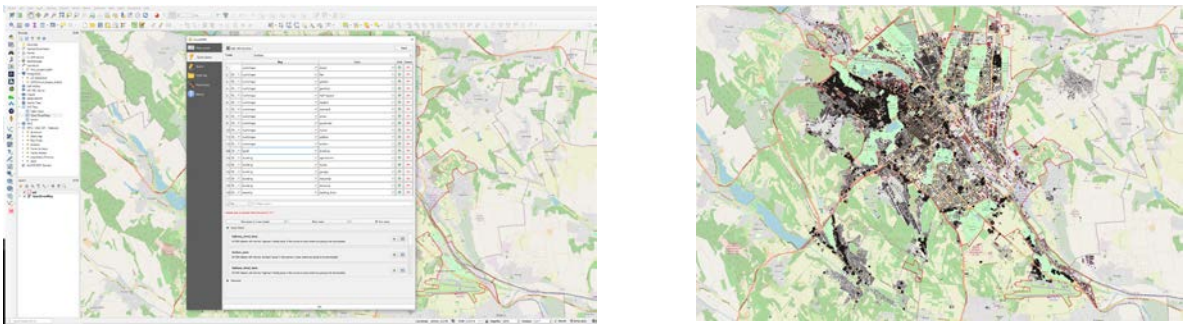

Figure 5. Query procedure for OSM data.

At the same time, another situation is attested in the analysis of residential buildings, using the same plugin, the query was performed based on the keyword constructions and the information referring to the residential buildings existing on the OSM was extracted for the AOI.

Analysing the obtained results, a discrepancy in the consistency of spatial data for different sectors of the Chisinau city was identified, namely from the OSM query (Figure 5) regarding constructions, where a total of 40954 units was obtained, and from the database of the P. I. Real Estate Cadastre - 3668 units. Thus, comparing the information provided by the relevant institution with the column in the attribute table building: levels and height, it was deduced that the information on the OSM requires updating, because the basic parameters for residential blocks: height (1085 units) and number of levels (17 units) are indicated at an insignificant number, while there is much more information (Figure 6).

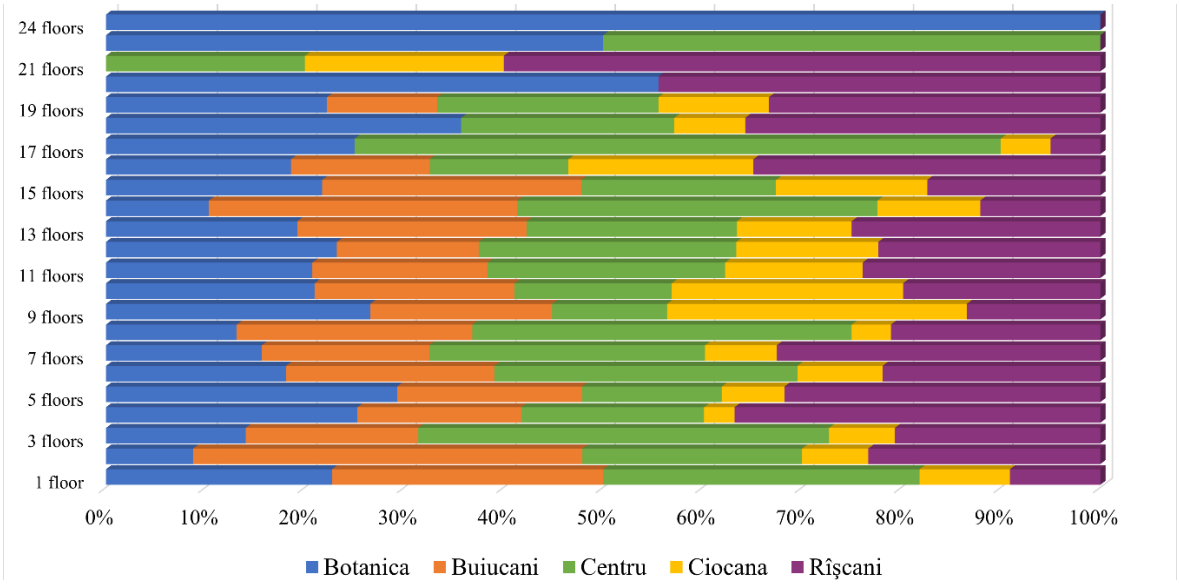

Figure 6. Analysis of residential buildings distribution in the Chisinau city [16].

Also, visually, by using the orthophoto image accessed through the visualization service (WMS) and by applying the Map Swipe tool plugin (Figure 7), entire sectors were identified where buildings are not represented on OSM. At the same time, by applying the Street View tool, it was established that many buildings are in reality private houses.

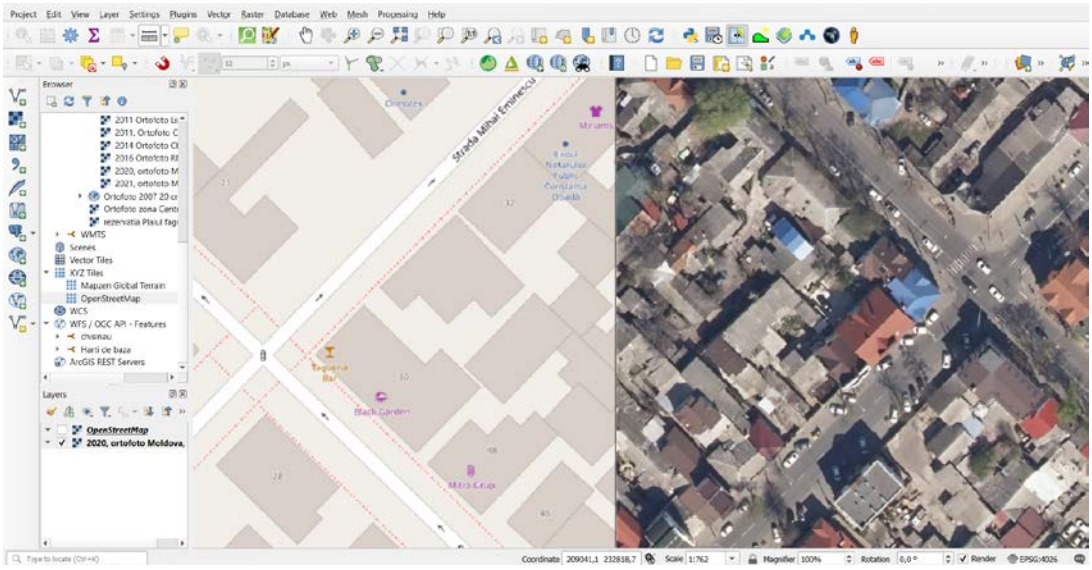

Figure 7. Applying the MapSwipeTool tool for spatial data comparison.

Another analysis was performed to assess the completeness of the data on road infrastructure. Thus, using the same plugin for downloading data from OSM, it was visually observed that the spatial data is much more qualitative, considering that this project has a great application for mobility and identifying the most optimal traffic directions. Also, the analysis of the availability of spatial data was performed with reference to the area/parking spaces available. Thus, for comparison, the data provided by the Chisinau City Hall (General Directorate of Architecture, Urbanism and Land Relations), through the download network services (WFS) and the data from OSM by applying the query using keywords, were used.

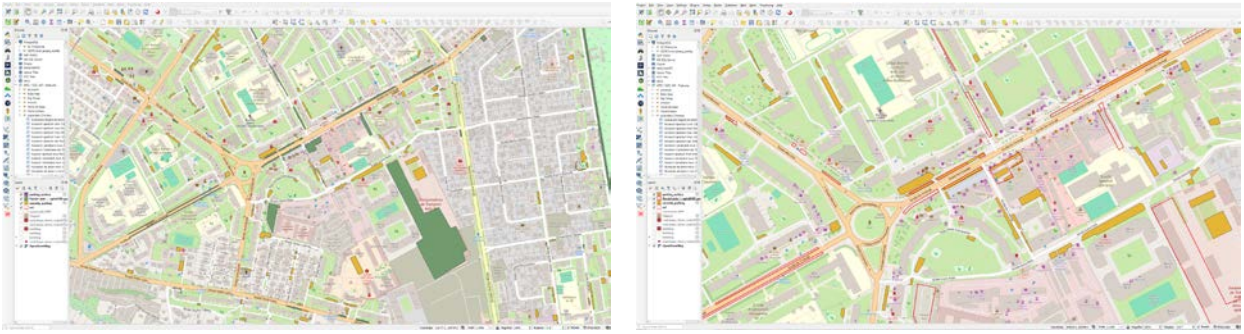

Figure 8. Comparison of data referring to parking available via download from OSM and SIGSNL download network services.

Following the visual analysis of the information, it was determined that it complements each other, and for a more detailed analysis of the current situation, also more layers and information sources should be used (Figure 8). The comparison with the data provided by the P. I. Real Estate Cadastre could not be carried out because from the available registers only information can be extracted referring to the garages within the residential blocks, the total number of which for the entire city of Chisinau is 3440, and the underground parking lots, which represent 12821 in number. Another analysis was carried out with reference to the spatial data about roads and access roads, and the initial information for the analysis was downloaded by Geofabrik and subsequently cropped for the area of interest (Figure 9).

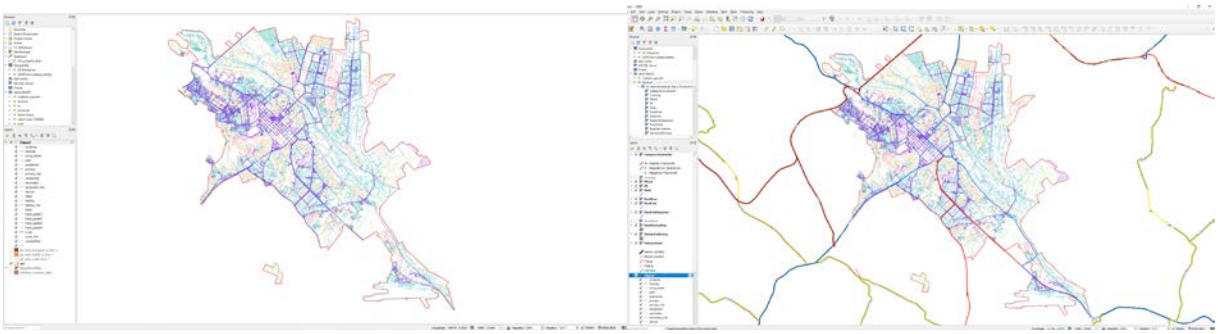

Figure 9. Comparison of data with reference to roads, OSM and the WMS service of the State Road Administration.

The comparison was made with the national data provided through visualization services by the State Road Administration, namely the spatial data set containing public roads - public utility roads intended for road and pedestrian traffic in order to meet the general road transport requirements of the national economy and the population and for the defense of the country. These roads represent public property of the state and ensure the main international road connections, the connection between the capital of the country and the cities-residences, municipalities and objects of republican importance, as well as the

connection between them [17] and through WMS visualization services - National public roads (Magistral, Republican and Regional ones).

4. Discussions

Accurate and up-to-date cartographic products are now an essential resource for a wide range of applications, education, science but also for the development of society in general. Producing and updating spatial data in a constantly changing world remains a major scientific and practical challenge especially for public institutions, where the process of producing and updating spatial data is currently very complex and bureaucratic. The involvement of citizens in the collection of geographic data has greatly influenced the development and use of maps and related data, having an impact on the performance of every routine activity. Digital resources such as Google Maps, Google Earth, Bing Maps and even maps that are generated by users through projects such as OSM are widely used by various categories of users. At the same time, verifying the correctness of these data is equally important, and the procedure for verifying the completeness and accuracy of these data remains an open problem that will continue to require a complex approach.

It has been shown that OSM is now widely used for applications such as web maps and navigation services, and OSM data has been used in areas such as urban planning [18], monitoring of sustainable development goals [19], disaster management [20], public health [21], to support crisis response during the COVID-19 pandemic [22], etc. Considering the very vast areas where spatial data can be used, the process of permanent analysis of consistency, accuracy is very important, especially for urban areas where a larger number of geographic information users are concentrated.

5. Conclusions

The development trend of VGI collection will become even more integrated with contemporary technologies, such as artificial intelligence, augmented reality, the Internet of Things (IoT) and gamification. Free and open global spatial data are valuable resources in the teaching-learning process for any level, but also with particular application in the economic development and research process in different fields. Thus, this evolution will transform open-source platforms into a fundamental pillar for various industries, increasingly involving communities and providing a collaborative framework for solving local and global problems.

The purpose of this research was to assess the completeness of VGI spatial data and in particular, to assess the completeness of data from the OSM project. Although there are previous researches on the quality and completeness of OSM data, this study is the first attempt carried out for the Chisinau city, Republic of Moldova. The methodology used consisted of comparing the completeness elements of OSM data with the NSDI Republic of Moldova spatial data and different sources and registers with data related to the topic of the presented research. In general, the results showed that OSM has accurate and up-to-date data, which indicates the usefulness of the data for developing projects in various fields of activity.

Conflicts of Interest: The author declares no conflict of interest.

References

1. Heipke, Ch. Crowdsourcing geospatial data. *ISPRS Journal of Photogrammetry and Remote Sensing* 2010, 65(6), pp. 550-557.
2. Wang, M.; Li, Q.; Hu, Q.; Zhou, M. Quality analysis of open street map data. *International Archives of the Photogrammetry, Remote Sensing and Spatial Information Sciences - ISPRS Archives* 2013, pp.155-158.

3. Anderson, J.; Dipto S.; Leysia P. Corporate Editors in the Evolving Landscape of OpenStreetMap. *ISPRS International Journal of Geo-Information* 2019, 8(5), 232.
4. Flanagin, A.; Metzger, M. The Credibility of Volunteered Geographic Information. *GeoJournal* 2008, 72, pp. 137-148.
5. Borkowska, S.; Pokonieczny, K. Analysis of OpenStreetMap Data Quality for Selected Counties in Poland in Terms of Sustainable Development. *Sustainability* 2022, 14, 3728.
6. Haklay, M. How Good Is Volunteered Geographical Information? A Comparative Study of OpenStreetMap and Ordnance Survey Datasets. *Environment and Planning B: Planning and Design* 2010, 37, pp. 682–703.
7. Fan, H.; Zipf, A.; Fu, Q.; Neis, P. Quality Assessment for Building Footprints Data on OpenStreetMap. *Int. J. Geogr. Inf. Sci.* 2014, 28, pp. 700-719.
8. Raifer, M.; Troilo, R.; Kowatsch, F.; Auer, M.; Loos, L.; Marx, S.; Przybill, K.; Fendrich, S.; Mocnik, F.-B.; Zipf, A. OSHDB: A Framework for Spatio-Temporal Analysis of OpenStreetMap History Data. *Open Geospat. Data Softw. Stand.* 2019, 4, 3.
9. Herfort, B.; Lautenbach, S.; Porto de Albuquerque, J.; Anderson, J.; Zipf, A. The Evolution of Humanitarian Mapping within the OpenStreetMap Community. *Sci. Rep.* 2021, 11, 3037.
10. National Geospatial Data Fund. Available online: https://geoportal.md/ (accessed on 25.11.2024).
11. Cara, O. Chisinau in Figures, Statistical Yearbook. National Bureau of Statistics of the Republic of Moldova, Chișinău, 2023, 116 p.
12. Brovelli, M.; Zamboni, G. A New Method for the Assessment of Spatial Accuracy and Completeness of OpenStreetMap Building Footprints. *ISPRS Int. J. Geo-Inform* 2018, 7, 289.
13. Geofabrik. Available online: https://download.geofabrik.de/ (accessed on 20.11.2024).
14. Van, O. Spatial data quality: from description to application. PhD Thesis, Wageningen Universiteit, Wageningen, 2006.
15. National Spatial Data Infrastructure of the Republic of Moldova. Available online: https://geoportalinds.gov.md (accessed on 29.11.2024).
16. Public Institution Real Estate Cadastre. Available online: https://ipcbi.gov.md/ro/content/e-cadastru (accessed on 29.11.2024).
17. Metadata. Available online: https://geoportalinds.gov.md (accessed on 29.11.2024).
18. Milojevic-Dupont, N.; Hans, N.; Kaack, L.H.; Zumwald, M.; Andrieux, F.; de Barros Soares, D. Learning from urban form to predict building heights. *PLoS ONE* 2020, 15, pp. 1–22.
19. Van Den Hoek, J.; Friedrich, H. K.; Ballasiotes, A. Development after Displacement: Evaluating the Utility of OpenStreetMap Data for Monitoring Sustainable Development Goal Progress in Refugee Settlements. *ISPRS Int. J. Geo-Inform.* 2021, 10, 153.
20. Scholz, S.; Knight, P. Volunteered Geographic Information for Disaster Risk Reduction-The Missing Maps Approach and Its Potential within the Red Cross and Red Crescent Movement. *Remote Sens.* 2018, 10, 1239.
21. Pinho, M.; Flueckiger, B.; Valentin, A.; Kasdagli, M.-I.; Kyriakou, K.; Lakerveld, J.; Mackenbach, J-D.; Joline W.J. Beulens, J.W.J.; Kees de Hoogh. The quality of OpenStreetMap food-related point-of-interest data for use in epidemiological research. *Health & Place* 2023, 83, 103075.
22. Mooney, P.; Grinberger Y.; Grinberger Y. OpenStreetMap Data Use Cases During the Early Months of the COVID-19 Pandemic. In: *COVID-19 Pandemic, Geospatial Information, and Community Resilience*, CRC Press, 2021, 16 p.

Citation: Sîrbu, R. Analysis methodology of openstreetmap data completeness (case study: Chisinau city). *Journal of Engineering Science* 2024, XXXI (4), pp. 157-165. https://doi.org/10.52326/jes.utm.2024.31(3).01.

Submission of manuscripts: jes@meridian.utm.md

Journal of Engineering Science *Vol. XXXI, no. 4 (2024), pp. 166 - 174*
Fascicle *Architecture, Civil and Environmental Engineering* *ISSN 2587-3474*
Topic *Environmental Engineering* *eISSN 2587-3482*

https://doi.org/10.52326/jes.utm.2024.31(4).12
UDC 556.5:311:631.841(478)"2019/2021"

STATISTICAL EVALUATION OF DATA ON THE POLLUTION OF THE PRUT RIVER WITH AMMONIUM NITROGEN

Galina Marusic, ORCID: 0000-0002-2984-2055,
Rodica Branişte, ORCID: 0000-0002-6935-8444,
Nina Sava, ORCID: 0000-0001-6827-2721,
Victor Ababii, ORCID: 0000-0002-0769-8144,
Viorel Cărbune, ORCID: 0000-0002-1556-4453,
Tamara Tiholaz*, ORCID: 0000-0001-2215-835X

Technical University of Moldova, 168, Ştefan cel Mare Blvd., Chisinau, Republic of Moldova
*Corresponding author: *Tamara Tiholaz, tamara.tiholaz@ati.utm.md*

Received: 10. 30. 2024
Accepted: 12. 02. 2024

Abstract. This paper analyzes the pollution of the Prut River with ammonium nitrogen (NH_4^+) during the period 2019–2021, focusing on exceedances of the maximum allowable concentration (MAC) of 0.2 mg/L. The analyzed data comes from measurements taken in various localities along the river. The results indicate constant pollution with significant exceedances of the MAC, the highest measured concentration being 3.85 mg/L. Descriptive analysis reveals an asymmetric distribution, with extreme values raising the average to 0.8456 mg/L. The 2019–2021 period was chosen because this interval recorded significant MAC exceedances. Urban localities, such as Leova and Lipcani, show the highest concentrations, and are correlated with intense human activities. The conclusions emphasize the need for urgent action to reduce pollution and protect aquatic ecosystems and public health.

Keywords: *aquatic ecosystem, ammonium nitrogen pollution, maximum allowable concentration, Prut River, statistical analysis.*

Abstract. Această lucrare analizează poluarea râului Prut cu azot provenit din amoniu (NH_4^+) în perioada 2019–2021, punând accent pe depășirile concentrației maxime admisibile (CMA) de 0,2 mg/L. Datele analizate provin din măsurători efectuate în diverse localități de-a lungul râului. Rezultatele arată o poluare constantă, cu depășiri semnificative ale CMA, cea mai mare concentrație măsurată fiind de 3,85 mg/L. Analiza descriptivă evidențiază o distribuție asimetrică, cu valori extreme care ridică media la 0,8456 mg/L. Perioada 2019–2021 a fost selectată din considerentul că în acest interval s-au înregistrat depășiri semnificative ale CMA. Localitățile urbane, precum Leova și Lipcani, prezintă cele mai mari concentrații, fiind corelate cu activitățile umane intense. Concluziile subliniază necesitatea unor măsuri urgente pentru reducerea poluării și protejarea ecosistemelor acvatice și a sănătății publice.

Cuvinte cheie: *ecosistem acvatic, poluare cu azot de amoniu, concentrație maximă admisibilă, râul Prut, analiza statistică.*

1. Introduction

Water quality is a key indicator of the overall state of the environment and a key determinant of human health, biodiversity and ecosystem sustainability. Water pollution, caused by anthropogenic activities, is a global challenge affecting freshwater resources that are essential for life. Chemical, microbiological and organic pollutants can alter the natural balance of aquatic ecosystems, endangering both flora and fauna and human uses of water resources [1,2].

High concentrations of pollutants, such as ammonium nitrogen (NH_4^+), pose a significant threat to the health of aquatic ecosystems and the quality of drinking water. Ammonium nitrogen typically originates from agricultural and industrial activities, negatively impacting aquatic biodiversity and contributing to water eutrophication. This study focuses on analyzing ammonium nitrogen concentrations in the Prut River during the period 2019–2021, which exceeded the maximum allowable concentrations (MAC). According to environmental regulations for the protection of aquatic life, the maximum allowable concentration (MAC) for ammonium nitrogen in freshwater is 0.2 mg/L. Measured concentrations exceeding acceptable limits can negatively affect the aquatic ecosystem [3-5].

Furthermore, prolonged exposure to contaminated water with ammonium nitrogen can have serious consequences for human health, including an increased risk of gastrointestinal disorders, methemoglobinemia ("blue baby syndrome") on infants, and other metabolic disturbances. Consumption of water with high concentrations of ammonium nitrogen can worsen the health condition of individuals with pre-existing sensitivities, such as kidney or liver health disorders. Therefore, detailed monitoring of water quality is significant for protecting public health and ecosystems [1,6].

Computational solutions and statistical methods are essential for evaluating water quality and understanding the spatio-temporal distribution of pollutants in river systems. Techniques such as histograms and box plots enable visual representation of data distribution, highlighting concentration variability and potential anomalies over time. Frequency analysis for concentration intervals further allows for the categorization of pollution levels, offering a clear overview of how often specific thresholds are exceeded. These methods provide critical insights into the behavior of ammonium nitrogen concentrations, enabling researchers to identify pollution trends, assess the severity of exceedances, and support decision-making processes for water resource management. By employing computational tools to process and analyze environmental data, it becomes possible to derive actionable insights that contribute to safeguarding aquatic ecosystems and ensuring compliance with environmental regulations [7–9].

2. Problem formulation

2.1. Water quality in the Prut River

Prut River, as an important source of freshwater in the Republic of Moldova, plays an important role in supplying with drinking water, irrigation, and maintaining aquatic biodiversity. The water quality of this river has been constantly monitored in recent years, showing significant variability in physicochemical and biological indicators. According to data published by the Agency of Environment of the Republic of Moldova and reports from the European Union on the management of the Danube River basin, the Prut River has experienced episodes of pollution with nutrients, including nitrogen and phosphorus, which contribute to eutrophication and affect the ecological balance of aquatic ecosystems [10,11].

According to the International Commission for the Protection of the Danube River (ICPDR, 2021) water quality in transboundary rivers in the region, including the Prut River, is significantly influenced by agricultural and urban activities. Between 2019 and 2023, values for key water quality indicators, such as dissolved oxygen concentrations, total nitrogen, and phosphorus, showed occasional exceedances of the limits set by European environmental standards (Water Framework Directive, 2000/60/EC). Furthermore, these deviations were primarily attributed to nutrients runoff from anthropogenic activities, which have a direct impact on aquatic life [7,12,13].

For an efficient and detailed analysis of data on ammonia nitrogen pollution in the Prut River, the use of computational techniques plays an important role. These techniques allow the processing of large volumes of data, identification of trends, and visualization of the spatiotemporal distribution of pollutant concentrations. Advanced statistical tools, combined with computational methods such as modeling and numerical simulation, provide an in-depth understanding of pollution phenomena.

Moreover, the use of specialized software for statistical analysis and data visualization, such as R or Python, enables the generation of precise and reproducible results. This issue contributes to the formulation of evidence-based solutions, essential for reducing pollution and protecting aquatic ecosystems [7,8,11,14].

2.2. Ammonium nitrogen pollution

Ammonium nitrogen (NH_4^+) is one of the most important pollutants that affect water quality in rivers, and has diverse origins: runoff from agricultural land, industrial discharges, and insufficiently treated wastewater. The monitoring of the Prut River during the period 2019–2021 highlighted frequent exceedances of the maximum allowable concentration (MAC) of 0.2 mg/L set for surface waters intended for the protection of aquatic life [10].

High ammonium nitrogen concentrations can cause significant negative effects, such as to reduce dissolved oxygen level, harm sensitive species and increase fish mortality. Studies have shown that NH_4^{++} concentrations reached values of up to 0.8 mg/L in some parts of the river during the analyzed period, indicating chronic pollution [4,5,15].

Beyond its impact on aquatic ecosystems, elevated ammonium nitrogen levels can affect the usability of water resources for human consumption, recreation, and agriculture. Excessive NH_4^+ concentrations require additional treatment to meet drinking water standards, increasing costs and operational challenges for local water utilities. Moreover, such pollution can degrade the aesthetic and recreational value of river ecosystems, further emphasizing the need for proactive measures to address this issue [4,5,15].

The persistence of high ammonium nitrogen levels in the Prut River underscores the need for integrated water resource management strategies that address pollution sources holistically. Collaboration between governmental bodies, local communities, and industries is critical to implementing effective solutions. Measures such as reducing fertilizer runoff, upgrading wastewater treatment facilities, and enhancing river monitoring networks can significantly mitigate ammonium nitrogen pollution and safeguard the river's ecological integrity. Despite existing regulations and regular monitoring, ammonium nitrogen pollution of the Prut River remains a persistent problem. A detailed statistical assessment of NH_4^+ concentrations in 2019-2021 is needed in order to identify trends, the main sources of pollution and its effects on the ecosystem. This analysis will provide a basis for proposing viable solutions to reduce pollution and improve water quality in the Prut River.

The lack of comprehensive and integrated approaches to address pollution sources further exacerbates the problem. In many cases, monitoring programs focus on isolated measurements rather than continuous assessments, limiting the ability to detect real-time pollution dynamics. Moreover, insufficient coordination between local authorities and industries hampers the enforcement of environmental regulations, allowing polluting activities to persist without significant penalties or remediation efforts.

Addressing the ammonium nitrogen problem in the Prut River requires not only a detailed statistical evaluation but also a multi-sectoral approach. Collaborative efforts between scientists, policymakers, and local communities are essential to developing targeted interventions. Such efforts should include public awareness campaigns, stricter enforcement of pollution limits, and investments in modernizing wastewater treatment systems to prevent further degradation of water quality. Additionally, expanding monitoring networks to include more frequent sampling and advanced analytical techniques can provide deeper insights into pollution patterns. Without immediate and sustained action, the ecological and economic impacts of ammonium nitrogen pollution will continue to worsen.

3. Solving the problem

In order to solve the formulated problem, were studied the data on ammonium nitrogen concentrations in the Prut River, Table 1.

Table 1

Exceedances of the MAC for ammonium nitrogen in the Prut River (2019-2021)

Nr	Locality	Date	The registered value (mg/L)
1.	Village Valea Mare	15.05.2019	0.5
2.	Town Leova	19.06.2019	3.85
3.	Town Ungheni	13.11.2019	0.62
4.	Village Valea Mare	13.11.2019	1.07
5.	Village Giurgiulesti	20.11.2019	0.55
6.	Village Valea Mare	12.02.2020	0.629
7.	Town Lipcani	03.05.2020	0.53
8.	Town Lipcani	05.06.2020	2.445
9.	Village Valea Mare	10.06.2020	0.434
10.	Town Lipcani	10.07.2020	0.439
11.	Town Ungheni	15.07.2020	0.818
12.	Village Valea Mare	15.07.2020	0.870
13.	Town Cahul	19.08.2020	1.123
14.	Town Leova	19.08.2020	0.685
15.	Village Giurgiulesti	19.08.2020	0.706
16.	Village Giurgiulesti	09.09.2020	0.418
17.	Town Lipcani	13.10.2020	0.413
18.	Village Valea Mare	14.10.2020	0.402
19.	Village Giurgiulesti	21.10.2020	0.584
20.	Town Lipcani	03.03.2021	0.937
21.	Village Valea Mare	10.03.2021	0.51
22.	Village Giurgiulesti	17.03.2021	0.488
23.	Village Pererita	23.03.2021	1.013
24.	Town Lipcani	06.04.2021	0.442
25.	Village Braniste	06.04.2021	0.417
26.	Town Lipcani	05.05.2021	0.503

These values represent the concentrations of ammonium nitrogen measured at various sections of the river and within a specific time interval. From Table 1, significant variations in the measured concentrations can be observed, depending on the localities, including:

Maximum concentrations by locality:

The highest recorded value**:**

- town Leova (3.85 mg/L, 19.06.2019) **– an alarming level, nearly 20 times higher than the MAC of 0.2 mg/L.**

Other significant exceedances**:**

- town Lipcani (2.445 mg/L, 05.06.2020);
- village Valea Mare (1.07 mg/L, 13.11.2019);
- town Cahul (1.123 mg/L, 19.08.2020).

Exceedances of the MAC by locality:

- village Valea Mare: Most of the measured concentrations exceed the MAC, with a maximum value of 1.07 mg/L;
- town Lipcani: presents two significant exceedances, including one of 2.445 mg/L;
- town Leova: records the highest value during the analyzed period;
- village Pererita: A single measurement, but significant, with an exceedance of 1.013 mg/L;
- village Giurgiulești: the values are more moderate, but the frequency of exceedances suggests consistent pollution.

General observations:

- geographic distribution of pollution: Localities near large cities (Leova, Cahul, Ungheni) tend to record higher values, likely due to more intense human activities**;**
- rural localities (Valea Mare, Giurgiulești, Pererita): frequent exceedances, but at lower values than in cities, may be associated with agricultural pollution sources**;**
- severity of pollution: MAC exceedances are variable, and some extreme values (over 3 mg/L) indicate episodes of acute pollution**.**

To obtain an overview of the data distribution presented in Table 1, a descriptive analysis was performed. The following results were obtained:

Table 2

Results of the descriptive analysis

Parameter	Value	Interpretation
Average	0.8456 mg/L	On average, the ammonium nitrogen concentration exceeds the maximum allowable concentration (MAC).
Median	0.629 mg/L	The median being lower than the average suggests a skewed distribution, influenced by a few high values.
Standard deviation	0.7865 mg/L	The high variance indicates a large dispersion of the data, with the presence of extreme values.
Minimum value	0.402 mg/L	The lowest measured value is above the MAC limit of 0.2 mg/L, indicating constant pollution.
Maximum value	3.85 mg/L	A severe exceedance of the MAC, suggesting episodes of acute pollution.

The data shows significant exceedances of the MAC (0.2 mg/L). For example, values of 2.445 mg/L and 3.85 mg/L are considered extreme and can be visualized as outliers. In

order to show the frequency with which concentrations occur in different intervals, a histogram was used, Figure 1.

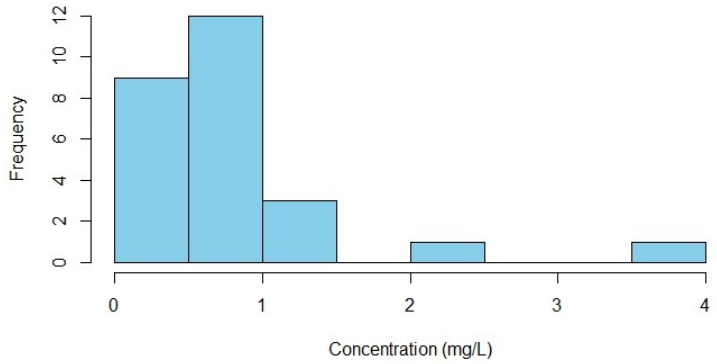

Figure 1. Histogram of Ammonium Nitrogen Concentrations in the Prut River.

From Figure 1, it can be noticed that most of the values are between 0.4 mg/L and 1.0 mg/L, but there are less frequent bars that exceed 2.0 mg/L and 3.0 mg/L. These highlight potential excessive pollution.

Figure 2 presents a boxplot graph, which summarizes the data distribution and highlights extreme values (outliers).

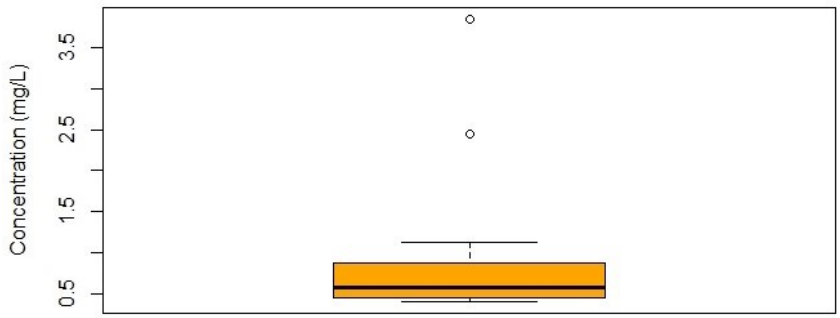

Figure 2. Boxplot of Ammonium Nitrogen Concentrations in the Prut River.

The thick line inside the rectangle represents the median (0.629 mg/L). The box represents the 25th and 75th percentiles (Q1 and Q3). The lines (whiskers) indicate values that fall within the normal range, while the points outside them are outliers. Significant outliers, such as 2.445 mg/L and 3.85 mg/L, are clearly outside the main distribution.

The evolution of the pollutant concentration during the observation period is presented in Figure 3. Each point represents a concentration value, and the line connects the observations to illustrate the variation. A dotted red line is included at 0.2 mg/L, representing the MAC. All values that exceed the MAC are above the MAC line.

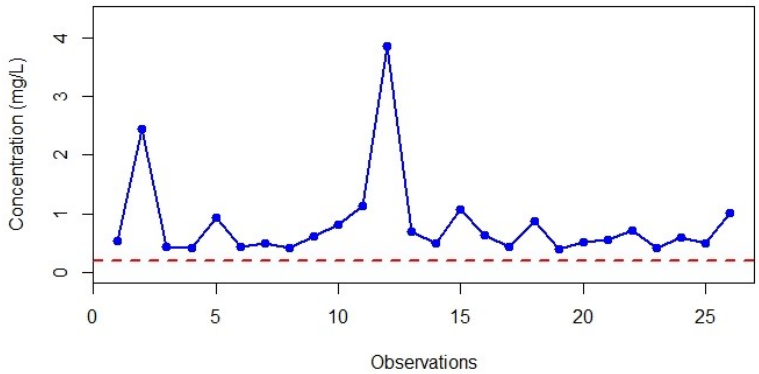

Figure 3. Ammonium Nitrogen concentration over time.

The results of the analysis in order to highlight how frequently the permissible limits of 0.2 mg/L are exceeded are presented in Table 3.

Table 3

Frequencies for concentration intervals

Concentration interval (mg/L)	Absolute frequency	Relative frequency (%)
0.0 – 0.5	13	50.0
0.5 – 1.0	9	34.6
1.0 – 1.5	2	7.7
1.5 – 2.0	0	0.0
2.0 – 2.5	1	3.8
2.5 – 3.0	0	0.0
3.0 – 4.0	1	3.8

From Table 3, the following can be observed:

- the majority of values (50%) are within the 0.0 – 0.5 mg/L range, indicating that at certain times, the ammonia nitrogen concentration was close to low values;

- 34.6% of the values are between 0.5 – 1.0 mg/L, and this range represents a significant exceedance of the MAC;

- concentrations greater than 2.0 mg/L are rare (7.6% in total), but they indicate severe pollution episodes.

There are 26 observations, and all exceed the MAC limit (0.2 mg/L). Therefore, the situation in the river indicates constant pollution.

4. Conclusions

The analysis of ammonium nitrogen concentrations in the Prut River for the period 2019–2021 highlights constant and significant pollution, all measured values exceeding the maximum allowable concentration of 0.2 mg/L. These exceedances are more pronounced in urban areas, such as Leova, where the maximum concentration reached 3.85 mg/L, nearly 20 times above the acceptable limit.

The analyzed data suggest a clear association between anthropogenic activities, such as intensive agriculture and the lack of proper wastewater treatment, and the high pollution levels. Rural localities, such as Valea Mare and Giurgiulești, frequently record exceedances of the MAC, but at more moderate levels, indicating more diffuse sources of pollution.

The distribution of concentrations is characterized by extreme values, reflected in the high standard deviation (0.7865 mg/L) and the presence of outliers. These aspects underline the need for strict monitoring policies and pollution reduction measures.

The use of statistical tools such as histograms, box plots, and frequency analysis provided valuable insights into the variability and trends in ammonium nitrogen concentrations. These methods revealed the magnitude and persistence of pollution, as well as its spatial and temporal distribution, supporting the hypothesis that both point and diffuse pollution sources significantly contribute to water quality degradation. Such analytical approaches are essential for effectively communicating the urgency of the issue to stakeholders and policymakers.

Implementing sustainable practices to mitigate pollution requires a multi-faceted approach, involving improved wastewater treatment infrastructure, promotion of environmentally friendly agricultural practices, and robust enforcement of environmental

regulations. Awareness campaigns targeting local communities and industries are crucial for fostering cooperation and accountability in reducing pollutant discharge into aquatic systems.

Future research should focus on extending the monitoring period and incorporating additional chemical and biological indicators to provide a more comprehensive assessment of water quality. The integration of advanced computational models, coupled with real-time monitoring systems, can further enhance the ability to predict and manage pollution events, ultimately contributing to the long-term protection of the Prut River ecosystem.

5. Recommendations

1. **Implementation of strict pollution reduction measures.** To improve wastewater treatment and to promote sustainable agricultural practices in the affected regions.
2. **Extensive and continuous monitoring.** To establish an automated monitoring system in order to identify quickly the episodes of severe pollution.
3. **Education and awareness of the local population.** To inform communities about the impact of human activities on water quality and health.
4. **Cross-border cooperation.** Since the Prut River is a transboundary river, cooperation with neighboring countries in order to implement integrated environmental protection solutions.

These conclusions and recommendations aim to protect the ecosystems of the Prut River and to reduce the risks of public health.

Conflicts of Interest: The authors declare no conflict of interest.

References

1. World Health Organization (WHO). Guidelines for Drinking-water Quality. Geneva, Switzerland, 2017. Available online: https://www.who.int/publications/i/item/9789241549950 (accessed on17.10.2024).
2. European Environment Agency (EEA). Regional water report. 2020. Available online: https://www.eea.europa.eu/en/analysis/publications/regional-water-report (accessed on 31.10.2024).
3. Carpenter, S. R.; Caraco, N. F.; Correll, D. L.; Howarth, R. W.; Sharpley, A. N.; Smith, V. H. Nonpoint pollution of surface waters with phosphorus and nitrogen. *Ecological Applications* 1998, 8(3), pp. 559–568.
4. De Vries, W.; Posch, M.; Simpson, D.; de Leeuw, F.A.A.M.; Van Grinsven, H.J.M.; Schulte-Uebbing, L.F.; Sutton, M.A.; Ros, G.H. Trends and geographic variation in adverse impacts of nitrogen use in Europe on human health, climate, and ecosystems: A review. *Earth-Science Reviews* 2024, 253, pp. 1-48.
5. Smith, V. H. Eutrophication of freshwater and coastal marine ecosystems: A global problem. *Environmental Science and Pollution Research* 2003, 10, pp. 126-139.
6. Zainurin, S.N.; Ismail, W.Z.W.; Mahamud, S.N.I.; Ismail, I.; Jamaludin, J.; Ariffin, K.N.Z.; Kamil, W.M.W.**.** Advancements in Monitoring Water Quality Based on Various Sensing Methods: A Systematic Review. *International Journal of Environmental Research and Public Health* 2022, 19(21), 14080.
7. Marusic, G.; Sava, N.; Braniște, R. Research on water quality in the Dniester River 2019-2021. *Annals of "Dunarea de Jos" University of Galați. Fascicle III* 2023, 45(1), pp. 5 -10.
8. Sava, N.; Marusic, G. Digital techniques for water pollution control. *Journal of Engineering Science* 2021, 28(2), pp. 138-148.
9. Giri, S.; Qiu, Z. Understanding the Relationship of Land Uses and Water Quality in Twenty First Century: A Review. *Journal of Environmental Management* 2016*,* 173*,* pp. 41–48.
10. Environmental Agency of the Republic of Moldova. Annual report. Quality of environmental components monitored in the environmental reference laboratory, year 2021. DGLRM, 2022. Available online: https://am.gov.md/sites/default/files/document/attachments/Anuar-DGLRM-2021-fin_0.pdf (accessed on 07.11.2024) [in Romanian].
11. Sava, N.; Marusic, G. State of water quality in the Prut River for the period of 2019-2021. In: *Proceedings of the 12th International Conference on Electronics, Communications and Computing*, Chisinau, Republic of Moldova, 20-21 October, 2022, pp. 140-146.

12. International Commission for the Protection of the Danube River (ICPDR). Danube River Basin Management Plan. Update 2021. Available online: https://www.icpdr.org/sites/default/files/nodes/documents/drbmp_2021_final_hires.pdf (accessed on 11.11.2024).
13. Directive 2000/60/EC of the European Parliament and of the Council establishing a framework for the Community action in the field of water policy (Water Framework Directive). Available online: https://www.eea.europa.eu/policy-documents/directive-2000-60-ec-of (accessed on 29.11.2024).
14. Branişte, R.; Marusic, G. Mathematical modeling of pollutant transport and dispersion processes in the Dniester River. *Journal of Engineering Science* 2020, 27(4), pp. 151-162.
15. Rabalais, N.N.; Nixon, S.W. Dedicated issue: Nutrient over-enrichment in coastal waters: global patterns of cause and effec. *Journal of Estuaries* 2022, 25(4), pp. 639-900.

Citation: Marusic, G.; Branişte, R.; Sava, N.; Ababii, V.; Cărbune, V.; Tiholaz, T. Statistical evaluation of data on the pollution of the prut river with ammonium nitrogen. *Journal of Engineering Science* 2024, XXXI (4), pp. 166-174. https://doi.org/10.52326/jes.utm.2024.31(3).01.

Submission of manuscripts: jes@meridian.utm.md

Journal of Engineering Science *Vol. XXXI, no. 4 (2024), pp. 175 - 192*
Fascicle *Food Engineering* *ISSN 2587-3474*
Topic *Biotechnologies, Food Chemistry and Food Safety* *eISSN 2587-3482*

https://doi.org/10.52326/jes.utm.2024.31(4).13
UDC 547.5:[634.86+663.2]

THE ROLE OF PROCYANIDINS IN GRAPES AND WINES: EFFECTS ON QUALITY AND COMPOSITION

Alexandra Arseni *, ORCID: 0009-0002-0166-4215,
Sorina Crudu, ORCID: 0009-0003-6697-4828

Technical University of Moldova, 168 Stefan cel Mare Blvd., Chisinau, Republic of Moldova
* Corresponding author: Arseni Alexandra, *alexandra.arseni@enl.utm.md*

Received: 10. 08. 2024
Accepted: 11. 22. 2024

Abstract. Proanthocyanidins in grapes and wine are oligomers and polymers of flavan-3-ols, predominantly connected through C4–C8 and/or C4–C6 bonds (B-type). These compounds significantly influence red wine's sensory profile, particularly its color and mouthfeel. In addition, proanthocyanidins are recognized for their antioxidant and radical-scavenging properties, capable of neutralizing reactive oxygen species and preventing cellular damage caused by oxidative stress. These properties give them an important role in protecting health, with beneficial effects on the body by reducing the risk of cardiovascular diseases and cancer. The aim of the article is to explore the role of proanthocyanidins in grapes and wine, focusing on their contributions to wine's sensory characteristics such as color, astringency, and mouthfeel. It aims to examine the factors influencing their composition, the transformations they undergo during winemaking and aging, and their broader implications for wine quality, stability, and health benefits. The objectives of the study are to investigate the physical, chemical, and biochemical properties of procyanidins, as well as the influence of factors such as grape variety, ripeness, health status, climatic conditions, viticultural techniques, grape processing methods, wine stabilization, and aging techniques on their content.

Keywords: *procyanidins, grapes, wine, antioxidant and antiradical activities.*

Rezumat. Proantocianidinele din struguri și vinuri sunt oligomeri și polimeri ai flavan-3-olilor, conectați predominant prin legături C4–C8 și/sau C4–C6 (tip B). Acești compuși influențează semnificativ profilul senzorial al vinului roșu, în special culoarea și senzația la gust. În plus, proantocianidinele sunt recunoscute pentru proprietățile lor antioxidante și antiradicalice, fiind capabile să neutralizeze specii reactive de oxigen și să prevină deteriorarea celulară cauzată de stresul oxidativ. Aceste proprietăți le conferă un rol important în protejarea sănătății, având un efect benefic asupra organismului prin reducerea riscului de boli cardiovasculare și cancer. Scopul articolului este de a explora rolul proantocianidinelor în struguri și vin, concentrându-se pe contribuția acestora la caracteristicile senzoriale ale vinului, cum ar fi culoarea, astringența și senzația în gură. Acesta își propune să examineze factorii care influențează compoziția lor, transformările pe care le suferă în timpul vinificației și învechirii și implicațiile lor mai largi pentru calitatea

vinului, stabilitate și beneficiile pentru sănătate. Obiectivele studiului constau în investigarea proprietăților fizice, chimice și biochimice ale procianidinelor, precum și influența unor factori precum soiul de struguri, gradul de maturitate, starea de sănătate, condițiile climaterice, tehnicile viticole utilizate, metodele de prelucrare a strugurilor, stabilizarea vinurilor și tehnicile de maturare a acestora, asupra conținutului lor.

Cuvinte-cheie: *procianidine, struguri, vin, activitate antioxidantă și antiradicalică.*

1. Introduction

Proanthocyanidins are a vital group of polyphenolic compounds found abundantly in grapes and wine, especially red varieties, and are known for their significant contributions to wine's sensory characteristics, including color, astringency, and mouthfeel. Structurally, proanthocyanidins are composed of flavan-3-ol units, forming complex oligomers and polymers linked through specific bonds [1,2]. Their levels and composition in wine vary widely due to factors like grape variety, ripening stage, environmental conditions, viticultural practices, and winemaking methods. These compounds not only enhance the sensory appeal of wines but also possess antioxidant properties, which can affect the aging stability and health benefits associated with moderate wine consumption [3,6]. As wine ages, particularly in oak barrels, interactions between proanthocyanidins, anthocyanins, and wood-derived compounds lead to further transformations, impacting both the chemistry and sensory profile of the final product. This article explores the nature of proanthocyanidins in grapes and wine, examining their roles in sensory perception, their evolution during winemaking and aging, and the broader implications for wine quality and consumer experience [4,5].

2. Structure of proanthocyanidins

Procyanidins are a class of flavan-3-ol oligomers and polymers that are part of the larger flavonoid family. These compounds are found in various fruits (e.g., grapes, apples, and berries), cocoa, and wine [6]. Their structure is based on the catechin and epicatechin monomers linked by carbon-carbon bonds [7].

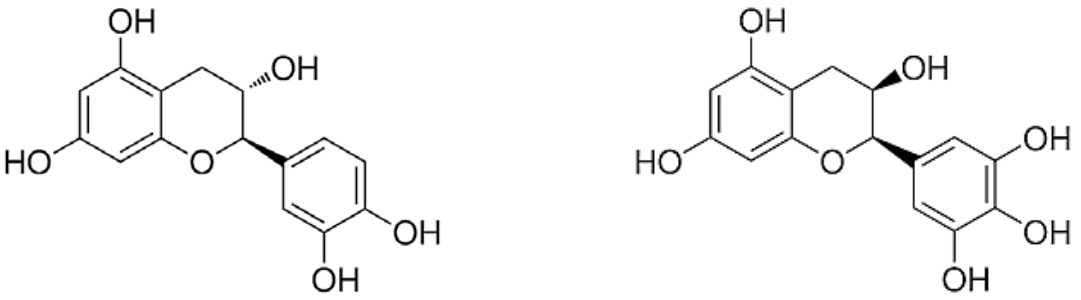

a) b)

Figure 1. Structure of catechin (a) and epicatechin (b) [8].

The chemical structure of procyanidins is based on monomeric units of catechin and epicatechin, which are flavan-3-ols characterized by a three-ring structure (A-ring, B-ring, and C-ring) with hydroxyl groups attached at specific positions [8,9].

The monomeric units can link together through carbon-carbon bonds to form oligomers and polymers. These linkages occur primarily between the carbon atoms at positions C4 and C8 (or sometimes C4 and C6) of the flavan-3-ol units. This bonding pattern is typical of B-type procyanidins (Figure 3), the most common form [7,8]. In contrast, A-type

procyanidins (Figure 2) have an additional ether bond, such as a C2-O-C7 linkage, which provides a distinct structural variation [8,9].

Procyanidins are classified by their degree of polymerization (DP), which refers to the number of monomer units in the compound. Dimers, trimers, and tetramers (DP = 2–4) are called oligomeric procyanidins, while those with a higher DP are considered polymers. Oligomeric forms are more soluble in water and tend to have higher biological activity, particularly as antioxidants. As the polymerization increases, solubility and bioavailability decrease, but the compounds may still contribute to dietary fiber and other functional properties [7,8].

The hydroxyl groups present on the aromatic rings of procyanidins contribute significantly to their chemical reactivity and biological activity. These groups make procyanidins powerful antioxidants, capable of scavenging free radicals and chelating metal ions. Some procyanidins also contain gallate groups, which enhance their antioxidant potential [6,10].

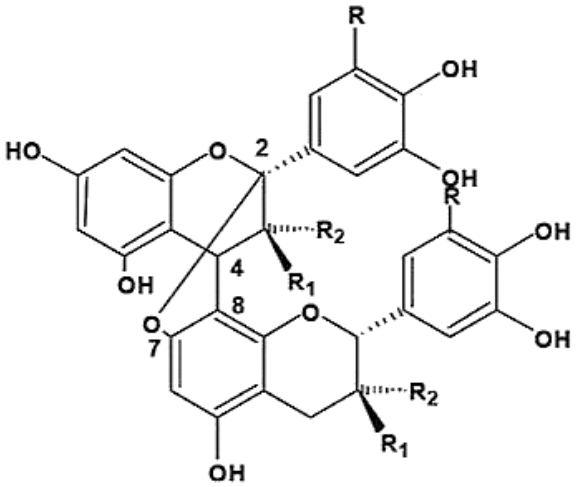

Figure 2. A-type proanthocyanidin [8].

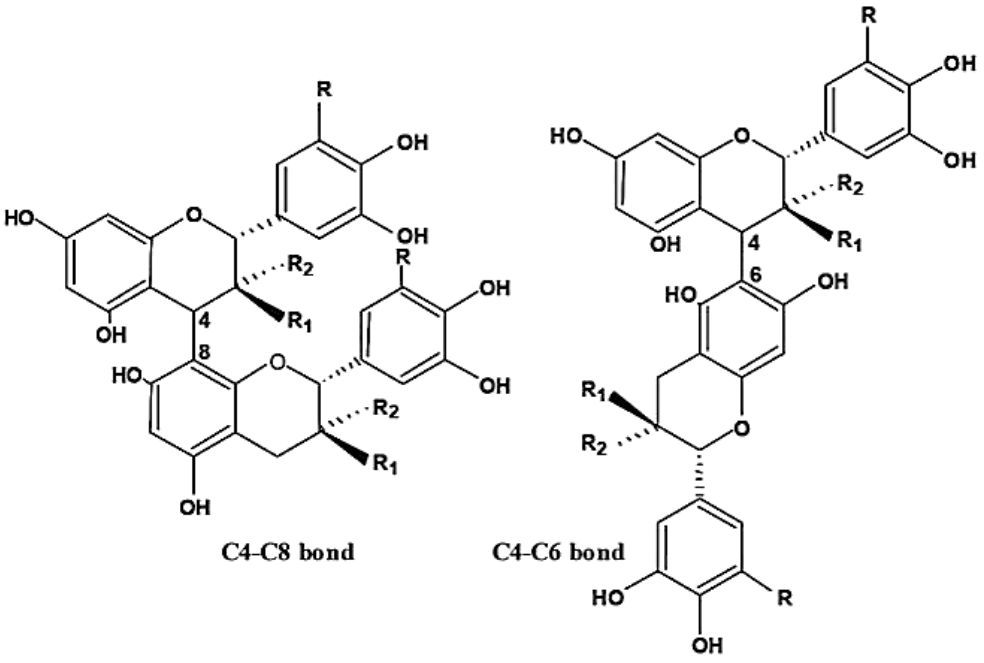

Figure 3. B-type proanthocyanidin [8].

The identification of procyanidins in grapes and wine is essential for understanding the role of these compounds in wine quality, health benefits, and aging potential. Several analytical methods, such as HPLC, LC-MS, NMR, and spectrophotometry, can be employed to quantify and characterize procyanidins, each with its own strengths and limitations [10-14]. A combination of these techniques is often used to gain a comprehensive understanding of procyanidin content and structure in winemaking.

3. The physical, chemical, biochemical, and physiological properties of procyanidins

Procyanidins are a diverse group of polyphenolic compounds with significant physical, chemical, biochemical, and physiological properties. These properties make them essential in food science, nutrition, and pharmacology [15].

Procyanidins display unique physical characteristics that influence their solubility, stability, and interaction with other compounds.

Table 1

Physical Properties

Property	Description	References
Solubility	Low molecular weight procyanidins (dimers, trimers) dissolve readily in water and polar solvents. Larger polymers are insoluble in water but dissolve in alcohols like ethanol.	[15]
Appearance	In pure form, procyanidins are colorless or pale yellow. In foods and beverages, they contribute to browning through oxidation.	[9,15]
Thermal stability	Procyanidins are stable at moderate temperatures but degrade or polymerize when exposed to prolonged heat.	[8,16]
Optical Activity	Due to chiral centers in their monomeric units, procyanidins are optically active, with measurable enantiomeric rotations.	[7,16]

The chemical properties of procyanidins are shaped by their unique structural features and their interactions with other compounds, which are critical to their functionality in food and biological systems [6,15].

- *Structure:* Procyanidins are composed of catechin and epicatechin monomers linked by C4-C8 or C4-C6 bonds, forming B-type procyanidins. Some forms, known as A-type procyanidins, include an additional ether bond, providing structural diversity [8,15].
- *Antioxidant Activity:* The numerous hydroxyl groups present in procyanidins make them highly effective at scavenging free radicals. This antioxidant property protects cells and food products from oxidative damage [17].
- *pH Sensitivity:* Procyanidins exhibit stability in acidic environments, which is why they remain functional in acidic foods and beverages like wine and fruit juices. However, they degrade in alkaline conditions, limiting their stability in such environments [18].
- *Protein Binding:* Procyanidins have a strong affinity for proteins, particularly salivary proteins. This interaction contributes to the astringent sensation experienced in foods and drinks such as red wine, enhancing sensory attributes [19].

These chemical properties underline the significance of procyanidins in food preservation, sensory quality, and health-related benefits.

At a molecular level, procyanidins demonstrate biochemical properties that significantly affect enzymatic activity, oxidative processes, and their interactions with

biomolecules. These compounds play a crucial role in inhibiting lipid peroxidation, thereby protecting cell membranes from oxidative damage and ensuring cellular stability. They also modulate enzymatic activity, with the ability to inhibit digestive enzymes such as amylase and lipase [20]. This enzymatic inhibition can slow the metabolism of carbohydrates and fats, contributing to potential therapeutic benefits. Additionally, procyanidins undergo polymerization through oxidative reactions, forming larger polymers. While this polymerization can reduce their bioavailability, it may simultaneously enhance specific functional properties in foods, such as texture or stability. These biochemical properties highlight the multifaceted roles of procyanidins in both biological systems and food applications [8,20].

Procyanidins provide numerous health benefits, making them valuable in nutrition and therapeutic applications [21].

Table 2

Physiological properties

Benefit	Description	References
Cardiovascular health	Improve blood vessel function by increasing nitric oxide levels, lowering blood pressure, and reducing LDL oxidation.	[21]
Anti-inflammatory effects	Reduce inflammation by downregulating pro-inflammatory cytokines like TNF-α and IL-6.	[22]
Gut microbiota support	Promote the growth of beneficial gut bacteria, acting as prebiotics, while smaller procyanidins are absorbed in the intestine.	[23,24]
Anticancer Activity	Inhibit cancer cell growth, induce apoptosis, and reduce angiogenesis through antioxidant and anti-inflammatory mechanisms.	[17,21]
Neurological protection	Cross the blood-brain barrier to protect neurons, reduce oxidative stress, and enhance cognitive functions.	[21]
Skin health	Protect against UV damage, enhance collagen stability, and combat signs of aging.	[25]

In conclusion, procyanidins are a versatile group of polyphenolic compounds with remarkable physical, chemical, biochemical, and physiological properties that make them highly valuable in food science, nutrition, and pharmacology. Their structural diversity, antioxidant activity, and interactions with proteins and enzymes allow them to enhance food stability, sensory quality, and health benefits. Physically, their solubility and stability characteristics influence their functionality in different environments, while chemically, their pH sensitivity and protein binding contribute to their role in food and beverages. Biochemically, their ability to modulate enzymatic activity and protect cells underscores their potential therapeutic uses [17,25].

Procyanidins' physiological benefits, such as promoting cardiovascular health, reducing inflammation, supporting gut microbiota, and offering neurological and skin protection, further emphasize their importance in nutrition and medical research. This multifaceted nature ensures that procyanidins remain a focus of interest for their applications in improving food quality and human health [21, 23].

Procyanidin's antioxidant effects are primarily due to their ability to neutralize free radicals, which are unstable molecules that can damage cells, proteins, and DNA. This damage is often linked to various chronic diseases, such as cancer, cardiovascular conditions, and aging. By scavenging these free radicals, procyanidins help to reduce oxidative stress and protect the body from these harmful effects [25,26].

In addition to scavenging free radicals, procyanidins can also chelate metal ions like iron and copper, which are known to promote the formation of reactive oxygen species (ROS) [27]. By binding to these metals, procyanidins prevent the initiation of oxidative damage. They also exhibit anti-inflammatory properties, which further complement their antioxidant actions. Since chronic inflammation can exacerbate oxidative stress, procyanidins' ability to reduce inflammation adds an extra layer of protection for the cells [24,28].

Studies suggest that procyanidins can enhance the body's own antioxidant defenses by stimulating the production of endogenous antioxidant enzymes, such as superoxide dismutase and glutathione peroxidase [29]. This strengthens the overall defense against oxidative damage. Moreover, procyanidins are effective at preventing lipid peroxidation, a process that leads to the oxidation of lipids and the formation of harmful compounds like malondialdehyde. This helps preserve the integrity of cell membranes and protects cells from oxidative damage [30].

By neutralizing free radicals, procyanidins also protect DNA from oxidative damage, which could otherwise lead to mutations and cancer. They also help protect proteins from oxidation, ensuring that proteins maintain their proper function and supporting overall cell health [25,31]. The antioxidant properties of procyanidins are believed to offer various health benefits, including promoting cardiovascular health, providing neuroprotection, and potentially reducing cancer risk [30,32].

In the winemaking industry, the presence of procyanidins in grape skins and seeds contributes to the health benefits associated with red wine. These compounds help preserve the wine's freshness and stability, contributing to its antioxidant-rich content. The antioxidant capacity of procyanidins in grapes also plays a role in the overall quality and aging potential of wine [33].

Procyanidins exhibit strong antiradical activity due to their ability to neutralize reactive oxygen species (ROS) such as hydroxyl radicals, superoxide anions, and peroxyl radicals. Their multiple hydroxyl groups donate hydrogen atoms, stabilizing these reactive species and preventing oxidative damage. They also chelate transition metals like iron and copper, reducing the formation of radicals via catalytic processes such as the Fenton reaction [33].

Additionally, procyanidins interrupt lipid peroxidation by stabilizing peroxyl radicals, thus protecting cellular membranes. The degree of polymerization influences their antiradical efficacy, with oligomeric procyanidins showing higher activity due to better bioavailability, while polymeric forms provide robust local antioxidant effects. Compared to simpler phenolics, procyanidins have superior scavenging capacity, amplified by their structural complexity and ability to act synergistically with other antioxidants [34].

Key Antiradical Mechanisms [34]:

- Free Radical Scavenging: Procyanidins effectively neutralize reactive oxygen species (ROS) such as hydroxyl radicals (·OH), superoxide anions ($O_2^{-}\cdot$), and peroxyl radicals (ROO·), thereby preventing oxidative damage to lipids, proteins, and DNA.

- Metal Chelation: Procyanidins chelate transition metals like iron (Fe^{2+}) and copper (Cu^{2+}), which catalyze the generation of free radicals through Fenton or Haber-Weiss reactions. This reduces the formation of highly reactive hydroxyl radicals.
- Regeneration of Antioxidants: Procyanidins can regenerate other antioxidants like vitamin C and vitamin E, enhancing the overall antioxidant defense system in cells.
- Inhibition of Lipid Peroxidation: Procyanidins interrupt the chain reactions of lipid peroxidation by stabilizing peroxyl radicals, protecting cell membranes and lipoproteins from oxidative damage [35].
- Antiradical Strength: The antiradical activity of procyanidins is influenced by their degree of polymerization (DP):
  - ✓ Oligomeric Procyanidins (low DP): Exhibit higher free radical scavenging efficiency due to better bioavailability and interaction with radical species.
  - ✓ Polymeric Procyanidins (high DP): Though less bioavailable, they possess strong local antioxidant effects in the gastrointestinal tract.
- Health Impacts of Antiradical Properties:
  - ✓ Cardiovascular Health: Procyanidins protect LDL cholesterol from oxidative modification, reducing the risk of atherosclerosis.
  - ✓ Anti-Aging Effects: Their ability to combat oxidative stress helps mitigate aging-related cellular damage.
- Neuroprotection: Procyanidins protect neurons by reducing oxidative stress, potentially lowering the risk of neurodegenerative diseases like Alzheimer's.

Table 3 is presenting the procyanidin content (measured in mg/100 g or mg/L) in various natural sources. The values may vary depending on the source, variety, and processing method [36-38].

Table 3

Procyanidin content in various natural sources and the impact of processing methods

Source	Procyanidin content	Unit	Processing Method	Impact on Procyanidins	References
Grapes (seeds)	350 - 500	mg/100 g	Crushing, extraction, drying	Minimal loss if carefully dried; extraction concentrates procyanidins	[39]
Grapes (skins)	10 - 25	mg/100 g	Fermentation, drying	Loss during fermentation unless skins are retained	[39]
Red wine	200 - 300	mg/L	Fermentation, maceration	Longer maceration increases content	[39]
White wine	10 - 20	mg/L	Fermentation without skin contact	Minimal procyanidins due to lack of maceration	[39]

Continuation Table 3

Apples	40 - 120	mg/100 g	Fresh, juice production, drying	Peeling reduces content; drying concentrates procyanidins	[40]
Cranberries	200 - 400	mg/100 g	Fresh, juice production, drying	Processing (juicing) may reduce content; drying retains high levels	[41]
Blueberries	50 - 100	mg/100 g	Fresh, freezing, drying	Freezing preserves content; heat drying may lead to slight loss	[41]
Cocoa beans	300 - 1200	mg/100 g	Fermentation, drying, roasting	Fermentation and roasting reduce content but release bioactive forms	[42]
Dark chocolate	200 - 500	mg/100 g	Grinding, conching, tempering	Higher cocoa content correlates with higher procyanidin levels	[42]
Green tea	50 - 100	mg/100 g	Drying, steaming, brewing	Steaming preserves content; prolonged brewing may increase extraction	[43]
Almonds	50–60	mg/100 g	Roasting, blanching, drying	Roasting may reduce content; raw almonds have slightly higher levels	[44]

Table 3 highlights the variation in procyanidin content across different natural sources, emphasizing the significant levels found in grapes and their derivatives, particularly red wine. Grapes, especially their seeds, are among the richest sources of procyanidins, with content ranging from 350–500 mg/100 g in seeds and 10–25 mg/100 g in skins.

This high concentration makes them a valuable raw material for health-promoting polyphenols.

Red wine, produced through maceration and fermentation processes that extract procyanidins from grape skins and seeds, contains 200–300 mg/L of these compounds. The prolonged contact with grape solids during winemaking contributes to its higher procyanidin levels compared to white wine, which undergoes minimal skin contact, resulting in only 10–20 mg/L [44].

The table underscores the critical role of processing in preserving and enhancing procyanidin content. For grapes and wine, proper handling during fermentation and maceration is essential to maximize the health benefits of these potent antioxidants. As such, grape-based products, particularly red wine, stand out as both a cultural and nutritional asset, providing significant amounts of bioactive compounds with antioxidant properties [45].

The biosynthesis of proanthocyanidins usually starts after flowering and fruit setting at 3~9 weeks post grape fruit anthesis. The biosynthesis of procyanidins in grapes begins in the phenylpropanoid pathway, where phenylalanine is converted into 4-coumaroyl-CoA through the action of enzymes like phenylalanine ammonia-lyase (PAL), cinnamate-4-hydroxylase (C4H), and 4-coumarate-CoA ligase (4CL). This intermediate then enters the flavonoid pathway, where it is used to synthesize naringenin chalcone through the activity of chalcone synthase (CHS). The chalcone is then isomerized into naringenin by chalcone isomerase (CHI) [46,47].

Next, naringenin undergoes hydroxylation by flavonoid 3'-hydroxylase (F3'H) or flavonoid 3',5'-hydroxylase (F3'5'H), leading to the formation of dihydroflavonols like dihydroquercetin or dihydromyricetin. These dihydroflavonols are then reduced by dihydroflavonol-4-reductase (DFR) to produce leucoanthocyanidins, which are further converted into flavan-3-ols, such as catechins and epicatechins, by the action of leucoanthocyanidin reductase (LAR) or anthocyanidin reductase (ANR) [46,47].

Procyanidins are then formed through the polymerization or oligomerization of these flavan-3-ol monomers. This process can occur enzymatically or non-enzymatically, leading to the creation of dimers, trimers, and larger procyanidin molecules. These procyanidins are transported and accumulated primarily in grape skins and seeds, where they serve various roles, including contributing to the grape's defense mechanisms and influencing the organoleptic properties of wine.

The biosynthesis of procyanidins is tightly regulated by environmental factors such as sunlight and temperature, as well as genetic factors. The final accumulation of procyanidins in the grape seeds and skins is important not only for the plant's defense but also for the sensory qualities of wine, especially red wines, where procyanidins play a key role in color, astringency, and antioxidant properties [48].

Procyanidins are a versatile and valuable group of polyphenolic compounds with significant physical, chemical, biochemical, and physiological properties. They are most notably found in grapes, particularly in seeds and skins, where they contribute to the antioxidant, astringent, and color characteristics of wine. Their physical properties, such as solubility and stability, influence their functionality in food and beverages, while their chemical properties—such as antioxidant activity, pH sensitivity, and protein binding—make them important for food preservation, sensory attributes, and health benefits.

The content of procyanidins varies significantly across different natural sources, with grapes and their derivatives (especially red wine) being rich sources of these compounds. The processing methods, such as fermentation and maceration in winemaking, play a critical role in enhancing or reducing procyanidin content. Grapes, particularly when processed into red wine, remain an important source of these bioactive compounds, contributing to the overall health benefits associated with moderate wine consumption [39,48].

In addition to their beneficial effects in human health, procyanidins' antioxidant and anti-inflammatory properties underscore their potential in therapeutic applications, making them essential in both nutrition and pharmacology. The understanding of their biosynthesis

in grapes also provides insight into how environmental and genetic factors can influence the quantity and quality of procyanidins in grape-based products, especially wines [47].

4. Effects of climate, soil, and grape variety on procyanidin accumulation in red wines

The accumulation of procyanidins in red wines is significantly influenced by environmental and cultivation factors, including climate, soil, and grape variety. Procyanidins, key polyphenolic compounds contributing to the astringency, color, and antioxidant properties of wines, are synthesized in grape skins and seeds, with their levels varying depending on several viticultural conditions. Understanding these factors is essential for optimizing wine quality, especially in relation to the desired sensory characteristics and health benefits associated with red wines [49].

Table 4

Effects of climate, soil, and grape variety on procyanidin accumulation in red wines

Factor	Description	Impact on procyanidin levels	References
Climate:			
Temperature	High temperatures increase anthocyanin synthesis and the rate of procyanidin polymerization. However, excessive heat can degrade procyanidins	Optimal temperatures (15-25°C) promote balanced synthesis of polyphenols.	[50]
Sunlight	UV exposure stimulates the production of phenolic compounds in grape skins.	Higher sunlight exposure enhances procyanidin content, especially in grape skins.	[50,52]
Rainfall	Excessive rainfall before harvest can dilute grape components, affecting polyphenol concentration.	Moderate rainfall allows procyanidin accumulation; excess rain may reduce levels.	[51,53,55]
Soil:			
pH	Soil pH affects nutrient availability and grape metabolism. Acidic soils tend to favor the synthesis of flavonoids, including procyanidins.	Slightly acidic soils (pH 5.5-6.5) are optimal for procyanidin production.	[54,58]
Nutrients	Rich soils with adequate nitrogen and potassium promote vine health and polyphenol synthesis.	High nutrient availability supports optimal vine growth and procyanidin synthesis.	[56,58]
Drainage	Well-drained soils prevent waterlogging, which can dilute phenolic content in grapes.	Good drainage ensures higher concentration of procyanidins in grape skins and seeds.	[57,58]

Continuation Table 4

Grape Variety	Different grape varieties naturally accumulate varying levels of procyanidins.	Red grape varieties, such as Cabernet Sauvignon, Merlot, and Pinot Noir, are known for higher procyanidin levels in their skins and seeds.	[59-61]

The balance between environmental conditions like climate and soil properties significantly impacts the polyphenolic content of grapes, especially procyanidins. For instance, optimal temperature and sunlight conditions enhance the production of polyphenolic compounds, while excessive rainfall or poor drainage can reduce their concentrations. Additionally, the choice of grape variety plays a crucial role, with certain varieties naturally yielding higher levels of procyanidins due to genetic factors [56,62].

5. The influence of winemaking technology on the accumulation of procyanidins in wines

Winemaking technology plays a crucial role in determining the levels of procyanidins, a class of polyphenolic compounds, in wines. These compounds, primarily found in grape skins and seeds, contribute to the astringency, color, and antioxidant properties of the final product. The winemaking process, including grape handling, fermentation techniques, maceration, and aging, significantly impacts procyanidin extraction and polymerization, influencing both the sensory and health-related properties of the wine [63-66].

Grape handling methods before fermentation can affect procyanidin extraction. The way grapes are crushed, sorted, and processed determines the extent to which procyanidins are released from the skins and seeds into the must [67].

Crushing is essential for releasing the polyphenols from grape skins and seeds. Mechanical crushing, if too aggressive, may lead to the breakdown of seeds and the release of undesirable compounds. However, moderate crushing facilitates the release of procyanidins, enhancing their concentration in the wine [67].

Cold soaking involves macerating the crushed grapes at low temperatures before fermentation. This technique allows the extraction of phenolic compounds, including procyanidins, without initiating fermentation. Cold soaking has been found to increase procyanidin content, especially in red wines, by promoting the diffusion of polyphenols from the skins into the must [68,69].

Fermentation is a pivotal step in the winemaking process that influences the solubility, polymerization, and degradation of procyanidins [69].

Fermentation temperature is critical for procyanidin extraction. Higher temperatures (25-30 °C) facilitate the release of polyphenols from grape skins and seeds. However, temperatures above this range may lead to the degradation of sensitive phenolic compounds, including procyanidins. Therefore, maintaining optimal fermentation temperatures is key to maximizing procyanidin levels [70].

The choice of yeast strain during fermentation can also influence the procyanidin content of the wine. Some yeast strains have been shown to enhance the extraction of polyphenols, while others may result in lower concentrations. Additionally, yeast-derived metabolites can interact with phenolic compounds, modifying the sensory properties of the wine.

Longer fermentation times, especially in red wines, allow for more extended contact between the juice and grape skins, increasing the extraction of procyanidins. Extended fermentation and maceration times are beneficial for extracting these compounds, as prolonged skin contact enhances the diffusion of phenolic compounds into the wine [71].

Maceration refers to the process of allowing the crushed grape skins to remain in contact with the fermenting juice to extract phenolic compounds, including procyanidins. The technique and duration of maceration can significantly impact procyanidin levels [71].

The length of time that grape skins are in contact with the wine during fermentation or post-fermentation maceration directly influences the level of procyanidins in the wine. The longer the skin contact, the higher the procyanidin content, as more polyphenols are extracted from the skins.

After fermentation, maceration may continue for days or weeks to further extract phenolic compounds. This process increases the concentration of procyanidins, contributing to the wine's flavor profile, color, and antioxidant properties [72].

Aging plays a significant role in the polymerization and stabilization of procyanidins in wine. Both the method and environment of aging affect the final concentration and characteristics of procyanidins in the wine [73].

The use of oak barrels in wine aging is a common practice that impacts the phenolic composition of the wine. Oak can contribute additional phenolic compounds to the wine, influencing its color, flavor, and tannin structure. However, oak aging can also promote the polymerization of procyanidins, leading to the formation of larger molecules that may have different sensory attributes (e.g., reduced astringency) [63,64,73].

In addition to barrel aging, bottle aging allows for the gradual oxidation and polymerization of procyanidins. Over time, this oxidation can lead to a more stable and smoother wine, with softer tannins and less astringency. However, the aging process may reduce the concentration of free procyanidins as they polymerize into larger structures [64,74].

Techniques to enhance procyanidin content:

Several techniques can be employed to optimize the extraction and preservation of procyanidins in wine, ensuring their health benefits and enhancing sensory qualities.

- **Enzyme treatment**. The use of enzymes such as pectinase during fermentation can help break down cell walls and improve the extraction of procyanidins and other polyphenols from grape skins and seeds. This results in a higher concentration of procyanidins in the wine [75-79].
- **Microoxygenation**. This technique involves introducing small amounts of oxygen into the wine during aging. Microoxygenation can promote the polymerization of procyanidins, reducing their astringency while enhancing their antioxidant properties and stability [80,81].
- **Pre-fermentation treatments.** Techniques like cryomaceration (macerating grapes at low temperatures before fermentation) can increase procyanidin extraction, particularly for certain grape varieties known to have high phenolic content [82-87].

Winemaking technology has a significant influence on the accumulation of procyanidins in wines. The extraction of procyanidins is affected by a variety of factors including berry size, grape handling, fermentation conditions, maceration techniques, and aging processes. Understanding the effects of temperature, fermentation time, maceration

duration, and aging methods can help winemakers optimize the levels of these important polyphenols in their wines. By utilizing specific winemaking practices, it is possible to enhance the sensory attributes and health benefits of wines, making them a more beneficial and enjoyable product for consumers [88-93].

6. Conclusions

In conclusion, proanthocyanidins, particularly procyanidins, play a crucial role in the sensory and health-related properties of wines, contributing to their color, astringency, and antioxidant potential. The physical, chemical, biochemical, and physiological characteristics of procyanidins have a significant impact on wine quality, with factors such as climate, soil, and grape variety influencing their accumulation in red wines.

The accumulation of procyanidins in red wines is strongly affected by climate, soil, and grape variety, each contributing to the wine's sensory characteristics and potential health benefits. Optimal conditions, such as moderate temperatures, adequate sunlight, and slightly acidic, well-drained soils, alongside the careful choice of grape varieties that naturally accumulate higher levels of procyanidins, are key to enhancing the polyphenol content and producing high-quality red wines.

Winemaking practices greatly influence the accumulation and characteristics of procyanidins in wine. By carefully managing factors such as grape handling, fermentation conditions, maceration, and aging, winemakers can optimize procyanidin levels, enhancing both the sensory experience and the health benefits of the final product.

Acknowledgments: The research was supported by Institutional Project, subprogram 02.04.05 Optimizing food processing technologies in the context of the circular bioeconomy and climate change, Bio-OpTehPAS, being implemented at the Technical University of Moldova.

Conflicts of Interest: The authors declare no conflict of interest.

References

1. Asproudi, A.; Piano, F.; Anselmi, G.; Stefano, R.; Bertolone, E.; Borsa, D. Proanthocyanidin composition and evolution during grape ripening as affected by variety: Nebbiolo and Barbera cv. *Journal international des sciences de la vigne et du vin* 2015, 49 (1). https://doi.org/10.20870/oeno-one.2015.49.1.93.
2. Barros, A.; Gironés-Vilaplana, A.; Teixeira, A.; Collado-González, J.; Moreno, D.A.; Gil-Izquierdo, A.; Rosa, E.; Domínguez-Perles, R. Evaluation of Grape (Vitis vinifera L.) Stems from Portuguese Varieties as a Resource of (Poly)Phenolic Compounds: A Comparative Study. *Food Research International* 2014, 65, pp. 375–384. https://doi.org/10.1016/j.foodres.2014.07.021.
3. Downey, M.O.; Dokoozlian, N.K.; Krstic, M.P. Cultural practice and environmental impacts on the flavonoid composition of grapes and wine: a review of recent research. *American Journal of Enology and Viticulture* 2006, 57, pp. 257–268. https://doi.org/10.5344/ajev.2006.57.3.257.
4. Gutiérrez-Escobar, R.; Aliaño-González, M. J.; Cantos-Villar, E. Wine Polyphenol Content and Its Influence on Wine Quality and Properties: A Review. *Molecules* 2021, 26 (3), 718. https://doi.org/10.3390/molecules26030718.
5. Merkyte, V.; Longo, E.; Windisch, G.; Boselli, E. Phenolic Compounds as Markers of Wine Quality and Authenticity. *˙Foods* 2020, 9, 1785. https://doi.org/10.3390/foods9121785.
6. Tsao, R. Chemistry and biochemistry of dietary polyphenols. *Nutrients* 2010, 2, pp. 1231–1246. https://doi.org/10.3390/nu2121231.
7. Chai, W. M.; Chen, C. M.; Gao, Y. S.; Feng, H. L.; Ding, Y. M.; Shi, Y.; Zhou, H. T.; Chen, Q. X. Structural analysis of proanthocyanidins isolated from fruit stone of Chinese hawthorn with potent antityrosinase and antioxidant activity. *Journal of Agricultural and Food Chemistry* 2014, 62(1), pp. 123–129. https://doi.org/10.1021/jf405385j.

8. Ribéreau-Gayon, P. The anthocyanins of grapes and wines. In: *Anthocyanins as Food Colors,* Academic Press, NY, SUA, 1982, pp. 209-244. https://doi.org/10.1016/B978-0-12-472550-8.50012-3.
9. Ursu, S. Phenolic compounds in grapes. *Meridian Ingineresc* 2010, 4, p. 78-83. ISSN 1683-853X.
10. Flamini, R.; De Rosso, M.; Bavaresco, L. Study of Grape Polyphenols by Liquid Chromatography-High-Resolution Mass Spectrometry (UHPLC/QTOF) and Suspect Screening Analysis. *Journal of Analytical Methods in Chemistry* 2015, 350259. https://doi.org/10.1155/2015/350259.
11. Flamini R. Recent applications of mass spectrometry in the study of grape and wine polyphenols, *ISRN Spectroscopy* 2013, 45, 813563. https://doi.org/10.1155/2013/813563.
12. Colombo, R.C.; Roberto, S.R.; Nixdorf, S.L.; et al. Analysis of the phenolic composition and yield of 'BRS Vitoria' seedless table grape under different bunch densities using HPLC–DAD–ESI-MS/MS. *Food Research International* 2020, 130, 108955. https://doi.org/10.1016/j.foodres.2019.108955.
13. de Rosso, M.; Tonidandel, L.; Larcher, R.; Nicolini, G.; Dalla Vedova, A.; de Marchi, F.; Gardiman, M.; Giust, M.; Flamini, R. Identification of new flavonols in hybrid grapes by combined liquid chromatography-mass spectrometry approaches. *Food Chemistry* 2014, 163 (1), pp. 244–251. https://doi.org/10.1016/j.foodchem.2014.04.110.
14. González-Manzano, S.; Santos-Buelga, C.; Pe, JJ.; Rez-Alonso, Ä.; Rivas-Gonzalo, J.C.; Escribano-Bailo, M.T. Characterization of the mean degree of polymerization of proanthocyanidins in red wines using liquid chromatography–mass spectrometry (LC-MS). *Journal of Agricultural and Food Chemistry* 2006, 54(12), pp. 4326–4332. https://doi.org/10.1021/jf060467e.
15. Zhanjie, X.; Peng, D.; Meiserb, P.; Jacoba, C. Proanthocyanidins: Oligomeric Structures with Unique Biochemical Properties and Great Therapeutic Promise. *Natural Product Communications* 2012, 7(3), pp. 381 – 388. https://doi.org/10.1177/1934578X1200700321.
16. Ebrahimnejad, H.; Burkholz, T.; Jacob, C. Flavanols and Proanthocyanidins. In: Recent Advances in Redox Active Plant and Microbial Products, Jacob, C.; Kirsch, G.; Slusarenko, A.; Winyard, P.; Burkholz, T. (eds), Springer, Dordrecht, 2014, pp. 211-232 https://doi.org/10.1007/978-94-017-8953-0_8.
17. Correia, P.; Araújo, P.; Ribeiro, C.; Oliveira, H.; Pereira, A. R.; Mateus, N.; de Freitas, V.; Brás, N. F.; Gameiro, P.; Coelho, P.; Bessa, L. J.; Oliveira, J.; Fernandes, I. Anthocyanin-related pigments: Natural allies for skin health maintenance and protection. *Antioxidants (Basel)* 2021, 10(7), 1038, https://doi.org/10.3390/antiox10071038.
18. Pradeep, M.; Harrison, R.; Hider, R.; Donaldson, I.; Kemp, B.; Tian, B. Development of Tannins and Methoxypyrazines in Grape Skins, Seeds, and Stems of Two Pinot Noir Clones during Ripening. *Journal of Agricultural and Food Chemistry* 2023, 71 (42), pp. 15754-15765. https://doi.org/10.1021/acs.jafc.3c04864.
19. Gombau, J.; Pons-Mercadé, P.; Conde, M.; Asbiro, L.; Pascual, O.; Gómez-Alonso, S. et al. Influence of grape seeds on wine composition and astringency of Tempranillo, Garnacha, merlot and cabernet sauvignon wines. *Food Science & Nutrition* 2020, 8, pp. 3442–3455. https://doi.org/10.1002/fsn3.1627.
20. Mohamedshah, Z.; Chadwick-Corbin, S.; Wightman, J. D.; Ferruzzi, M. G. Comparative assessment of phenolic bioaccessibility from 100% grape juice and whole grapes. *Food & Function* 2020, 11 (7), 6433-6445. https://doi.org/10.1039/D0FO00792G.
21. Cassidy, A. Berry anthocyanin intake and cardiovascular health. *Molecular Aspects of Medicine* 2016, 61, pp. 76–82. https://doi.org/10.1016/j.mam.2017.05.002.
22. Han, F.; Yang, P.; Wang, H.; Fernandes, I.; Mateus, N.; Liu, Y. Digestion and Absorption of Red Grape and Wine Anthocyanins through the Gastrointestinal Tract. *Trends in Food Science & Technology* 2019, 83, pp. 211–224. https://doi.org/10.1016/j.tifs.2018.11.025.
23. De Las, H. N.; Galiana, A.; Ballesteros, S.; Olivares-Alvaro, E.; Fuller, P. J.; Lahera, V.; et al. Proanthocyanidins maintain cardiac ionic homeostasis in aldosterone-induced hypertension and heart failure. *International Journal of Molecular Sciences* 2021, 22(17), 9602. http://doi.org/10.1016/j.mam.2022.101146.
24. Rodríguez-Pérez, C.; García-Villanova, B.; Guerra-Hernández, E.; Verardo, V. Grape seeds proanthocyanidins: An overview of in vivo bioactivity in animal models. *Nutrients* 2019, 11, 1–18. https://doi.org/10.3390/nu11102435.
25. Thomas, S. *Grapes: Phenolic Composition, Antioxidant Characteristics and Health Benefits*. Thomas, S., Ed.; Nova Science Publishers, Hauppauge, NY, USA, 2017, 199 p. ISBN: 978-1-53611-068-5.
26. Rivero-Pérez, M.D.; Muñiz, P.; González-San José M.L. Antioxidant profile of red wines evaluated by total antioxidant capacity, scavenger activity and biomarkers of oxidative stress methodologies. *Journal of Agricultural and Food Chemistry* 2007, 55, pp. 5476-5483. https://doi.org/10.1021/jf070306q.

27. Sturza, R.; Scutaru, I.; Duca, G. Redox processes in grapes processing. In: *Environmental and Technological Aspects of Redox Processes*, IGI Global, Hershey, PA, 2023, 31. https://doi.org/10.4018/979-8-3693-0512-6.ch015
28. Packer, L, Rimbach, G, Virgili, F. Antioxidant activity and biologic properties of a procyanidin-rich extract from pine (Pinus maritima) bark, pycnogenol. *Free Radical Biology and Medicine* 1999, 27, pp. 704–724. https://doi.org/10.1016/S0891-5849(99)00090-8.
29. Garrido, I.; Uriarte, D.; Hernández, M.; Llerena, J.L.; Valdés, M.E.; Espinosa, F. The Evolution of Total Phenolic Compounds and Antioxidant Activities during Ripening of Grapes (Vitis vinifera L., Cv. Tempranillo) Grown in Semiarid Region: Effects of Cluster Thinning and Water Deficit. *International Journal of Molecular Sciences* 2016, 17, 1923. https://doi.org/10.3390/ijms17111923.
30. Bagchi, D.; Swaroop, A.; Preuss, H. G.; Bagchi, M. Free radical scavenging, antioxidant and cancer chemoprevention by grape seed proanthocyanidin: An overview. *Mutation Research-Fundamental and Molecular Mechanisms of Mutagenesis* 2014, 768, pp. 69–73, https://doi.org/10.1016/j.mrfmmm.2014.04.004.
31. Jordão, A.M.; Simões, S.; Correia, A.C.; Gonçalves F.G. Antioxidant activity evolution during Portuguese red wine vinification and their relation with the proanthocyanidin and anthocyanin composition. *Journal of Food Processing and Preservation* 2012, 36, pp. 298-309, https://doi.org/10.1111/j.1745-4549.2011.00588.x.
32. Martins, G. R.; Mattos, M. M. G.; Nascimento, F. M,; Brum, F. L.; Mohana-Borges, R.; et al. Phenolic Profile and Antioxidant Properties in Extracts of Developing Açaí (Euterpe oleracea Mart.) Seeds. *Journal of Agricultural and Food Chemistry* 2022, 70 (51), pp. 16218-16228. https://doi.org/10.1021/acs.jafc.2c07028.
33. Torres, N.; Goicoechea, N.; Morales, F.; Antolín, M.C. Berry Quality and Antioxidant Properties in Vitis vinifera Cv. Tempranillo as Affected by Clonal Variability, Mycorrhizal Inoculation and Temperature. *Crop and Pasture Science* 2016, 67, 961–977. https://doi.org/10.1071/CP16038.
34. Su, X.; Howell, A.B.; D'Souza, D.H. Antiviral effects of cranberry juice and cranberry proanthocyanidins on foodborne viral surrogates-A time dependence study in vitro. *Food Microbiology* 2010, 27, pp. 985–991, https://doi.org/10.1016/j.fm.2010.05.027.
35. Costa, E.; Cosme, F.; Jordão, A.M.; Mendes-Faia, A. Anthocyanin Profile and Antioxidant Activity from 24 Grape Varieties Cultivated in Two Portuguese Wine Regions. OENO One 2014, 48, 51. https://doi.org/10.20870/oeno-one.2014.48.1.1661.
36. Vilas Boas, A.C.; Henrique, P.d.C.; Lima, L.C.d.O.; Decarlos Neto, A. Antioxidant Activity, Anthocyanins and Organic Acids Content of Grape Juices Produced in Southwest of Minas Gerais, Brazil. *Ciênc. Agrotecnol.* 2014, 38, pp. 480–486. https://doi.org/10.1590/S1413-70542014000500007.
37. Cristea, E.; Sturza, R.; Patras, A. The influence of temperature and time on the stability of the antioxidant activity and colour parameters of grape marc ethanolic extract. *Annals of the University Dunarea de Jos of Galati, Fascicle VI: Food Technology* 2016, 39/2, 96-104, ISSN 1843-5157 /ISSNe 2068-259X.
38. Cristea, E.; Sturza, R.; Jauregi, P.; Niculaua, M.; Ghendov-Moșanu, A.; Patras, A. Influence of pH and ionic strength on the color parameters and antioxidant properties of an ethanolic red grape marc extract. *Journal of Food Biochemistry* 2019/4, 43 (4). e12788. ISSN 1745-4514. http://dx.doi.org/10.1111/jfbc.12788.
39. Waterhouse, A.L.; Sacks, G. L.; Jeffery, D. W. Understanding Wine Chemistry. Wiley, NJ, SUA, 2016, 472 p. https://doi.org/10.1002/9781118730720.
40. Guyot, S.; Le Bourvellec, S.; Marnet, N.; Drilleau, J.F. Procyanidins are the most Abundant Polyphenols in Dessert Apples at Maturity. *Food Science and Technology* 2002, 35(3), pp. 289-291, https://doi.org/10.1006/fstl.2001.0843.
41. Borges, G.; Degeneve, A.; Mullen, W.; Crozier, A. Identification of flavonoid and phenolic antioxidants in blackcurrants, blueberries, raspberries, red currants, and cranberries. *Journal of Agricultural and Food Chemistry*, 2010, 58(7), 3901–3909. https://doi.org/10.1021/jf902263n.
42. HammerstoneSheryl, J.; Lazarus, A.E.; Mitchell, A.E; Schmitz, H. Identification of Procyanidins in Cocoa (Theobroma cacao) and Chocolate Using High Performance Liquid Chromatography/Mass Spectrometry. *Journal of Agricultural and Food Chemistry* 1999, 47(2), pp. 490-496. https://doi.org/10.1021/jf980760h.
43. Henning, S. M.; Niu, Y.; Lee, N. H. Bioavailability and antioxidant activity of tea flavonoids after ingestion of different amounts of green tea by humans. *Free Radical Biology and Medicine* 2004, 36(9), pp. 1465–1474. https://doi.org/10.1093/ajcn/80.6.1558.
44. Osete-Alcaraz, A.; Belén Bautista-Ortín, A.; Ortega-Regules, A.; Encarna Gómez-Plaza. Combined Use of Pectolytic Enzymes and Ultrasounds for Improving the Extraction of Phenolic Compounds During Vinification. *Food and Bioprocess Technology* 2019, 12 (8), pp. 1330-1339. https://doi.org/10.1007/s11947-019-02303-0.

45. Manach, C.; Williamson, G.; Morand, C.; Scalbert, A.; Rémésy, C. Bioavailability and bioefficacy of polyphenols in humans. *The American Journal of Clinical Nutrition* 2005, 81(1 Suppl), pp. 230S-242S. https://doi.org/10.1093/ajcn/81.1.230S.
46. Rousserie, P.; Rabot, A.; Geny-Denis, L. From flavanols biosynthesis to wine tannins: what place for grape seeds? *Journal of Agricultural and Food Chemistry* 2019, 67, pp. 1325–1343, https://doi.org/10.1021/acs.jafc.8b05768.
47. He, F.; Pan, Q.H.; Shi, Y.; Duan, C.Q. Biosynthesis and genetic regulation of proanthocyanidins in plants. *Molecules* 2008, 13, pp. 2674–2703. https://doi.org/10.3390/molecules13102674.
48. Yang, N.; Gao, J.; Hou, R. Z.; Xu, X. L.; Yang, N. Q.; Huang, S. S. Grape seed Proanthocyanidins inhibit migration and invasion of bladder cancer cells by reversing EMT through suppression of TGF-β signaling pathway. *Oxidative Medicine and Cellular Longevity* 2021, 1–10. https://doi.org/10.1155/2021/5564312.
49. Rouxinol, M.I.; Martins, M.R.; Barroso, J.M.; Rato, A. E. Wine Grapes Ripening: A Review on Climate Effect and Analytical Approach to Increase Wine Quality. *Applied Biosciences* 2023, 2, 347–372. https://doi.org/10.3390/applbiosci2030023.
50. Blancquaert, E.H.; Oberholster, A.; Ricardo-da-Silva, J.M.; Deloire, A.J. Grape Flavonoid Evolution and Composition Under Altered Light and Temperature Conditions in Cabernet Sauvignon (Vitis vinifera L.). *Frontiers in Plant Science 2019*, 10, 1062, https://doi.org/10.3389/fpls.2019.01062.
51. Bonada, M.; Jeffery, D.W.; Petrie, P.R.; Moran, M.A.; Sadras, V.O. Impact of elevated temperature and water deficit on the chemical and sensory profiles of Barossa Shiraz grapes and wines. *Australian Journal of Grape and Wine Research* 2015, 21, pp. 240–253, https://doi.org/10.1111/ajgw.12142.
52. Del-Castillo-Alonso, M.Á.; Monforte, L.; Tomás-Las-Heras, R.; Martínez-Abaigar, J.; Núñez-Olivera, E. Phenolic Characteristics Acquired by Berry Skins of Vitis vinifera Cv. Tempranillo in Response to Close-to-Ambient Solar Ultraviolet Radiation Are Mostly Reflected in the Resulting Wines. *Journal of the Science of Food and Agriculture* 2020, 100, pp. 401–409. https://doi.org/10.1002/jsfa.10068.
53. Chacón-Vozmediano, J.L.; Martínez-Gascueña, J.; García-Romero, E.; Gómez-Alonso, S.; García-Navarro, F.J.; Jiménez-Ballesta, R. Effects of Water Stress on the Phenolic Compounds of 'Merlot' Grapes in a Semi-Arid Mediterranean Climate. *Horticulturae* 2021, 7, 161. https://doi.org/10.3390/horticulturae7070161.
54. Fraga, H.; Malheiro, A.C.; Moutinho-Pereira, J.; Santos, J.A. An Overview of Climate Change Impacts on European Viticulture. *Food and Energy Security* 2012, 1, 94–110. https://doi.org/10.1002/fes3.14.
55. Mira de Orduña, R. Climate change associated effects on grape and wine quality and production. *Food Research International* 2010, 43(7), pp. 1844-1855. https://doi.org/10.1016/j.foodres.2010.05.001.
56. Rouxinol, M.I.; Martins, M.R.; Salgueiro, V.; Costa, M.J.; Barroso, J.M.; Rato, A.E. Climate Effect on Morphological Traits and Polyphenolic Composition of Red Wine Grapes of Vitis vinifera. *Beverages* 2023, 9, 8. https://doi.org/10.3390/beverages9010008.
57. Cohen, S.D.; Tarara, J.M.; Kennedy, J.A. Assessing the impact of temperature on grape phenolic metabolism. *Analytica Chimica Acta* 2008, 621(1), pp. 57-67. https://doi.org/10.1016/j.aca.2007.11.029.
58. Wang, R.; Sun, Q.; Chang, Q. Soil Types Effect on Grape and Wine Composition in Helan Mountain Area of Ningxia. PLOS ONE 2015, 10(2). https://doi.org/10.1371/journal.pone.0116690.
59. Liang, N.N.; Zhu, B.Q.; Han, S.; Wang, J.H.; Pan, Q.H.; Reeves, M.J.; Duan, C.Q.; He, F. Regional Characteristics of Anthocyanin and Flavonol Compounds from Grapes of Four Vitis vinifera Varieties in Five Wine Regions of China. *Food Research International* 2014, 64, pp. 264–274. https://doi.org/10.1016/j.foodres.2014.06.048.
60. Gutiérrez-Gamboa, G.; Zheng, W.; Martínez de Toda, F. Strategies in vineyard establishment to face global warming in viticulture: a mini review. *Journal of the Science of Food and Agriculture* 2020, 101, pp. 1261–1269. https://doi.org/10.1002/jsfa.10813.
61. Ferrer, M.; Echeverría, G.; Carbonneau, A. Effect of berry weight and its components on the contents of sugars and anthocyanins of three varieties of Vitis vinifera L. under different water supply conditions. *South African Journal of Enology and Viticulture* 2014, 35, pp. 103–113. https://doi.org/10.21548/35-1-989.
62. Yan, Y.; Song, C.; Falginella, L.; Castellarin, S.D. Day temperature has a stronger effect than night temperature on anthocyanin and flavonol accumulation in 'merlot' (Vitis vinifera L.) grapes during ripening. *Frontiers in Plant Science* 2020, 11,1095. https://doi.org/10.3389/fpls.2020.01095.
63. Jordão, A.M.; Ricardo-da-Silva, J.M. Evolution of Proanthocyanidins during Grape Maturation, Winemaking, and Aging Process of Red Wines. *Red Wine Technology Elsevier, Academic Press* 2018, pp. 177–193, ISBN: 978-0-12-814399-5.

64. Jordão, A.M.; Ricardo-da-Silva, J. M. Chapter 12 - Evolution of Proanthocyanidins During Grape Maturation, Winemaking, and Aging Process of Red Wines. *Red Wine Technology* 2019, pp. 177-193. https://doi.org/10.1016/B978-0-12-814399-5.00012-8.
65. Niculescu, V.-C.; Paun, N.; Ionete, R.-E. The Evolution of Polyphenols from Grapes to Wines. *Grapes and Wines* 2018.https://doi.org/10.5772/intechopen.72800.
66. Ortega, T.; De La Hera, E.; Carretero, M.E.; Gomez-Serranillos, P.; Naval, M.V.; Villar, A.M.; Prodanov, M.; Vacas, V.; Arroyo, T.; Hernandez, T.; Estrella, I. Influence of grape variety and their phenolic composition on vasorelaxing activity of young red wines. *European Food Research and Technology* 2008, 227, pp. 1641–1650. https://doi.org/10.1007/s00217-008-0888-9.
67. Allegro, G.; Pastore, C.; Valentini, G.; Filippetti, I. The evolution of phenolic compounds in vitis vinifera l. red berries during ripening: analysis and role on wine sensory—a review. *Agronomy* 2021, 11, pp. 1–14. https://doi.org/10.3390/agronomy11071289.
68. Nogales-Bueno, J.; Hernández-Hierro, J.M.; Rodríguez-Pulido, F.J.; Heredia, F.J. Determination of Technological Maturity of Grapes and Total Phenolic Compounds of Grape Skins in Red and White Cultivars during Ripening by near Infrared Hyperspectral Image: A Preliminary Approach. *Food Chemistry* 2014, 152, pp. 586–591. https://doi.org/10.1016/j.foodchem.2013.12.030.
69. Lisjak, K., Lelova, Z., Žigon, U., Bolta, Š.V.; Teissedre, P.L.; Vanzo, A. Effect of extraction time on content, composition and sensory perception of proanthocyanidins in wine-like medium and during industrial fermentation of cabernet sauvignon. *Journal of the Science of Food and Agriculture* 2020, 100, pp. 1887–1896. https://doi.org/10.1002/jsfa.10189.
70. Guchu, E.; Ebeler, S. E.; Lee, J.; Mitchell, A. E. Monitoring selected monomeric polyphenol composition in pre- and post-fermentation products of Vitis vinifera L. cv. Airén and cv. Grenache noir. *LWT-Food Science and Technology* 2015, 60(1), pp. 552–562. https://doi.org/10.1016/j.lwt.2014.09.019.
71. Yacco, R. S.; Watrelot, A. A.; Kennedy, J.A. Red Wine Tannin Structure–Activity Relationships during Fermentation and Maceration. *Journal of Agricultural and Food Chemistry 2016*, 64 (4), pp. 860-869. https://doi.org/10.1021/acs.jafc.5b05058.
72. Ghanem, C.; Taillandier, P.; Rizk, Z.; Nehme, N.; Souchard, J. P.; Rayess, Y. Evolution of Polyphenols during Syrah Grapes Maceration: Time versus Temperature Effect. *Molecules* 2019, 24 (15), 2845, https://doi.org/10.3390/molecules24152845.
73. He, F.; Pan, Q.H.; Shi, Y.; Duan, C.Q. Chemical synthesis of proanthocyanidins in vitro and their reactions in aging wines. *Molecules* 2008, 13, pp. 3007–3032.https://doi.org/10.3390/molecules13123007.
74. McRae, J.M.; Schulkin, A.; Kassara, S.; Holt, H.E.; Smith, P.A. Sensory properties of wine tannin fractions: implications for in-mouth sensory properties. *Journal of Agricultural and Food Chemistry United States* 2013, 61, pp. 719–727. https://doi.org/10.1021/jf304239n.
75. Moreno-Olivares, J.; Paladines-Quezada, D.; Giménez-Bañón, M.; Bleda-Sánchez, A.; Cebrián-Pérez, A.; Gómez-Martínez, J.; Gil-Muñoz, R. Proanthocyanidins composition in new varieties descended from Monastrell. *Science of food and Agriculture* 2023, 103(10), pp. 5039-5049. https://doi.org/10.1002/jsfa.12578.
76. Segade, S.R.; Bautista-Ortín, A.B.; Paissoni, M.A.; Giacosa, S. Changes in Skin Flavanol Composition as a Response to Ozone-Induced Stress during Postharvest Dehydration of Red Wine Grapes with Different Phenolic Profiles. *Journal of Agricultural and Food Chemistry* 2020, 68 (47), pp. 13439-13449. https://doi.org/10.1021/acs.jafc.0c04081.
77. Gil-Muñoz, R; Moreno-Olivares, J.; Paladines-Quezada, D.; Cebrían-Pérez, A.; Fernández-Fernández, J.; High anthocyanin level of grape hybrids from Monastrell and their wines. *International Journal of Horticulture & Agriculture* 2018, 3, pp. 1–8. https://doi.org/10.15226/2572-3154/3/2/00122.
78. Pérez-Porras, P.; Belén Bautista-Ortín, A.; Jurado, R.; Gómez-Plaza, E.. Using high-power ultrasounds in red winemaking: Effect of operating conditions on wine physico-chemical and chromatic characteristics. *LWT* 2021, 138, 110645. https://doi.org/10.1016/j.lwt.2020.110645.
79. Mosele, J.; Souza da Costa, B.; Bobadilla, S.; Motilva, M.J. Phenolic Composition of Red and White Wine Byproducts from Different Grapevine Cultivars from La Rioja (Spain) and How This Is Affected by the Winemaking Process. *Journal of Agricultural and Food Chemistry* 2023, 71 (48), pp. 18746-18757. https://doi.org/10.1021/acs.jafc.3c04660.
80. Gómez-Plaz, E.; Olmos, O.; Bautista-Ortín, A.B. Tannin profile of different Monastrell wines and its relation to projected market prices. *Food Chemistry* 2016, 204, pp. 506–512, https://doi.org/10.1016/j.foodchem.2016.02.124.

81. Gil-Muñoz, R.; Bautista-Ortín, A.B.; Ruiz-García, Y.; Fernández-Fernández, J.I.; Gómez-Plaza, E. Improving phenolic and chromatic characteristics of monastrell, merlot and syrah wines by using methyl jasmonate and benzothiadiazole. Oeno One 2017, 51, pp. 17–27. https://doi.org/10.20870/oeno-one.2017.51.1.1814.
82. Cosme, F.; Ricardo-da-Silva, J.M.; Laureano, O. Effect of various proteins on different molecular weight proanthocyanidin fractions of red wine during wine fining. *American Journal of Enology and Viticulture* 2009, 60, pp. 74–81, ISSN: 0002-9254.
83. Kwak, S. C.; Cheon, Y. H.; Lee, C. H.; Jun, H. Y.; Yoon, K. H.; Lee, M. Y.; et al. Grape seed proanthocyanidin extract prevents bone loss via regulation of osteoclast differentiation, apoptosis, and proliferation. *Nutrients* 2020, 12(10), 3164. https://doi.org/10.3390/nu12103164.
84. Corrales, M.; Toepfl, S.; Butz, P.; Knorr, D.; Tauscher, B. Extraction of anthocyanins from grape byproducts assisted by ultrasonics high hydrostatic pressure or pulsed electric fields: A comparison. *Innovative Food Science & Emerging Technologies* 2008, 9, pp. 85–91. https://doi.org/10.1016/j.ifset.2007.06.002.
85. Bautista-Ortín, A.B.; Busse-Valverde. N.; Fernández-Fernández, J.I.; Gómez-Plaza, E.; Gil-Muñoz, R. The extraction kinetics of anthocyanins and proanthocyanidins from grape to wine in three different varieties. *Journal international des sciences de la vigne et du vin* 2016, 50, pp. 91–100. https://doi.org/10.20870/oeno-one.2016.50.2.781.
86. Nallathambi, R.; Poulev, A.; Zuk, J. B.; Raskin, I. Proanthocyanidin-rich grape seed extract reduces inflammation and oxidative stress and restores tight junction barrier function in Caco-2 colon cells. *Nutrients 2020*, 12(6), 1623. https://doi.org/10.3390/nu12061623.
87. Natolino, A.; Passaghe, P.; Brugnera, G.; Comuzzo, P. Intensification of grape marc (Vitis vinifera) exploitation by subcritical water-ethanol extraction: Effect on polyphenol bioactivities and kinetic modelling. *Journal of Food Engineering* 2024, 381, 112185. https://doi.org/10.1016/j.jfoodeng.2024.112185.
88. Boulet, J.-C.; Ducasse, M.-A.; Cheynier, V. Ultraviolet Spectroscopy Study of Phenolic Substances and Other Major Compounds in Red Wines: Relationship between Astringency and the Concentration of Phenolic Substances: UV Spectroscopy of Red Wine Components. *Australian Journal of Grape and Wine Research* 2017, 23, pp. 193–199.https://doi.org/10.1111/ajgw.12265.
89. Jiménez-Martínez, M.D.; Bautista-Ortín, A.B.; Gil-Muñoz, R.; Gómez-Plaza, E. Fining with purified grape pomace. Effect of dose, contact time and varietal origin on the final wine phenolic composition. *Food Chem Elsevier Ltd* 2019, 271, pp. 570–576. https://doi.org/10.1016/j.foodchem.2018.08.009.
90. Bautista-Ortín, A.B.; Ruiz-García, Y.; Marín, F.; Molero, N.; Apolinar-Valiente, R.; Gómez-Plaza, E. Remarkable proanthocyanidin adsorption properties of monastrell pomace cell wall material highlight its potential use as an alternative fining agent in red wine production. *Journal of Agricultural and Food Chemistry* 2015, 63, pp. 620–633, https://doi.org/10.1021/jf503659y.
91. Tu, M.; Fang, J. H.; Zhao, R. K.; Liu, X. Y.; Yin, W. C.; Wang, Y.; Wang, X. H.; Wang, X. P.; Fang, Y. L. CRISPR/Cas9-mediated mutagenesis of VvbZIP36 promotes anthocyanin accumulation in grapevine (Vitis vinifera). *Horticulture Research* 2022, 9, uhac022. https://doi.org/10.1093/hr/uhac022.
92. Gil-Muñoz, R.; Moreno-Olivares, J. D.; Paladines-Quezada, D. F.; et al. Elicitors: a strategy to improve phenolic composition in wines. Acta *Horticulturae* 2020, 1274, pp. 9-16. https://doi.org/10.17660/ActaHortic.2020.1274.2.
93. Gil Cortiella, M.; Úbeda, C.; del Barrio-Galán, R.; Peña-Neira, A. Impact of berry size at harvest on red wine composition: a winemaker's approach. *Journal of the Science of Food and Agriculture* 2020, 100, pp. 836–845. https://doi.org/10.1002/jsfa.10095.

Citation: Arseni, A.; Crudu, S. The role of procyanidins in grapes and wines: effects on quality and composition. *Journal of Engineering Science* 2024, XXXI (4), pp. 175-192. https://doi.org/10.52326/jes.utm.2024.31(3).01.

Submission of manuscripts: jes@meridian.utm.md